Wave Rotor Application for Micro Gas Turbines

(Alternative Format Thesis)

Tuechler, Stefan

Award date:
2020

Awarding institution:
University of Bath

Wave Rotor Application for Micro Gas Turbines

submitted by

Stefan Tüchler

for the degree of Doctor of Philosophy

of the

University of Bath

Department of Mechanical Engineering

May 2020

Contents

List of Figures

Acknowledgements

First and foremost, I would like to thank my supervisor Dr. Colin Copeland for his active support throughout my thesis, inspiring discussions and invaluable guidance through the challenges of the project.

I would also like to gratefully acknowledge the help of Kevin Gray, whose expertise in design helped realise the experimental campaign and guaranteed its successful completion.

Furthermore, I would like to express my sincere gratitude to my colleagues at PVRC/IAAPS for their support throughout my research, namely Adamos Adamou, Dr. Zhihang Chen, Dr. Tomasz Duda, Dr. Ian Kennedy, Dr. Zheng Liu, Kate Powers, Dr. Giovanni Vorraro, Dr. Yang Zhang. It was a pleasure working with and learning from you all.

I would like to specifically acknowledge Dr. Pavlos Dimitriou for organising my research stay in Kōriyama, which allowed me to gain experience in combustion modelling and to have a fantastic time in Japan.

Furthermore, I would like to thank Dr. Julien Hoessler for the invaluable opportunity of applying my skills and gaining experience in the thrilling world of Formula 1 at McLaren Racing.

My parents, Maria and Helmut as well as my sister Eva and brother Thomas for their unflagging support throughout my time abroad.

Finally, I would like to thank my partner, Alice, for her unwavering support and sheer endless patience during my PhD.

Abstract

There is an increasing demand for compact, portable and endurable power sources in both the civilian and military markets. Gas turbines are a proven technology excelling at high energy and power density, reliability and flexibility. However, downscaling turbomachinery entails severe penalties in component and system efficiency as well as service life due to increased rotational speeds, greater tip clearance and larger relative roughness effects.

In this thesis, an alternative to turbomachinery is proposed using on a non-axial, throughflow wave rotor turbine that combines shaft power extraction as well as fluid compression and expansion through shock and rarefaction waves within a single rotating device. The thesis is written in the alternative thesis format and is based on five academic articles that address the performance characteristics of such a pressure-exchange device.

The first paper introduces the concept of a micro-wave rotor gas turbine based on a throughflow wave rotor with non-axial channel shape. The study uses a time-marching quasi-one-dimensional wave action model that is able to accurately capture the wave pattern within a wave rotor channel. The model is coupled with a steady-flow combustor model and identifies leakage and combustor pressure drop as major performance affecting parameters.

The second publication addresses an experimental study centred on an innovative four-port, three-cycle micro-wave rotor. The study seeks to characterise the wave rotor and further elaborates on the challenges in exploiting wave rotor technology. In addition, reasonably high compression and expansion efficiencies are achieved. In the third paper, the results from the second paper are then used in conjunction with literature data to validate and calibrate the quasi-one-dimensional model.

The fourth paper introduces a shape-optimisation study that seeks to enhance the shaft power output of the baseline wave rotor turbine. To do so, a reduced order quasi-two-dimensional transient CFD model is coupled to a hybrid algorithm. The optimisation technique trains a Kriging surrogate model with data from a genetic algorithm and alternates the search area based on global exploration and local exploitation, thus ensuring improved coverage of the design space compared to standard evolutionary algorithms. The optimisation routine results in a wave rotor candidate design that predicts a power output improvement of 80%. The numerical results indicate that the increase in shaft power stem from increased incidence losses leading to a 3% drop in pressure ratio.

Finally, the fifth and final paper verifies the numerical results through an

experimental campaign comparing both a baseline and an optimised rotor. The experimental results support the validity of the reduced-order CFD model to accurately predict performance trends. Implications of the camberline change on performance are discussed as well.

Nomenclature

Ψ	Anti-diffusion flux
γ	Ratio of specific heats
ν	Courant–Friedrichs–Lewy number [-]
ω	Weighting factor
ρ	Density [kg/m^{-3}]
θ	Diffusive flux vector, flux limiter
E	Total energy [J/kg^{-1}]
R	Specific gas constant [J/kg^{-1}K^{-1}]
T	Temperature [K]
U	State vector
A	Anti-diffusion operator
D	Diffusion operator
F	Flux vector
U	State vector
c_p	Specific heat capacity [J/kg^{-1}K^{-1}]
p	Pressure [Pa]
r	Gradient
t	Time [s]

u	Velocity [m/s]
x	Cell size [m]
TV	Time variation
CFD	Computational fluid dynamics
COP	Coefficient of performance
EGR	Exhaust gas recirculation
FAE	Fresh air exhaustion
FCT	Flux corrected transport
HPA	High pressure air
HPG	High pressure gas
LDA	Laser Doppler anemometry
LPA	Low pressure air
LPG	Low pressure gas
MRF	Multiple reference frame
PWS	Pressure wave supercharger
RAS	Robotic and autonomous systems
TVD	Time variation diminishing
UAS	Unmanned aircraft systems

Chapter 1

Introduction

1.1 Thesis Motivation

Over recent years, a growing demand for robotic and autonomous systems (RAS) in both the civilian and defence markets has developed. Applications range from unmanned aircraft systems (UAS) to autonomous marine robots and mobile power packs used in the military [1]. These devices are compact, but do require high energy dense power sources in order to operate continuously for extended periods of time. At present, battery systems fail to meet these requirements due to low energy density and large volume required [2].

Gas turbines, on the other hand excel at high specific energy and power density [3]. Moreover, they are a well established technology, compact in size, reliable and can accommodate various types of fuels [4]. However, the performance of gas turbines is significantly affected by downsizing. In particular, downscaling a given design to match a certain set of requirements for lower power output entails substantial performance penalties pertaining to efficiency, design and operation. In order to maintain similar enthalpy levels and pressure changes it is necessary to run at considerably larger rotational speeds. This, in turn, has knock-on effects on service life and reliability as well as on design decisions, for example with respect to the choice of bearings. In addition, heat transfer between compressor and turbine sides become more pronounced the smaller the size [5]. Also, as most radial turbomachinery is unshrouded, tip leakage losses increase as well as a larger relative surface roughness. All these factors combined contribute to a decline in both component efficiencies and thermal efficiency [6–8].

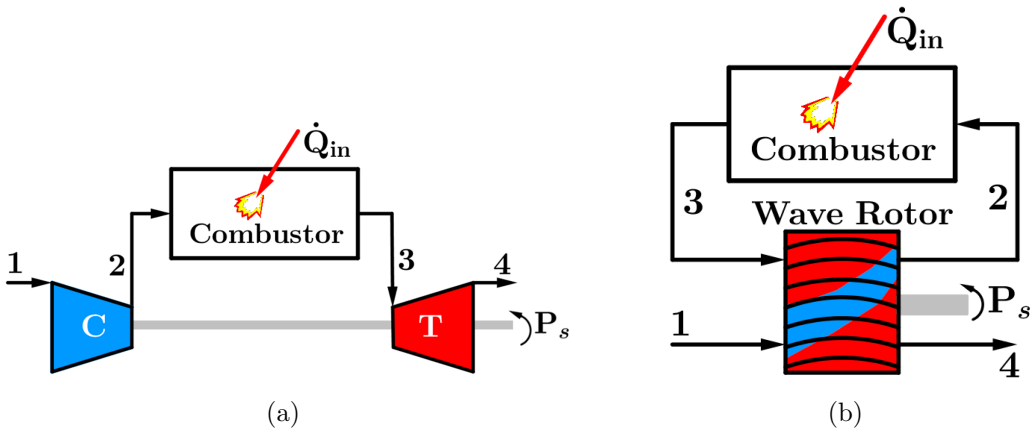

Figure 1-1: (a) Depicts a schematic for a gas turbine without heat recuperation consisting of an axial or radial compressor, the combustion chamber, where chemical energy is converted into heat and a turbine extracts and transfers work via a shaft to the compressor. (b) The wave rotor concept combines both features in one device. It houses two streams, namely cold air being compressed by means of shock compression and directed to the combustor while a hot gas stream is expanded through a series of expansion waves and expelled to the ambient.

Substituting the compressor and turbine, as seen in the schematic in Figure 1-1(a), with a non-axial wave rotor, as illustrated in Figure 1-1(b), combines compression, expansion and shaft power generation within a single device, which can potentially mitigate several of the aforementioned shortcomings.

1.2 Wave Rotor: Operating Principle

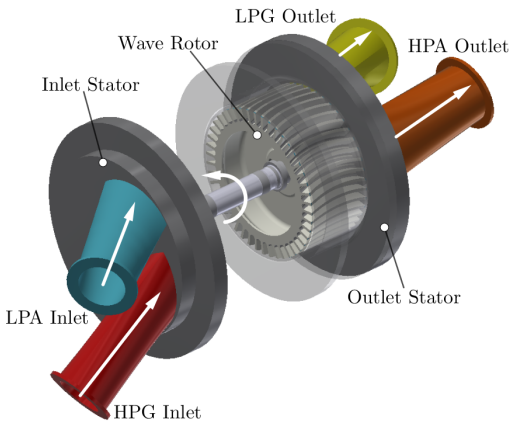

Figure 1-2: Main wave rotor components consisting of stator endplates and spinning rotor.

Wave rotors are unsteady flow devices that consist of an array of channels or passages aligned along a cylindrical drum, shown in Figure 1-2(a). The example shown here features one dominant flow direction from the inlet side towards the outlet side. To

each side of the spinning rotor, stator endplates are located that house port openings connected to in- and outlet manifold and combustor. The fundamental principle relies on the exchange of energy between two fluid media, namely exhaust gas and fresh air, through shock and expansion waves. These waves are triggered by periodically exposing the port openings to the rotating rotor channels.

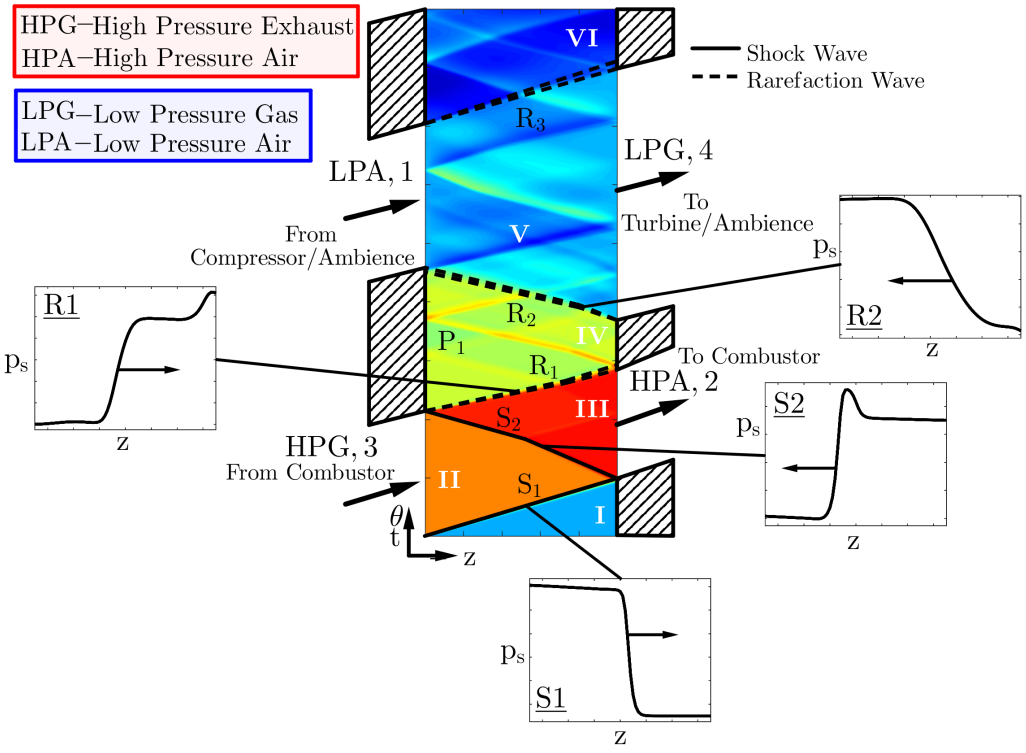

Figure 1-3: Unfolded view of the wave pattern of a four-port throughflow wave rotor showing in the z-θ- or z-t-plane. As the channel passes through the port arrangement it is compressed twice by primary (S1) and secondary S2 shock waves before entering the HPA port. Closure of the HPG port and opening of the LPG port spark rarefaction waves, R1 and R2, that expand the exhaust gases before they are expelled through the LPG port.

The concept becomes clearer when unwrapping the circumference and plotting the wave pattern on a two-dimensional z-θ-plane, as shown in Figure 1-3. This allows one to follow a channel as it travels along the circumference and passes port openings in the process. In the illustrated example, a four-port throughflow (fluid flow only in one direction) rotor is depicted. The device features two high pressure ports, namely a high pressure exhaust gas (HPG) and high pressure air (HPA), that are connected to the combustion chamber. It further shows two low pressure ports, the low pressure air intake (LPA), from where the fresh air is drawn (either from ambient or from an upstream compressor) into the rotor channels, and the low pressure gas port (LPG),

through which the hot exhaust gases are expelled to the ambient or alternatively further expanded through an additional turbine.

Initially, the fluid within the passage is assumed to be at rest and uniform. By exposing the left hand side of the channel to the high pressure, high temperature exhaust gas from the combustor (HPG) sets off a right travelling, primary shock wave (S1). Upon reaching the other end of the channel the HPA port is opened and the shock wave is reflected resulting in a secondary, left running shock wave (S2). These two shock waves compress the incoming fresh air and essentially represent the work done by a compressor in the traditional gas turbine.

Closing the HPG port sparks an expansion fan or rarefaction wave (R1), which expands the exhaust gases to an intermediate pressure level. Impingement of the head of R1 on the right hand side marks the closure of the HPA port, which usually brings about a hammer shock like pressure wave. Opening the low pressure exhaust port (LPG) leads to further expansion of the gases (R2) before the gases are ejected to the ambient. The low pressure inlet port opens as soon as (R2) reaches the left hand side of the channel. Premature opening of the LPA port could lead to flow reversal into the opening port. Finally, the closure of the LPA port generates weak expansion waves before the cycle is repeated.

The wave rotor houses both compressed and expanded streams within the same domain. In throughflow designs the wave pattern in Figure 1-3 generally corresponds to the temperature distribution given in Figure 1-4(a). In such a scenario, scavenging of the channels with fresh charge through the LPA port is insufficient ($L_{p,c} < L$) and a particular amount of exhaust gases coming from the combustor are rerouted back to the combustor inlet. This is termed exhaust gas recirculation (EGR) and corresponds to scenario I in Figure 1-4(b).

Similarly, if the velocity of the high enthalpy flow through the HPG port cannot is too low ($L_{p,h} < L$) to direct the cold, compressed gas stream towards the HPA outlet port, fresh air is expelled unused through the LPG port and does not take part in the combustion process. This is termed fresh air exhaustion (FAE). In general, these two phenomena are dictated by the ratio of inlet mass flow rates through HPG and LPA port as well as by the backpressure by both LPG and HPA ports. One parameter frequently used is the ratio of the inlet mass flow rates,l termed loop flow ratio λ. This is given in Equation 1.2.1. Variation in λ for a given $\dot{m}_{\mathrm{HPG}}$ will determine the mass entering through the LPA port and thus define the penetration length $L_{p,c}$

$$\lambda = \frac{\dot{m}_{\mathrm{HPG}}}{\dot{m}_{\mathrm{LPA}}} \tag{1.2.1}$$

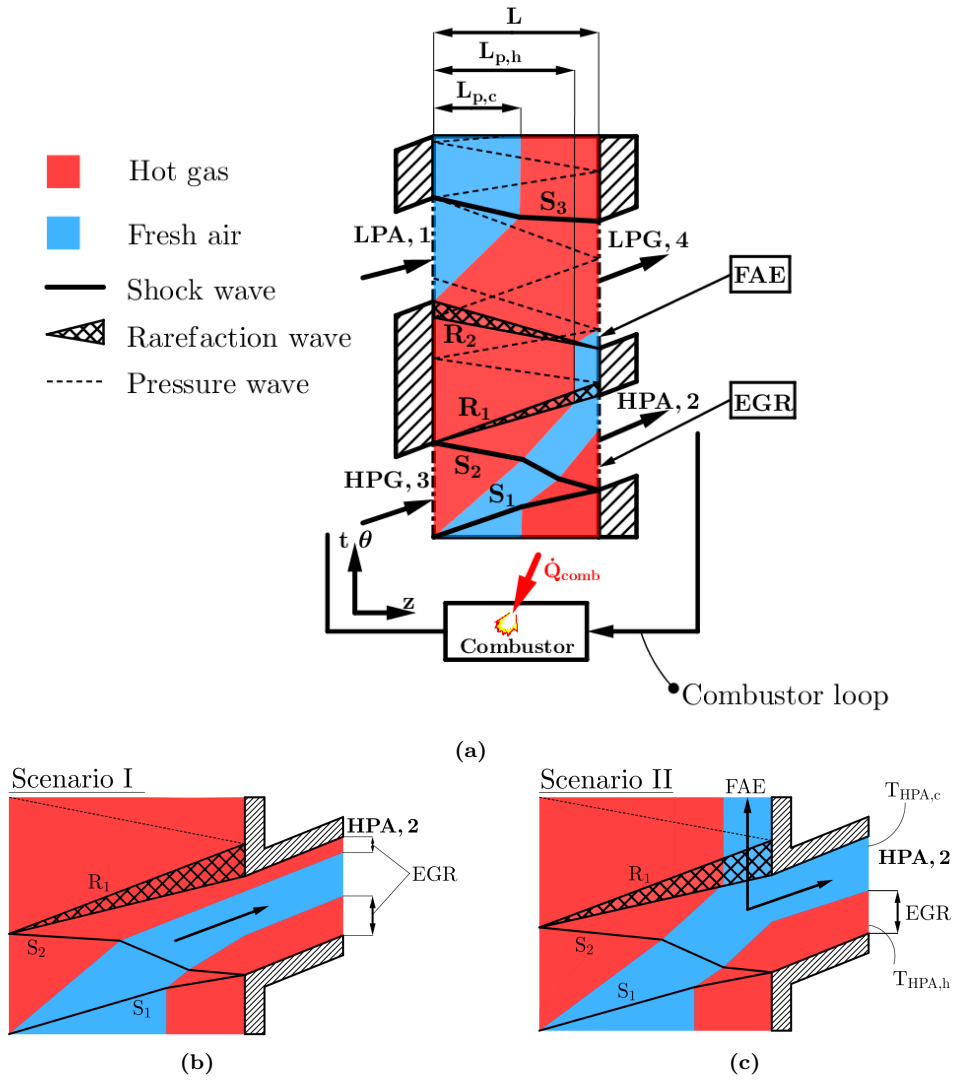

Figure 1-4: (a) Schematic showing distribution of compressed and expanded streams within the rotor leading to fresh air exhaustion (FAE) through the LPG port and exhaust gas recirculation (EGR) through the HPA port. Variations in hot and cold inlet mass flow rates and backpressure dictate the amount of EGR and FAE. This can lead to scenario in (b), where only EGR without FAE occurs, while (c) outlines the more general situation where both EGR and FAE take place.

One distinct advantage of such an unsteady flow device over steady (e.g. diffusers) or crypto-steady[1] flow devices (e.g. turbomachinery) is illustrated in Figure 1-5.

[1]Crypto-steady flow denotes flow that is steady in a certain (moving) reference frame, such as turbomachinery under steady operating conditions.

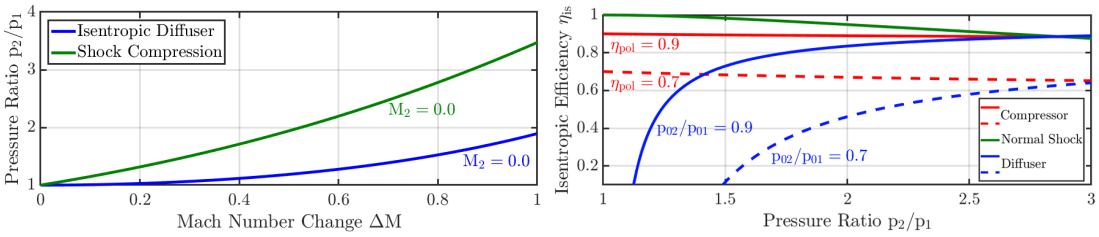

(a) (b)

Figure 1-5: (a) Static pressure ratio plotted versus Mach number change for steady (diffuser - lower, blue curve) and unsteady (moving, normal shock wave - upper green curve) compression assuming that the fluid Mach number downstream of the device is zero. For a given change in Mach number, unsteady compression features a higher pressure ratio. (b) Isentropic efficiency plotted versus static pressure ratio for compressor (red curves), diffuser (blue curve) and shock compression (green curve). For shock compression no wall friction or shock-boundary layer interaction was considered. The compressor performance was derived using different polytropic efficiencies and for the diffuser different total pressure losses were considered. It is shown that shock compression represents a highly efficient technique for low to medium pressure ratios.

In comparison with steady flow devices (lower, blue curve in Figure 1-5(a)) and assuming the Mach number downstream is reduced to zero, shock compression (top, green curve) as witnessed in a wave rotor accounts for a larger static pressure ratio for any given Mach number change. Furthermore, as diffusers often become rather large in size to prevent undesired flow separation, compression in an unsteady fashion yields higher pressure ratios over a smaller distance. Figure 1-5(b) exhibits isentropic efficiency as a function of pressure ratio and compares compression through a moving shock without wall friction (solid green line), a compressor (blue lines) with different polytropic efficiencies (0.9 and 0.7) and diffusers (red lines) with different total pressure loss (0.1 and 0.3). It becomes apparent that for static pressure ratios of below approximately three, unsteady compression features higher isentropic efficiency. This signifies that for the same pressure ratio, several stages of diffusion or increases in kinetic energy are necessary to obtain the same pressure ratio. As a result, unsteady devices can be built compactly. Nonetheless, it shall be added that wall friction and potential shock-boundary layer interaction would reduce shock efficiency.

The geometry of a wave rotor does not feature any complex surfaces and comprises relatively simple channel shapes facilitating the manufacturing process. Furthermore, since the port arrangement is a function of the circumferential velocity, it is possible to run the wave rotor at considerably lower speeds than turbomachinery of comparable size making it less susceptible to high speed fatigue. The rotational speed increases when scaled down, however, although they are still lower than turbomachinery of similar dimension. Alternating exposure to hot and cold gases introduces

a certain level of self-cooling capabilities that potentially allows to running a higher combustor outlet temperature to raise thermal efficiency.

1.3 Thesis Structure

This PhD thesis is structured in five chapters and presented as thesis by publication. A total number of five conference and journal publications form the main five chapters of this thesis. These are summarised in Table 1.1. While each paper serves distinctive objectives, there do exist particular similarities and overlaps. This is the case between Paper III and Paper V, which build on the developed quasi-one-dimensional model introduced in Paper I. In addition, the experimental approach used throughout this study is shared by both Paper II and Paper V. To ensure continuity and cohesion between the chapters, each paper is preceded by a brief introduction that summarises and contextualises the presented work within the overarching narrative. In addition, a brief conclusion at the end of each paper summarises main points.

Table 1.1: List of articles in this thesis.

Number	Thesis chapter	Publication	Status	Objective
I	2.2	S. Tüchler and C.D. Copeland, "Parametric Numerical Study on the Performance Characteristics of a Micro-Wave Rotor Gas Turbine," *Proceedings of the International Gas Turbine Congress 2019 Tokyo*, IGTC-2019-200, Nov, 2019, Tokyo, Japan. [122]	Published	Propose Q1D model of wave rotor based gas turbine
II	3.2	S. Tüchler and C.D. Copeland, "Experimental Results from the Bath μ-Wave Rotor Turbine Performance Tests," *Journal of Energy Conversion and Management*, Vol. 189, pp.33-48, 2019. [123]	Published	Explore wave rotor turbine experimentally
III	3.3	S. Tüchler and C.D. Copeland, "Validation of a Numerical Quasi One-Dimensional-Model for Wave Rotor Turbines with Curved Channels," *Journal of Engineering for Gas Turbines and Power*, GTP-19-1313, Vol. 142, No. 2, pp. 0210171-02101715, 2020. [124]	Published	Validate Q1D model against experiments and literature data
IV	4.2	S. Tüchler and C.D. Copeland, "Numerical optimisation of a micro-wave rotor turbine using aquasi-two-dimensional CFD model and a hybrid algorithm," *submitted to Shock Waves*, SHOC-D-19-00092, 2020.	Under review	Propose optimisation framework for wave rotor turbines
V	4.3	S. Tüchler and C.D. Copeland, "Experimental and Numerical Assessment of an Optimised, Non-Axial Wave Rotor Turbine," *Applied Energy*, Vol. 268, 115013, 2020. [126]	Published	Validate optimisation results and understand effect on gas dynamics

Having set out the background and context of the research, the following sections present a literature review of wave rotor machinery. The review begins with a general introduction to the various fields of application of wave rotors, before examining numerical approaches for design and gas dynamic modelling in more detail. This starts with simple analytical relations based on Rankine-Hugoniot relations and builds more complexity with one-dimensional and higher dimensional computational fluid dynamics (CFD) methods. Finally, experimental approaches applied to wave rotors are discussed.

In the subsequent Chapter 2, a numerical quasi-one-dimensional model is introduced that computes the flow field within a single wave rotor channel as it rotates around the circumference. The model is then used to estimate the performance potential of a micro-wave rotor gas turbine, identifying the most influential performance affecting parameters.

Chapter 3 describes the experimental results from the initial proof-of-concept experiments of a non-axial, small-scale wave rotor turbine. The tests focus on the rotor itself and use an open-loop test layout for performance characterisation to evaluate the interaction between loop flow ratio, leakage and speed sensitivity. The results from the experimental tests are then used to validate the numerical model along with data available from the open literature.

Chapter 4 is dedicated to the optimisation of the initial prototype for higher power output. To this end, a combined CFD-hybrid algorithm approach is introduced. The optimised rotor is then tested and compared against the baseline design in terms of global performance variables and in addition, effects of the change in channel camber on gas dynamics are discussed.

Finally, Chapter 5 commences with an overall discussion of the results, including strengths and limitations of this research, concluding with a discussion of the outlook of future work.

1.4 Literature Review

Wave rotors have been the subject of a considerable number of research studies examining the performance of various types of pressure exchangers through numerical simulation [9–14, 18–21, 28–34, 83, 85] and experimental testing [96–102, 108, 111, 112, 115–117, 120, 121]. Various types of wave rotors have been proposed ranging from axial to radial machines and from reverse-flow to throughflow types. A brief summary of these types of wave rotors is given in Figure 1-7. Wave rotors can appear in both axial and radial shapes, as given in Figure 1-7(a) and (b). Additionally, along with

the previously mentioned throughflow type, shown in Figure 1-7(c), it also possible to arrange the ports differently to enforce a change in flow direction within the channels. This results in the reverse-flow design shown in Figure 1-7(d). Reverse-flow designs do not necessarily entail EGR, but leave a particular amount of gas trapped within the channels not being expelled through any of the outlet ports.

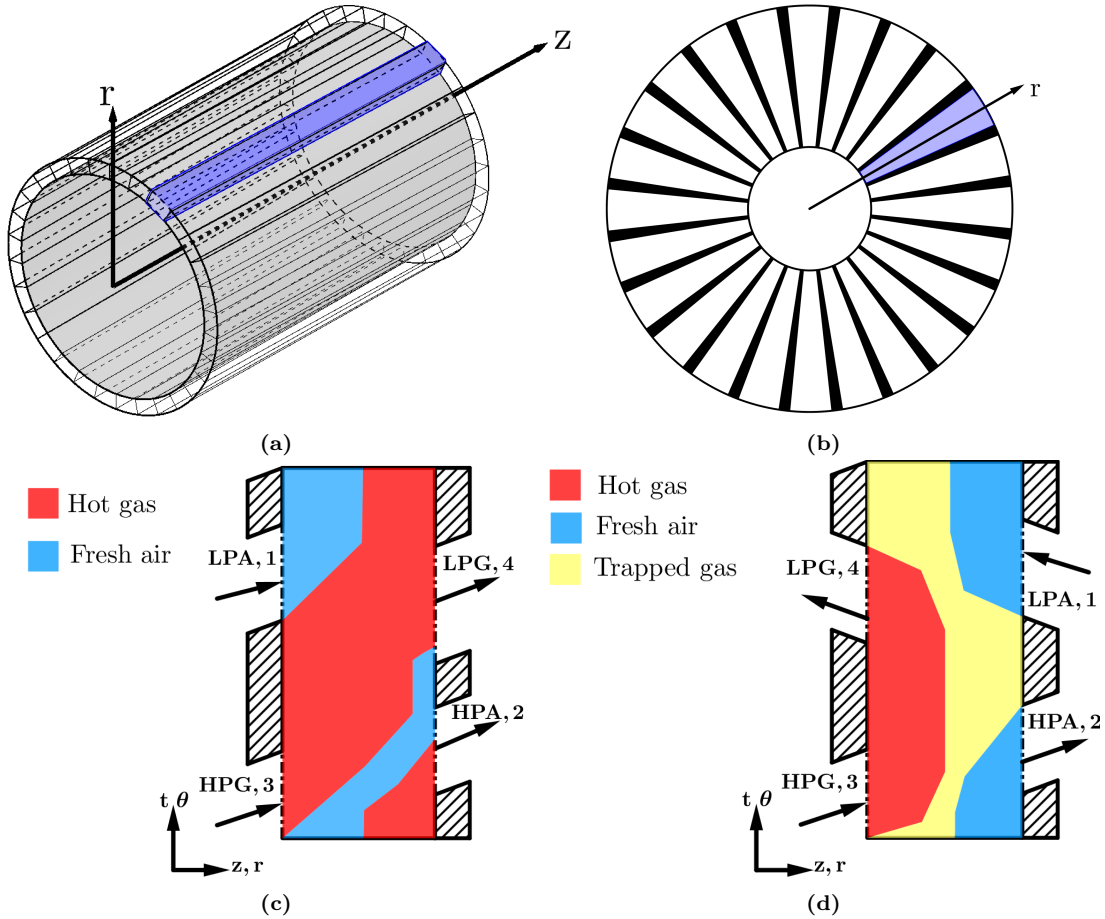

Figure 1-7: Wave rotors can be classified into a) axial, where the primary flow direction is parallel to the rotational axis and b) radial types, where the flow direction predominantly follows the radial direction. Additionally, wave rotors can either follow one primary flow direction across all ports, as it is the case with c) throughflow devices. Alternatively the flow can turn inside the channels leading to a d) reverse-flow design. In this case, it is possible to inhibit internal EGR. However, a certain amount of gas remains trapped within the channels.

Applications are targeted at enhancing thermal cycles and thus reducing energy consumption. A summary of the most prominent wave rotor applications is presented in Figure 1-8. The most commercially successful wave rotor application is found for both diesel and gasoline based internal combustion engines [36–40] as a pressure wave supercharger (PWS). The wave rotor functions in a similar fashion as a conven-

tional turbocharger by harnessing residual heat in the exhaust gases to pressurise the incoming charge air. Assigned the trade name Comprex® it has found its way into passenger vehicles [41, 42] and has been tested by a number of manufacturers [43, 44]. Guzzella et al. [39] consider the PWS system's excellent dynamic behaviour to be superior to waste heat turbochargers, with potential benefits to fuel economy noted. This is confirmed by Lei et al. [38], who further point out enhanced exhaust emissions as a consequence to the wave rotor's inherent internal exhaust gas recirculation (EGR).

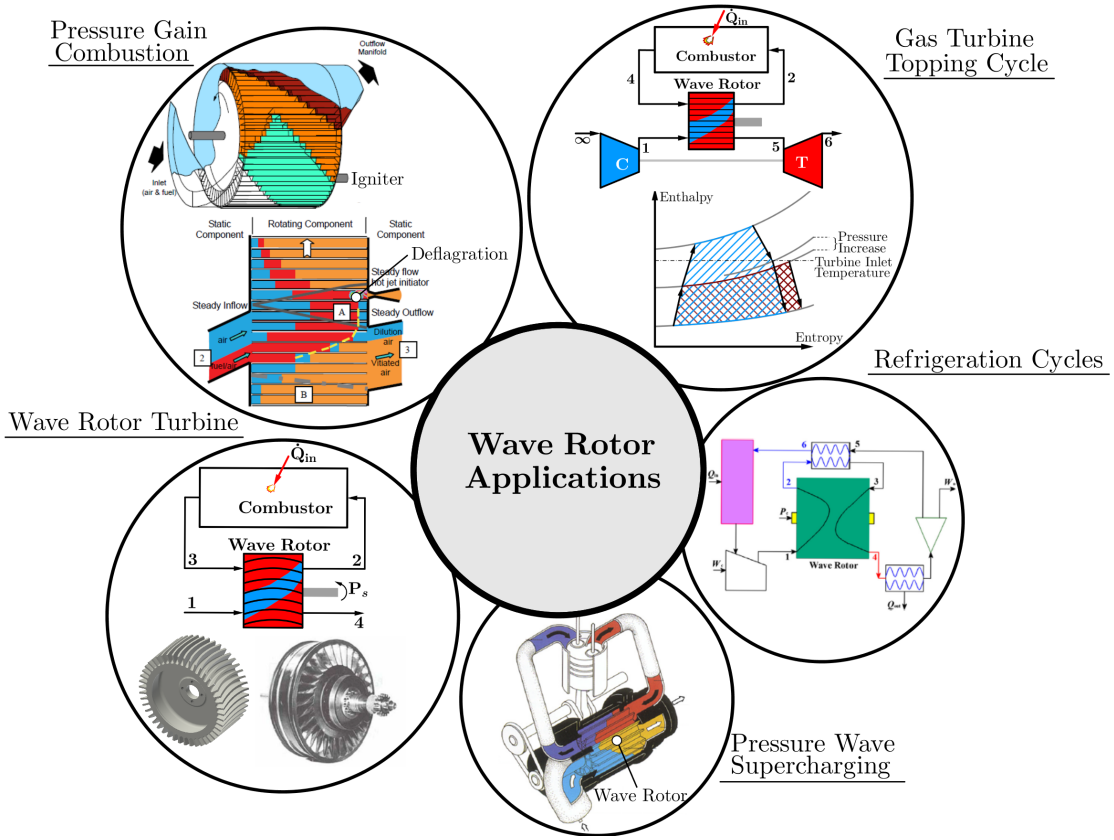

Figure 1-8: Summary of wave rotor applications aimed at enhancing thermal cycles and reducing energy consumption. These range from gas turbine enhancement through to pressure gain combustion [58, 68], topping cycles [45, 51] and wave rotor turbines [76, 77]. Furthermore, wave rotors can be applied to internal combustion engines as a supercharging devices [38, 40] as well as to refrigeration cycles [71, 73].

Wave rotors have also been suggested as a means to enhance gas turbine cycles, increasing thrust and power output while reducing fuel consumption [45–55]. In this instance, the wave rotor is working together with an axial compressor and turbine arrangement effectively achieving a pressure increase prior to the exhaust gases being expanded through the turbine and thus being able to generating greater power output for a given fuel flow rate. According to Akbari et al. [46] wave rotor topping on sim-

ple gas turbines can increase overall efficiency and work output by up to 34%, despite potential drawbacks in terms of integration, maintenance and additional pipework and weight. For recuperated machines, the potential advantage decreases to below 10% as more of the otherwise wasted exhaust heat is reused to preheat the air prior to the combustor. Welch et al. [47,48] come to similar conclusions for small and intermediate turboshaft engines, assuming additional weight imposed by the wave rotor to be less than 20% of the overall engine weight. However, for large turbofan engines the benefit in fuel consumption reduces to around 5-7%. Wilson and Paxson [52] point out that a performance benefit vanishes, the higher the overall pressure ratio of the gas turbine becomes. Instead of resorting to a pure pressure-exchanger to complement the cycle, Welch [55] and Lenoble [56] suggested gas turbine topping through a wave engine that includes on-rotor combustion, generating additional shaft power. This aims to modify the standard Brayton-cycle towards a Humphrey-cycle, using the constant-volume combustion within the rotor channels and resulting in lower entropy production [66–68]. Extensive research in the field of pressure-gain combustion in wave rotors has been done by Nalim et al. [57–65]. Numerical predictions indicated a 40% pressure gain and 20-30% benefit in fuel savings [59, 60]. On-rotor combustion can accommodate both premixed-deflagration as well as non-premixed combustion and premixed/non-premixed autoignition modes. Furthermore, it is noted that the internal gas dynamics strongly interact with the combustion characteristics leading to potentially higher sensitivity to variations in operating conditions and in particular the fuelling strategy [61]. In addition, leakage and non-uniform temperature distributions and life cycle fatigue due to pressure fluctuations require additional attention.

Refrigerating cycles are another field of application for wave rotors [69–75]. Kharazi et al. [69] substituted a standard condenser with a three-port wave rotor resulting a 22% improvement in the coefficient of performance (COP). Since the wave rotor is used to pressurise, desuperheat and condense the superheated vapour in one single device, a considerably more compact size can be achieved. Hu et al. [70,71,73,75] proposed further modifications to the cycle by using a four-port wave rotor recycling the otherwise wasted expansion work through an additional heat exchanger.

The majority of wave rotor research revolves around axial designs using straight channels. Relatively little research has been done looking at the effect of cambered channels and on exploiting flow energy to extract shaft power. In fact, to the author's knowledge, there have been merely three more or less successful endeavours to produce a functioning wave rotor turbine. The first, most successful and probably best documented was done by Pearson [76, 77] in the mid 1950s in collaboration with the Ruston-Hornsby Turbine Company. The engine consisted of a single cycle wave rotor of

229 mm in diameter and 76 mm in length. Instead of axial passages, a helical shape was applied to cater for momentum change and hence torque extraction. The engine was experimentally tested on a test rig, ran for 300 hours and produced 26 kW (35 bhp) at a design speed of 18,000 rpm. Despite excessive leakage and unsatisfactory scavenging a maximum pressure ratio of 5.4 was achieved and the maximum cycle temperature was 1250 K, while the actual wave rotor temperature was 723 K proving self-cooling capabilities of the wave rotor. What is more is that Pearson ran the engine from 3,000 to 18,000 rpm giving reasonable performance which was enabled using stator pockets [78]. Unfortunately, further research was suspended when the engine was destroyed due to overspeeding and funding was subsequently cancelled.

A couple of years later, General Electric pursued a similar engine [79], also with helical channel shape, although a reverse flow design was chosen. No information is available regarding the size and shape of the channels. However, testing proved to yield very low torque, presumably due to inaccurate flow field calculation [44], albeit it is not stated how much power was generated [80].

The third effort was done by the General Power Corporation, who engaged in wave rotor development for a period of approximately 20 years. According to Akbari et al. [81] the design suffered from excessive blade curvature and proved to yield very low torque upon testing, so that the continuation of the program was abandoned.

More recently, there has been a renewed interest in wave rotors with cambered wall profiles. Weber [78] introduced a compound wave engine concept that combines a wave rotor with slanted channels, a combustor and a conventional precompressor and low- and high pressure turbine. As such, the concept resembles a topped up gas turbine. Lead by Michigan state University and Warsaw University of Technology, the concept was taken up in the early 2000s and modified to incorporate a radial, reverse flow wave rotor [82–85]. Akbari et al. [86, 87] incorporated the external combustion chamber within the wave rotor channels itself to achieve constant-volume combustion and pressure-gain to further enhance efficiency.

1.4.1 Wave Rotor Design and Modelling

1.4.1.1 Analytical Design Procedures

Successful operation of wave rotors depends foremost on the arrangement of ports relative to each other. This in turn is influenced by pressures and temperatures prevailing in these ports, as they dictate the strength of shock and expansion waves. The development of one-dimensional computational codes - despite numerous simplifications - takes considerable effort, while the application of more elaborate

three-dimensional computational fluid dynamics (CFD) software is often restricted by computational resources, particularly bearing in mind the unsteady nature of the flow phenomena. To bypass these shortcomings, several research efforts were dedicated to the generation of a port solution through analytical schemes. These preliminary design procedures are based on thermodynamic considerations, are computationally inexpensive and as such, can be implemented with relative ease. The studies of Akbari and Müller [9,10] introduced a gas dynamic analysis for a reverse flow pressure wave supercharger. The former study, [9], focuses on wave rotor enhanced cycles for gas turbines, while the latter [10] zeros in on pressure wave superchargers, such as for internal combustion engines (ICE). Nonetheless, the design procedures for both follow the same principles. The analysis commences assuming the channel is initially filled with fresh air at zero velocity. It is further assumed that the flow is inviscid, adiabatic and one-dimensional. Finally, expansion waves are considered as thin waves. The computation requires a target wave rotor pressure ratio, combustor pressure loss, compression and expansion efficiencies as well as the total temperature in the low pressure side. Consequently, the charging zone is split into regions according to the trajectory of fresh air and exhaust gases as the channel travels past the ports, as shown in Figure 1-9.

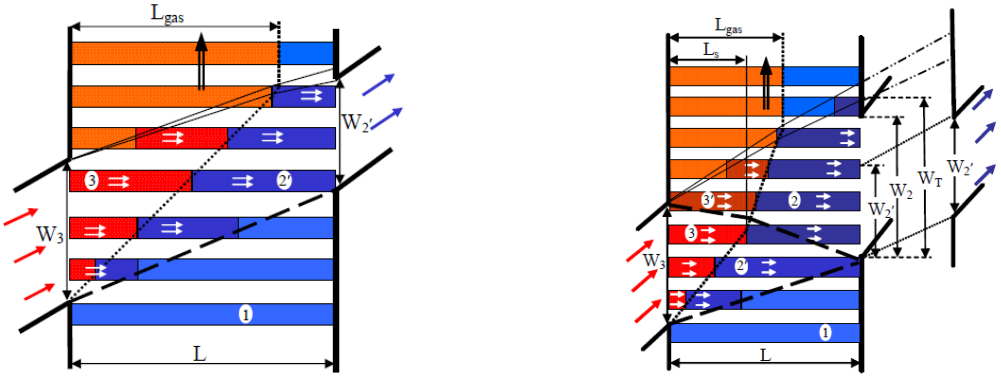

Figure 1-9: High pressure charging zone outlining the demarkation line between exhaust gas and fresh air as a single channel travels along the circumference. Two cases outlining the trajectory of shock and rarefaction waves are given, where (a) represents a simplified situation without a secondary shock wave, while (b) features a secondary shock wave and consequently an additional flow turning point [10].

The procedure then puts forward a number of simultaneous equations that can be solved for the pressure ratios of primary and secondary shock waves along with penetration lengths of the exhaust gases into the wave rotor channel. As a result, one can arrange the charging zone ports such that the arrival of the shock waves coincides with port

opening or closure.

The authors of the two studies presented restrict their gasdynamic procedure to reverse flow configurations, stating that - without giving specific reasons - it be inapplicable for through flow configurations. Pohořelský et al. [53] and Iancu et al. [11] presented an algebraic design process that lends itself to the application of throughflow, reverse flow, as well as any wave engines and wave disk engines. The procedure in both publications is founded on shock wave and expansion wave relations. However, the scheme is not confined to the high pressure region, but allows calculating the entire wave pattern as well as the corresponding air/gas interface. Both studies use more intricate simulation methods in order to validate their algorithm. The former study uses the one-dimensional commercial software GT-POWER along with a two-dimensional CFD simulation in ANSYS Fluent.

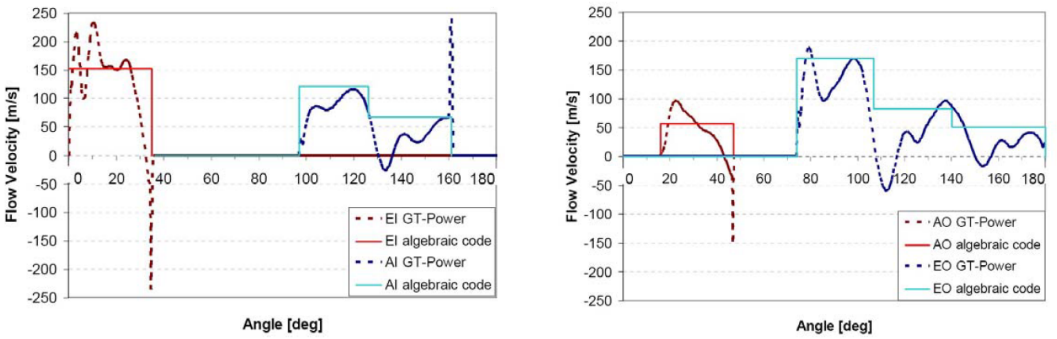

(a) (b)

Figure 1-10: Comparison of port velocity distribution for inlets (a) and outlets (b) for the same port solution predicted by the analytical algorithm and a 1D-wave action code GT power. The algebraic model predicts constant port velocities, while the 1D code reveals considerable variations as well as flow reversals due to misalignment of waves and the port openings and closings [53].

Figure 1-10 gives a comparison of the validation study with GT-Power and depicts the velocity distribution at both inlet and outlet ports. While the analytical model gives constant port velocities, the one-dimensional code takes into account secondary pressure waves and can thus accommodate for a variation in velocity. In addition, it can highlight situations when flow discontinuities impinge prematurely causing flow reversal, which is shown by the negative velocity peaks in the two plots. The 2D-CFD simulation helps confirm the phenomenon of internal EGR and reproduces the respective wave pattern.

The study by Iancu et al. [11] compared the algebraic solution with 1D and 3D-CFD computations regarding the opening and closing times of ports, showing that the algebraic code is well suited to providing an initial port solution, while ensuring a

reasonably small computational time compared to higher order CFD models.

1.4.1.2 One-Dimensional Modelling

The research studies in the previous section illustrate that algebraic models can deliver fairly good initial port solutions. Nevertheless, they rest upon a significant number of simplifications and struggle when one considers flow reversal, or situations when it is inaccurate to consider the fluid to be initially at rest and at uniform temperature. Under such conditions, one-dimensional codes can yield a more in-depth insight into sensitivities and overall performance at acceptable resource costs. In the literature, an extensive and well documented description of 1D modelling of wave rotors was introduced by Paxson at NASA [12–14]. The model devised by Paxson [12] solves the time-dependant Euler equations numerically through an explicit finite volume based method. The code assumes the flow to be adiabatic, inviscid and models air as an ideal gas. The numerical scheme is explicit and solves the hyperbolic system of equations using a Lax-Wendroff time variation diminishing (TVD) scheme based on Roe's method. The TVD method uses a flux limiter, in this case the so called superbee, which ensures the nonphysical oscillations produced by the second order scheme are diminished. Validation of the code is done by comparison with a series of shock tube tests and with experimental data of a pressure divider provided through the literature by Kentfield [16, 17].

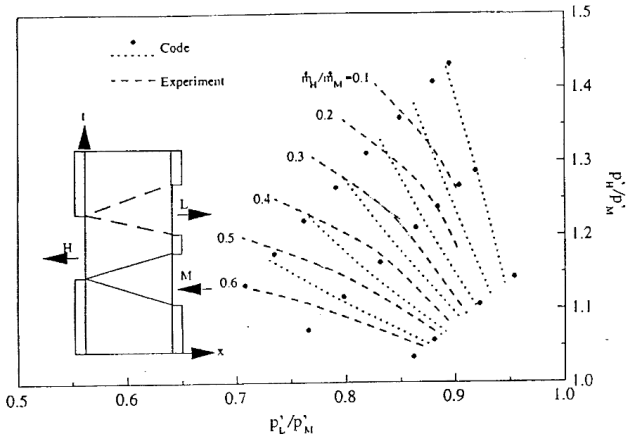

Figure 1-11: Experimental pressure divider performance map compared with numerical results from the NASA 1D wave rotor code. The map shows non-dimensionalised high pressure port total pressure versus low pressure port total pressure. The pressure divider wave pattern (or x-t diagram) is shown as well, outlining the position of the three ports. For the same p_{0L}/p_{0M} the NASA wave rotor code overestimates the high pressure port total pressure p_{0H}/p_{0M} [12].

The principle of a pressure divider is shown in Figure 1-11. Air enters at

medium total pressure on the lower right and is split into two outgoing flows, where one is at a higher stagnation pressure and the other at lower stagnation pressure compared to the inlet pressure. It depicts a pressure divider performance map for both experimental and numerical data. It exhibits curves of constant mass flow ratios and exemplifies that for the same low pressure port total pressure p_{0L}/p_{0M}, the numerical model overpredicts the high pressure total pressure p_{0H}/p_{0M}. The author appoints these discrepancies to a number of factors; firstly, the effect of finite opening and closing time, which results from the fact that a channel is not exposed to the port conditions instantaneously. Secondly, viscous effects, such as momentum loss due to wall friction and thirdly, leakage flows as a result of a finite gap between rotor and stator end plates. Finally, losses due to windage effects and duct losses are not accounted for in the model either.

In an improved version of the initial code, Paxson and Wilson [13] mitigated major sources of error and implemented a procedure to account for non-instantaneous opening and closing of ports by altering the imposed boundary conditions. The authors implemented a mixing zone between the first cell and the boundary, such that the pressure increases more gradually and the generated shock wave travels at reduced speed, such as shown in Figure 1-12.

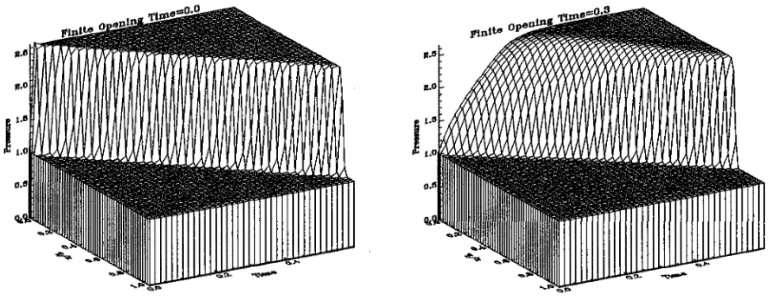

(a) (b)

Figure 1-12: Comparison of shock formation over time in a tube exposed to a high pressure at x/L=0. Not accounting for finite opening time assumes the full pressure is instantly reached, while a more gradual increase in shock formation can be witnessed if the finite opening time is accommodated for [13].

Additionally, source terms were added to account for viscous effects as well as leakage. The enhanced model was then put to the test and the results compared against the experimental data, as shown in Figure 1-13. In relation to the inviscid simulation, the results show better agreement with the experimental data. Furthermore, the authors were able to validate the unsteady data of their model with experimental data from a pressure divider developed at NASA-Lewis [108]. In the experiments, static pressure probes were used to trace the static pressure at three different locations

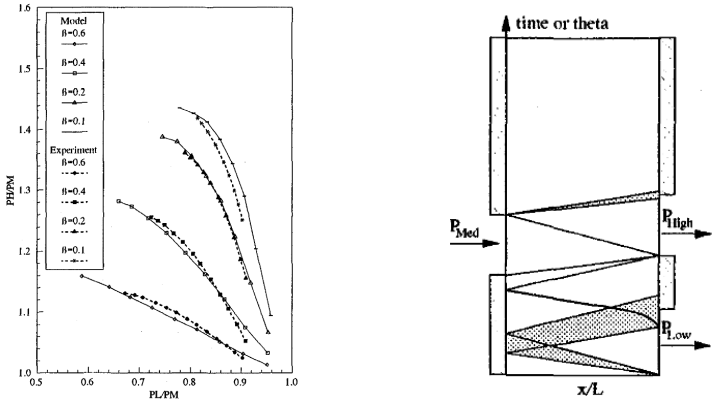

(a) (b)

Figure 1-13: Experimental pressure divider performance map compared with numerical results from an improved NASA 1D wave rotor code. Accounting for leakage, viscous effects and finite opening times results in a better approximation of the experimental data [12].

$x/L = 0.025$, $x/L = 0.5$ and $x/L = 0.975$ during the wave rotor rotation. Normalised pressure distributions along a full rotor rotation at the latter two locations are displayed in Figure 1-14. The predicted traces approximate the trends of the experimental data well. In Figure 1-14 (b), the pressure distribution of the code without leakage model is given as well. It can be seen that the pressure is underpredicted while the low pressure port is open. Conversely, the static pressure is at a higher level than in the experiments just after the high pressure port is closed. This again, emphasizes the knock-on effect of flow leakage on wave rotor performance and accentuates the necessity for it to be taken into account in the modelling stage.

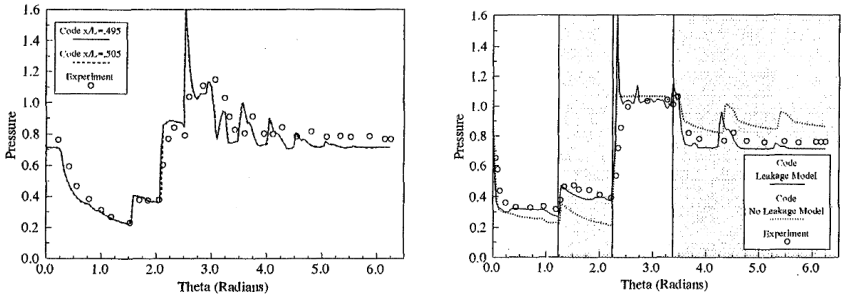

(a) (b)

Figure 1-14: Unsteady and non-dimensionalised static pressure at $x/L = 0.5$ (a) and $x/L = 0.975$ (b) compared with experimental data from NASA-Lewis [108]. The code solution features a pronounced pressure spike at around 2.5 radians at both axial locations. In (b), the pressure trace with and without the leakage model is given. At circumferential positions of around 0 to 2 radians, the static pressure is underpredicted, while the code overpredicts pressure in the vicinity of the high pressure port, from approximately 3 radians onwards [13].

Wave rotor port ducts are usually angled with respect to the axial alignment of the rotating channels, such that the flow in the channels runs entirely axial in a rotating frame of reference. This will, however, not be the case in off-design conditions. Here, the passage walls will turn the misaligned flow to some extent. In their study, Paxson and Wilson [14], address the issue of neglecting the circumferential velocity component for calculating the boundary static properties. The 1D model was modified in order to be able to account for flow turning by defining an effective flow angle $\beta_{eff} \neq \beta_{duct}$. The effective flow angle was calculated according to an empirically derived formula, based on wave rotor test data. The new model was then extensively tested against various wave rotor pressure divider designs, which differed with respect to their length (varied between $L = 0.229$ and $L = 0.457$) and their passage width (achieved by varying the number of passages from 65 to 130). For each of these configurations a different loss mechanism will be dominant. For instance, narrow passages signify a reduced effect of finite opening time or a smaller length represents reduced influence from frictional losses. One of the outcomes of the study was that secondary losses, such as through flow turning, can have a significant influence on wave rotor performance.

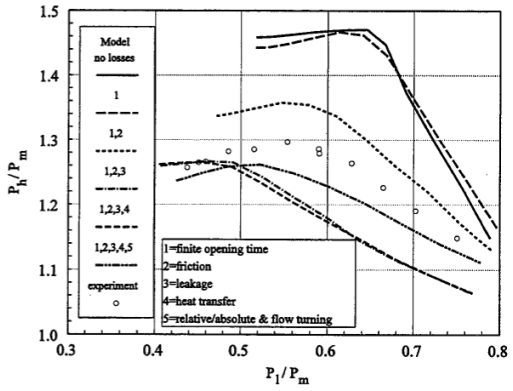

Figure 1-15: Comparison of experimental data for a short rotor with wide passages with the numerical model. The influence of various loss mechanisms on the performance is shown as well, with friction and leakage being dominant [12].

Figure 1-15 shows the effect of including several loss mechanisms on the model outcome with respect to experimental data of a short pressure divider with wide channels. Friction and leakage seem to be the most dominant in this instance. The authors emphasise that the need for further validation of improvement in the numerical approximation can be achieved by accounting for incidence losses, although viscous and leakage losses remain dominant [15].

The NASA code was subsequently used to examine the dynamic and tran-

sient behaviour of a four port wave rotor, conducted by Paxson [18, 19]. To model the influence of heat addition in the combustor a lumped parameter model was included. The first study [18] investigates the transient response of the port mass flow rates and pressures and temperatures in the exhaust and combustor to a step input in heat addition. Initially, the wave rotor was run at the design speed before a step change in heat addition was applied. The transient data suggests a swift response, shown in Figure 1-16 (a), with the behaviour of the wave rotor being an order of magnitude quicker than the dynamics of combustor, cavity and valve volumes. The study further considered stability of operation and drew a correlation between the choice of combustor and valve volume. It appeared that reducing the combustor volume lead to an earlier onset of instabilities, similar to surge witnessed in turbomachinery. This eventually results in unacceptably large combustor temperatures, as can be seen in Figure 1-16(b).

The author also tested the characteristics of a freewheeling rotor, where the inlet ducts are aligned in such a way that the momentum change due to flow turning overcomes the rotor inertia, bearing friction as well as any other source of drag induced by the rotor rotation. In the process, friction was ignored and inertia was computed assuming the rotor to be manufactured from steel. Torque was assumed to stem only from the flow turning at the duct-rotor transition, thus generating rather low values of torque. A step reduction in heat input ensures the flow turning and thus requires a change in rotor speed to achieve freewheeling. This expresses itself in rotor speed change as seen in Figure 1-16(c). It is finally concluded that the combustor pressure and temperature react quickly to the step change and that the wave rotor performance is relatively insensitive to variations in speed.

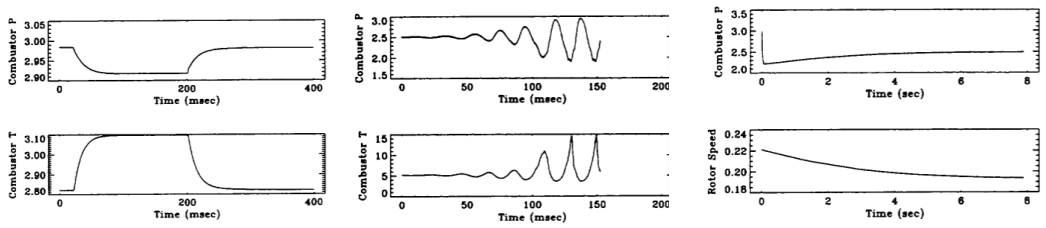

(a) (b) (c)

Figure 1-16: Dynamic behaviour of combustor temperature and pressure of a four port wave rotor. (a) shows the response to a step change in heat addition. Increasing combustor heat addition results in higher combustor temperature and a reduced combustor pressure. Instable behaviour is shown in (b) with combustor pressure and temperature exhibiting increasing amplitudes. Freewheeling rotor behaviour is given in (c), where misalignment of duct flow alters torque changing the stable operating rotational speed [18].

The second numerical study [18, 19] on dynamic behaviour looked into transient start-up behaviour and tried to answer the question of which start up scenario proves to be

most promising. Several procedures were numerically tested, such as ramping up heat addition and rotor speed separately or in conjunction. This would require an electric motor, in order to bring the rotor up to speed. Furthermore, the study also looked into the opportunity of supplying combustor plenum air injection for start-up. This turned out to be most promising, since it features no reverse combustor flow in the initial phase of start-up, but would require a small external air supply for any real life application. The author concludes that combustor flow reversal is of major importance, since it inhibits the combustor from providing a stable flame.

The NASA-Lewis wave rotor code was furthermore utilised for an optimisation study of a wave rotor application as a gas turbine topping device. This was carried out by Wilson and Paxson [20]. The optimisation routine sought to find a favourable combination of wave rotor geometric parameters, such as diameter, length and channel height, as well as rotational speed and port timing to obtain a maximum increase in topped specific power output. The code uses the ratio of exhaust to inlet port stagnation temperature and the wave rotor expansion ratio to determine inlet stagnation pressure and temperature along with exhaust outlet static pressure. Moreoever, port timing is adjusted so that incoming and generated waves are appropriately timed and inlet and outlet mass flow rates are matched. Interestingly, the code does not determine high pressure port timing and the respective boundary conditions. The optimisation procedure was then applied to different gas turbine sizes to determine an appropriate wave rotor size. The study indicates that for a compression ratio of 8 and a fixed turbine inlet temperature of approximately 1300 K, an optimised wave rotor can increase specific power by 28%, while reducing specific fuel consumption by 17.5%.

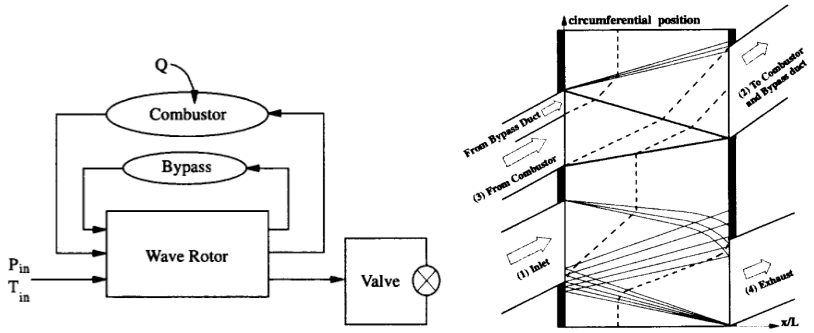

Figure 1-17: EGR bypass duct schematic (a) for the 1D-simulation and the corresponding wave pattern showing the air/gas interface [21].

While throughflow wave rotors can fully exploit self-cooling capabilities, they experience a portion of the exhaust gas being redirected into the combustor, termed

internal EGR. Paxson and Nalim [21] addressed this issue by introducing a bypass duct for the recirculated exhaust gases. The underlying principle is shown in Figure 1-17. This could potentially enable a reduced wave rotor wall temperature by around 18% and a reduction in combustor inlet temperature by 17%. Nevertheless, the bypass ducting would require a more complex ducting and thus, has an effect on overall system integration in a gas turbine environment. In addition, the required combustor pressure drop to balance the cycle increases by around 2 percentage points to 11%. One issue mentioned by the authors is the potential inability of one-dimensional models to predict the air/gas demarcation accurately, making confirmation via experimental means indispensable.

Purely axial wave rotors feature a constant cross section. Paxson and Lindau [22] adapted the original one-dimensional model to account for changes in radial passage height for an axial, four-port, throughflow wave rotor. Several different height profiles were examined ranging from simple converging profiles to more complex convergent-divergent profiles. The simulations were compared with higher-order CFD simulations and revealed that a convergent-divergent profile significantly improved performance. Although the exact mechanisms remain unclear, the modified height profile resulted in a 4% increase in pressure ratio.

Non-axially shaped channel shapes in a one-dimensional environment were first considered by Welch et al. [23, 24]. The model is again based on the inviscid Euler equations and considers a passage-averaged description of the wave rotor flow. In addition, the model includes source terms accounting for flow turning. The results from the passage-averaged model were compared to results from two-dimensional CFD simulations and determined that the one-dimensional model significantly overpredicts wave turbine performance parameters. The model has been further enhanced by an incidence loss model by Jagannath [25]. Nalim et al. [26] extended Paxson's model with an additional source vector to include chemical reaction and turbulence, with the aim of developing a simulation tool for premixed pressure-gain combustors. The numerical study found that detonation modes result in the highest throughput mass flow rates, although the modes themselves prove sensitive to port timings and the boundary conditions in the ports. To complete combustion, it is either necessary to ensure very high flame speeds or extending burn time over multiple cycles. Using Welch's model, the one-dimensional wave rotor combustion model was extended by Jagannath and Nalim [27] to predict pressure-gain and shaft power generation.

In a similar fashion to the NASA-Lewis program, one-dimensional codes were written by Fatsis et al. [28, 29], Nagashima et al. [30] and Akbari et al. [31]. The first two numerical studies aimed to validate a 1D-model using the NASA three-port

pressure divider geometry. The model is similar to Paxson's and consists of an explicit second-order accurate scheme based with TVD properties. The superbee limiter was used, although further limiters (minmod, van Albada) were implemented in the model. Source terms for friction and leakage were included, too. The latter study also includes the simulation of a four-port reverse flow rotor, which was validated using unsteady static pressure distribution with experimental values from the literature. The research effort of Nagashima et al. [30] aimed to use a four port wave rotor for the topping of a ultra-micro gas turbine. Their model included the effect of gradual passage opening and was verified using transient data from 2D simulations, which featured good agreement. The 1D tool was subsequently used to study the effect of port adjustment and gap clearances on the overall wave pattern. A comparison of different port adjustments and the implications to the pressure before the lower pressure gas port opens is given in Figure 1-18. The authors conclude that the larger the distance between the high pressure air port (Air-HP) and the lower pressure gas port (Gas-LP), the more pronounced the effect on gas leakage mass flow and pressure loss becomes.

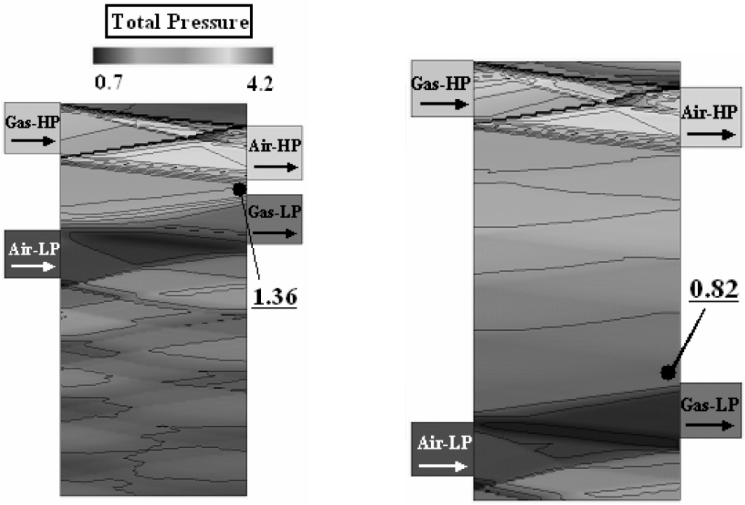

Figure 1-18: Total pressure contours produced by a one-dimensional code for two different port arrangements and the same gap clearances. The port arrangement in (a) features a smaller distance between the high pressure region and the low pressure region, while (b) exhibits a larger distance. There should be a reasonable amount of distance to allow the flow to become stable. However, the larger the distance, the higher the pressure loss and the less favourable the wave rotor performance is when applied as a topping device to a gas turbine [30].

The knock-on effect of leakage on wave rotor performance has been emphasised earlier and was the topic of a numerical study by Akbari et al. [31]. The authors propose a methodology that occupies itself with a more thorough approach towards leakage

modelling instead of resorting to a lumped capacitance model. The research combined the 1D wave rotor solver of NASA with a segmented boundary leakage model that can take into account the type of sealing and the clearance gap in circumferential direction.

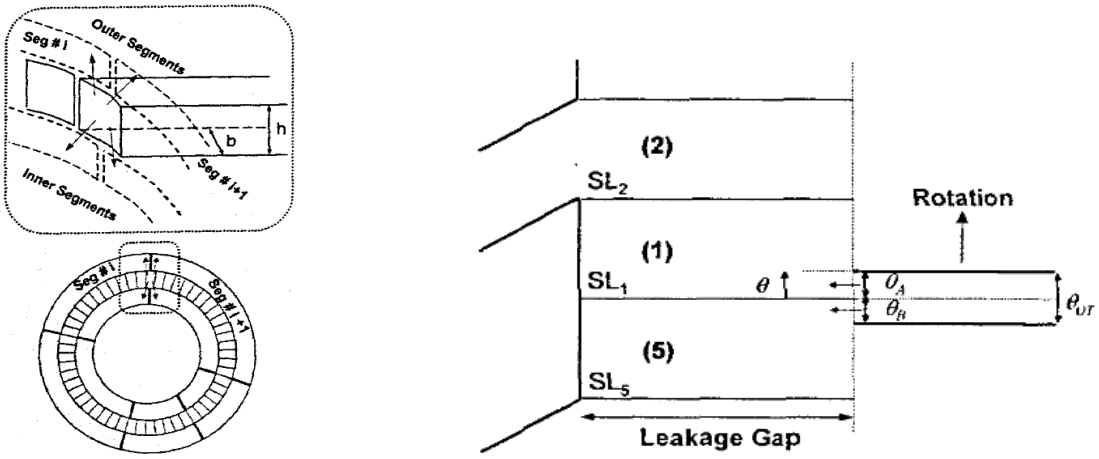

(a) (b)

Figure 1-19: The segmented boundary leakage model divides the multiple leakage paths into segments. Thus the approach takes into account (a) circumferential leakage as well as (b) leakage at different locations along the circumference. Furthermore, overlap of a channel at two adjacent segments is also taken into consideration [31].

Multiple stationary leakage segments, shown in Figure 1-19(a), where comparable levels of temperature and pressure can be expected, are introduced in axial and radial direction and are connected through a flow network. The approach also takes into account gradual opening and closing of channels with respect to the segments, see Figure 1-19(b). Overall, the authors report that pressures and temperatures of leakage flows can thus be predicted with higher accuracy and that heat transfer analysis is facilitated, ultimately resulting in a better estimation of wave rotor component performance.

A one-dimensional in-house solver based on a second order Lax-Wendroff scheme with artificial viscosity was introduced by Piechna [32] and found application in a number of research efforts on both axial [11, 34] and radial [33, 83, 85] wave rotors. Iancu et al. [11] as well as Piechna et al. [34] employed the code to determine port timing and rotor geometry. The former study examined both through flow and reverse flow designs with fixed boundary conditions and rotational speed. A single rotation through a cycle was considered to compare the results with an analytical study. Therefore, the code was not run until a "steady" operation had been reached and the mass flow rates in the high pressure region where not matched. The latter study used the one-dimensional code to determine the port timing of a reverse flow design

used as a topping device for a small micro gas turbine. Again, boundary conditions in the ports were fixed so that the high pressure ports featured the same total pressure, i.e. no pressure loss through the combustor is considered. It is not stated whether this results in matched mass flow rates (neglecting fuel addition in the combustor). A combined approach of analytical and one-dimensional simulation tools was proposed by Chan et al. [35] for pure pressure-exchange wave rotors. An initial port solution was devised through Rankine-Hugoniot shock and expansion wave relations and further refined using a one-dimensional model. Although the numerical model does not feature any source terms or mechanism to account for leakage, experimental validation showed good agreement for pressure ratios and trends for internal EGR and fresh air exhaustion (FAE) were captured as well.

1.4.1.3 Two and Three-Dimensional Modelling

Increasing model complexity by expanding to two- and three-dimensions enables study into the effect of rotational phenomena, such as Coriolis effects due to rotation, or fluid dynamic related effects, namely flow separation or finite passage opening due to the changing overlap of port opening and rotor channel. Furthermore, interaction between channels can also be studied in this way. Compared to one-dimensional models there are relatively few two- or three-dimensional simulation studies on wave rotors available [30, 33, 34, 83, 85, 88, 89, 91, 91, 93–95]. This is based on the fact that they are by far more resource intensive. While a one-dimensional code can claim several minutes, a comprehensive multidimensional CFD-study can easily require several days to run. In contrast to crypto-steady devices such as classical turbomachinery, that allow numerical simulation to take place in a steady state using multiple reference frames (MRF), wave rotors, being unsteady flow devices, do not allow such simplifications and require transient computations, which substantially adds to CPU time.

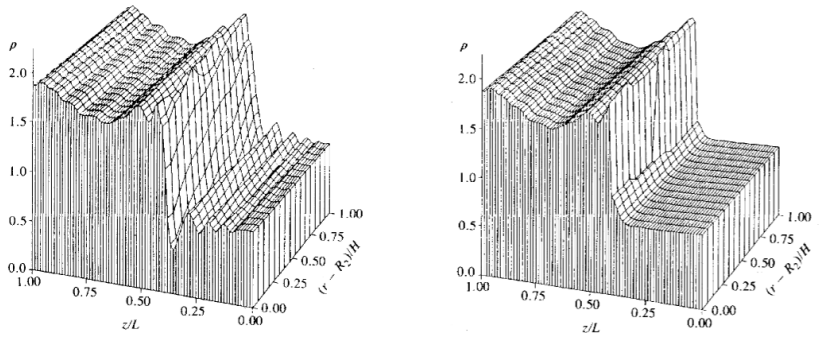

Figure 1-20: Comparison of the density field for conventional Navier-Stokes equations without (left) and with (right) the application of a second fractional step method near the interface. The additional fractional step and conversion to Lagrangian form result in a sharper resolution of the contact surface [89].

A first step from one-dimensional studies to higher dimensions was performed by Hongde [88] and Zhang and So [89]. Here, the domain of interest is in the meridional plane of the wave rotor, so that rotational effects can be taken into account, while neglecting finite opening time as there is no partial overlap of the channel plane with the ports. Both studies were performed on reverse flow systems, such as the Comprex® pressure wave supercharger. Hongde [88] solved the inviscid Euler equations in cylindrical coordinates using a second-order accurate MacCormack finite-difference scheme with artificial dissipation. No allowance for friction, finite passage opening or leakage was made. Stagnation properties at inlet and static pressures at outlet were imposed and the code ran until periodicity between cycles was ensured. The grid resolution was relatively low, with ten nodes in the radial and 41 nodes in the axial direction. The simulation results, in particular the port mass flow rates, were compared with experiments and 1-D simulations and found that both 1D and 2D overestimated the experimental values, due to the fact that leakage flows were not considered. Zhang and So [89] sought to determine an accurate treatment of the air/gas interface. The study claims that the truncation error of finite difference equations leads to a smeared demarkation. To avoid this issue, the authors apply a method of fractional steps [90] to split the Navier-Stokes equations into inviscid Euler equations and a diffusion type equation. First the Euler equations are solved, whose solution is then used to solve the second diffusion-type equation using a central difference scheme. Near the interface however, the same method is used to split the Euler equations into sets of one-dimensional equations and transform to Lagrangian form. This results in a formulation without an explicit density appearing in the spatial derivatives and which can be solved without any numerical smearing of the interface, as seen in the density plot in Figure 1-20.

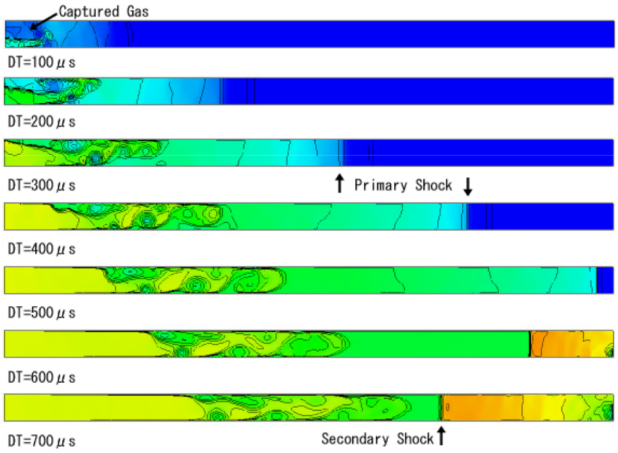

Figure 1-21: CFD pressure contour showing primary shock wave and the reflected secondary shock wave [91].

The aforementioned studies assumed that the channels are exposed to the ports instantly. As already hinted by Paxson and Wilson [13], this represents a major simplification. Elaborate numerical models lend themselves to explore the sensitivity to non-instantaneous port exposure. In the studies of Nagashima et al. [30] and Okamoto et al. [91] a 2D Reynolds averaged Navier-Stokes (RANS) solver was used to look at this effect and its ramification on wave propagation of primary and secondary shock waves. The code did not consider the influence of turbulence and assumed laminar flow. Numerical results were compared with experimental data derived from tests on a single channel.

A pressure contour plot showing pressure wave evolution over time is presented in Figure 1-21. It depicts the formation of a right moving primary shock wave and the subsequent reflected secondary shock wave travelling to the left. The authors compared the velocities of primary and secondary shock waves and found good agreement with the experiments. Further, it is stated that leakage does not affect primary shock wave speed, but diminishes secondary shock wave velocity.
For a more detailed investigation of gradual passage opening two different cell widths of 8 mm and 16 mm were considered. The results indicate that with increasing gradual passage opening time, the primary shock wave becomes less distinguishable. The secondary shock wave experiences interference with the vortices that are formed as a consequence of the opening jet into the channel, which is seen in both experiments and numerical results in Figure 1-22(a).

Another effect pointed out by the two studies is that an interaction wave is formed as a consequence of connected cells through an axial clearance. Figure 1-22(b)

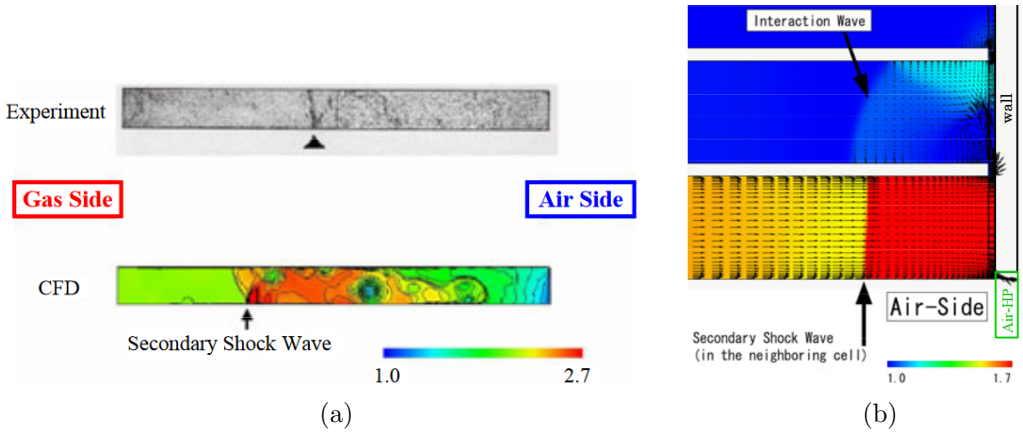

Figure 1-22: (a) Top plot shows Schlieren image of the reflected, secondary shock wave for larger axial clearance, while the bottom plot shows the corresponding density contour from the CFD result. Both display the interference of the shock wave with the air/gas interface, due to a more complicated demarcation shape between gas and air in the case of greater channel width. (b) Depicts the interaction effects of neighbouring channels. The creation of a secondary shock wave at high pressure causes a left running interaction wave in the neighbouring channel. A larger clearance weakens the shock strength of the secondary shock wave [91].

illustrates a left running interaction wave that is formed as a result of the reflected secondary shock wave. Increasing the axial clearance seems to allow more energy from the secondary shock to be transferred to the neighbouring channel, ultimately decreasing the shock strength of the secondary shock wave. This is also reported by Liu and Liu [92], who used two-dimensional CFD to develop an analytical closed-form leakage loss model that accurately predicts shock wave attenuation as a function of leakage gap.

The findings concur with the conclusions made by Larosiliere [93] in the early 1990s who performed 3D numerical studies on a single and straight wave rotor channel. It is deduced that longer opening times, corresponding to wider channels or lower rotor speeds, correspond to a distorted and complex shape of the air-gas interface. This is attributed to a number of reflected compression waves along the channel walls. In addition, it is emphasised that the distorted interface shape enhances mixing between the two constituents and thus fosters losses. It is evidenced that a higher wheel speed can reduce the finite opening time, at the cost of increasing centripetal and Coriolis effects that lead to a three dimensional distortion of the air/gas interface.

Finally, one should bear in mind the effect on port timing as wheel speed is altered. Welch [94] computed the two-dimensional flow field in a three-port pressure divider and a four port wave rotor and compared the results with 1D and experimental data, which was available for the latter application.

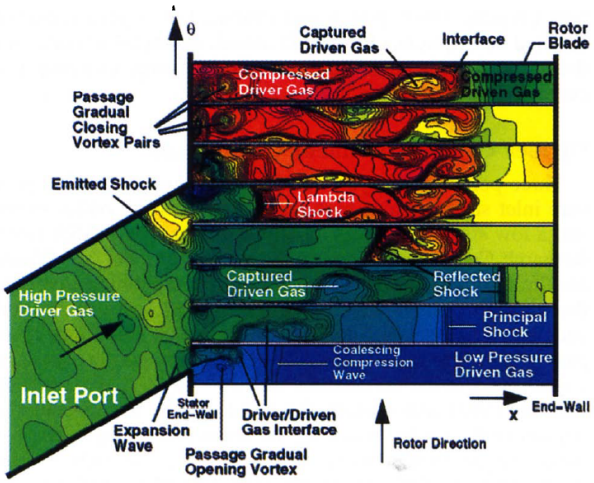

Figure 1-23: Density contour showing main flow features exhibited within the rotor passages when exposed to a high pressure inlet port. The jet formed as a result of finite opening and closing lead to the formation of a vortex and subsequently to trapped fresh gas. The interaction of the reflected shock wave with the gas accounts for a lambda shock pattern and a skewed air/gas interface [94].

In this study it was acknowledged that interface skewing occurs as a consequence of shock and expansion waves and interface interaction. The study further points out the significance of loss mechanisms such as shock-boundary layer interaction and separating flows. Figure 1-23 depicts the charging process of an angled inlet port containing the high pressure driving gas. Gradual exposure of the channels to the inlet port generates a jet that evolves into a vortex. This vortex revolves and entrains some of the driven gas. Additional vortices are formed as a result of gradual closing of the passages. The contour plot further illustrates the complicated shape of the air/gas interface. Moreover, since it is assumed that the initial conditions within the channel are uniform, the primary, or principal, shock wave resembles a normal shock wave. The reflected shock wave, however, interferes with vortices and the air/gas interface, therefore yielding a lambda-shock pattern. It shall be noted that for the discretisation of the rotors 115 nodes in axial and 41 nodes in tangential direction were used, while for inlet and outlet ports 85 nodes in axial and 151 in tangential direction were used.

In the axial wave rotor studies by Piechna et al. [34] and Iancu et al. [11, 33] the commercial software package Ansys Fluent was used to analyse the unsteady flow in both throughflow and reverse flow axial wave rotors. Piechna et al. [34] compared the results of two-dimensional with three-dimensional results and found - besides a highly skewed contact surface - that centripetal and Coriolis accelerations cause a distortion of moving shock waves. Iancu et al. [11, 33] used 2D simulations to confirm the results of simpler 1D and analytical design tools and noted that 2D simulations are useful

for fine tuning, but require far too excessive computational resources to be used for initial geometry design studies. The study further introduces a reduced order model, where a multi-cycle wave rotor can be reduced to a single cycle per rotation, so that the tangential velocity remains constant. However, no comments are made concerning implications due to the increase in centripetal acceleration.

Further 2D studies on radial wave rotors were completed by Piechna et al. [83, 85]. The first study considers a radial wave rotor and used 2D CFD to confirm the results of a one-dimensional code. The focus of the second study was on torque generation and used curved channels for torque generation. It features a closed high pressure loop, which take the combustion chamber into account through a model of constant heat flux. The design has, as shown in Figure 1-24(a), curved channels to extract torque. However, the four port design per cycle showed high variations in torque and overall, no power could be extracted. Increased curvature of the channels resulted in a design that produced torque, albeit it being small in value. Thus, an additional recirculation passage was added, as seen in Figure 1-24(b), although no comments were made as to how successful this measure was.

The previously presented studies assume adiabatic walls. However, the range of temperatures involved is substantial and thus heat transfer effects are crucial. Deng et al. [95] investigated the effect of heat transfer on the flow field for various wave rotor sizes. The numerical study considered a single straight cell of a throughflow wave rotor with 69 mm length located at a radius of 23.5 mm. Three size factors (1, 1/3 and 1/10) were considered, which were discretised using 101 nodes in both radial and tangential direction and 201 nodes in axial direction. To accurately capture the wall heat transfer coefficient the dimensionless wall distance y^+ was kept lower than unity. In the solid region a three-dimensional diffusion equation (Fourier's Law) was employed and discretised using seven nodes. Subsequently, adiabatic and conjugate heat transfer boundary conditions were imposed and the effects on pressure and temperature patterns over a cycle analysed. The study found that heat transfer from the wall increases the temperature and pressure of fresh and cold intake air and in addition, weakens the strength of shock waves within the channels. Moreover, at the induction ports large heat fluxes occur, which are largest when considering the smallest size. In contrast to Piechna et al. [34] who stated that the rotation of the channel leads to hotter gases remaining closer to the shroud, Deng et al. found lower temperature fluid pushed to the outer wall. Finally, there is a noticeable difference in temperature of the high pressure discharge fluid that is directed towards the combustor.

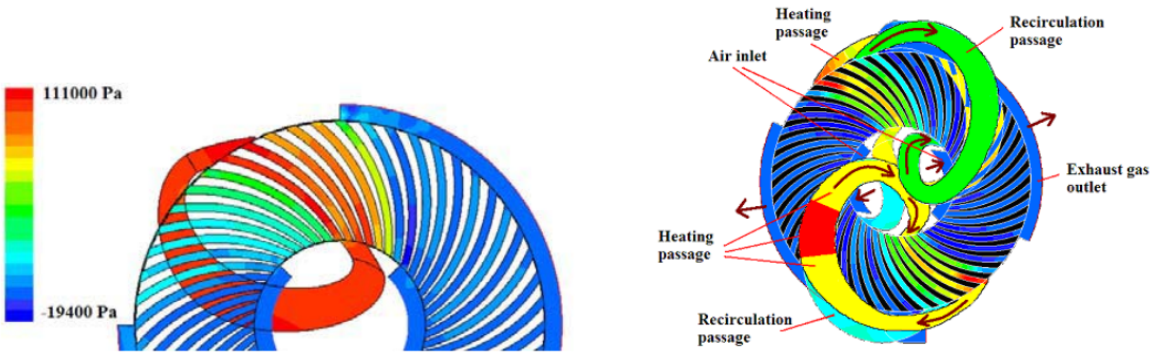

(a) (b)

Figure 1-24: (a) Pressure contour of a radial wave rotor for torque generation showing the closed high pressure loop mimicking the influence of the combustor. Note the curved channels for torque extraction. (b) Additional recirculation passage for further torque generation and further channel fluid decompression [83].

1.4.2 Wave Rotor Experimental Testing

With the exception of Pearson [76, 77], Klapproth [79] and GPC [81] the vast majority of experimental studies in open literature address purely axial channels. The success of the Comprex® PWS is founded on extensive experimental testing of the wave rotor in combination with dynamics of the combustion engine [38,39,39,40,96–99]. Figure 1-25(a) exhibits a schematic of a pressure-wave supercharged ICE. The experimental work done by Guzzella et al. [39] opted for a PWS system instead of a conventional turbocharger due to the improved transient response and better scaling properties when used for small displacement volumes. Also, the engine exhibited reasonable pollutant emissions. In particular, İçingür et al. [96] and Lei et al. [99] observed that NO_x can potentially be reduced substantially, but requires more accurate EGR control. Insufficient and inaccurate control leads to large amounts of EGR to be recirculated causing engine torque to drop sharply during transient manoeuvres, as shown in Figure 1-25(b). Thus, Spring et al. [98] developed a novel controller system that uses scavenging mass flow rate calculated from air-to-fuel ratios in the exhaust manifold as a measure of redirected EGR. The controller then maintains the scavenging mass flow rate above a pre-defined threshold. Experimental implementation of the controller verified that engine torques rise smoothly and continuously during transient manoeuvres.

Decoupling the pressure wave superchargers from the ICE allows a more isolated and focused characterisation of the wave rotor. A series of laboratory tests with this objective, coupled with steady flow combustors, have been conducted by the Air Force Institute of Technology [100–107]. Smith [104] successfully tested a Comprex

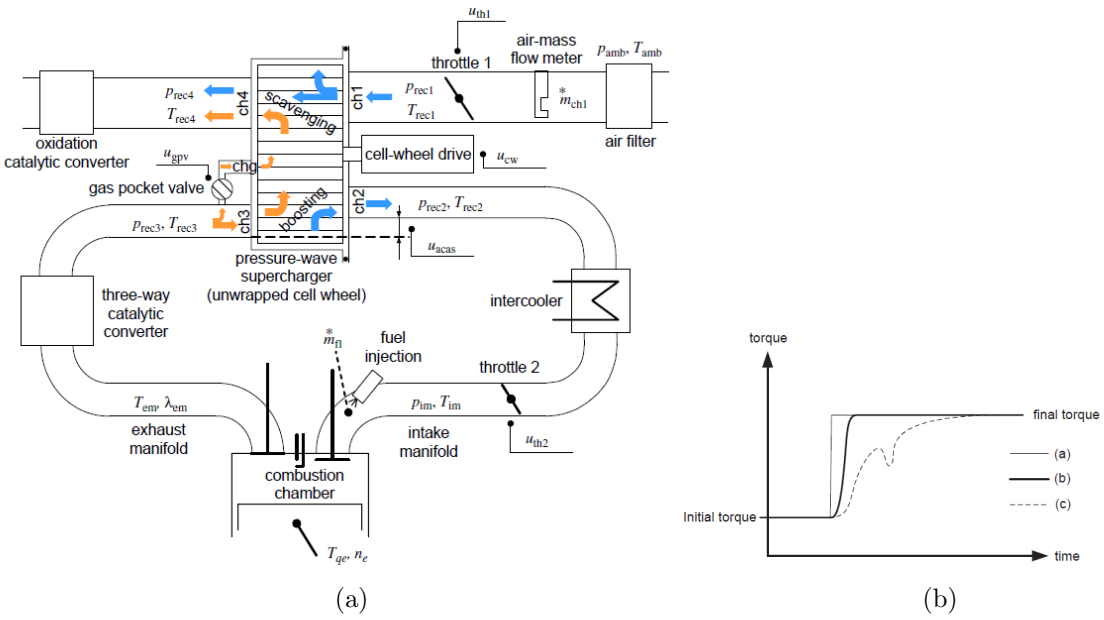

Figure 1-25: (a) Schematic of a pressure-wave supercharged internal combustion engine (b) Transient response to a step change in target torque showing a drop in torque as a consequence of insufficient EGR control [98].

PWS aimed for a 100cc two-stroke engine and compared the results with numerical data from NASA's wave rotor code, showing good agreement between the numerical and experimental data. The experimental testing used an open-loop approach, where the high pressure inlet is decoupled from the outlet. If not accounted for, this test layout allows the wave rotor to operate at conditions where the mass flow rates are not balanced. Mataczynski et al. [105–107] used a similar test rig layout with an open-loop design, but used a modified wave rotor, as seen in Figure 1-26(a), with two cycles per revolution and a far lower design mass flow rate of approximately 0.024 kg/s at a design speed of 34,500 rpm. The tests also reached higher peak temperatures more similar to what can be expected when running in concert with an ICE. Comparison of the experimental data with Paxson's model showed only minor discrepancies at design conditions. However, larger differences at off-design conditions are exhibited due to increased effects of endwall pockets used to dampen undesired waves, which were not accounted for in the code.

McClearn [103] further developed the the test setup replacing the electrical heaters by a steady-flow can-type combustor specifically designed for the wave rotor. The fuel used for the tests was a mixture of ethylene and hydrogen. The wave rotor ran at 38,500 rpm, with a design mass flow rate of around 0.0375 kg/s. Using the combustor enabled to peak temperatures to reach approximately 1000°C and up to

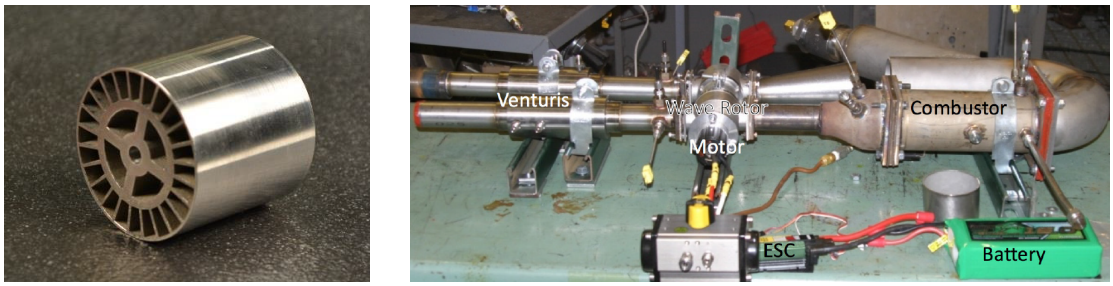

(a) (b)

Figure 1-26: (a) Example wave rotor made from Inconel 718 developed by Mataczynski [106]. (b) Closed-loop setup to test an axial wave rotor in combination with a burner used by Lapp et al. [102].

2.8 kW of power in the exhaust gas stream. The change from an open-loop testing layout to a closed-loop setup is shown in Figure 1-26(b). This was completed by Lapp et al. [101, 102], who used McClearn's burner coupled to a small-scale axial wave rotor spinning at 60,000 rpm to produce 500 W of exhaust power at design conditions.

The extensive numerical campaign at NASA Lewis/Glenn Research Center was also accompanied by wave rotor experiments on three-port [108, 109] and four-port wave rotors [111, 112, 114]. The three-port wave rotor investigated by Wilson and Fronek [108] consists of one inlet port and two outlet pressure ports. Shock waves generated during the opening of the medium pressure port to the channels ensure the fluid exits the rotor channels at higher pressure, while the expansion fans produced upon exposing the wave rotor channels to the second outlet duct ensure a lower pressure than seen at the inlet. The three-port wave rotor geometry and corresponding wave pattern are shown in Figure 1-27.

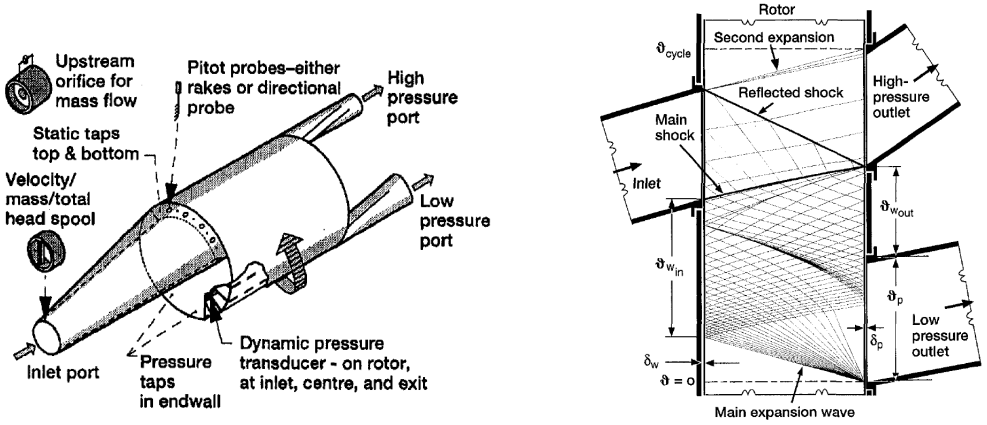

(a) (b)

Figure 1-27: (a) Three-port wave rotor schematic and (b) wave pattern within three-port wave rotor [109].

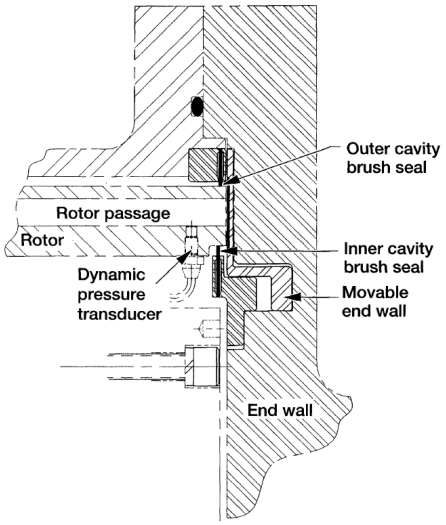

Figure 1-28: Wave rotor cross section.

The study coined non-dimensional parameters for finite passage opening time, friction and leakage that allow comparison between different rotor types. Furthermore, the authors examined the effect of leakage on rotor efficiency and showed that reducing the rotor clearance from 0.5 mm to 0.127 mm can effectively double efficiency. It shall be noted that the definition of efficiency for a three-port wave rotor is the product of compression and expansion efficiency, as defined by Kentfield [16]. Subsequent statistical analysis of the performance data of two different lengths and passage widths revealed that besides leakage, friction and finite passage opening effects, wave rotor performance is also sensitive to pressure losses as a consequence of incidence losses and pressure gains as a result of work being transferred to the gas by the rotor [109]. In addition, Wilson mentions entrance and exit losses associated with the thickness of the wall separating neighbouring passages. Hendricks et al. [110] retrofitted the three-port wave rotor with bidirectional brush seals. The brush seals were attached at both inner and outer diameter to reduce leakage flows from the rotor passages into the outer and inner leakage cavities, as shown in the cross-sectional schematic in Figure 1-28. The application of the seals significantly enhanced measured efficiency from 36% to 45%. However, it shall be noted that all tests were run at low temperatures.

In addition to the three-port wave rotor, a four-port throughflow wave rotor was tested and characterised by Wilson et al. [111,112,114]. The rotor is 266 mm long and has a mean radius of 85 mm, as is shown Figure 1-29(a). Wave rotor and stator are tweaked for performance in a gas turbine topping cycle [20]. To do so, Paxson's

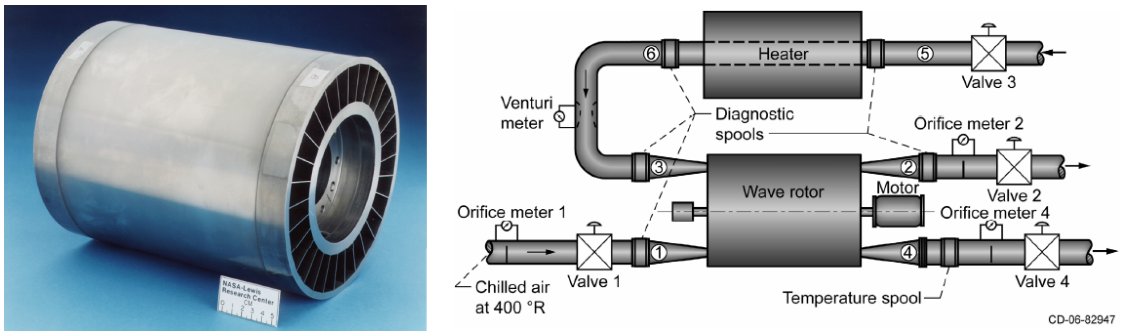

(a) (b)

Figure 1-29: (a) NASA Lewis four port wave rotor and (b) open-loop test layout for experimental characterisation [111].

one-dimensional code was used to find the best combination of port arrangement, duct flow angles and rotor dimensions for maximum output pressure ratio for the downstream turbine [111,113]. The wave rotor featured a movable endwall to allow for rotor expansion and was tested using electrical heaters as a source of heat. In order to avoid high exit temperatures from the electrical heater of approximately 600°C, a chilled air supply was used for the low pressure inlet port reducing the minimum inlet temperature to -50°C. For full control over the ratio of inlet mass flow ratios, termed loop flow ratio, high pressure in- and outlets were decoupled using an open-loop layout, as shown in Figure 1-29(b).

In the process, rotor speed and inlet mass flow rates were varied and a maximum pressure ratio across the low pressure zone of 1.17 was achieved. Wilson et al. [112] proposed an alternative formulation of efficiency to address the shortcomings of standard adiabatic efficiency calculations. This assumes equal compression and expansion efficiency and takes heat transfer between hot and cold gas streams into account.

Purdue University, Indiana University and Rolls-Royce [58,115,116] designed a dedicated testing rig for an axial wave rotor constant volume combustor [58]. Individual rotor cells were equipped with pressure, temperature and ion probes to track combustion. The experiments used a wave rotor of 786 mm length and 197 mean cell radius and housed 20 axial cells. At design speed the rotor spins at 2100 rpm and experiences mass flow rates of 4.5 kg/s. Initial tests performed by Matsutomi et al. [115] and Nalim et al. [58] showed stable deflegrative combustion over a range of equivalence ratios from 0.39-1.01, but showed a greater flame speed than initially expected in the order of 180-200 m/s.

Although some of the studies referenced used pressure and temperature probes

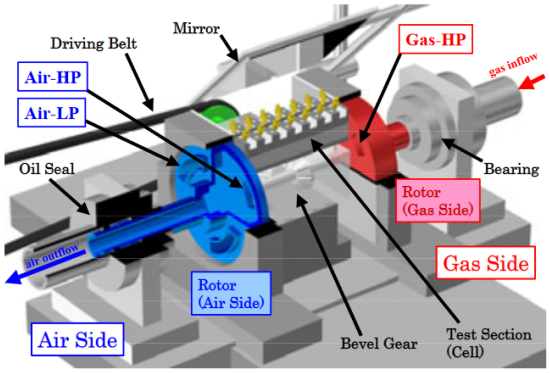

Figure 1-30: Experimental setup to visualise wave propagation in a single, stationary test cell. Ports on each side of the channel are rotated through a driving belt to simulate the opening and closing of the channels to the ports. [91].

to infer the behaviour of wave dynamics within the rotor cells, most of them are predominantly interested in the characteristics of global wave rotor parameters. Depending on the rotor size a detailed experimental examination of the gas dynamics within the rotor channels may be difficult to achieve due to the limited accessibility for optical equipment and the fact that most wave rotors spin at high rotational speeds and operate under high pressures and temperatures. Okamoto et al. [30,91,117,118] introduced an experimental concept that enables visualisation of shock waves through Schlieren method and flow velocity measurement through Laser Doppler Anemometry (LDA).

The experimental setup features a stationary and transparent single cell, shown in Figure 1-30. The cell remains stationary, while the the endplates housing the port openings can be positioned at a variable distance from the test section and are rotated through a driving belt. This allows gradual passage opening effects to be reproduced. The cell also features three neighbouring cells in order to account for the effect of channel-to-channel interaction caused by circumferential leakage. The experimental Schlieren indicate that greater axial leakage promotes interaction between channels and causes interaction waves caused by the reflection of shock waves in the adjacent channels.

A similar setup was used by Li et al. [119] to further assess flame propagation and pressure gain behaviour of a single, straight wave rotor channel. Minimum and maximum pressure gain were 0.2 bar and 6 bar respectively and varies considerably depending on rotational speed. The tests confirmed stable operation over a wide range of equivalence ratios, but does not comment on the flame speeds exhibited during the experiments. An experimental facility for a proof-of-concept radial wave rotor combustor developed by Michigan State University and Warsaw University of Technology

was developed by Parraga-Ramirez et al. [120]. The setup featured six optical ports to record high speed images, infrared images and laser diagnostics of the combustion dynamics within the channels. Initial tests were performed, but the prototype engine generated low thermal efficiency and fell short of achieving target shaft power [121].

1.4.3 Gaps of Knowledge

The presented literature review aimed at providing a summery of the fields of application for wave action pressure exchange machinery and an insight into the various modelling techniques used to devise and numerically characterise wave rotors. In addition, an overview of previous experimental campaigns was given.

The main gap in the literature stems from the fact that the majority of studies deals with straight channelled wave rotors. This pertains to both experimental campaigns as well as simulation studies. Those studies that have successfully tested wave rotor turbines with cambered channels are poorly reported, such as the Pearson rotor or efforts by General Electric and General Power Corporation. As a result, the effect of adding camber to the channels is lacking both experimental and numerical research. Finally, designs generated using numerical models are not optimised in any strategic and methodical manner revealing another gap in wave rotor research.

1.5 Aims and Objectives

This literature review reveals a broad range of research studies and endeavours aimed at investigating the characteristics of wave rotors using both numerical and experimental methods. However, the majority of these efforts focus on purely axial machines, while non-axial wave rotor turbines remain insufficiently investigated. Against this background, this thesis seeks to expand the knowledge of power generating wave rotors through both numerical and experimental means and seeks to

"analyse and understand the characteristics and potential trade-offs of a micro-wave rotor that functions both as a pressure-exchanging device and power generating turbine."

To this end, this research study focuses on the following objectives:

1. Understand the performance characteristics and sensitivity of a micro-wave rotor gas turbine.
2. Explore the sensitivity of wave rotor turbines with respect boundary and operating conditions.

3. Validate the numerical model using data from the experiments and open literature and outline capabilities and limitations of the model.
4. Explore the optimisation potential of wave rotor turbines and investigate the relationship between pressure-exchange and power generation.

Chapter 2

Performance Characteristics of Non-Axial, Micro-Scale Wave Rotor Gas Turbines

2.1 Content Summary and Thesis Context

This chapter incorporates a conference paper that comprises a numerical based study on the performance characteristics of a micro-scale wave rotor gas turbine. The objective of the paper is twofold; first of all, it shall introduce the quasi-one-dimensional numerical model as an inexpensive tool to estimate the performance of wave rotors with cambered, non-axial wall profiles. Secondly, it shall shed light on the viability of the micro-wave rotor based gas turbine concept as a potential substitute for traditional turbomachinery.

The paper is based on a validated quasi-one-dimensional numerical model, which follows a single wave rotor channel as it periodically passes discrete in- and outlet ports. The flow in wave rotor channels can be considered quasi-one dimensional as variations in the conserved variables occur predominantly along the primary flow direction, which follows a streamline along the cambered channels. Although in reality there will be variations in the plane normal to the flow direction, theses are relatively smaller. The code was developed in-house from scratch as part of this PhD project using the Matlab IDE. To accurately compute shock strength, position and speed the model is based on the conservative flow equations in conjunction with the shock capturing method of Richtmyer. This enables shock and expansion waves to be part of the solution and there is no shock associated loss in mass, momentum and enery. This is

in contrast to non-conservative methods that require bespoke shock fitting methods to prevent erroneous jump conditions. It solves the discretised balance equations for mass, momentum and energy using second-order finite-differences and a flux limiter to prevent dispersive errors in the vicinity of shocks. Details of the numerical scheme used to resolve shock and expansion waves with acceptable accuracy are given in Appendix A. The model is applied to a non-axial wave rotor with symmetrically cambered channels coupled with a simple steady-flow combustor model. The combustor model uses heat release rate as an input and computes the corresponding outlet temperatures and pressure losses through Rayleigh relations. The model is then used to explore the sensitivity of wave rotor performance metrics including thermal, compression and expansion efficiency and estimated shaft power output to changes boundary conditions. These encompass combustor pressure loss, heat release rate, loop flow ratio, backpressure, leakage. In addition, the effects of wall camber and heat recuperation are investigated. Major performance affecting parameters are discussed and potential weaknesses of a micro-wave rotor turbine are highlighted. It is concluded that among leakage, overall combustor pressure loss is of primary importance to fully exploit the wave rotor potential. Furthermore, power generation through incidence and camber shape is identified as a significant limiting factor that requires careful handling, but also offers potential for optimisation.

2.2 Paper I: Parametric Numerical Study on the Performance Characteristics of a Micro-Wave Rotor Gas Turbine

Conference paper presented at *International Gas Turbine Congress 2019 Tokyo*, Tokyo, Japan and published in the associated conference proceedings [122]:

S. Tüchler and C.D. Copeland, "Parametric Numerical Study on the Performance Characteristics of a Micro-Wave Rotor Gas Turbine," Proceedings of the International Gas Turbine Congress 2019 Tokyo, IGTC-2019-200, Nov, 2019, Tokyo, Japan.

Statement of authorship

S. Tüchler (candidate): development and implementation of numerical model, data analysis, preparation of tables and figures, writing and compilation of manuscript. Presented the contents of the paper at the conference.

C.D. Copeland (supervisor): supervision of numerical modelling work, review and edit-

ing of manuscript.

Copyright

Parametric Numerical Study on the Performance Characteristics of a Micro-Wave Rotor Gas Turbine

Stefan Tüchler[1], Colin D. Copeland[1]

Abstract— **In this paper, an alternative micro-gas turbine is proposed, where the traditional compressor-turbine arrangement is replaced by an axial, throughflow wave rotor. The investigated wave rotor features symmetrically cambered wall profiles and angled port arrangement for shaft power extraction and uses shock and rarefaction waves for pressure exchange and to achieve gas compression and expansion within a single device.**

A validated quasi-one-dimensional model that solves the laminar Navier-Stokes equations using a two-step Richtmyer TVD scheme with minmod flux limiter is employed to characterise and examine micro-gas turbine behaviour. The model accounts for wall heat transfer, flow leakage, wall friction and inviscid blade forces. In addition, modified boundary conditions consider finite passage opening effects and a simple steady-flow combustor model is defined that links the high pressure in- and outlet ports.

The model is used to conduct a parametric study to investigate the effects of leakage gap, heat release rate, exhaust backpressure, as well as profile camber on gas turbine performance with a focus on generated combustor compression and expansion efficiency, shaft power and system efficiency. The implications of combustor pressure loss as well as effects of a potential recuperator are discussed as well. The results identify axial leakage and combustor pressure loss as primary drivers for enhanced performance. Finally, the results reinforce the capacity of wave rotors to compress and expand gas efficiently, while thermal efficiency remains below 10 percent.

NOMENCLATURE

Variables

$\dot{m}$	Mass flow rate [kg/s]
$\dot{Q}$	Rate of heat flow [W]
F	Flux vector
S	Source term vector
U	State vector
C_D	Discharge coefficient [-]
c_p	Specific heat capacity at const. pressure [J/kg-K]
c_v	Specific heat capacity at const. volume [J/kg-K]
A	Cross-sectional area [m^2]
a	Speed of sound [m/s]
C	Absolute velocity [m/s]
D	Diameter [m]
e	Specific internal energy [J/kg]
f	Friction factor [-]
H	Channel height [m]
h	Specific enthalpy [J/kg]
htc	Convective heat transfer coefficient [W/m^2-K]
k	Surface roughness [m]
L	Length [m]
m	Mass [kg]
Nu	Nusselt number [-]
P	Power [W]
p	Pressure [Pa]
Pr	Prandtl number [-]
q	Heat flux [W/m^2]
R	Specific gas constant [J/kg-K]
r	Radius [m]
Re	Reynolds number [-]
S	Wetted area [m^2]
s	Specific entropy [J/kg-K]
T	Temperature [K]
T	Volume [m^3]
t	Time [s]
u	Relative velocity [m/s]
x,z	Cartesian coordinates

Sub- and Superscripts

ax	Axial
b	Blade
c	Cold, compression
cav	Leakage cavity
cc	Combustion chamber
ch	Channel
f	Friction
h	Hot, hydraulic
hr	Heat release
i	In
int	Interface
is	Isentropic
lk	leakage
o	Out
p	Penetration
s	Static
t	Total
TT	Total-to-total
w	Wall
x	Expansion

Abbreviations

EGR	Exhaust gas recirculation
FAE	Fresh air exhaustion
HPA	High pressure air
HPG	High pressure gas
LPA	Low pressure air
LPG	Low pressure gas
OPL	Overall pressure loss
TVD	Time variation diminishing

[1]Powertrain and Vehicle Research Centre (PVRC), Department of Mechanical Engineering, University of Bath, Bath, Claverton Down, Bath BA2 7AY, United Kingdom S.Tuechler@bath.ac.uk, C.D.Copeland@bath.ac.uk

Greek Symbols

β	Blade angle [°]
δ	Axial leakage gap [m]
η	Efficiency [-]
γ	Ratio of specific heats [-]
λ	Loop flow ratio [-]
μ	Dynamic viscosity [kg/m-s]
ω	Angular speed [rad/s]
Π	Pressure ratio [-]
Ψ	EGR/FAE rate [-]
ρ	Density [kg/m^3]
τ	Time constant [s]
Θ	Leakage function
θ	Azimuth angle [°]
ζ	Loss coefficient [-]

I. INTRODUCTION

A. Background

Over the past years, a growing demand for robotic and autonomous systems in both the civilian and defence market has developed. Applications range from unmanned aircraft systems to autonomous marine robots and mobile power packs used in the military [1]. These devices need to be compact and require energy dense power sources in order to operate continuously for several hours or days. At present, battery systems fail to meet these requirements due to their low energy density and the large volume required for installation [2].

Gas turbines on the other hand excel at high specific energy and power density [3]. Moreover, they are a well established technology, compact in size, reliable and can accommodate various types of fuels [4]. However, the performance of gas turbines is significantly affected by downsizing. In particular, downscaling a given design to match a certain set of requirements for lower power output entails substantial performance penalties pertaining to efficiency, design and operation. To maintain similar enthalpy levels and pressure changes it is necessary to run at considerably larger rotational speeds to the detriment of reliability. Heat transfer between hot and cold parts becomes more pronounced the smaller the unit size [5]. Also, tip leakage losses increase along with frictional losses due to larger relative surface roughness. All these factors combined contribute to a decline in both component efficiencies and thermal efficiency [6]–[8].

Substituting compressor and turbine in a standard gas turbine arrangement, given in Figure 1(a), by a wave rotor unit, as shown in Figure 1(b), allows to combine compression, expansion and shaft power generation within a single device and can potentially mitigate several of the aforementioned shortcomings. One distinct advantage of such an unsteady flow device over steady (e.g. diffusers) or crypto-steady flow devices is a high compression efficiency and that compression can occur within a compact volume. Since the port arrangement is a function of the circumferential velocity, it is possible to run the wave rotor at considerably lower speeds than turbomachinery of comparable size, with the result of making it less susceptible to high speed fatigue.

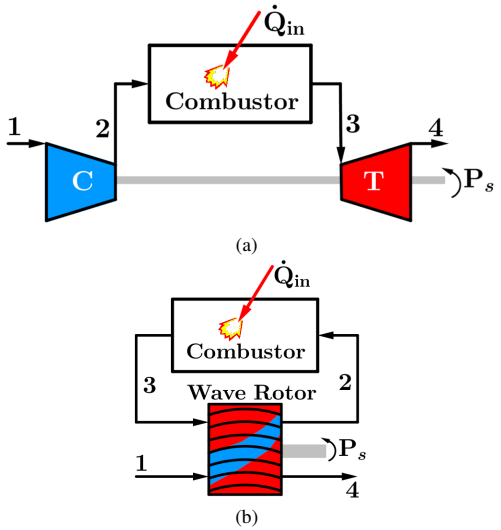

Fig. 1: (a) depicts a schematic for an unrecuperated gas turbine consisting of axial or radial compressor connected via a shaft to a turbine and a combustor in between. (b) The wave rotor concept combines both features in one device. It houses two streams, namely cold air being compressed by means of shock compression and directed to the combustor while a hot gas stream is expanded through a series of expansion waves and expelled to the ambience.

Finally, exposure to hot and cold gases introduces a certain level of self-cooling capacity that potentially allows to run at a higher combustor outlet temperatures.

The wave rotor is an unsteady flow device that relies on exchange of energy through shock and expansion waves and consists of an array of channels or passages aligned along a cylindrical drum, shown in Figure 2(a). To each side of the spinning rotor, stator endplates are located that house port openings connected to in- and outlet manifolds and the combustor. Unfolding the circumference and plotting the wave pattern and temperature distribution on a two-dimensional θ-z-plane results in the schematic presented in Figure 2(b). Exposing the channel to the left with the high pressure, high temperature exhaust gas from the combustor outlet port (high pressure gas-HPG) sets off a right travelling, primary shock wave (S1). Upon reaching the other end of the channel the high pressure air (HPA) port is opened and the shock wave is reflected resulting in a secondary, left running shock wave (S2). These two shock waves compress the incoming fresh air and essentially represent the work done by a compressor in the traditional gas turbine.

Closing the HPG port sparks an expansion fan or rarefaction wave (R1), which expands the exhaust gases to an intermediate pressure level. Impingement of the head of R1 on the right hand side marks the closure of the HPA port, which brings about a hammer shock. Opening the low

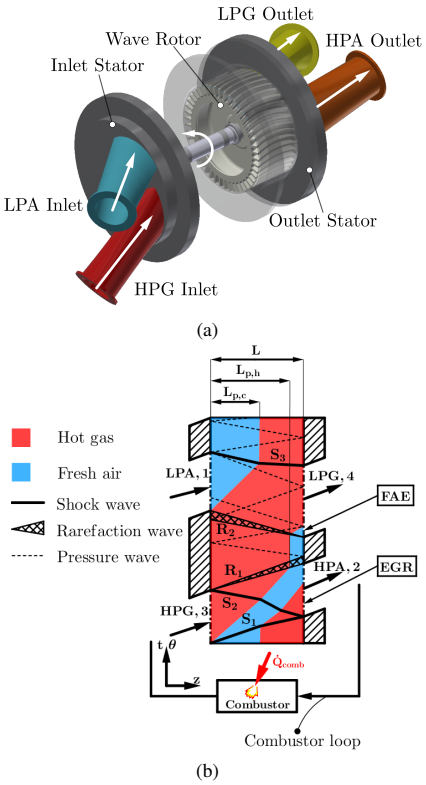

Fig. 2: (a) Main components of a generic four-port, single cycle throughflow wave rotor consisting of inlet and outlet stator endplates and rotor/bearing assembly. (b) Unfolded view of the wave pattern experienced as a single channel passes through the port arrangement of a four-port throughflow wave rotor showed in the θ-z plane [9].

pressure exhaust port (LPG) leads to further expansion of the gases (R2) before the gases are ejected to the ambience. The low pressure inlet port opens as soon as (R2) reaches the left hand side of the channel. Finally, the closure of the LPG port generates another (relatively weak) shock wave (S3), which is further reflected and attenuated on the channel sides before the cycle is repeated.

An intrinsic feature of throughflow wave rotors is internal exhaust gas recirculation (EGR), as pointed out Figure 2(b). The amount of EGR is foremost a function of the fresh air scavenging achieved through opening of the LPA port. The higher the penetration length $L_{p,c}$, the higher the amount of exhaust gases expelled through the LPG port. In effect, $L_{p,c}$ is governed by the mass flow imbalance between the high and low pressure inlet ports. Defining the mass flow or loop flow ratio of high- to low pressure inlet as λ=$\dot{m}_{\mathrm{HPG}}/\dot{m}_{\mathrm{LPA}}$ gives a measure of this mass flow imbalance. The loop flow ratio is generally $>$1, in particularly for cases where LPA draws air from the ambience without any upstream pressurisation. Equally, if pressure and temperature in the HPG duct drop below a certain threshold, it is possible that the hot gas penetration length $L_{p,h}$ does not reach the HPA port, leading to fresh air exhaustion (FAE). While a certain percentage of EGR can potentially have favourable effects with respect to combustion and emission characteristics, FAE is generally an undesirable effect, as it represents air being compressed and subsequently expelled without being further used throughout the cycle.

B. Literature Survey

Wave rotors have been proposed as a means of enhancing thermodynamic cycles for a large spectrum of applications, showing promising results potential in gas turbine topping cycles [10], [11], supercharging of internal combustion engines [12]. More recently, there has been a renewed interest in wave rotor applications for constant-volume combustors [13]–[15] and refrigeration cycles [16], [17].

One of the earliest applications of wave rotors focused on the development of a wave rotor engine [18]–[22]. Weber's shock wave engine concept [18] was an axial, single-cycle, throughflow device with angled blades for shaft power extraction combined with classical turbomachinery. Cycle efficiency of the entire system was predicted to be in the range of 29% to 36%. While Weber's proposed engine remained a concept, General Electric and General Power Corporation designed and built a wave engine that was experimentally tested, but failed to produce the predicted power output. This lead to suspension of the project. Pearson's wave engine [19], [20] encompassed a rotor of approximately 230 mm in diameter with a design speed of 18,000 rpm and produced up to 26 kW at design conditions, where thermal efficiency varied between 4-9%. Recently, a radial wave disk engine concept was introduced by Michigan State University and Warsaw University of Technology [23]–[25] for sub 1kW shaft power output. Computational fluid dynamics simulations in one- [23] and two-dimensions [25] were carried out showing a two-step compression system thermal efficiency of approximately 13-16% and 10% respectively, while a single-compression system would merely operate at 2% [24] at the benefit enhanced operation stability.

This paper seeks to investigate the characteristics of a small scale wave rotor gas turbine through a parameteric study. The foundations of the study are a throughflow wave rotor with symmetrically cambered wall profiles previously characterised experimentally [9] and a validated quasi-one-dimensional numerical model that accounts for wall friction, flow leakage, wall heat transfer, inviscid blade forces [26]. The study examines the effects of inlet mass flow ratio (i.e. loop flow ratio), heat addition, exhaust backpressure, leakage, combustor pressure loss, camber profile and recuperation on wave rotor performance with a focus on thermal efficiency, adiabatic efficiencies, power output and combustor temperature.

II. METHODOLOGY

A. Numerical Quasi One-Dimensional Model

1) Governing Equations: The model is based on the one-dimensional compressible and unsteady Navier-Stokes equation defined as

$$\frac{\partial \mathbf{U}}{\partial t} + \frac{\partial \mathbf{F}(\mathbf{U})}{\partial z} = \mathbf{S} \tag{1}$$

where the state vector takes the form

$$\mathbf{U} = \begin{pmatrix} \rho \\ \rho u \\ \rho E \end{pmatrix} \tag{2}$$

while the flux vector is defined as

$$\mathbf{F} = \begin{pmatrix} \rho u \\ \rho u^2 + p - \tau_{zz} \\ \rho u \left(E + \dfrac{p}{\rho} - \tau_{zz} + q_z \right) \end{pmatrix} \tag{3}$$

Heat flux is given by Fourier's law and viscous stress simplified through Stokes' hypothesis to yield

$$q_z = -k\frac{\partial T}{\partial z}, \qquad \tau_{zz} = \frac{4}{3}\mu\frac{\partial u}{\partial z} \tag{4}$$

Model closure is achieved through the ideal gas equation, stating p=ρRT. Air is treated as a calorically imperfect gas with specific heat capacity being a function of temperature, that is c_p=$f(T)$. The right hand side of Equation 1 denotes the source vector that accommodates for wall friction, wall heat transfer, inviscid profile forces and losses as well as flow leakage between the rotor and the stators.

2) Discretisation Scheme: The flow equations of Equation 1 are integrated explicitly in time using a two-step second-order accurate scheme of Richtmyer with a TVD scheme using a Roe and Baines minmod flux limiter. The first step consists of a first-order Lax-Friedrichs method, while the following second step represents a mid-point Leapfrog approach. The resulting algebraic equations are given in Equation 5 and 6.

$$\begin{aligned} \mathbf{U}_{i+1/2}^{n+1/2} &= \frac{1}{2}\left(\mathbf{U}_{i+1}^{n} + \mathbf{U}_{i}^{n}\right) - \frac{\Delta t}{2\Delta z}\left(\mathbf{F}_{i+1}^{n} - \mathbf{F}_{i}^{n}\right) \\ &\quad - \frac{\Delta t}{4}\left(\mathbf{S}_{i+1}^{n} - \mathbf{S}_{i}^{n}\right) \\ \mathbf{U}_{i-1/2}^{n+1/2} &= \frac{1}{2}\left(\mathbf{U}_{i}^{n} + \mathbf{U}_{i-1}^{n}\right) - \frac{\Delta t}{2\Delta z}\left(\mathbf{F}_{i}^{n} - \mathbf{F}_{i-1}^{n}\right) \\ &\quad - \frac{\Delta t}{4}\left(\mathbf{S}_{i}^{n} - \mathbf{S}_{i-1}^{n}\right) \end{aligned} \tag{5}$$

$$\begin{aligned} \mathbf{U}_{i}^{n+1/2} &= \mathbf{U}_{i}^{n} - \frac{\Delta t}{\Delta z}\left(\mathbf{F}_{i+1/2}^{n+1/2} - \mathbf{F}_{i-1/2}^{n+1/2}\right) \\ &\quad - \frac{\Delta t}{2}\left(\mathbf{S}_{i+1/2}^{n+1/2} - \mathbf{S}_{i-1/2}^{n+1/2}\right) \end{aligned} \tag{6}$$

The time step is chosen adaptively based on the maximum wave speed within the domain $\max_{i}(|u_i^n| + a_i^n)$ and a fixed Courant number of 0.7 [27].

3) Boundary Conditions: In this study, boundary conditions are implemented through a cell-centred approach with fictitious cells outside of the domain boundaries, as shown in Figure 3.

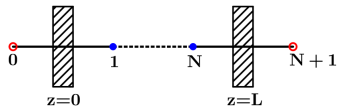

Fig. 3: Implementation of boundary conditions using fictitious image cells outside of the domain.

The model distinguishes between inlet and outlet boundaries as well as reflective walls. The importance of finite passage opening effects on performance has been addressed in a number of research studies [28]–[30]. To account for finite passage opening effects, a function tracks the overlap between the channel and the ports taking channel width into account. Assuming an isentropic change across the the step in cross section, one can formulate quasi-steady boundary equations for mass, momentum and energy [26] and solve the system of equations using wave and pathline compability equations [27]. This is done in a similar fashion to Paxson and Wilson [31]. The effect of this procedure on the formation of the shock waves is shown in Figure 4. Neglecting finite opening effects leads to an immediate formation of a right trevelling shock wave as soon as the wave rotor channel is exposed to an inlet port and a sudden drop in pressure as soon as the port closes, as shown in Figure 4(a). Including finite passage opening effects leads to a more gradual build up in pressure as the overlap increases. This is exemplified in Figure 4(b).

4) Source Terms Modelling: The friction source term assumes

$$\mathbf{S}_f = \begin{pmatrix} 0 \\ s_{f,2} \\ s_{f,3} \end{pmatrix} = \begin{pmatrix} 0 \\ -C_f \rho \dfrac{2f}{D_h}|u|u \\ \rho \dfrac{2f}{D_h}|u| c_p (T_w\text{-}T) \text{-} C_f \rho \dfrac{2f}{D_h}|u| u \dfrac{u_\theta}{u} \omega r \end{pmatrix} \tag{7}$$

where the friction factor is determined as a function of Reynolds number and hydraulic diameter and follows [27].

$$f = \begin{cases} \dfrac{0.25}{\left[\log_{10}\left(\dfrac{k}{3.7D_h} + \dfrac{5.74}{Re^{0.9}}\right)\right]^2} & \text{for } 5000 \geq Re \geq 10^8 \\ \dfrac{64}{Re_D} & \text{for } Re < 5000 \end{cases}$$

$$\text{where } Re_D = \frac{\rho u D_h}{\mu(T)} \tag{8}$$

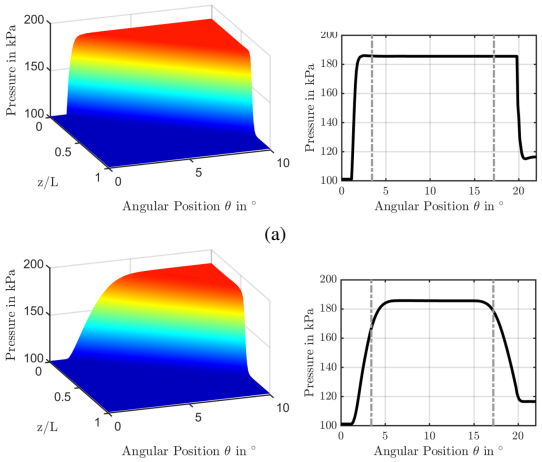

Fig. 4: Formation of a shock wave without (a) and with (b) finite passage opening effects taken into account through the boundary conditions. The right hand plots illustrate static pressure within the channel at z/L=0 and the dashed grey line mark opening and closure of the port respectively.

Dynamic viscosity is assumed temperature dependant and computed using Sutherland's law. Equation 7 features the wall temperature T_w, which is a result of wall heat transfer and was approximated through a lumped capacitance model that follows a first-order differential equation, as given in Equation 9.

$$\frac{dT_w}{dt} = -\frac{1}{\tau}\left(T_w - T_i\right) \quad \text{with} \quad \tau = \frac{mc_p}{htcS} \tag{9}$$

where c_p refers to the specific heat capacity of the material, S the wetted surface of the wall passage and htc the convective heat transfer coefficient that was determined through Dittus-Boelter flat plate heat transfer correlation (Nu=$0.0243Re^{0.8}Pr^{0.4}$) and solved using Heun's method.

Inviscid profile forces are solved assuming the flow follows a meridional streamline along the curved channels. The corresponding source terms are given by

$$\mathbf{S}_v = \begin{pmatrix} 0 \\ s_{b,2} + s_{loss_{b,2}} \\ s_{b,3} + s_{loss_{b,3}} \end{pmatrix} = \begin{pmatrix} 0 \\ F_{b,z} + F_{loss,z} \\ (F_{b,\theta} + F_{loss,\theta})\omega r \end{pmatrix} \tag{10}$$

where the tangential force per unit volume is proportional to the change in tangential absolute velocity C_θ between two consecutive cells (see Figure 5) and can be stated as

$$F_{b,\theta} = \frac{\dot{m}}{V}\left(C_{\theta,o} - C_{\theta,i}\right) \tag{11}$$

In the model, the wall shape profile are defined through a Bézier curve with the number and location of the control points being an input provided by the user. An example resulting in a symmetric camber is given in Figure 5.

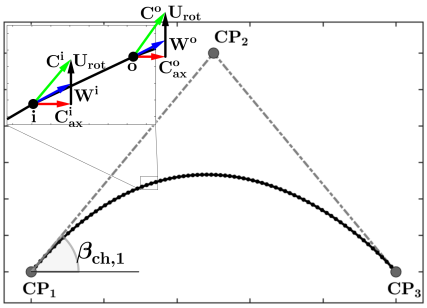

Fig. 5: Example of Bézier curve with three control points yielding a symmetric wall shape profile and detailed view of local velocity triangles at two consecutive nodes

To account for incidence losses and misalignment of the flow with the channel profile, an entropy based loss term (Δs =-$R \cdot \ln$(1-ζ_{loss})) was introduced as

$$F_{loss,\theta} = \frac{\rho T |C_{ax}|}{|U|}\frac{\Delta s}{\Delta z} \tag{12}$$

The loss coefficient ζ is a function of rotational speed and was calibrated using experimental data [26]. The model includes the the port flow angles through applying the port flow angle at the image cell to include the effect of flow turning at from the port into the channel. Irreversibilites generated due to the port-channel flow turning are not directly accounted for, but implicitly contained within the ζ loss factor. Flow leakage occurs at either passage end at the rotor/stator interface and assumes the following form

$$\mathbf{S}_v = \begin{pmatrix} s_{lk,1} \\ 0 \\ s_{lk,3} \end{pmatrix} = \begin{pmatrix} -C_D\sqrt{\frac{2\gamma}{\gamma-1}}\left(\frac{\delta_{lk}}{H_{ch}\Delta z}\right)\sqrt{p\rho}\Phi \\ 0 \\ -C_D\sqrt{\frac{2\gamma}{\gamma-1}}\left(\frac{\delta_{lk}}{H_{ch}\Delta z}\right)h\sqrt{p\rho}\Phi \end{pmatrix} \tag{13}$$

where H_{ch} represents the channel height, δ_l the leakage gap and h the specific enthalpy. The discharge coefficient C_D is fixed at 0.64. The leakage function Φ is defined as

$$\begin{aligned} \Phi &= \sqrt{\left(\frac{p_{\text{cav}}}{p}\right)^{2/\gamma} - \left(\frac{p_{\text{cav}}}{p}\right)^{(\gamma+1)/\gamma}} \\ &\text{for } \frac{p_{\text{cav}}}{p} > \left(\frac{2}{\gamma+1}\right)^{\gamma/(\gamma-1)} \\ \Phi &= \sqrt{\left(\frac{2}{\gamma+1}\right)^{2/(\gamma-1)} - \left(\frac{2}{\gamma+1}\right)^{(\gamma+1)/(\gamma-1)}} \\ &\text{for } \frac{p_{\text{cav}}}{p} < \left(\frac{2}{\gamma+1}\right)^{\gamma/(\gamma-1)} \end{aligned} \tag{14}$$

5) Submodels: The approach used to model leakage cavity pressure follows the correlations given by Paxson [32] and Fatsis [33]. The cavity pressure p_{cav} in Equation 14 is updated after every completed cycle using a lumped capacitance model, as given in the mass and energy balances shown in Equation 15. The leakage cavity is assumed to be perfectly sealed without any interaction with the ambience. The first-order system is integrated using an explicit Runge-Kutta scheme and yields cavity mass and temperature, which in combination with the equation of state exhibit cavity pressure for the current time step.

$$\begin{aligned} \frac{dm_{\mathrm{cav}}}{dt} &= A\Delta x\left(\sum_i s^l_{1,i} + \sum_i s^r_{1,i}\right) \\ \frac{d}{dt}(m_{\mathrm{cav}} e_{\mathrm{cav}}) &= \dot{Q}_{\mathrm{wht}} + A\Delta x\left(\sum_i s^l_{3,i} + \sum_i s^r_{3,i}\right) \\ \text{where} \quad e_{\mathrm{cav}} &= c_{\mathrm{v}} T_{\mathrm{cav}} \end{aligned} \tag{15}$$

where the wall heat transfer term $\dot{Q}_{\mathrm{wht}}$ was approximated through heat transfer from the rotor wall and the cavity temperature.

The combustor model links the high pressure charging zone (HPA and HPG ports) and is used to provide the corresponding boundary conditions, that is total pressure and temperature at the combustor outlet and static pressure at the inlet. It is implemented in a similar fashion to the leakage model. Temperature and mass in the combustor are determined from the following system of first-order equations, which is again integrated in time after each cycle is completed

$$\begin{aligned} \frac{dm_{\mathrm{c}}}{dt} &= \sum_i \dot{m}_i \\ \frac{d}{dt}(m_{\mathrm{c}} e_{\mathrm{c}}) &= \dot{Q}_{\mathrm{hr}} + \sum_i h_i \dot{m}_i \\ \text{where} \quad e_{\mathrm{c}} &= c_{\mathrm{v}} T_{\mathrm{c}} \end{aligned} \tag{16}$$

$\dot{Q}_{\mathrm{hr}}$ refers to the heat released through combustion. Combustor pressure can then again be inferred through the ideal gas equation. The additional mass due to fuel injection is neglected. The combustor inlet conditions are determined using Rayleigh flow relations that include an additional factor to account for cold flow pressure losses.

B. Baseline Wave Rotor

The baseline wave rotor considered throughout this study is a small-scale throughflow rotor with symmetrically cambered wall profiles, as displayed in Figure 6. The rotor is 60 mm in diameter, 30 mm in length and each channel is approximately 2.9 mm in width and 6 mm in height. Finally, the rotor houses 46 channels with a maximum profile angle of 21.5°. It was designed to provide approximately 400-500 W shaft power output at a peak cycle temperature of 750°C and peak total inlet pressure of 285 kPa at a design rotational speed of 32,000 rpm. The main geometric dimensions are summarised in Table I.

The corresponding port solution and expected main shock and rarefaction waves are depicted in the schematic of Figure 7. During each cycle (θ_{cycl}=120°), the rotor passages are exposed to a high- and low pressure in- and outlet ports. While experimental testing on the rotor were done in an open loop configuration, the model connects the high pressure ports HPA and HPG through the steady-flow combustor model.

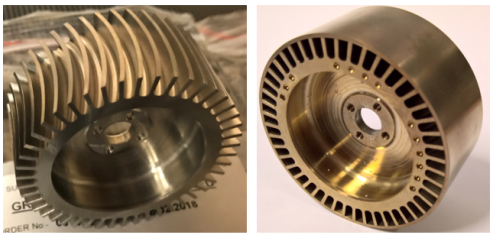

Fig. 6: Wave rotor turbine with symmetrically cambered profiles serving as a baseline model.

TABLE I: Dimensions of the Bath μ-wave rotor.

Dimensions Bath μ-Wave Rotor	
Rotor diameter [mm]	60
Number of channels	46
Channel shape	sym. cambered max. $\lvert\beta_{ch}\rvert$ = 21.5°
Channel length [mm]	30
Channel width [mm]	2.9
Channel height [mm]	6
Nominal clearance [mm]	variable 0.1 - 0.4
Number of cycles per revolution	3
Design rotational speed [rpm]	32,000

C. Discretisation Sensitivity Study

In order to ensure the results are independent of the discretisation length Δz of the cartesian grid, while computation time is kept to a minimum, a grid sensitivity study is performed. In the process, the number of cells n_z in the computational domain is varied 15 to 120 corresponding to a non-dimensional cell size Δz/L ranging from 0.071 to 0.008. The results of this study are given in Figure 8 and reveal that for a cell count of 75 the relative error with respect to the maximum cell number investigated of 120 is within 2.3%. This appears to be an acceptable compromise between numerical accuracy and the required CPU time to reach a limit cycle.

D. Numerical Campaign

The main objective of this study is to characterise the behaviour and sensitivity of the wave rotor gas turbine to changes in operating conditions. To do so, the following parameters shall be considered; starting from the baseline rotor geometry given in Table I and the port solution shown

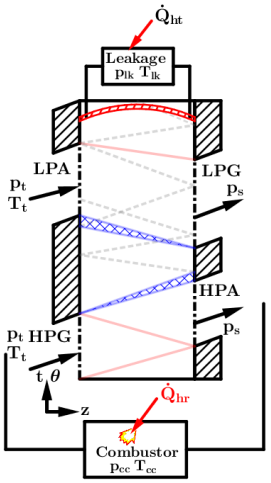

Fig. 7: Model schematic showing port arrangement and expected wave pattern for the treated four-port throughflow wave rotor turbine. The schematic further outlines the sub-models used for leakage that is active at the ends of the rotor channel and the combustor that connects the high pressure ports HPG and HPA.

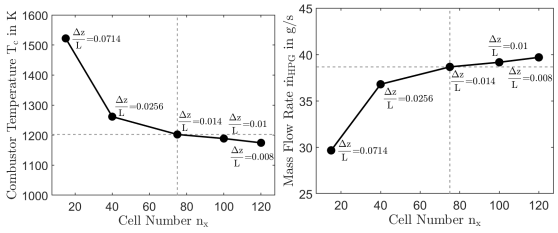

(a) (b)

Fig. 8: Results of mesh sensitivity study for (a) combustor outlet temperature and (b) mass flow rate through the HPG port. Annotations show nondimensional cell size Δz/L. The dashed line show the results for n_z=75, which corresponds to the mesh size used for further simulations.

in Figure 7 the effect of heat release and loop flow ratio on dependant variables such as thermal efficiency, compression/expansion efficiency, shaft power output, combustor outlet temperature, pressure ratio and EGR/FAE rate shall be investigated. Furthermore, the influence of combustor pressure loss on the performance parameters is investigated as well. To do so, heat release is varied between 26 kW and 18 kW, while loop flow ratio is varied from 1.2 to 1.6. Loop flow ratio dictates scavenging of channels after opening of the LPA port. To vary loop flow ratio, it is assumed that pressurised air at 300 K is available. This of course would necessitate an upstream compressor, which ultimately would act as a parasitic load diminishing thermal efficiency. This parasitic load is, however, not accounted in this study.

The next set of simulations examines how increased rotor/stator leakage and LPG backpressure influence wave rotor gas turbine behaviour. This is followed by a study on the consequences of increased and reduced wall profile camber on the dependant variables. To do so, the centre control point defining the wall contour (see Figure 3) is perturbed vertically to yield one case with lower blade camber (max.$|\beta_{ch}|$=15.7°) and one case with a higher camber (max.$|\beta_{ch}|$=27.3°) compared to the baseline profile. The final study considers a recuperated cycle as shown in Figure 9. To simplify the computations and point out the potential benefit of utilising exhaust gas temperature to preheat the combustor inlet temperature, it is estimated that the heat exchanger operates at 100 percent effectiveness, yielding $T_{t,\mathrm{HPA}}$ equal to $T_{t,\mathrm{LPG}}$. Flow through the recuperator will incur pressure losses, which is accommodated for through a 2% higher LPG backpressure than ambient.

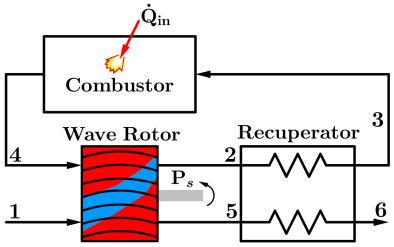

Fig. 9: Schematic including an additional heat recuperator utilising residual heat from the exhaust stream to preheat air before entering the combustor thus raising thermal efficiency at the cost of higher backpressure and pressure loss in the combustor loop.

All simulations commence from the same initial and boundary conditions. Wave rotor rotational speed is maintained at design speed of 32,000 rpm. Heat release is kept constant as well. To expedite the simulation and reach a limit cycle swiftly, where mass flow rates in the ports and temperatures and pressures in the leakage cavity and combustor are in steady-state, initial pressures and temperatures in the combustor and cavity are set to 250 kPa and 700°C, while thermodynamic conditions within the channel are set equal to ambient conditions (p=101.3 kPa and T=300 K).

E. Performance parameters

A summary of the range and scope of independant variables and the corresponding dependant variables examined in this study are given in Table II.

As stated previously, the loop flow ratio denotes the ratio of the high pressure and low pressure inlet massflow rates $\dot{m}_{\mathrm{HPG}}/\dot{m}_{\mathrm{LPA}}$. Compression pressure ratio and combustor pressure loss are defined as

TABLE II: Summary of independent and dependent variables used to characterise the wave rotor gas turbine.

Parameter	Unit	Range
Loop flow ratio λ	[mm]	1.2-1.6
Heat release $\dot{Q}_{hr}$	[kW]	14-26
Axial Leakage Gap δ_z	[mm]	0.1-0.35
LPG backpressure p_{LPG}	[kPa]	p_∞/1.0-p_∞/0.90
Combustor Pressure Loss $\Delta p_{\mathrm{HPG\text{-}HPA}}/p_{\mathrm{HPG}}$	[-]	0%-4%
max.$\lvert\beta_{ch}\rvert$	$^\circ$	15.7-27.3
Combustor outlet temperature T_c	[K]	
Avg. rotor temperature T_w	[K]	
Shaft power output P_s	[W]	
Thermal efficiency η_{th}	[-]	
Compression/expansion efficiency $\eta_{c,x}$	[-]	
Pressure ratio Π_{TT}	[-]	
EGR rate Ψ_{EGR}/FAE rate Ψ_{FAE}	[-]	

$$\begin{aligned}\Pi_{TT} &= \frac{p_{t,\mathrm{HPA}}}{p_{t,\mathrm{LPA}}}\\ \Delta p_c &= 1-\frac{p_{t,\mathrm{HPG}}}{p_{t,\mathrm{HPA}}}\end{aligned} \tag{17}$$

Thermal efficiency is calculated using predicted shaft power output P_s and first law resulting in

$$\eta_{th} = \frac{P_s}{\dot{m}_{\mathrm{HPG}}\overline{c_p}(T_{\mathrm{HPA}}-T_{\mathrm{HPG}})} \tag{18}$$

Compression and expansion efficiency are determined splitting up hot and cold gas streams and taking EGR and FAE into account, as presented by Chan et al. [34] and taking heat internal heat transfer into account. The corresponding equations therefore read

$$\begin{aligned}\eta_c &= \frac{\dot{m}_{\mathrm{LPA}}c_{p,c}(T^{is}_{\mathrm{HPA,c}}\text{-}T_{\mathrm{LPA}}\text{-}\Delta T_c)+\dot{m}_{\mathrm{EGR}}c_{p,h}(T^{is}_{\mathrm{HPA,h}}\text{-}T_{\mathrm{LPG}}\text{-}\Delta T_c)}{\dot{m}_{\mathrm{LPA}}c_{p,c}(T_{\mathrm{HPA,c}}\text{-}T_{\mathrm{LPA}})+\dot{m}_{\mathrm{EGR}}c_{p,h}(T_{\mathrm{HPA,h}}\text{-}T_{LPG})}\\ \eta_x &= \frac{\dot{m}_{\mathrm{LPG}}c_{p,h}(T_{\mathrm{HPG}}\text{-}T_{\mathrm{LPG}}\text{-}\Delta T_x)+c_{p,c}\dot{m}_{\mathrm{FAE}}(T_{\mathrm{HPA}}\text{-}T_{\mathrm{LPG,c}}\text{-}\Delta T_x)}{\dot{m}_{\mathrm{LPG}}c_{p,h}(T_{\mathrm{HPG}}\text{-}T^{is}_{\mathrm{LPG}})+c_{p,c}\dot{m}_{\mathrm{FAE}}(T_{\mathrm{HPA}}\text{-}T^{is}_{\mathrm{LPG,c}})}\end{aligned} \tag{19}$$

where ΔT_c and ΔT_x account for the heat transfer between hot and cold gas streams within the wave rotor [35]. Since the exact values for this is not known, it is assumed that they are equal. This is assumption becomes more accurate the closer loop flow ratio is to unity. In order to be able to solve the equation both compression and expansion efficiency are assumed to be equal η_c=η_x.

Furthermore, the equation takes mixing through EGR and FAE in the outlet ports into account. To compute EGR and FAE the interfaces between hot and cold gas flows are tracked at each cycle and time step using Equation 20

$$\begin{aligned}m^t &= m^{t-1}+\Delta t u^{t-1}\\ \text{with } t &= t^{t-1}+\Delta t\end{aligned} \tag{20}$$

Since the channel geometry is discretised into a finite number of elements, u^{t-1} needs to be interpolated from the the two nodes closest to the position at time t. Equation 20 is evaluated for both inlet ports (HPG and LPA), which are finally terminated as soon as z=L and give out the final interface position $\theta^{\mathrm{int}}_{\mathrm{HPG,LPA}}$. If $\theta^{\mathrm{int}}_{\mathrm{LPA}}$ is in between opening and closure of the HPA port, EGR rate can be evaluated. Similarly, in the case of $\theta^{\mathrm{int}}_{\mathrm{HPG}}$ being within the LPG port, FAE is present and can be calculated accordingly.

III. RESULTS AND DISCUSSION

A. Variation in Loop Flow Ratio and Heat Release

The effect of a variation in loop flow ratio own performance is given in Figure 10 depicting three contour plots of normalised static pressure (Fig. 10(a)) and normalised static temperature (Fig. 10(b)) for different flow ratios (λ=1.2, 1.4 and 1.6). The pressure contour reveals that the wave dynamics within the channel remains relatively stable in the depicted λ range. The temperature plots reveal that, as one approaches a loop flow ratio of unity, higher LPA inlet pressures are necessary in order to supply the required mass flow rate $\dot{m}_{\mathrm{LPA}}$. As a consequence, one can witness a greater penetration of cold flow into the channel and thus lower EGR rates. At constant heat release, higher loop flow ratio yields an increase in combustor outlet temperature, as can be seen comparing temperature contours for λ=1.2 and 1.6. Furthermore, due to the higher LPA inlet pressure the HPG port is faced with greater backpressure resulting in reduced hot air penetration length $L_{p,h}$ ultimately leading to an onset of FAE, as shown in the enhanced view in Figure 10(b). Overall, higher loop flow ratio results in higher combustor inlet temperature, which in turn gives a higher combustor outlet temperature for a given heat release rate.

Figure 11 presents estimates for shaft power output, thermal efficiency and combined compression/expansion efficiency as a function of loop flow ratio and combustor pressure loss for a fixed combustor pressure loss of 3%. The data indicate that the variation of predicted shaft power output with loop flow ratio is almost linear. Higher heat release increases total enthalpy reaching the wave rotor channels through the HPG port and thus results in increased extraction of torque. As a direct consequence of this, thermal efficiency appears to increase with lower loop flow ratio. In terms of compression/expansion efficiency higher heat release rates indicate greater adiabatic efficiency. In contrast to thermal efficiency, an increase in loop flow ratio appears to improve compression/expansion efficiencies. This may stem from a higher pressure ratio necessary to reach the limit circle as shown in Figure 12. The kink at 18 kW heat input and low loop flow ratios of 1.2 and 1.3 is a result of onset of FAE, which lowers the average LPG outlet temperature and results in an increase in compression/expansion efficiency.

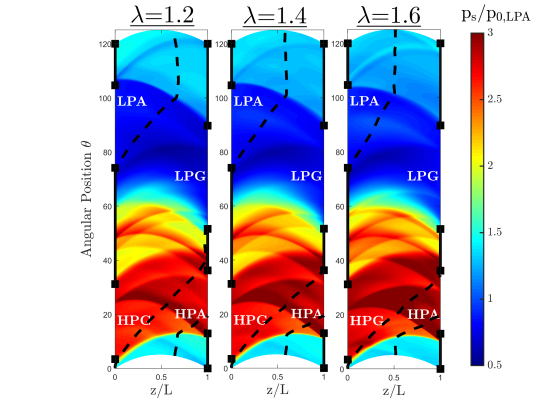

Fig. 10: Comparison showing (a) normalised static pressure and (b) normalised static temperature for three different loop flow ratios for a constant heat release. The pressure contour plots outline a relatively stable position of the shock and expansion waves with respect to the ports. The temperature field implies a reduction in cold air penetration length $L_{p,c}$ as well as an increase in maximum temperature within the computational domain as a consequence of increased EGR rate.

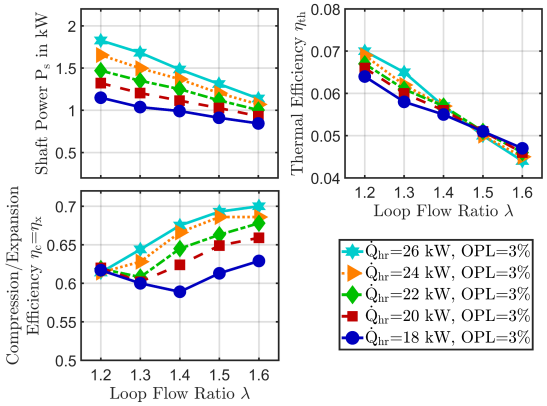

Fig. 11: Estimated effect of variation in loop flow ratio for various heat release rates and a fixed combustor OPL on shaft power, thermal- and compression/expansion efficiency.

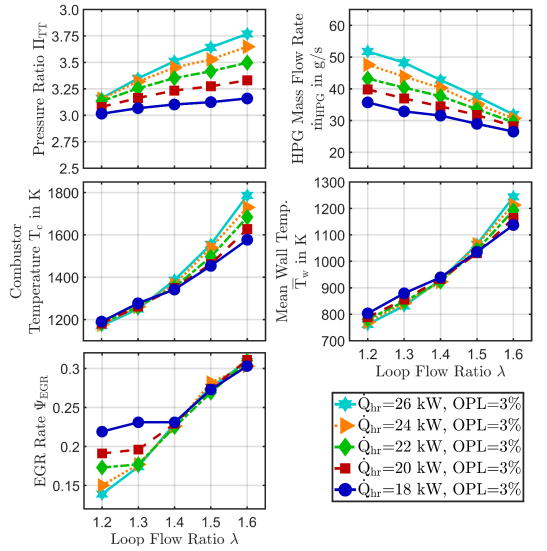

Fig. 12: Estimated distribution of (a) pressure ratio, combustor temperature and mean rotor wall temperature and (b) combustor loop mass flow rate and its associated EGR rate. Data are plotted against loop flow ratio and for a variety of heat release rates at constant combustor OPL.

Nonetheless, FAE is undesired as it increases EGR and represents flow that is expelled unused.

Greater loop flow ratios represent a smaller fresh air mass flow rate and thus result in considerably higher combustor temperatures as given in Figure 12 for a given heat release rate. Estimated wall temperature remains approximately 400 K below the peak cycle temperature, reflecting the self-cooling capabilities of wave rotors. However, this can be expected to be a rather optimistic prediction, as the rotor is in direct contact with the internal leakage cavity, whose temperature at the limit cycle is above the values presented in Figure 12. Finally, the graphs present combustor mass flow rate $\dot{m}_{\mathrm{HPG}}$, which increases the more fuel is injected and the higher the generated pressure ratio is.

The next step is to examine performance behaviour at constant loop flow ratio, as heat release and combustor pressure loss are varied. Obviously, pressure loss across the combustor cannot simply be altered for a given geometry and combustor type. However, the following results introduce the

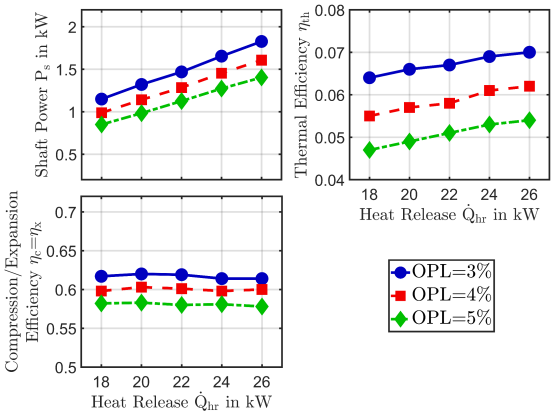

Fig. 13: Graphs outlining the effect of different combustor overall pressure losses with variation in heat release for shaft power, thermal efficiency and combined compression and expansion efficiency. Loop flow ratio is maintained at 1.2.

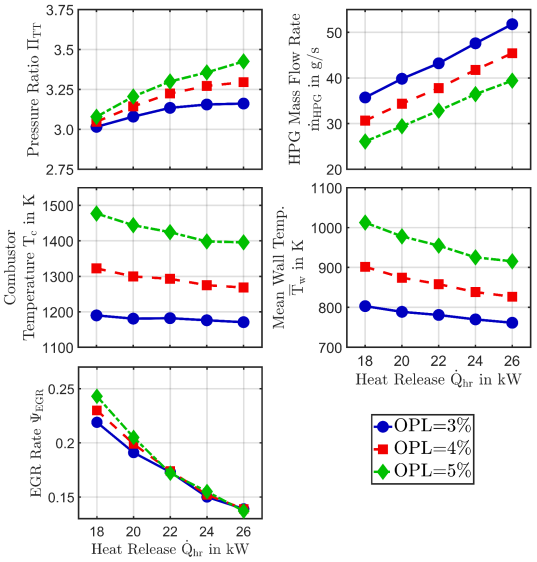

Fig. 14: Variation of estimates for (a) total-to-total pressure ratio, combustor temperature, average rotor wall temperature as well as for (b) combustor mass flow rate and EGR rate for three different combustor OPL.

potential benefits a low pressure loss combustor can offer. This can directly be witnessed examining Figure 13, which outlines benefits for generated torque, thermal efficiency as well as and combined compression/expansion efficiency. Higher combustor pressure loss necessitates a considerably higher pressure ratio and combustor outlet temperature in order to reach the limit cycle, as given in Figure 14.

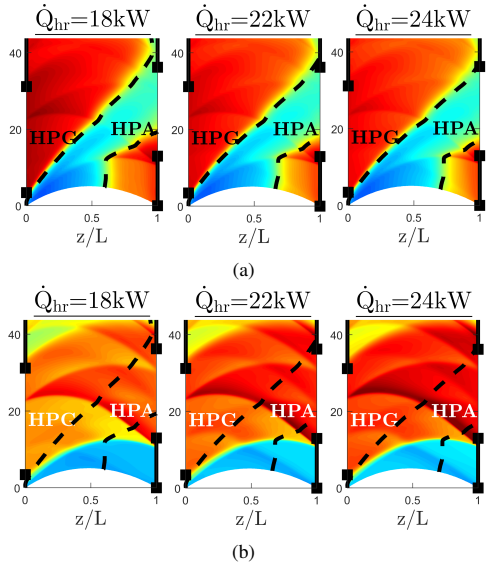

Fig. 15: Contour plots for (a) normalised static pressure and (b) normalised static temperature. The position of primary and secondary shock waves remains relatively stable. The temperature contour indicates the effect of variation in heat release rate on the location of the fresh air stream at the HPA port. Reducing heat release signifies a reduction in combustor mass flow rate and thus lower hot gas penetration length $L_{p,h}$. Further reduction in heat release will lead to the onset of FAE.

Depending on the rotor material chosen, higher pressure losses can thus lead - despite rotor self cooling capabilities - to average wall temperatures exceeding thermal limits and thus have a knock-on effect on service life. Low pressure losses however imply reduced thermal stresses and therefore allow to resort to less temperature resilient and thus more cost effective rotor materials. Despite lower pressure ratio with a decreased OPL, the reduced combustor outlet temperature of approximately 200 K between OPL=3% and OPL=5% accounts for higher density and as a result larger mass flow rates through the HPG port varying between approximately 36 g/s to 52 g/s at OPL=3%. The lowest predicted EGR rate for all OPL occurs for higher heat release and gradually increases as heat release is decreased. The reason for this is exemplified in the temperature contours of Figure 15(a) showing the high pressure zone of HPG and HPA ports. At higher heat input higher combustor mass flow rates ensure sufficient scavenging of channels. Reducing injected fuel flow rate and thus heat release yields lower combustor mass flow rates entering through the HPG port. This reduces $L_{p,h}$ until a portion of the cold, compressed stream does not reach the HPA port, but is carried over and expelled as FAE through the LPG port. This behaviour is illustrated in the contour plots at $\dot{Q}_{hr}$=18 kW and in the

EGR and combustor temperature at OPL=5% in Figure 14. Although variation in heat release rate constitute higher mass flow rates through the channels, the overall wave dynamics and shock wave distribution does not appear to vary significantly, as illustrated in Figure 15(b).

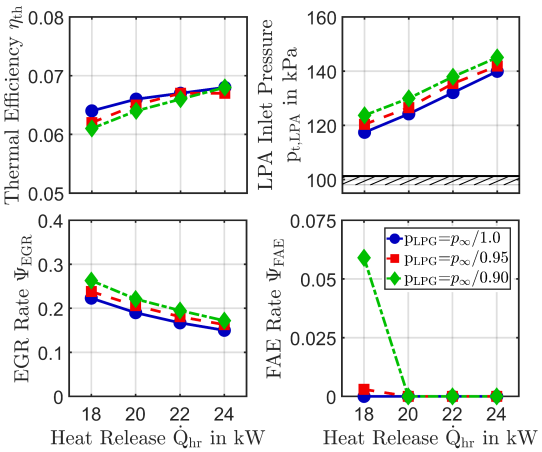

Fig. 16: Effect of exhaust backpressure on thermal efficiency, LPA inlet pressure, EGR and FAE rate as heat input is varied. Data were gathered for a constant loop flow ratio of 1.2 and constant combustor pressure loss of 3%.

B. Exhaust Backpressure

Employing the wave rotor in combination with a recuperator or a power turbine located downstream of the exhaust outlet port (LPG), inevitably increases backpressure experienced by the wave rotor. The implications of such a variation in boundary conditions are treated in Figure 16 for three different levels of backpressure ranging from ambient conditions (p_∞) to rather large levels of 11% higher than ambient. Interestingly, the effect of this proves negligible for predicted shaft power output, combustor temperatures and mass flow rates. Albeit rather small, one can note a gentle decrease in estimated thermal efficiency, in particular visible at lower heat input. As expected, for a given loop flow ratio the delivery pressure necessary to maintain a particular low pressure mass flow rate will increase the higher the backpressure exerted through the LPG port, as given in the top right hand side graph of Figure 16. Similar as seen before, EGR rate gradually increases as heat release rate is reduced. In this scenario, EGR rate proves approximately five percentage points lower when comparing ambient pressure at LPG to the maximum imposed backpressure of $p_\infty/0.90$. Finally, while moderate backpressures exhibit mere hints of FAE onset, large backpressure appear to promote undesirable FAE rates sooner.

C. Axial Leakage Gap

Figure 17 illustrates a comparison of estimated shaft power, thermal efficiency and compression/expansion efficiency for three different axial leakage gaps at constant loop flow ratio of λ=1.2. The simulation data confirms a significant impact on wave rotor gas turbine performance. As one approaches the theoretical limit of 0 mm both torque output and thus thermal efficiency increase considerably up to approximately 8%. Also, compression/expansion efficiency benefit from lower leakage with maximum values of 70%.

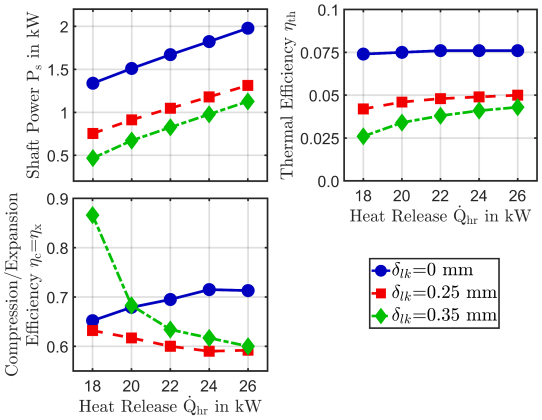

Fig. 17: Impact of axial leakage variation from a theoritcal ideal of 0 mm to up to 0.35 mm on predicted shaft power output, thermal efficiency and compression/expansion efficiency.

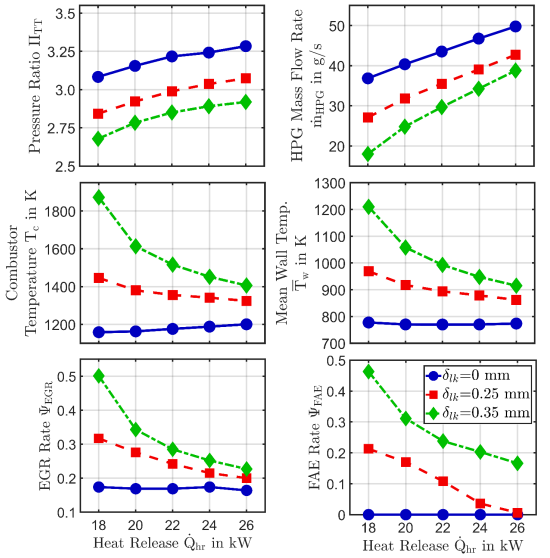

Fig. 18: Graphs indicating the implications of various axial leakage distances on (a) pressure ratio, combustor outlet temperature and average rotor wall temperatures, as well (b) combustor mass flow rate, EGR and FAE rates.

The strong increase towards lower heat release rates for the maximum investigated leakage distance, is rooted in an excessive amount of EGR and FAE, similarly to the one noted in Figure 11 and 12. Associated with the high compression/expansion efficiencies at low leakage is a large pressure ratio of up to 3.25, which decreases to below 3 for higher leakage, as given in Figure 18.

At the limit cycle for high axial leakage, there appears to be an unacceptably high demand for combustor outlet temperature at approximately 1800 K, while the peak cycle temperature for moderate leakages ranges in between 1100 to 1400 K. This implies average wall temperatures below 1000 K. As increased rotor-stator distances promote higher leakage flows from the ports/channels into the leakage cavity the net mass flow rates through the combustor decreases accordingly compared with lower leakage cases. This is shown in Figure 18. As already indicated through the compression/expansion efficiencies, high leakage gaps foster higher EGR and FAE rates as given in the centre and right hand side graphs of Figure 18. This is primarily caused as leakage mass flow rates increases relative to to overall port mass flow rates, which compromises scavenging capabilities.

D. Wall Camber

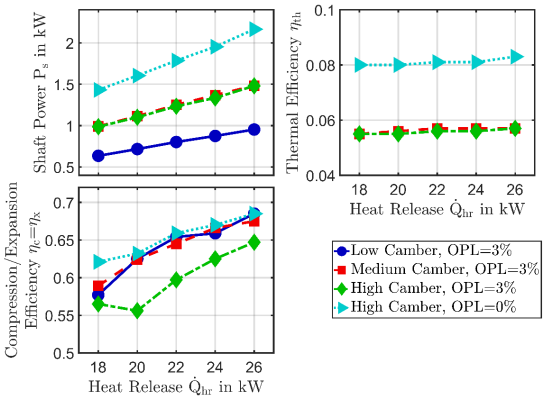

Fig. 19: Effect of different wall camber and heat input angles on shaft power, thermal efficiency and compression/expansion efficiency. Low, medium and high camber designs are compared at constant combustor pressure loss OPL=3%. results for a theoretical design with zero combustor pressure are presented as well.

In order to examine the effect of wall camber, three levels of symmetrically cambered wall profiles were investigated at constant loop flow ratio of 1.2 and OPL=3%. In addition, the high wall camber case was run at zero overall pressure loss, indicating the effect of pressure gain combustion on the performance variables. The results for shaft power, thermal efficiency and compression/expansion efficiency are given in Figure 19.

As lower camber signifies reduced momentum transfer, the

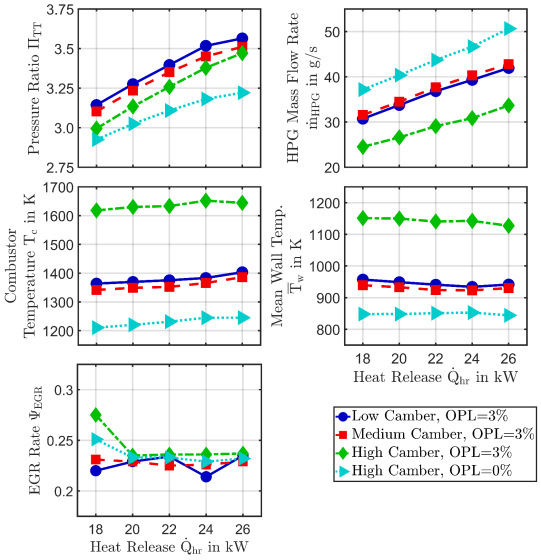

Fig. 20: Simulation results comparing distributions for (a) pressure ratio, combustor temperature and mean rotor wall temperature, and (b) combustor mass flow rate and EGR rate at constant loop flow ratio of 1.2 .

low camber case features low levels of generated torque and thermal efficiency compared with higher camber geometries. However, compression and expansion efficiency remain at a reasonably high level between approximately 60% and 70%. Interestingly, medium and and high camber designs feature comparable levels of shaft power and thus thermal efficiency levels of approximately 6%, which is a result of higher combustor outlet temperature and lower mass flow rate as given in Figure 20. However, if one were to employ a combustor not being subject to pressure losses, thermal efficiency can be further advanced to 8%. The reason for this is that lower pressure losses enables mass flow rates to recover beyond the level of medium and low camber at OPL=3%. In addition, combustor temperatures are significantly reduced. These results emphasise the findings shown in Figure 14 and 15 stating the importance of a low pressure loss combustor design or the application of pressure gain combustion.

E. Heat Recuperation

The final test deals with the potential of employing a recuperator that uses exhaust energy to preheat the charge air upstream of the combustor. Despite the advantage of reducing the necessary heat input for a given temperature difference between HPA and HPG port, one needs to account for an increase in total pressure loss across the combustor loop and increased back pressure at the LPG port. In addition, loop flow ratio needs to be sufficiently low in order to guarantee EGR rates are reasonably low and thus mixed-

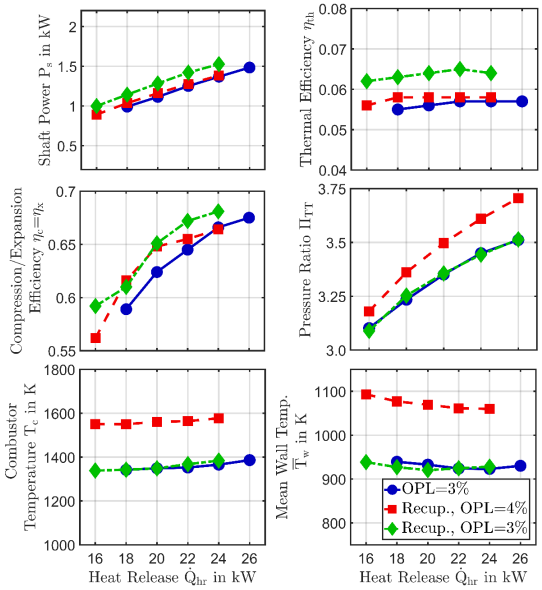

Fig. 21: Variation of predicted shaft power, thermal efficiency, compression/expansion efficiency as well as pressure ratio, combustor outlet temperature and mean rotor wall temperature for unrecuperated (λ=1.4, OPL=3%) and recuperated designs (λ=1.4, OPL=3% and OPL=4%).

out HPA temperatures remain below temperature in the LPG port. The air-to-air heat exchanger effectiveness is assumed to be unity.

Comparing an unrecuperated case with a fixed combustor pressure loss of 3% and loop flow ratio of 1.4 with two recuperated cases with OPL=3% and OPL=4% respectively and an increased backpressure at the LPG port of $p_\infty/0.98$ yields the results illustrated in Figure 21. Examining both shaft power and thermal efficiency graphs, it transpires that for a higher combustor loop pressure loss the recuperated machine cannot yield an improvement. This is mainly a consequence of a relatively small temperature difference between the temperatures in the HPA and LPG port of approximately 30-40 K and the penalty incurred by increased pressure losses. If one were to assume a similar combustor pressure loss, then a thermal efficiency benefit could be witnessed. As a result, it can be concluded that the application of a recuperator in the presented scheme is not desirable and will likely incur higher losses than without heat recuperation. In addition, it is noteworthy that the interaction of hot and cold streams within the wave rotor channels itself already acts as internal recuperation, which limits the additional benefit of an external air-to-air heat exchanger.

IV. CONCLUSIONS AND OUTLOOK

In this paper a quasi-one-dimensional wave action model was used to assess the performance of a micro gas turbine that employs a wave rotor turbine with cambered wall profiles for shaft power extraction. A parametric study was conducted aimed at identifying key performance parameters. To conclude, the main findings of the study can be summarised as follows:

- Estimated compression/expansion efficiencies throughout the study vary within approximately 60 to 70 % indicate the virtue of shock wave compression and expansion.
- The simulation results for thermal efficiency prove to be rather low at around 6-7%. This is owed to the nature of torque extraction, which occurs in a pulsatile manner and is thus less efficient compared to crypto-steady turbomachines. However, the presented wall profile is a simple, symmetrical arc that may not represent the ideal shape for torque generation. Also, in combination with low pressure loss combustors or pressure-gain combustors higher system efficiencies may be achievable.
- Increased profile camber results in greater torque extraction. However, for a given combustor pressure loss there appears to be a limit in camber at which combustor temperature reaches an unacceptably high level at the limit cycle and thus resulting in low mass flow rates and compromised system efficiencies.
- Leakage is a primary performance parameter that needs to be kept at a minimum in order to achieve acceptable and stable operating conditions.
- A loop flow ratio towards unity appears favourable in terms of shaft power output and thermal efficiency. In the event that no upstream pressurisation is used, this is limited by ambient stagnation properties, resulting in loop flow ratios of approximately 1.5 to 1.6 for the presented design.
- The simulation results suggest the application of an external air-to-air recuperator does not lead to a performance benefit. Any reduction in required heat input in the combustor is offset by an increase in pressure losses and higher exhaust backpressure. In addition, direct contact between hot and cold gas streams within wave rotor channels act as internal heat recuperation upstream, therefore limiting the effect of an additional external heat exchanger.

REFERENCES

[1] Special Interest Group, Robotic & Autonomous Systems, "RAS 2020 Robotics and Autonomous Systems," The Knowledge Transfer Network, July 2014.

[2] Defence Science and Technology Laboratory. Competition Document: Beyond Battery Power. DSTL. Accessed: 2017-Nov-10. [Online]. Available: https://www.gov.uk/government/publications/cde-themed-competition-beyond-battery-power/competition-document-beyond-battery-power

[3] T. Verstraete, Z. Alsalihi and R. A. Van den Braembussche, "Numerical Study of the Heat Transfer in Micro Gas Turbines," *J. Turbomach*, vol. 129, no. 4, pp. 835–841, 2007.

[4] A. Marcellan, W.P.J. Visser and P. Colonna, "Potential of Micro Turbine Based Propulsion Systems for Civil UAVs: A Case Study," in *ASME Turbo Expo 2016: Turbomachinery Technical Conference and Exposition Volume 1: Aircraft Engine; Fans and Blowers; Marine*, 06 2016, p. V001T01A031.

[5] R.A. Van den Braembussche, "Micro Gas Turbines - A Short Survey of Design Problems," Neuilly-sur-Seine, France: RTO, Educational Notes RTO-EN-AVT-131, 2012.

[6] M.J. Vick, "'High Efficiency Recuperated Ceramic Gas Turbine Engines for Unmanned Air Vehicle Propulsion," PhD Thesis, Imperial College London, 2012.

[7] N. Müller and L.G. Fréchette, "Performance Analysis of Brayton and Rankine Cycle Microsystems for Portable Power Generation," in *Proceedings of IMECE2002 ASME International Mechanical Engineering Congress & Exposition*, 11 2002.

[8] A.J. Head and W.P.J. Visser, "Scaling 3-36kW Microturbines," in *ASME Turbo Expo 2012: Turbine Technical Conference and Exposition Volume 5: Manufacturing Materials and Metallurgy; Marine; Microturbines and Small Turbomachinery; Supercritical CO2 Power Cycles*, 06 2012, pp. 609–617.

[9] S. Tüchler and C.D. Copeland, "Experimental Results from the Bath -Wave Rotor Turbine Performance Tests," *Journal of Energy Conversion and Management*, vol. 189, pp. 33–48, 3 2019.

[10] L. Pohořelský, P. Sané, T. Rozsas, N. Müller, "Wave Rotor Design Procedure for Gas Turbine Enhancement," in *Proceedings of the ASME Turbo Expo 2008*, ser. ASME Turbo Expo 2008: Power for Land, Sea, and Air, vol. 1. American Society of Mechanical Engineers, 2008, pp. 847–860.

[11] A. Fatsis, "Performance Enhancement of One and Two-Shaft Industrial Turboshaft Engines Topped With Wave Rotors," *International Journal of Turbo & Jet-Engines*, vol. 35, no. 2, pp. 137–147, 2018.

[12] M.R. Mataczynski, M.J. McClearn, F.R. Schauer, D.E. Paxson, D.E and J.L. Hoke, "Design and Testing of a Small Pressure Wave Supercharger for an Industrial Diesel Engine," *AIAA SciTech Forum - 55th AIAA Aerospace Sciences Meeting*, 2017.

[13] J. Li, E. Gong, L. Yuan, W. Li and K. Zhang, "Experimental Investigation on Pressure Rise Characteristics in an Ethylene Fuelled Wave Rotor Combustor," *Energy & Fuels*, vol. 31, no. 9, pp. 10 165–10 177, 2017.

[14] H.D. Perkins and D.E. Paxson, "Summary of Pressure Gain Combustion Research at NASA," *NASA/TM2018-219874*, 2018.

[15] J. Li, E. Gong, L. Yuan, W. Li and K. Zhang, "Experimental Investigation on Flame Formation and Propagation Characteristics in an Ethylene Fuelled Wave Rotor Combustor," *Energy & Fuels*, vol. 32, no. 2, pp. 2366–2375, 2018.

[16] J. Zhao and D. Hu, "An Improved Wave Rotor Refrigerator Using an Outside Gas Flow for Recycling the Expansion Work," *Shock Waves*, vol. 27, no. 2, pp. 325–332, 2017.

[17] D. Hu, Y. Yu, P. Liu, X. Wu and Y. Zhao, "Improving Refrigeration Performance by Using Pressure Exchange Characteristic of Wave Rotor," *Journal of Energy Resources Technology, Transactions of the ASME*, vol. 141, no. 2, 2019.

[18] H.E. Weber, *Shock Wave Engine Design*. New York: John Wiley & Sons, 1996.

[19] R.D. Pearson, "A Gas Wave-Turbine Engine Which Developed 35 HP and Performed Over a 6:1 Speed Range," in *Proceedings ONR/NAVAIR Wave Rotor Research and Technology Workshop*. Naval Postgraduate School, 1985.

[20] ——, "Pressure Exchangers and Pressure Exchange Engines," in *The Thermodynamics and Gas Dynamics of Internal-Combustion Engines, Volume II*, J.H. Horlock and D.E. Winterbone, Ed. New York: Oxford University Press, 1986, ch. 16, pp. 903–943.

[21] A. Mathur, "Design and Experimental Verification of Wave Rotor Cycles," in *Proceedings ONR/NAVAIR Wave Rotor Research and Technology Workshop*. Naval Postgraduate School, 1985.

[22] R. Taussig, P. Cassady, J. Zumdieck, W. Thayer and E. Klostermannt, "Investigation of Wave Rotor Turbofans for Cruise Missile Engines," Final Report Submitted by MSNW to DARPA, Tech. Rep., 1983.

[23] J. Piechna, "Feasibility Study of the Wave Disk Micro-Engine Operation," *J. Micromech. Microeng.*, vol. 16, 2006.

[24] J. Piechna and D. Dyntar, "Numerical Investigation of the Wave Disk Micro-Engine Concept," *International Journal of Gas Turbine, Propulsion and Power Systems*, vol. 2, no. 1, 2008.

[25] ——, "Hybrid Wave Engine Concept and Numerical Simulation of Engine Operation," *The Archive of Mechanical Engineering*, vol. LVII, no. 1, 2010.

[26] S. Tüchler and C.D. Copeland, "Validation of a Numerical Quasi One-Dimensional Model for Wave Rotor Turbines with Curved Channels," *J. Eng. Gas Turbines Power.*, GTP-19-1313.

[27] D.E. Winterbone and R.J. Pearson, *Theory of Engine Manifold Design: Wave Action Methods for IC Engines*. London and Bury St Edmunds, United Kingdom: Professional Engineering Publishing Limited, 2000.

[28] S. Eidelmann, "The Problem of Gradual Opening in Wave Rotor Passages," *Journal of Propulsion and Power*, vol. 1, no. 1, pp. 23–28, 1985.

[29] ——, "Gradual Opening of Skewed Passages in Wave Rotors," *Journal of Propulsion and Power*, vol. 2, no. 4, pp. 379–381, 1986.

[30] L.M. Larosiliere, "Three-Dimensional Numerical Simulation of Gradual Opening in a Wave Rotor Passage," *AIAA-93-2526*, 1993.

[31] D. Paxson and J. Wilson, "An Improved Numerical Model for Wave Rotor Design and Analysis," *AIAA*, Jan. 1993.

[32] D.E. Paxson, "A Numerical Model for Dynamic Wave Rotor Analysis," *AIAA-95-2800*, 1995.

[33] A. Fatsis, M. Vrachopoulos, S. Mavrommatis, A. Panoutsopoulou and F. Layrenti, "A Computational Method for Pressure Wave Machinery to Internal Combustion Engines and Gas Turbines," vol. 52, 04 2006, pp. 49–58.

[34] S. Chan, H. Liu and F. Xing, "Defining the Thermodynamic Efficiency in a Wave Rotor," *J. Eng. Gas Turbines Power*, vol. 140, no. 11, pp. 112 601–1–112 601–11, 2016.

[35] J. Wilson, G.E. Welch and D.E. Paxson, "Experimental Results of Performance Tests on a Four-Port Wave Rotor," *NASA/TM2007-214488*, 2007.

Errata Paper I

The axial coordinate is denoted by z and, as a result of this, the cell width in equation 15 should read Δz. In section III.A. the mentioned *limit circle* is misleading and should read *limit cycle* instead.

Addendum to Paper I

The finite axial clearance between the rotor and stator within the wave rotor housing gives rise to leakage paths as shown in Figure 2-1. The cross sectional schematic in Figure 2-1(a) shows the location of the main leakage cavity located within the volume between rotor shaft, rotor and stator. This corresponds to the leakage cavity represented in the wave rotor model. It shall be noted that this is assumed to be perfectly sealed, which gives rise to both elevated pressures and temperatures within the cavity. Figure 2-1(b) indicates an additional leakage path connecting the ports and leakage cavity with neighbouring channels fostering channel-to-channel interaction. Since the model assumes a single channel only this path cannot be captured by the model.

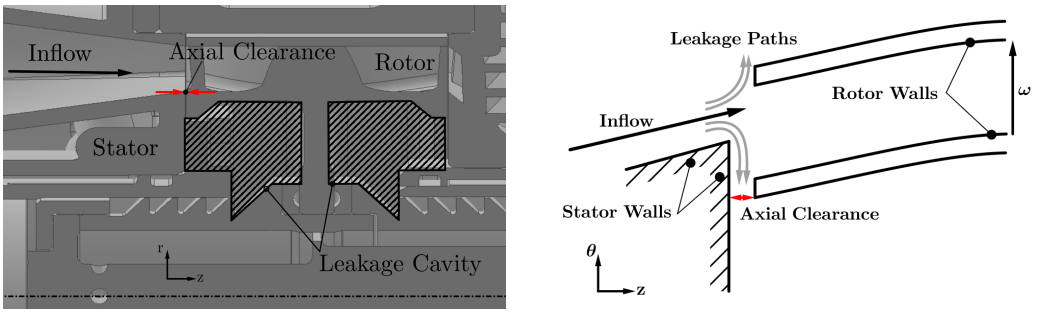

(a) (b)

Figure 2-1: The axial clearance between rotor and stator opens up a leakage path a) towards the inner rotor cavity and b) between the rotor channels. The numerical model considers only the first leakage path and does not take inter-channel leakage into account.

2.3 Summary and Implications of Paper I

The numerical data identify combustor pressure loss and axial leakage as the primary performance affecting parameters, while the system appears to be less sensitive to exhaust backpressure from the low pressure outlet. The paper also indicates further potential of wave rotor based gas turbines in combination with the renewed current interest in pressure-gain combustion. While additional heat recuperation remains an effective approach to raise thermal efficiency for standard (micro-)gas turbines, the

data suggests this is not the case for a wave rotor micro-gas turbine. Compressed and expanded streams are in direct contact with each other within the wave rotor channels resulting in internal heat recuperation. In combination with increased pressure losses across the combustor loop, these factors are primarily responsible for the compromised benefit.

A crucial implication of the chapter presented pertains to thermal efficiency. While compression and expansion efficiency are reasonably high and in the range of 60-70% the wave rotor gas turbine exhibits similarly poor thermal efficiencies as gas turbines of comparable size in the range of 6-7%. This renders the presented concept an efficient gas generator, yet a poor gas turbine. The main source of this limitation lies in the power generating process of wave rotors. This is pulsatile in nature due to the discrete arrangement of ports and is thus limited to a rather brief period - mainly where the channels are exposed to the high temperature, high pressure gas exiting the combustor - in which a channel contributes to shaft power generation. This limitation is inherent to wave action pressure exchangers, but may be partially alleviated through camberline optimisation and increasing the number of cycles per revolution. This results in an increased number of inlets and reduces the time a channel is idle and does not contribute to power generation. However, it shall be noted that such a measure increases ducting complexity to combine the multiple in- and outlet port ducts into manifolds.

Chapter 3

Experimental Investigation of a Non-Axial, Micro-Scale Wave Rotor Turbine and Quasi-One-Dimensional Model Validation

3.1 Content Overview and Thesis Context

This chapter features two comprehensive journal articles. The first article in Section 3.2 is dedicated to characterising a micro-wave rotor turbine experimentally, as well as to assess the performance potential and possible conflict of objectives. It provides a comprehensive experimental performance test of a micro-wave rotor turbine prototype with symmetrically cambered channels. The experimental work presented was carried out at the University of Bath gas stand and uses electric heaters as the main source of heat and an eddy-current dynamometer to measure shaft power and rotor speed. The tests were run in an open-loop configuration, where the high pressure in- and outlet ports are not directly connected and the corresponding mass flow rates in the combustor loop matched using gates valves and mass flow meters. The study focuses on the sensitivity of shaft power, outlet temperature distribution and achieved compression pressure ratio as wave rotor speed, peak inlet temperature and axial leakage gaps are varied. In addition to shaft power and pressure ratio measurements, temperature

probes in the high pressure exhaust duct are used to infer the behaviour of internal EGR, as independant variables are varied. Finally, an efficiency calculation taking into account both heat transfer between cold and hot gas streams as well as EGR rates is proposed to estimate a combined compression/expansion efficiency of wave rotors running at elevated temperatures.

The second publication in Section 3.3 seeks to link the laboratory tests with the in-house developed quasi-one-dimensional wave rotor model of Chapter 2 by using the generated experimental data as well as literature data to validate the numerical model. To this end, data from the open literature on low temperature pressure dividers is used to provide steady state as well as transient validation. This ensures that both the steady conditions in the ports and the transient evolution of the shock and expansion waves within the channels are accurately reflected. High temperature data from the in-house experiments are used to correlate the predictive modelling capabilities of the numerical model with respect to shaft power, pressure ratio and outlet temperature. Finally, implications of leakage variation due to thermal expansion are discussed.

3.2 Paper II: Experimental Results from the Bath μ-Wave Rotor Turbine Performance Tests

Article published in *Energy Conversion and Management*, [123]:

S. Tüchler and C.D. Copeland, "Experimental Results from the Bath μ-Wave Rotor Turbine Performance Tests," Energy Conversion and Management, Vol. 189, pp.33-48, 2019.

Statement of authorship

S. Tüchler (candidate): development and implementation of methodology, experimental work, data analysis, preparation of tables and figures, writing and compilation of manuscript.

C.D. Copeland (supervisor): supervision of experimental work, review and editing of manuscript.

Copyright

Experimental Results from the Bath μ-Wave Rotor Turbine Performance Tests

Stefan Tüchler[a,*], Colin D. Copeland[a]

[a]*Powertrain and Vehicle Research Centre, Department of Mechanical Engineering, University of Bath, Claverton Down, Bath BA2 7AY, United Kingdom*

Abstract

This paper details an extensive experimental investigation of a novel throughflow micro-wave rotor with symmetrically cambered passage profiles designed for shaft power output as well as pressure exchange. This is the first time comprehensive experimental data from a power generating wave rotor is presented in a peer-reviewed journal. Moreover, the significance and renewed interest in wave rotors for a wide range of applications from refrigeration to micro-gas turbines makes this experimental programme extremely valuable to many fields of research.

The wave rotor is a four port, three-cycle unit of 60 mm in diameter, 30 mm in length and houses 46 channels. The unit was experimentally tested on a gas stand in open-loop configuration using electrical heaters as a source of heat for the high pressure inlet and pressurised air for both inlet ducts. Throughout testing, the mass flow rates among high pressure in- and outlet were balanced.

A series of tests were conducted investigating the effect of variation in rotational speed, ratio of inlet mass flow rates (loop flow ratio), axial clearances and peak inlet temperature on wave rotor performance. The results show the importance of minimum axial clearance for maximum energy transfer as well as for reduced mixing of hot and cold flows. The competing relationship between pressure ratio, high pressure zone pressure difference, internal exhaust gas recirculation and fresh air exhaustion is also highlighted. Finally, measurements of the temperature distributions in the high pressure outflow show the effect of rotational speed, loop flow ratio and centrifugal forces on the fresh air stream location and its mixing with the hot gas stream.

A peak shaft power of 450 W and a peak pressure ratio of approximately 1.63 were obtained close to the design speed that were in line with expectations for clear-

*Corresponding author

Email address: S.Tuechler@bath.ac.uk (Stefan Tüchler)

ances and temperatures under investigation. Using a new approach to calculating efficiency that assumes equal values for expansion and compression, a peak figure of 80% was obtained indicating the superiority that such designs have over similarly sized traditional turbomachinery.

Keywords: Wave rotor turbine, Wave action, Experimental testing, Pressure exchange

---

Nomenclature

ΔT Temperature difference [K]

c_p Specific heat capacity at constant pressure [J/kg-K]

A Cross-section area [m^2]

D Diameter [m]

F Non-dim. friction [-]

G Non-dim. leakage [-]

L Length [m]

M Mach number [-]

R Specific gas constant [J/kg-K]

T Temperature [K], non-dim. finite passage opening[-]

U Tangential velocity [m/s]

$\dot{m}$ Mass flow rate [kg/s]

a Speed of sound [m/s]

h Height [m]

t Time [s]

w Width [m]

z Axial coordinate [m]

Π Pressure ratio [-]

Ψ EGR rate [-]

β Blade angle [°]

δ Leakage gap [m]

η Efficiency [-]

γ Ratio of specific heats [-]

λ Loop flow ratio [-]

ν Kinematic viscosity [m^2/s]

ω Angular speed [rad/s]

θ Angular coordinate [rad]

EGR Exhaust gas recirculation

FAE Fresh air exhaustion

FS Full scale

HPA High pressure air

HPG High pressure gas

LPA Low pressure air

LPG Low pressure gas

PE Pressure exchanger

PWS Pressure wave supercharger

RF Reverse flow

SLM Selective laser melting

TF Throughflow

c Cold, compression

ch Channel

h Hydraulic, hot

is Isentropic

m Mixed

s Static

t Total

x Expansion

1. Introduction

1.1. Background and Operating Principle

Wave rotors are a type of dynamic pressure exchange machinery, where energy is transferred through shock waves. The technology bears the potential to further enhance thermal cycles and thus reduce global energy consumption and increase thermodynamic efficiency. As a result, wave rotors have been suggested in a range of fields of application, ranging from pressure gain combustors [1, 2], to gas turbine topping cycles [3, 4], wave rotor turbines [5], pressure wave superchargers for internal combustion engines [6, 7] and refrigeration cycles [8, 9], as summarised in Figure 1.

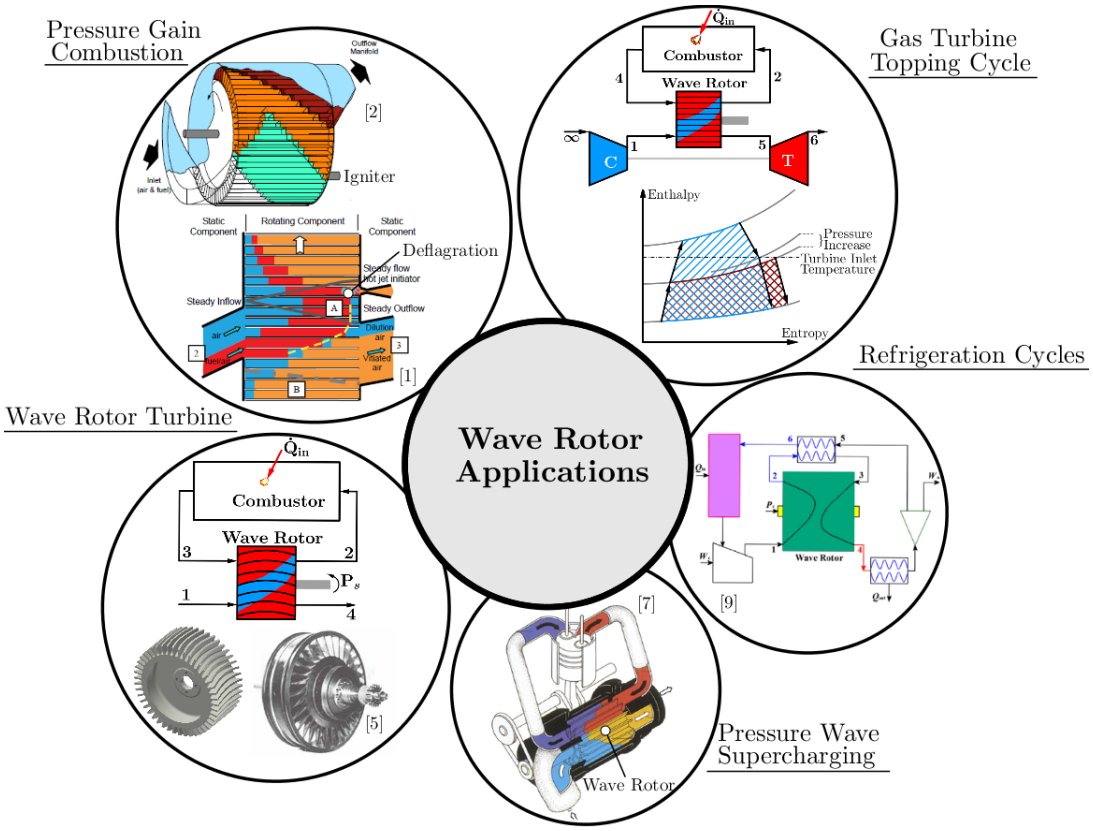

Figure 1: Summary of wave rotor applications aimed at enhancing thermal cycles and reducing energy consumption. These range from gas turbine enhancement through pressure gain combustion [1, 2], topping cycles [3, 4] and wave rotor turbines [5]. Furthermore, wave rotors can be applied to internal combustion engines as a supercharging device [6, 7] and to refrigeration cycles [8, 9].

The principle involves shock and expansion waves travel along discrete channels arranged around the circumference of a cylindrical drum. This process is unsteady and does not require additional moving parts. To each side of the rotor, there are stator endplates containing port openings, as shown in Figure 2(a). The rotor channels are then periodically exposed to the thermodynamic conditions in the ports triggering the generation of shock and expansion waves. Introducing channel camber and an angled arrangement of inlet and outlet ports additionally allows to employ the wave rotor as a turbine for shaft power extraction.

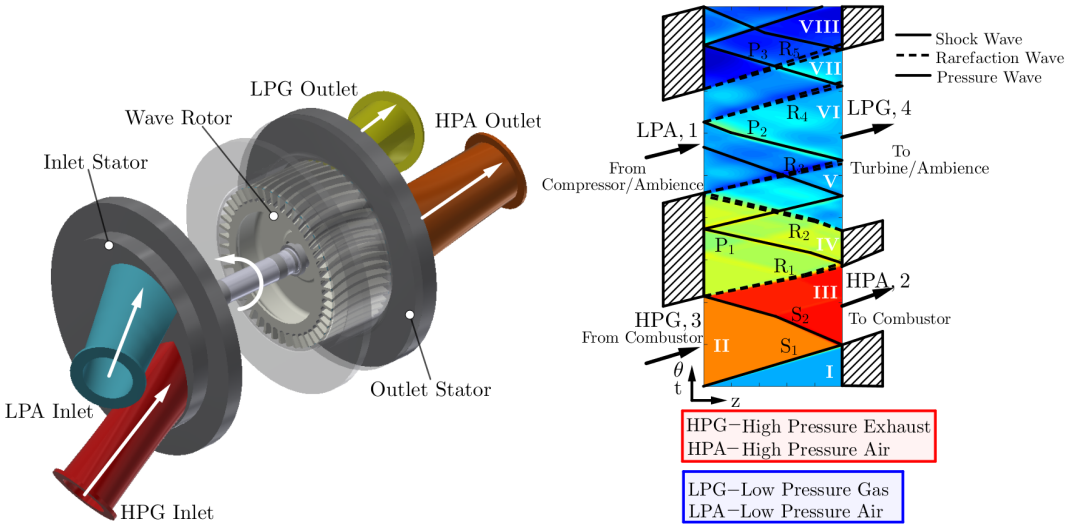

Figure 2: (a) Main components of a generic four-port, single cycle throughflow wave rotor consisting of inlet and outlet stator endplates and rotor/bearing assembly. (b) Unfolded view of the wave pattern experienced as a single channel passes through the port arrangement of a four-port throughflow wave rotor showed in the θ-z plane.

In order to examine the wave action processes taking place within a single channel, one can examine the unwrapped wave pattern on a two-dimensional θ-z-plane, as done in Figure 2(b). The device features two high pressure ports, namely a high pressure exhaust gas (HPG) and high pressure air (HPA), that form the combustor loop. It further shows two low pressure ports, the low pressure air intake (LPA), from where the fresh air is drawn-either from ambience or from an upstream compressor-into the rotor, and the low pressure gas port (LPG), through which the hot exhaust gases are expelled to the ambience or alternatively further expanded by a turbine.

Initially, pressure and temperature within the channels are close to ambient conditions. Exposing the channel to the left with the high pressure, high temperature exhaust gas from the combustor (HPG) sets off a right travelling, primary shock wave (S1). Upon reaching the other end of the channel the HPA port is opened and the shock wave is reflected resulting in a secondary, left running shock wave (S2). These two shock waves compress the incoming fresh air and their strength governs the compression ratio achieved by the rotor.

Closing the HPG port sparks an expansion fan or rarefaction wave (R1), which expands the exhaust gases to an intermediate pressure level. Impingement of the head of R1 on the right hand side marks the closure of the HPA port, which prompts a hammer shock like pressure wave (P1). Opening the low pressure exhaust port (LPG) leads to further expansion of the gases (R2) before the gases are ejected to the ambience. The low pressure inlet port opens as soon as (R2) reaches the left hand side of the channel. Finally, closure of the LPA port generates weak pressure waves before the cycle is repeated.

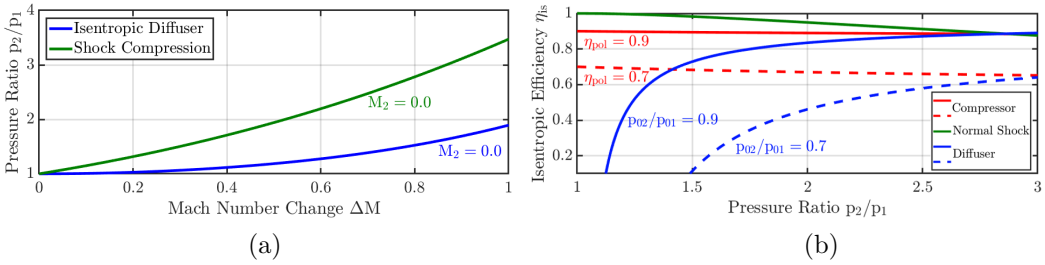

Figure 3: (a) Static pressure ratio plotted versus Mach number change for steady (diffuser - lower, blue curve) and unsteady (moving, normal shock wave-upper green curve) compression (amended from [10]). (b) Isentropic efficiency plotted versus static pressure ratio for compressor (red curves), diffuser (blue curve) and shock compression (green curve) (amended from [11]).

The geometry of a wave rotor does not feature any complex surfaces and comprises simple channel shapes. Due to the presence of both the hot expanded gas stream and the cold air stream the wave rotor is inherently self-cooled and the material temperature remains below the peak cycle temperature. Another distinct advantage of unsteady flow devices over steady, such as diffusers, or crypto-steady flow devices (compressor/turbine turbomachinery arrangement) is illustrated in the graphs of Figure 3. In comparison with steady flow devices (lower, blue curve in Fig. 3(a)) and assuming the Mach number downstream is reduced to zero, shock compression (top, green curve) as witnessed in a wave rotor accounts for a larger static pressure ratio for any given Mach number change. Furthermore, as diffusers become large in

size to prevent undesired flow separation, compression in an unsteady fashion yields higher pressure ratios over a smaller distance.

Looking at the isentropic efficiency in Fig. 3(b) and comparing compression through a moving shock without wall friction (solid green line), a compressor (blue lines) with different polytropic efficiencies (0.9 and 0.7) and diffusers (red lines) with different total pressure loss (0.1 and 0.3) considered, it becomes apparent that for static pressure ratios of approximately three, unsteady compression features higher isentropic efficiency. This signifies that for the same pressure ratio, several stages of diffusion or increases in kinetic energy are necessary to obtain the same pressure ratio. As a result, unsteady devices can be built compact. Nonetheless, it should be added that wall friction and potential shock-boundary layer interaction would reduce shock efficiency.

1.2. Literature Survey

Over the past decades numerous research studies from a variety of research institutes have been dedicated towards the investigation of dynamic pressure exchange machinery, such as wave rotors. Early research efforts aimed at introducing pressure exchangers of straight channel profiles as a means to enhance gas turbine cycles [3, 4, 12] and internal combustion engines [6, 7, 13, 14]. More recent studies further pursue gas turbine [15–18] and reciprocating engine [14, 19, 19–22] enhancement. In addition, the field of applications has been extended through the application of wave rotors in refrigeration cycles [8, 9, 23–26] and pressure-gain combustors [1, 2, 27–33]. In comparison with the amount of numerical research on wave rotor design and performance, there are relatively few studies dedicated to the experimental characterisation of wave rotors. The bulk of them were conducted at NASA Glenn Research Center. Initial studies were done predominantly on pressure exchangers and equalisers, where temperatures are generally low. One of the first studies was conducted by Kentfield at Imperial College London [34, 35] on a rotor of an approximately 200 mm diameter rotor spinning at 6000 rpm with a focus performance and efficiency maps of pressure divider and equaliser. The effect of leakage variation on the achieved pressure ratios of a pressure divider was investigated by Wilson and Fronek [36] implying a linear relationship between axial clearance and pressure ratio. A follow-up study further investigated the effects of friction and finite opening timing and determined a squared relationship between efficiency, friction factor and finite opening timing factor, respectively. A four-port throughflow wave rotor suitable for usage in a gas turbine topping cycle was experimentally characterised by Wilson et al. [37, 38]. The tests were conducted with a chilled air supply for the LPA inlet, limiting the

necessary heat supplied by the heater. Sweeps of inlet mass flow rate, loop flow ratio were conducted and the sensitivity of the low pressure section pressure p4/p1 and temperature ratios T4/T1 to variations investigated. Most recent experimental work carried out by the US Air Force Research Laboratory by Mataczynski et al.[14, 20, 39], McClearn et al. [40, 41], Lapp et al.[19] and Reinhart et al. [22]. The first set of studies dealt with a four-port reverse flow pressure wave supercharger for downsized ICE engines. The rotor was designed for a rotational speed of 34,500 rpm and had a mean diameter of 34 mm. The tests yielded promising result, despite suffering from rotor dynamic and premature bearing failures due to insufficient bearing sealing. This limited the peak cycle temperature to around 360°C. Both McClearn et al. [40, 41] and Lapp et al. [19] used an external combustor in their wave rotor testing providing a peak cycle temperature of around 840°C. The former study investigated a small-scale rotor of 42 mm in diameter and a target rotational speed of 38,500 rpm with a target exhaust power of 1.8 kW, while the rotor of the latter study measured 36 mm in diameter and had a target rotational speed of 60,000 rpm delivering an exhaust stream power of 500W. Reinhart et al. [22] tested a small scale wave rotor and coupled the wave rotor to a compression ignition engine examining the effect of the small-scale pressure-wave supercharger on engine performance.

All of the mentioned studies deal with straight channels. There are, however, few studies in the public domain on cambered profiles. These wave rotor turbines with cambered passage walls aim at acting both as pressure exchangers while producing shaft power through momentum change of the flow. Most efforts date back to the late 20^{th} century and, unfortunately, documentation of these endeavours is fragmentary. Pearson [5, 42] carried out successful tests at the University of Bath on a single cycle, through-flow wave rotor with helical passage shape leading to a power output of around 26 kW at a rotational speed of 18,000 rpm. The machine achieved a thermal efficiency of approximately 10 % before being subsequently destroyed as a result of overspeeding, which resulted in suspension of the project. Other efforts by General Electric and General Power Corporation were also ceased as the generated shaft power output was deemed insufficient [43, 44]. Research studies carried out at Michigan State University and Warsaw University of Technology introduced a radial, reverse flow wave-disk engine that uses shock-waves and curved channels to create shaft power and energy exchange. The concept has been extensively investigated through numerical means [45–48] and although an experimental facility was introduced [49] and filed for patent [50], no experimental results have thus far been reported in the open literature.

This paper aims at addressing this gap by presenting a small scale wave rotor turbine with symmetrically cambered profiles that enable shaft power output of ap-

proximately 400-500W at a design speed of 32,000 rpm while performing as a pressure exchanging device. To the authors' knowledge, this is the first time detailed experimental results of a power generating wave rotor turbine are presented. This study therefore aims to make an important contribution to the body of knowledge in-so-far as to share quantitative evidence both of the enormous potential that wave rotors offer but some of their unique operating characteristics and challenges as well. It will demonstrate experimentally how efficient shock compression and shaft power can be achieved in a relatively simple design through the shock expansion of a hot gas. What is more, given the small size of the test device, this can be accomplished at a fraction of the rotation speed of more traditional turbomachinery. However, a wave rotor is subject to internal fluid heat and mass exchange and is sensitive to the stator-rotor gap.

The structure of the paper is thus as follows: Firstly, performance parameters of wave rotors are presented before the design including stationary and rotational components is introduced and a comparison of the rotor with other examples with respect to friction, finite opening time and leakage is done. This is followed by an introduction of the experimental setup, instrumentation and the scope of experimental tests. After that ensues a discussion of experimental results including issues faced during testing, before conclusions are drawn.

2. Methodology

2.1. Performance Parameters

The investigated wave rotor is a four-port throughflow design, where wave action accommodates for compression and expansion of the working fluid. Figure 4(a) indicates these shock and expansion waves as well as the distribution of fresh and hot gases through the wave rotor cycle near design conditions. As previously stated, hot gases enter through the HPG port, while fresh air enters through the LPA port. Generally, the mass flow rates through these two inlet ports $\dot{m}_{\mathrm{HPG}}$ and $\dot{m}_{\mathrm{LPA}}$ are unequal and vary depending on operating conditions.

The ratio of the inlet mass flow rates is referred to as loop flow ratio λ, as seen in Equation 1.

$$\lambda = \frac{\dot{m}_{\mathrm{HPG}}}{\dot{m}_{\mathrm{LPA}}} \tag{1}$$

Mass flow rates entering through HPG and LPA ports respectively is governed by the stagnation properties in the corresponding ports and back pressure on the outlet

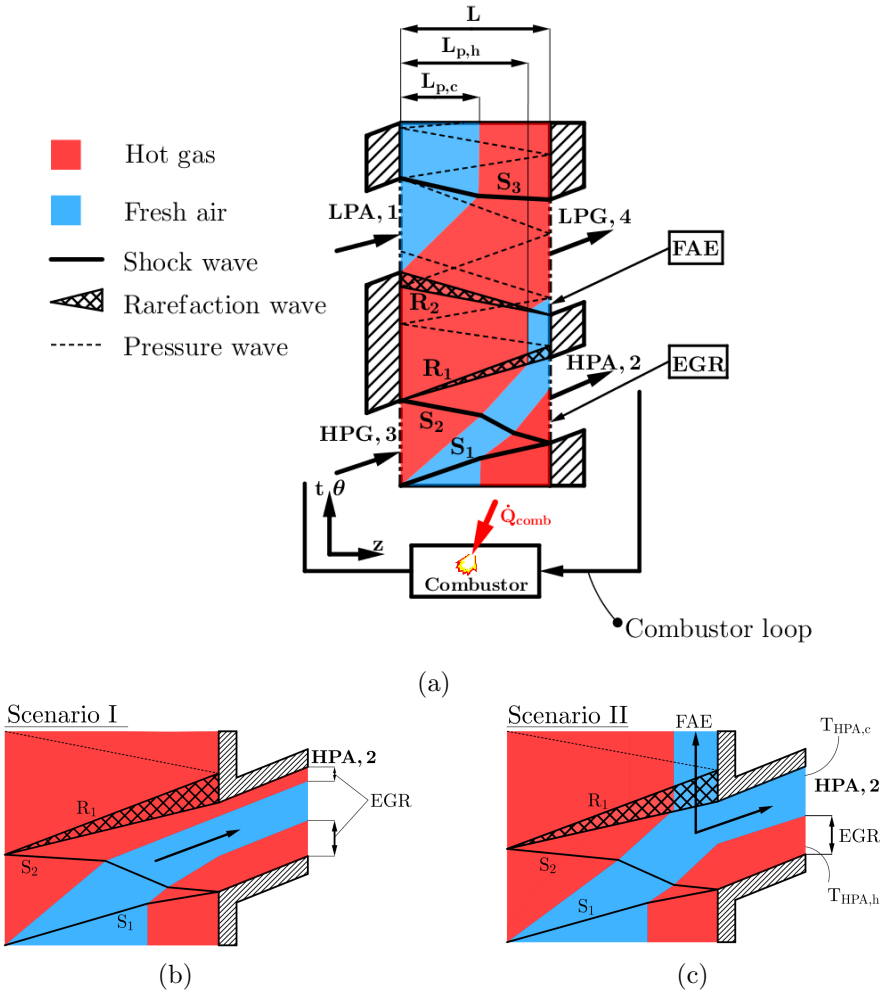

Figure 4: (a) Wave rotor cycle schematic showing general distribution of fresh and hot exhaust gases within the rotor leading to fresh air exhaustion (FAE) through the LPG port and exhaust gas recirculation (EGR) through the HPA port. The amount of EGR and FAE are a function of the hot and cold mass flow rates. (b) shows a closeup of a scenario including solely EGR without FAE while (c) depicts a situation, where both EGR and FAE occur.

side. Variation in λ for a given $\dot{m}_{\mathrm{HPG}}$ will determine the mass entering through the LPA port and thus define the penetration length $L_{p,c}$ of the fresh air into the channel. Operating at moderately elevated pressures results in a $L_{p,c}/L$ of approximately 0.5.

This signifies that there will be a certain amount of hot gases that do not leave the domain through the LPG port, but are carried over through the HPA port. This inherent characteristic of wave rotors is referred to as exhaust gas recirculation (EGR).

The hot gas penetration length $L_{p,h}$ is considerably greater than its cold air correspondent, due to the generally higher mass flow rate. However, depending on the thermodynamic conditions in the port and the rotational speed of the rotor it may be that it is not sufficient to scavenge the entire channel- such as is the case in scenario I in Figure 4(a)- resulting in some fresh air remaining within the channel after it has passed the HPA port exit. This fresh air is then transferred and expelled unused through the LPG port, resulting in fresh air exhaustion (FAE). This corresponds to scenario II shown in Figure 4(b).

Defining efficiency is more problematic for wave rotors compared to traditional turbomachinery. The traditional enthalpy based efficiency definition assumes adiabatic conditions and thus yields erroneous values with compression efficiency being considerably under- and expansion efficiency overpredicted with values greater than 1. This is caused by the fact that both the hot expanded gas stream and the colder compressed air stream are transported within the same channels and thus in direct contact with each other. This gives rise to heat exchange between the two streams, which acts as an internal recuperator, but renders a consistent definition of wave rotor compression and expansion efficiency difficult. In addition, internal EGR and FAE exacerbate this issue leading temperature sensors located in the respective outflow ports measuring mixed out temperatures of hot and cold fluid streams.

In order to incorporate both effects a modified approach is proposed. In general, HPG and HPA ports are connected through the combustor, as shown in Figure 4(a), therefore mass flow rates through the respective ports (ignoring added fuel mass) will generally be equal in steady-state operation. Since loop flow ratio is generally greater than unity, the mass flow rate entering through the HPA port is then composed of both the fresh air supply $\dot{m}_{\mathrm{LPA}}$ and the internally circulated exhaust gas $\dot{m}_{\mathrm{EGR}}$. Thus, following the general flow pattern as illustrated in Figure 4 with internal EGR being present in the HPA port and neglecting FAE, flow leakage and the effect of rotational speed variation, the amount of EGR may be approximated as the difference in fresh air mass entering through the LPA port and the air/gas mixture mass exiting the wave rotor through the HPA port. Thus the amount of EGR becomes solely a function of loop flow ratio λ as described in Equation 2.

$$\begin{aligned} \dot{m}_{\mathrm{EGR}} &= \dot{m}_{\mathrm{HPA}} - \dot{m}_{\mathrm{LPA}} \\ \psi_{\mathrm{EGR}} &= \frac{\dot{m}_{\mathrm{HPA}} - \dot{m}_{\mathrm{LPA}}}{\dot{m}_{\mathrm{HPA}}} = \frac{\lambda - 1}{\lambda} \end{aligned} \tag{2}$$

Using Equation 2 in combination with the mixed out temperature $T_{\mathrm{HPA},m}$ in the HPA port and assuming the EGR temperature entering the HPA port is approximately the HPG inlet temperature ($T_{\mathrm{HPA},h} \approx T_{\mathrm{HPG}}$) one can determine the cold flow temperature $T_{\mathrm{HPA},c}$ in the HPA port through mass averaging, as done in Equation 3.

$$T_{\mathrm{HPA,c}} = \frac{\dot{m}_{\mathrm{HPA}} T_{\mathrm{HPA,m}} - \dot{m}_{\mathrm{HPA}} T_{\mathrm{HPA,h}}}{\dot{m}_{\mathrm{LPA}}} \tag{3}$$

Thus, actual compression and expansion work can be formulated according to the first law of thermodynamics as

$$\begin{aligned} \dot{W}_c &= \dot{m}_{\mathrm{LPA}} c_{p,c} \big(T_{\mathrm{HPA,c}} - T_{\mathrm{LPA}}\big) + \dot{m}_{\mathrm{EGR}} c_{p,h} \big(T_{\mathrm{HPA,h}} - T_{\mathrm{LPG}}\big) \\ \dot{W}_x &= \dot{m}_{\mathrm{LPG}} c_{p,h} \big(T_{\mathrm{HPG}} - T_{\mathrm{LPG}}\big) \end{aligned} \tag{4}$$

Actual compression work in Equation 4 takes into account contribution from the compressed air stream and the recirculated EGR stream. Thus, one can formulate the equations for isentropic compression and expansion efficiency as the ratio of actual to isentropic work defined in Equation 4. Including an additional temperature difference to account for the change in temperature due to internal heat transfer across the two streams yields

$$\begin{aligned} \eta_c &= \frac{\dot{m}_{\mathrm{LPA}} c_{p,c} \big(T^{is}_{\mathrm{HPA}} - T_{\mathrm{LPA}}\big) + \dot{m}_{\mathrm{EGR}} c_{p,h} \big(T^{is}_{\mathrm{HPA,h}} - T_{\mathrm{LPG}}\big)}{\dot{m}_{\mathrm{LPA}} c_{p,c} \big(T_{\mathrm{HPA,c}} - T_{\mathrm{LPA}} - \Delta T_c\big) + \dot{m}_{\mathrm{EGR}} c_{p,h} \big(T_{\mathrm{HPA,h}} - T_{\mathrm{LPG}} - \Delta T_c\big)} \\ \eta_x &= \frac{\dot{m}_{\mathrm{LPG}} c_{p,h} \big(T_{\mathrm{HPG}} - T_{\mathrm{LPG}} - \Delta T_x\big)}{\dot{m}_{\mathrm{LPG}} c_{p,h} \big(T_{\mathrm{HPG}} - T^{is}_{\mathrm{LPG}}\big)} \end{aligned} \tag{5}$$

where $c_{p,c}$=1005J/kg-K and $c_{p,h}$=1160J/kg-K refer to specific heats at constant pressure for cold and hot stream respectively, while $\dot{m}_{LPA}$ and $\dot{m}_{LPG}$ denote mass flow rates through the respective low pressure in- and outlet ports. The additional variables in Equation 5 introduced through ΔT_c and ΔT_e renders the system of equations underdetermined and thus not solvable. Only if one assumes that both temperature differences as well as both compression and expansion efficiency to be equal, that is $\Delta T_c = \Delta T_x$ and $\eta_c = \eta_x$, the system is left with one equation and one unknown and is thus solvable.

It should be noted that the resulting equation is an approximation and effects

that cannot be captured with the proposed formulation, such as leakage flows and variations in rotational speed will impart an effect isentropic efficiency. The approach proposed by Wilson et al. [51] includes heat transfer but does not take fluid mixing into account, which results in significant underprediction of efficiencies. The method suggested in this study seeks to include both effects using reasonable approximations.

2.2. Bath μ-Wave Rotor Design

The rotor features a mean channel diameter of 60 mm, 46 channels with a maximum blade angle of 21.5° and completes three cycles per revolution. The geometric dimensions of the rotor and the corresponding port solution is shown in Figure 5 and a summary of the most important parameters including design operating conditions are given in Table 1.

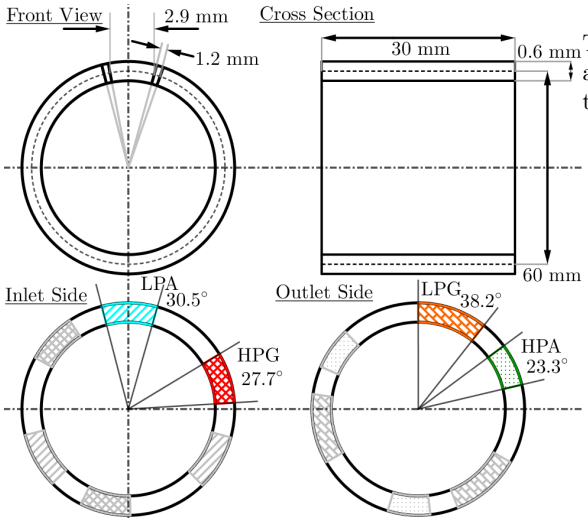

Figure 5: Schematic showing rotor dimensions as well as port solution.

Table 1: Summary of geometric parameters and design conditions for the Bath μ-wave rotor.

Parameter	Value
Rotor diameter [mm]	60
Number of channels	46
Channel shape	sym. camber max. $\lvert\beta_{ch}\rvert$=21.5°
Channel length [mm]	30
Channel width [mm]	2.9
Channel height [mm]	6
Nominal clearance [mm]	var. 0.1-0.4
Number of cycles per revolution	3
Design speed [rpm]	32,000
T_{HPG} [K]	1023
p_{HPG} [kPa]	285
p_{LPG} [kPa]	103

To facilitate comparison among different wave rotor designs Wilson and Fronek [36] and Nagashima et al. [3] defined non-dimensional parameters for finite passage opening T, viscosity F and leakage flow G. These are given as

$$T = \frac{wa}{UL},\ F = \frac{\sqrt{\nu L/a}}{D_h},\ G = \frac{2\delta}{h} \tag{6}$$

Table 2 lists a comparison of these non-dimensional performance parameters for various realised wave rotors. This allows direct comparison and although this is

somewhat difficult to do for pure pressure exchangers operating at low temperatures and wave rotor turbines operating at high temperatures, one can see that the Bath μ-wave rotor performs similarly with respect to finite opening timing effects despite a relatively short rotor length. As expected, due to the small size compared with larger designs viscous losses become more pronounced and is similar to the micro wave rotor study conducted at USAF [40]. Nonetheless, the by far most significant loss mechanism for the wave rotor turbine is leakage between both stators and the rotor. At the design clearance of 0.1 mm this is at best similar to the ABB Comprex and the two USAF designs. However, as alluded to in the next section, it is expected that this parameter is significantly higher during experimental testing as a consequence of uneven thermal expansion of stators and the shaft-rotor assembly. Therefore, the G-parameter will most likely range between values of approximately 0.2-0.23.

Table 2: Comparison of realised wave rotors with the University of Bath (UoB) μ-wave rotor turbine (amended from [3]).

	Kentfield 3-port PE [34]	NASA 3-port PE [36]	USAF[19] PWS 4-port TF	USAF[40] PWS 4-port TF	ABB [52] Comprex 4-port RF	Pearson [5] 6-port TF wave engine	UoB 4-port TF μ-wave turbine
T	0.39†	0.082†	0.29†	0.21†	0.467	0.3†	0.37†
F	0.0046†	0.017†	0.0082†	0.0121†	0.0067	n.a.	0.013†
G	0.0064	0.025-0.075	0.032	0.038	0.030	n.a.	0.033-0.132

† - based on atmospheric values

Figure 6(a) shows an exploded view of the wave rotor unit in CAD. It exhibits the wave rotor itself with its 46 curved channels along with an outer sleeve that is manufactured separately and subsequently installed with an interference fit on to the wave rotor by shrink-fitting. Additionally, inlet and outlet stator with the respective openings that trigger shock and expansion waves are highlighted as well. They feature appropriate flanges and clamps to connect the stator pipes to the manifolds. A central housing connects the two stators. Towards the inlet side, the centre bolt with shaft that connects the wave rotor with the dynamometer is shown as well. The connection of dynamometer and wave rotor unit is done through a two-plane coupling. Reference surfaces on the dynamometer side and the wave rotor mounting bracket ensure proper alignment of both units. The bearing housing contains the two roller bearings (and bearing preload spacer) separated by a spacer. Provisions for cooling channels between inner and outer bearing housing are made to ensure a controlled thermal management of the sealed-for-life bearings.

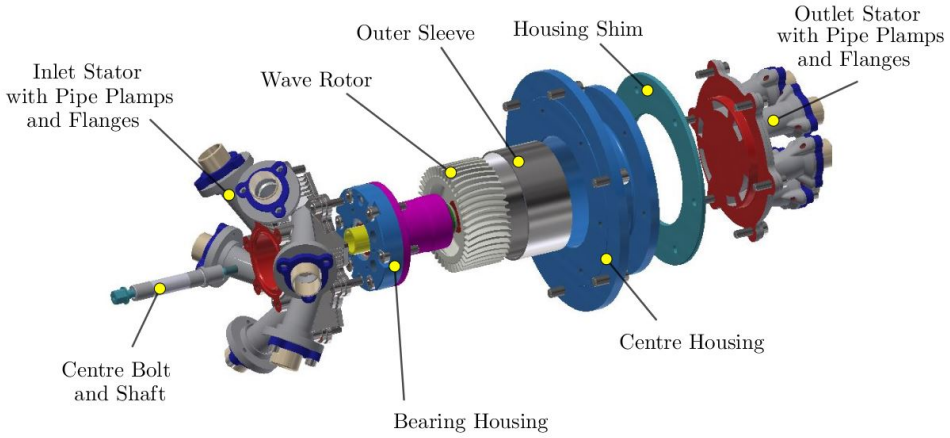

Figure 6: Exploded view of the wave rotor assembly.

The final manufactured parts are shown in Figure 7. Both stators were produced from Inconel 625 using selective laser melting (SLM) additive manufacturing technique and machined to their final finish. This can be seen in Figure 7(a). The rotor, its sleeve and the centre casing were machined from solid, after which rotor and outer sleeve were mated to give the final shrouded version, as given in Figure 7(b). Figure 8(a) depicts the assembled wave rotor device including in- and outlet manifolds that distribute the flow to the respective port. In addition, the hose couplings for the cooling circuit of the bearing housing as well as the single-plane coupling that connects the wave rotor device to the dynamometer are shown in Figure 8(b).

(a) (b)

Figure 7: Manufactured parts: (a) inlet on top and outlet stator on the bottom. (b) Rotor showing channel curvature and its outer sleeve.

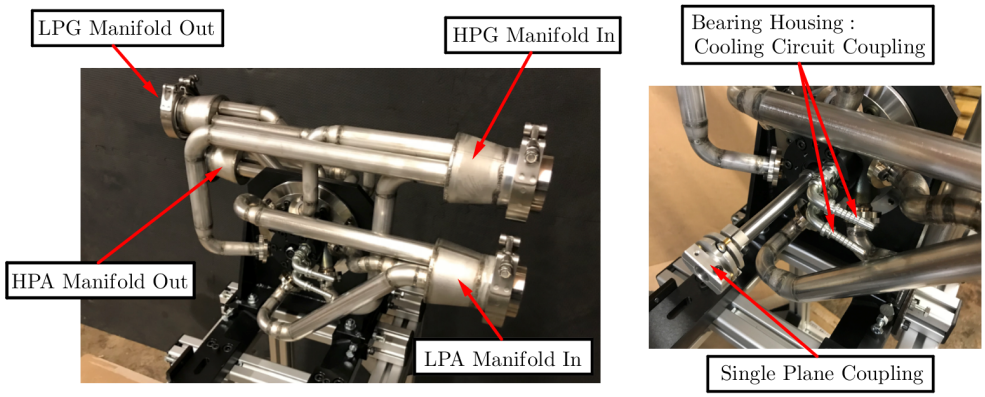

(a) (b)

Figure 8: (a) Assembled wave rotor machine with in- and outlet manifolds. (b) Couplings for bearing housing water cooling circuit and single-plane coupling to link wave rotor with load cell.

2.3. Experimental Setup

2.3.1. Gas Stand Layout and Instrumentation

For the characterisation of the wave rotor, laboratory experiments were performed on the University of Bath turbocharger gas stand. The setup allows to perform variation of operating conditions, such as dynamometer excitation load, loop flow ratio λ, mass flow rates and inlet pressures in the high- and low pressure inflow ducts,

as well as the backpressure through both high- and low pressure outflow ducts. In this scenario, one can measure both generated power and generated pressure ratio, as well as the corresponding port outlet temperatures.

The wave rotor gas stand, as depicted in the schematic of Figure 9, consists of an open-loop configuration and is able to provide a maximum source pressure of 7 bar absolute generated from a set of external rotary type compressors. Moisture in the delivered air stream is removed via a refrigerated and compressed air drier conditioning the incoming dry air to approximately 15°C. The incoming air pressure can be regulated via a regulator valve (element 2 in Figure 9). Pressure and mass flow rates delivered on both high and low pressure legs are controlled via an actuated ball valve and two pneumatically controlled 2" variable orifice control valves (elements 4) located on each of the high and low pressure pipework legs. The high pressure leg further features a differential pressure V-cone mass flow meter (element 5) with a flow range from 0.015 kg/s to 0.15 kg/s and a Bowman air-to-air heat exchanger (element 6) that preheats the incoming (cold) air using the hot exhaust gas that would normally be expelled without being used. Downstream of the heat exchanger sits an Axis Design electric heater (element 7), able of providing up to 44 kW to the flowing air stream, resulting in a maximum deliverable temperature of around 750°C. It is noteworthy that pipework between the electric heater and the wave rotor is fully insulated in order to minimise heat losses between rotor and the heater outlet. On the low pressure leg the incoming air is directed through another differential pressure V-cone mass flow meter (element 8) with a mass flow range from 0.005kg/s-0.05kg/s before reaching the wave rotor inlet manifold.

Both wave rotor bearing housing and eddy-current dynamometer have dedicated cooling circuits (elements 16 and 17 respectively) that should ensure smooth and continuous operation. Cooling water is fed via the main water valve from the university pond and filtered before running through the respective cooling circuits. A pressure sensor upstream of the dynamometer cooling circuit ensures the maximum allowable pressure of 1.9 barA at the inlet of the dynamometer cooling pipes is not exceeded during testing. In addition, a flow meter was installed on the cooling circuit of the bearing housing ensuring a water flow rate of approximately 2 L/min.

On the high and low pressure outflow legs two pneumatically actuated variable orifice control valves (elements 11 and 14 respectively) control the backpressure experienced by the wave rotor. In this scenario the gate valve on the HPA leg provides the means to match the mass flow rates in the high pressure zone HPG-HPA. This requires the computation of the mass flow rate through the HPA leg, which is achieved through a 2" differential pressure V-cone mass flow meter (element 13) with a rated flow range from 0.015 kg/s to 0.15 kg/s. Due to temperature limitations of the mass

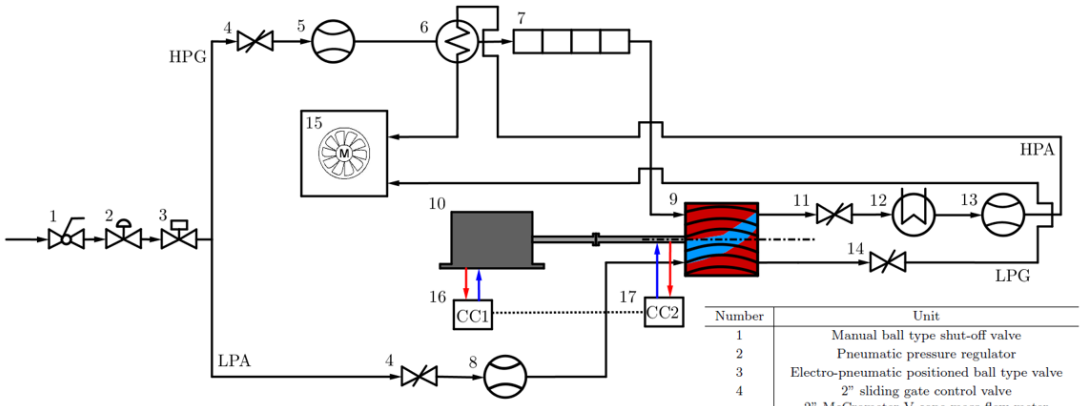

Number	Unit
1	Manual ball type shut-off valve
2	Pneumatic pressure regulator
3	Electro-pneumatic positioned ball type valve
4	2" sliding gate control valve
5	2" McCrometer V-cone mass flow meter Siemens DSIII dp-sensor
6	Bowman air-to-air heat exchanger
7	44kW electric heater
8	1" McCrometer V-cone mass flow meter Siemens DSIII dp-sensor
9	Wave rotor
10	Magtrol WB43 HS eddy-current dynamometer
11	1" sliding gate control valve
12	Bowman air-to-water heat exchanger
13	2" McCrometer V-cone mass flow meter Siemens DSIII dp-sensor
14	0.5" sliding gate control valve
15	Electrically controlled ceiling extraction fan
16	Pond water fed dynamometer cooling unit with pressure transducer
17	Pond water fed wave rotor bearing housing cooling unit with mass flow sensor

Figure 9: Schematic of the wave rotor gas stand test setup.

flow meter instrumentation, in particular the PT100 sensor necessary for air density calculation, a Bowman air-to-water heat exchanger is located upstream of the mass flow meter in order to reduce the hot exhaust gas temperature down to approximately 30°C.

Wave rotor performance data are gathered by means of the sensors listed in Table 3.

The list gives an account of all the sensors used throughout the campaign including their measurement range and accuracy. In order to quantify the combined uncertainty of all measured data, the British Standard [53] is used, assuming a rectangular distribution and thus equal probability for all values. This encompasses pressure transducers and thermocouples located just upstream of the intake manifolds and downstream of the outflow manifolds. Mass flow rates are determined through differential pressure sensors and Bernoulli's theorem for the conservation of energy along a streamline. PRT temperature sensors and pressure transducers located on the high pressure side of the v-cone allow calculation of flow density and together with the

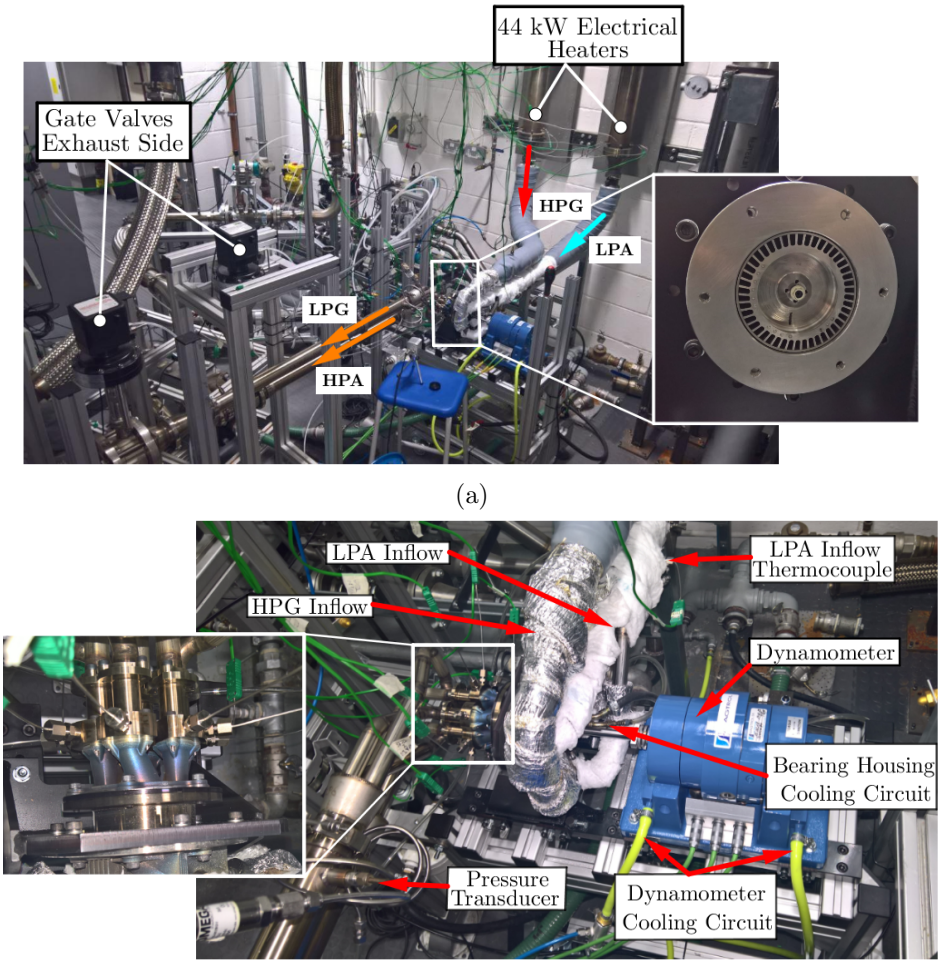

Figure 10: (a) Photograph as taken from the gas stand showing experimental setup. In particular, the electrical heaters upstream of the wave rotor machine can be seen. It is important to note that merely the HPG heater is in use throughout this study. Furthermore, the wave rotor within the centre housing as well as the downstream gate valves are highlighted. (b) Photograph showing wave rotor gas stand including coupling to the dynamometer, cooling circuits to dynamometer and bearing housing, insulated inflow ducts with instrumentation (thermocouple shown, pressure transducer not visible), instrumented outflow ducts as well as thermocouple arrangement close to the rotor outlet.

Table 3: List of sensors used throughout testing including their measurement range and their accuracy as stated by their manufacturers. It is noteworthy that response times and sampling frequency are not reported as the sensors measure steady state data.

Sensor	Range	Nominal Accuracy
1.5 mm K-type thermocouple	-200°C - 1260°C	±0.0075T from 333°C to 1200°C ±2.5°C from -40°C to 333°C
PRT	-50°C - 200°C	$\pm 0.3 + 0.005T$
V-cone mass flow meter	0.015 kg/s - 0.015kg/s (HPG, HPA) 0.005 kg/s - 0.05kg/s (LPA)	±0.5%
Static pressure	0 barG - 7 barG (HPG, HPA) 0 barG - 2 barG (LPG) 0 barA - 3.5 barA (LPA)	0.08%
Differential pressure	0 bar-0.06 bar (HPG, HPA) 0 bar - 0.0049768 bar (LPA)	±0.5%
Rotor Torque	0-1.5 Nm	$\pm 0.3\% FS$
Rotor Speed	0-65,000 rpm	$\pm 0.1\% FS$

differential pressure yield flow velocity. Using mass flow rates in conjunction with the static temperature and pressure probes one can determine total port properties through the first law of thermodynamics, as done in Equation 1.

$$p_t = p_s \left(1 + \frac{(\gamma - 1)}{2} \frac{\dot{m}^2 T_s R}{p_s^2 \gamma A^2} \right)^{\gamma/(\gamma-1)} \tag{7}$$

Total-to-total pressure ratio is thus defined as

$$\Pi_c = \frac{p_{t,HPA}}{p_{t,LPA}} \tag{8}$$

In addition to the manifold in- and outflow conditions additional measurement sections with a set of thermocouples was installed around two rotor lengths downstream of the rotor-outlet stator interface, as shown in Figure 10. This should allow measurement of the outflow temperatures from HPA and LPG ports and give a notion of the temperature distribution and the behaviour of internal exhaust gas recirculation (EGR) in the HPA duct by making use of periodicity and placing the thermocouples ends at various positions within the duct as indicated in Figure 11(a), which combined give the measurement points shown in Figure 11(b). Each thermocouple position is assigned a number and it is important to notice that thermocouples 1 and 3 are positioned towards the outer diameter, while 2 and 4 towards the centre. Due to the limited amount of space within the 15mm duct only six probes could

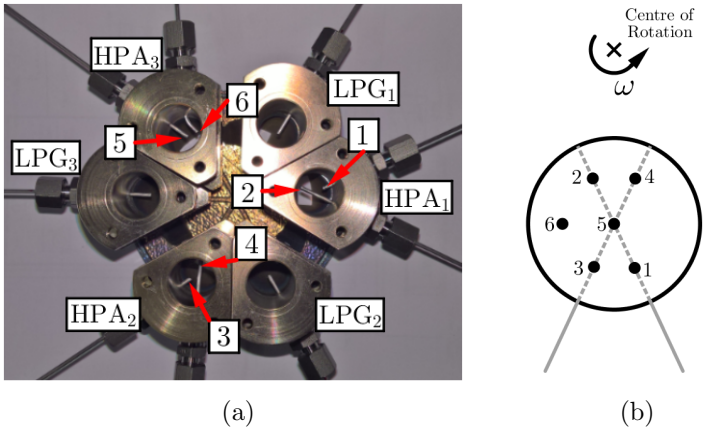

(a) (b)

Figure 11: (a) measurement sections for thermocouple installation just downstream of the outlet stator. Each LPG measurement section features a single temperature probe located in the centre of each duct. For the HPA duct the temperature probes were arranged at different positions resulting in the distribution shown in (b).

be fitted across all three HPA ducts. In addition, limited accessibility of the stator ports required to place the measurement section relatively far downstream of the rotor outlets, increasing the risk of thermal diffusion smearing the cold/hot gas interface.

2.3.2. Experimental Campaign

The laboratory experiments seek to investigate the behaviour of the designed wave rotor turbine and the sensitivity of outlet temperatures, total-to-total pressure ratio (defined in Equation 8) and power output as rotational speed, loop flow ratio λ (as given in Equation 1) and inlet temperatures are varied. Table 4 summarises all test conditions. Firstly, loop flow sweeps from 1.7 to 3.2 in increments of 0.5 are performed at 500°C. In addition rotational speed is swept in steps of 2,000 rpm from 22,000 rpm to the design speed of 32,000 rpm. This is repeated for increased inlet temperature of 600°C, albeit solely at loop flow ratio 1.7.

In addition, the effect of increased axial leakage gap is identified, too. Initial test for λ and rotational speed sweeps are carried out at a nominal leakage gap of 0.2/0.25 mm. Experiments at elevated inlet temperature of 600°C are then performed at both 0.2/0.25 mm and 0.3/0.3 mm nominal leakage gap in an effort to investigate the effect of increased leakage on the dependant variables. It is noteworthy that the baseline model was designed for an axial clearance of 0.1 mm at both in- and outlet. However, during experimental testing it soon transpired the target clearance was difficult to

Table 4: Test conditions for the initial wave rotor turbine laboratory experiments.

Inlet Temperature T in °C	Loop Flow Ratio	Rotational Speed in rpm	Nominal Leakage Gap in mm
500	(1.7/2.2/2.7/3.2)	22,000-32,000	0.2/0.25
600	1.7		0.2/0.25 0.3/0.3

achieve as a result of uneven thermal expansion between the rotor assembly and both in- and outlet stator. The compact size of the rotor in combination with the pressurised and thermally elevated environment prevailing within the stator housings preclude the application of a standard gap measurement sensor. Therefore, it was not possible to determine the actual leakage gap when all machinery was running in thermal equilibrium and throughout this study nominal clearances are given only.

The start-up procedure followed the following routine: Initially, all outlet valves are completely opened, the heater and brake both turned off. Then, the flow through the HPG duct is gradually increased by opening the corresponding gate valve. As soon as the rotor starts spinning, the brake excitation is increased maintaining a rotational speed of around 15,000 rpm. After that, the LPA inlet valve is opened as well and the brake excitation adjusted accordingly to maintain rotational speed. In the process, both inlet valves are then alternatively opened such that the loop flow ratio stays within a range of 1.7-2.0 until the maximum mass flow rate reaches approximately 35-40 g/s. As soon as this condition is reached the heater demand temperature is set to 100° C. When this is reached and the thermal camera indicates an approximate thermally stable condition, the temperature is increased in 50° C steps up to the desired testing temperature.

3. Results and Discussion

3.1. Experimental Results

3.1.1. Limitations and Issues

Initial tests commenced with a nominal (cold) clearance of 0.1 mm on both in- and outlet. It was found that when the inlet temperature is increased in short intervals, the rotor - being housed in a closed volume - heats up quicker than the thermally more inert housing components. This resulted in thermal expansion of the rotor towards the inlet side resulting in contact with the inlet stator face. The incurred damage was not catastrophic and resulted in minor scratches to rotor and stator, as shown in Figure 12. As a result, the temperature increments were reduced to the aforementioned 50°C and sufficient time allowed for all components to thermally expand sufficiently. Furthermore, it was decided to start testing with rather conservative clearances of 0.2 mm/0.25 mm and 0.3 mm/0.3 mm at in- and outlet respectively.

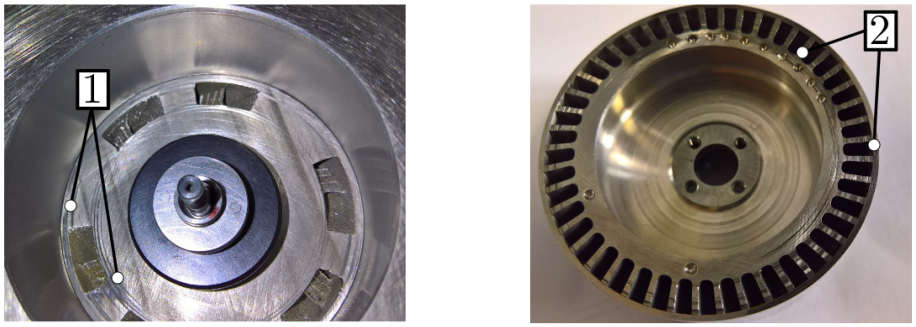

(a) (b)

Figure 12: Minor damage to rotor and stator as a result of quick temperature increase and transiently imbalanced expansion between rotor and stator.

Extended exposure to elevated temperatures proved problematic with respect to bearing service life, despite the water-cooled bearing housing. It transpired that exposing the machine to around 600° C for around an hour results in all the lubrication from the bearings to be completely evaporated despite the cooled bearing housing. Interestingly, the bearing seals and cages were not destroyed showing no signs of discolouration through heat exposure. This may indicate that the anticipated heat conduction through the shaft is less problematic than anticipated and that the air temperature reaching the bearing closest to the rotor suffices to evaporate the lubricant completely.

3.1.2. Loop Flow Ratio and Rotational Speed Variation

The results shown in Figure 13 illustrate wave rotor performance data as a function of loop flow ratio and wave rotor speed done at 500°C HPG inlet temperature and a nominal clearance of 0.20 mm on the inlet and 0.25 mm on the outlet side. In particular, the graphs shown in Figure 13(a) depict total-to-total pressure ratio, relative difference between HPG and HPA total pressures, LPA inlet pressure, while Figure 13(b) displays shaft power output and averaged HPA and LPG outlet temperature respectively.

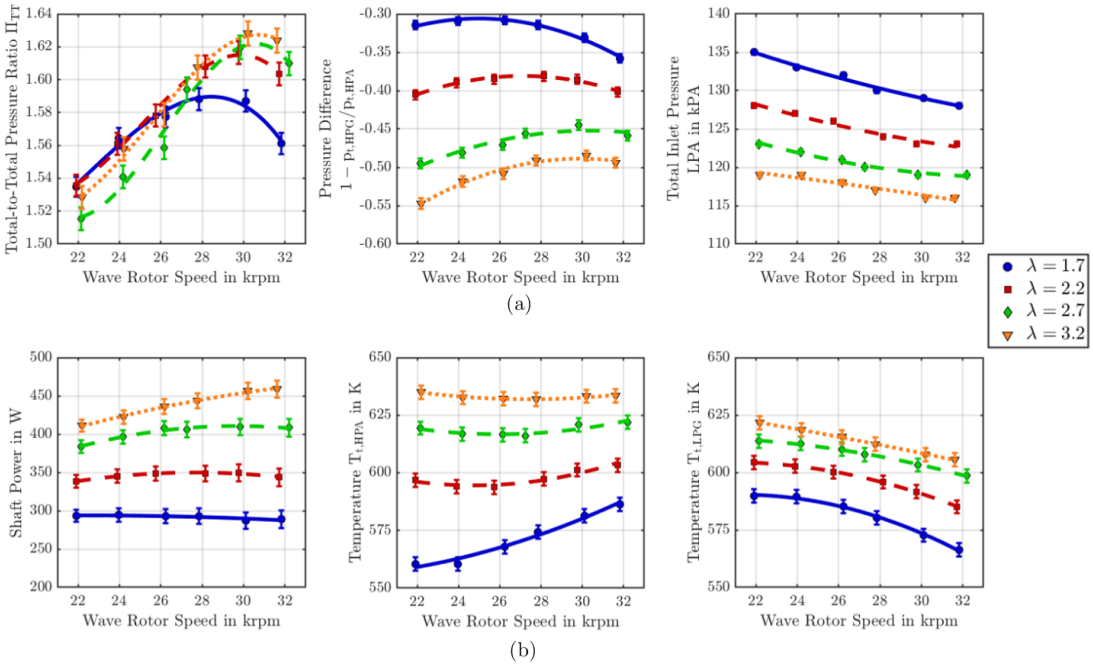

Figure 13: Wave rotor performance data for variations in loop flow ratio and rotational speed at 500°C HPG inlet temperature and a nominal clearance of 0.20 mm on inlet and 0.25 mm on outlet side. (a) Wave rotor data of total-to-total pressure ratio (left), relative pressure difference in the combustor loop between HPG and HPA (centre) as well as the total inlet pressure in the LPA inlet. (b) gives shaft power output (left) and demonstrates averaged total temperature at HPA and LPG (centre and left respectively).

Pressure ratio variations with rotational speed follows a parabolic distribution across all loop flow ratios. Variations are, however, rather subtle, implying relatively small sensitivity to changes in loop flow ratio and rotational speed. Nonetheless, there seems to be an increase in the achieved pressure ratio for higher λ ratios and

there appears to be a drift of the peak towards higher rotational speeds with greater λ ratios.

As the tests were conducted at relatively large leakage gaps (in particular at the outlet side) and lower total inlet temperature, the recorded relative difference across the combustor is rather large and would necessitate (an unrealistically strong) pressure gain combustor linked in between. Nonetheless, it becomes apparent that lower loop flow ratios result in smaller required 'pressure gain'. In addition, while the peak in relative error tends to be more towards higher rotational speeds, it appears to shift towards lower rotational speeds with decreasing loop flow ratio.

Higher loop flow ratios signify lower LPA inlet pressures, as seen in the right hand side graph of Figure 13(a). This signifies lower average pressure prevailing within the passages and thus lower resistance as the channel is exposed to the HPG port leading to higher mass flow rates and greater power extraction.

Variation in rotational speed yields relatively small changes in wave rotor power with an increasing gradient towards lower rotational speeds when λ ratios are increased, as illustrated in the left hand graph of Figure 13(b). The reason for witnessing an absolute increase in power output for higher loop flow ratios is founded on the fact that the results as shown were generated for constant inlet pressures resulting in variations in inlet mass flow rates through the HPG inlet.

Examining the outlet temperature distribution for HPA and LPG illustrated in the bottom centre and right graphs of Figure 13(b) shows that an increase in loop flow ratio results in both an increase of HPA and LPG outlet temperature, which is to be expected as higher loop flow ratios indicate less cold air being fed to the rotor. Therefore, at constant inlet temperature, loop flow ratios converging towards unity contribute lower outlet port temperatures and lower internal EGR rates. In addition, one should remember that the expanded and compressed stream are in thermal contact with each other within the channels and basically act as an internal recuperator, where the hot exhaust gases heat up the incoming fresh air. From the data it transpires FAE close to the design speed at 32,000 rpm. This manifests itself in a lower LPG temperature and higher HPA temperature. As speed is reduced, FAE is gradually diminished, which accounts for a reduced amount of EGR in the HPA port. Therefore, mixed-out temperatures in the HPA port decline with decreasing rotor speed. Conversely, LPG port temperatures increase as FAE decreases through lower wave rotor speed. The data thus show that, in order to minimise FAE and EGR it is desireable to operating towards the lower end of the speed range, while for pressure ratio and combustor loop pressure difference, one would want to operate closer towards the design speed.

A detailed investigation of the outlet temperature distribution is provided by

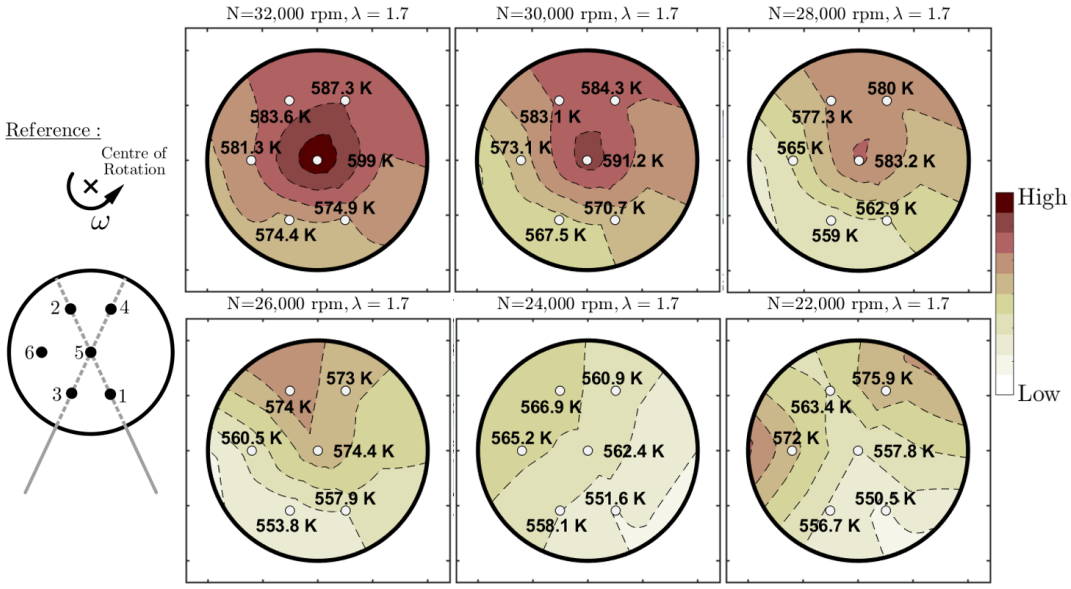

Figure 14: Contour plot showing temperature distribution in the measurement section downstream of the HPA port. Data outlines the both the effects of rotational speed variation and centrifugal forces on the HPA temperature distribution for a constant loop flow ratio of 1.7.

the contour plots in Figure 14. All data were gathered for a λ ratio of 1.7 and gives further details on the interaction of cold and hot streams as well as exhaust gas recirculation. The temperature differences are relatively small, which is in part a result of diffusion and flow mixing taking place between the hot and cold fluid streams. Nonetheless, significant information from the data can be extracted and inferences regarding the characteristics made. The temperature probes reveal that- as one might expect- the colder stream appears to be moved towards the outer shroud of the wave rotor as a consequence of the centrifugal forces, which manifests itself in slightly lower temperatures towards probes 1 and 3. This trend is shown throughout all rotational speeds. The reduction in FAE in the LPG port and EGR in the HPA ducts with decreasing rotor speed is also reflected in the contour plots resulting in lower detected minimum temperature that increases from around 550 K for 22,000 rpm to 575 K at the design speed of 32,000 rpm.

The effect of varying loop flow ratio on the HPA temperature distribution can be witnessed in Figure 15. The location of the cold stream appears to remain relatively unchanged with centrifugal forces still accounting for pushing it outwards. Nonetheless, one can see that increased EGR rate accounts for considerably larger HPA outlet

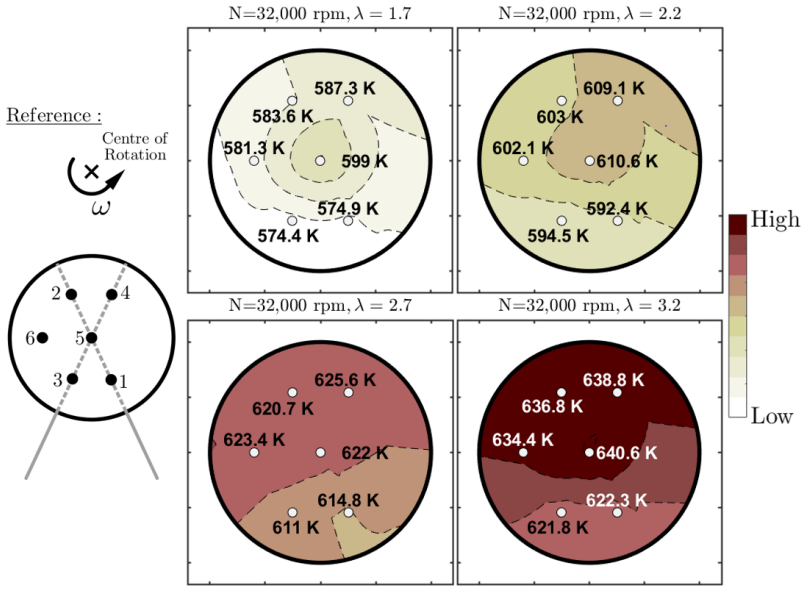

Figure 15: Contour plots created with data collected in the measurement sections downstream of the HPA port exhibiting the effect of loop flow variation on the high pressure exhaust temperature distribution.

temperatures with the maximum increasing from 599 K at λ=1.7 to 641 K at λ=3.2. Based on temperature alone, higher inlet temperature signifies less temperature rise demanded from the combustor; however, higher EGR rates signify less oxygen in the delivered air/gas mixture and thus potential ramifications regarding flame stability.

Using the efficiency equation introduced in Equation 5 results in the estimated compression/expansion efficiency distribution given in Figure 16. The maximum efficiency is witnessed for λ=3.2 and is at around 80%. Interestingly, efficiency appears to decrease as one approaches a loop flow ratio of unity, which is in part a result of a more distinct effect of FAE that becomes more pronounced the closer the wave rotor operates to its design speed of 32,000 rpm and the lower the loop flow ratio λ (as seen in the bottom right plot of Figure 13). Although the effects of FAE are not directly incorporated into the efficiency formula, it is implicitly accounted for through the mixed out temperatures in the LPG port used for the calculation of isentropic expansion ratio. For higher loop flow ratios the cold air stream is generally narrower and EGR rates at a higher level leaving variations in rotational speed with less of an effect on efficiency and also lower variations for loop flow ratios of 2.2 and higher.

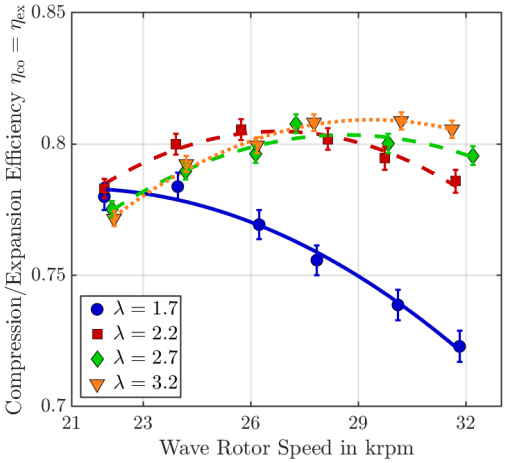

Figure 16: Variation in compression/expansion efficiency with loop flow ratio and rotational speed.

3.1.3. Axial Leakage Variation

Laboratory results concerning the impact of increased axial leakage on wave rotor performance are demonstrated in Figure 17(a) and (b). Data were collected for two different nominal leakage gaps of 0.2/0.25 mm and 0.3/0.3 mm respectively, for constant HPG inlet temperature of 500°C and constant HPG inlet pressure of approximately 275 kPA and a constant loop flow ratio of 1.7.

In the top left plot, a pronounced effect of increased leakage on the produced pressure ratio can be witnessed. In detail, the achieved pressure ratio undergoes a reduction of approximately 15%. The reason for this lies predominantly in a more pronounced interaction between neighbouring rotor channels and a significant reduction in the reflected, secondary pressure wave. As lower leakage yields higher pressure ratios and thus enhanced energy transfer it is logical that the relative difference across the combustor loop is reduced and less 'pressure gain' necessary, as disclosed in the top right chart of Figure 17(a).

Interestingly, for reduced axial leakage, shaft power output appears to be reduced. One would expect a rather similar level of power output, in particular as boundary conditions regarding inlet pressures and mass flow rates are of similar degree. The reason for the shown difference most likely lies in the fact that soon after testing of the low leakage case, a bearing failure was detected. It is thus likely that the bearings exerted a larger parasitic drag and thus a reduction in measured torque for the low leakage experiments. For high leakage tests a fresh set of bearings was installed, resulting in a larger reported power output.

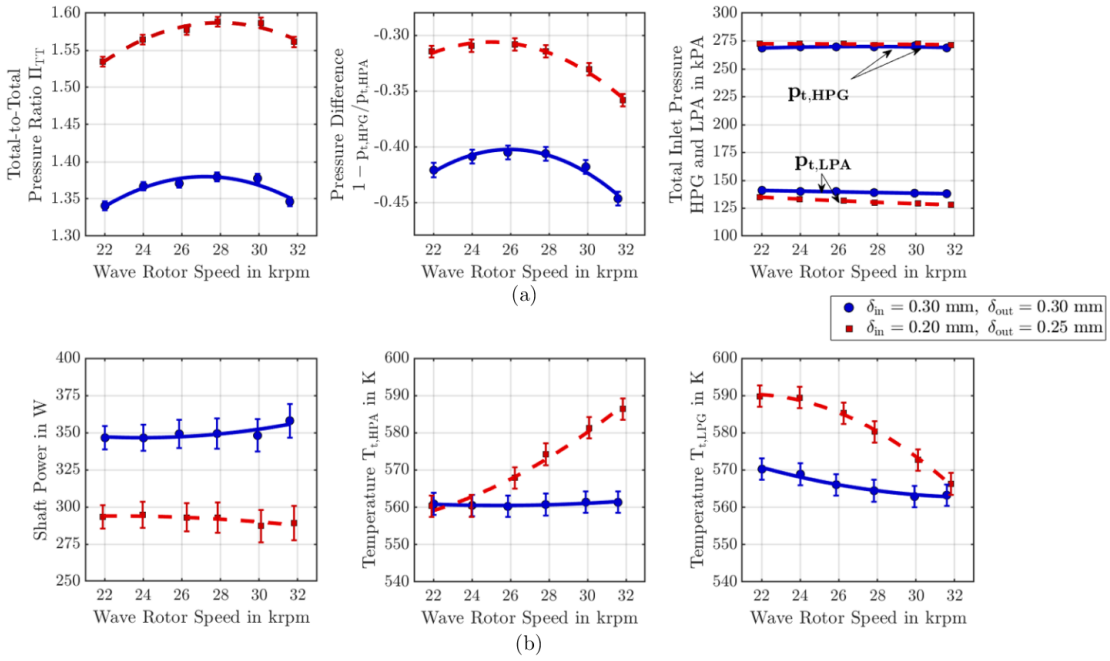

Figure 17: Wave rotor performance data for variations in nominal leakage clearance and rotational speed at 500°C HPG inlet temperature. (a) gives total-to-total pressure ratio (left), relative pressure difference in the combustor loop between HPG and HPA (centre) as well as the total inlet pressure in the HPG and LPA inlet (right). (b) displays shaft power output (left) and averaged total temperature at HPA (centre) and LPG (right).

Reduced axial leakage fosters less interaction among rotor passages and with the leakage cavity. As a consequence, one can clearly distinguish between the effect of FAE and EGR in both HPA and LPG averaged outlet temperatures as shown in Figure 17(b). As laid out previously, there is some amount of FAE and a maximum amount of EGR close to the design speed at 32,000 rpm. This is gradually reduced when the rotor spins at lower speeds. However, at larger leakage gaps this effect is greatly attenuated and HPA outlet temperature becomes less sensitive to changes in rotor speed. A possible contributor to this reduced sensitivity may stem from the previously noted interaction among channels and hence, greater diffusion and mixing taking place within the channel allowing for instance more hot air ingestion into the channel as it passes by the LPA port and before it is even exposed to the hot conditions in the HPG port.

The effect of increased axial clearance gaps on compression/expansion efficiency

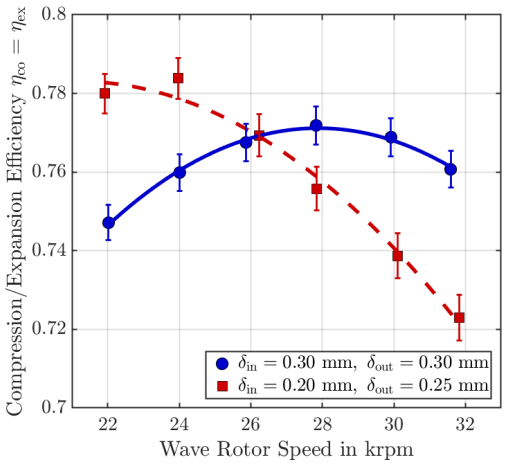

Figure 18: Variation in compression/expansion efficiency with loop flow ratio and rotational speed for two different nominal leakage gaps at constant peak inlet temperature.

for a loop flow ratio of 1.7 and a peak inlet temperature of 500°C is shown in Figure 18. At lower clearance the effect of FAE is more pronounced leading to a drop in efficiency as one approaches higher rotational speeds. As already seen in Figure 16 and in combination with the mixed out temperatures given in Figure 17, increased leakage gap leads to less sensitive efficiency distributions with respect to rotational speed. The increased leakage gap acts in a similar way to a higher loop flow ratio in that respect.

3.1.4. Inlet Temperature Variation

The final comparison conducted deals with the effect of HPA inlet temperature variation from 500°C to 600°C with rotational speed and constant HPG inlet pressure of approximately 275 kPA and a constant loop flow ratio of 1.7. All data were collected using a nominal leakage gap of 0.3/0.3 mm and is displayed in Figure 19.

An increase in inlet temperature at constant inlet boundary conditions (inlet pressure and mass flow rate) represents an increase in enthalpy and thus more energy being transferred to the rotor. As a result more energy can be transferred between hot and cold stream through wave action and more power extracted through momentum change. This is exemplified in the pressure ratio and power output graphs given in Figure 17(a) and (b). At constant LPA inlet pressure this increase in energy transfer is reflected in a maximum increase in pressure ratio of approximately 5.5% for rotational speeds greater than 26,000 rpm. In conjunction with this, the pressure

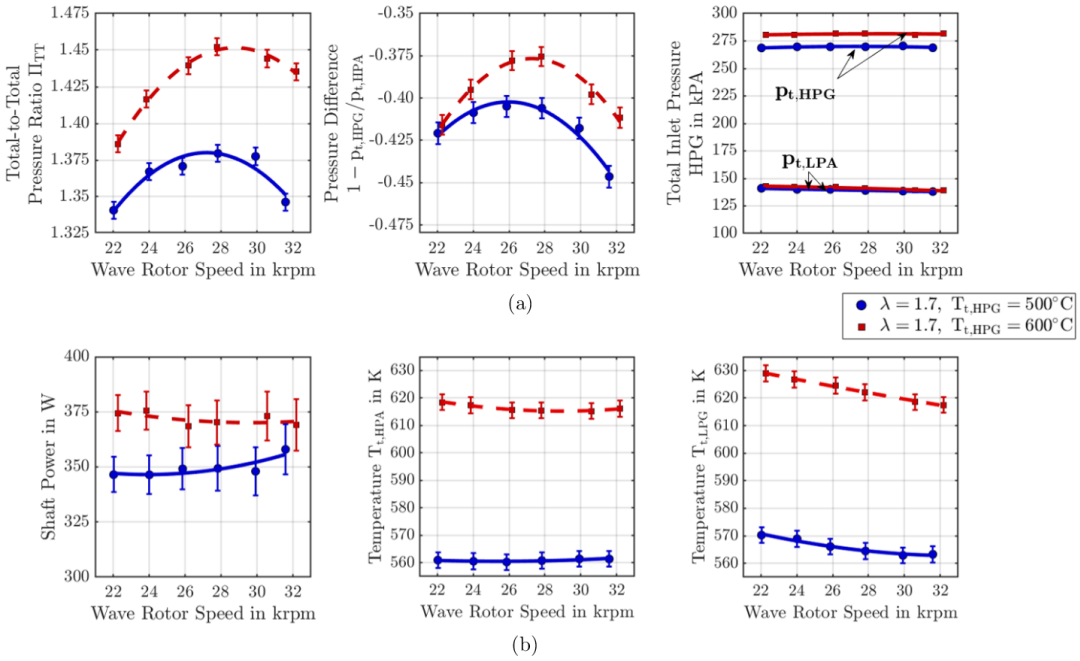

Figure 19: Wave rotor performance data for variations in peak inlet temperature and rotational speed for a nominal axial clearance of 0.3 mm at the in- and 0.3 mm at the outlet side. (a) shows total-to-total pressure ratio (left), (right) and relative pressure difference in the combustor loop between HPG and HPA as well as the total inlet pressure in the LPA inlet, while shaft power output (left) averaged total temperature at HPA (centre) and LPG (right) are shown in (b).

difference across the 'combustor loop', as defined in Figure 4, decreases accordingly.

Impingement of shock and expansion waves on the other end of each wave rotor channel ideally coincides with opening and closing of the respective ports. Thus, altering wave rotor speed changes the location of impingement and as a consequence the strength the reflected shock wave. This is the reason for the parabolic variation of pressure ratio with wave rotor speed, displayed in the top left graph of Figure 19(a). Furthermore, shaft power output increases can be reported to range within 8% and 3%.

The increase in inlet temperature results in approximately 60°C higher temperature at the outlet throughout all rotational speeds. However, as a consequence of the increased leakage gap - in particular on the outlet side - there appears to be a pronounced interaction among channels and the leakage cavity resulting in a smeared and well-mixed out temperature distribution in both outlets. This effectively

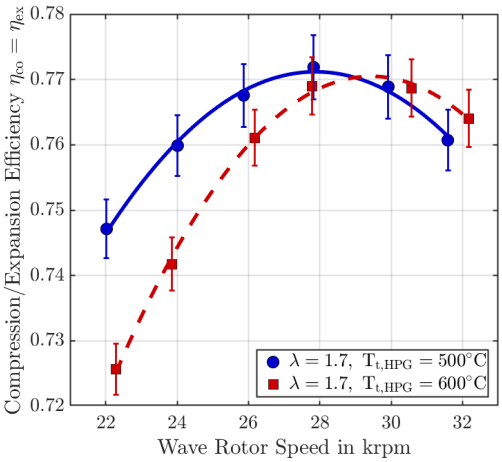

Figure 20: Variation in compression/expansion efficiency with loop flow ratio and rotational speed for two different inlet temperatures at constant axial clearance.

blurs out the effects of FAE and EGR rendering the outlet temperature distribution insensitive to changes in rotational speed, as already described in Figure 17. However, LPG outlet temperature still shows mild sensitivity to rotor speed which hints towards FAE being present at approximately 32,000 rpm. Gas ingestion from the leakage gap and interaction between hot and cold gas streams seem to smear this sensitivity out for the HPA port (centre graph of Figure 19(b)). Nonetheless, the witnessed sensitivity at higher leakage, shown in bottom right graph of Figure 19(b), is reduced compared to lower leakage given in the bottom right distribution shown in Figure 13(b).

The effect of increased peak inlet temperature on compression/expansion efficiency for a loop flow ratio of 1.7 and constant leakage gaps of 0.3/0.3 mm is shown in Figure 20. Despite the increase in compression ratio, as shown in the top left graph of Figure 19(a), no significant change in the efficiency distribution can be reported, except for an slight shift towards higher rotational speeds and a more pronounced drop-off towards lower rotational speeds.

4. Conclusions and Outlook

In this paper a novel four-port, three-cycle small scale wave rotor turbine has been introduced and successfully characterised experimentally on the University of Bath gas stand. In conclusion, the main points of this paper can be listed as follows:

- A prototype of the designed rotor was manufactured as a machined-from-solid component and mated with its outer sleeve, while stator components were manufactured using the additive manufacturing based SLM technique. The machine was subsequently installed in a test cell and experimentally tested in an open-loop configuration, where electrical heaters and a set of industrial compressors supply hot and pressurised air. An eddy-current dynamometer was used to measure shaft power output.
- Experimental testing was done with the objective of characterising wave rotor turbine performance through variation of the following parameters:
  - Loop flow ratio λ was varied at fixed hot gas temperature 500°C and nominal clearance gap 0.2 mm inlet, 0.25 mm outlet. The results showed that lower loop flow ratio results in a total pressure ratio increase of around 3% when loop flow ratio is increased from 1.7 to 3.2, although this results in higher pressure difference across combustor loop (connecting the HPG and HPA ports). In addition, outlet temperature increased gradually as a consequence of the reduced cold air mass flow rate. The maximum shaft power output for this test series was around of 450 W at loop flow ratio 3.2.
  - Variations in axial leakage comparing results for nominal clearance gap of 0.2 mm at in- and 0.25 mm at the outlet with increased gaps of 0.3 mm at in- and 0.3 mm on the outlet side suggest a significant effect on energy transfer and thus the achieved pressure ratio. Furthermore, increased leakage gap promotes diffusion and mixing of the conditions in neighbouring channels and thus smeared out effects of FAE and EGR.
  - Increasing hot inlet gas temperature from 500°C to 600°C implies an increase in both the attained pressure ratio of around 5% and shaft power increase of 3% to 8%. The increase can be identified as a consequence of the increase in inlet enthalpy.
  - Variations in rotational speed from 22,000 up to the design speed of 32,000 rpm exhibits a parabolic variation of pressure ratio with speed, with the peak pressure being between 28,000 and 30,000 rpm for a loop flow ratio of 1.7. Shaft power shows little sensitivity to rotational speed variation, while outlet temperature implies a decrease in FAE and EGR rate with decreasing rotational speed.
- The test results show that by reducing rotational speed, it is possible to reduce the amount of FAE through the LPG port and decrease EGR rate through

the HPA port. However, the results suggest a conflicting relationship for these parameters with the achieved compression pressure ratio and thus the pressure loss across the HPG and HPA ports. The peak of these parameters lie close to the design speed at approximately 30,000 rpm.

- A method was proposed for computing isentropic efficiency using loop flow ratio as an estimator for EGR rate and taking heat transfer between hot and cold gas streams into consideration. Efficiency computations show high compression/expansion efficiencies in the region of 72% to 82% emphasising the capability of wave rotors to efficiently compress and expand gaseous media.

- Excessive exposure of bearings to heat through hot air ingestion and heat conduction along the shaft limited the peak cycle temperature to 600°C. Future tests shall address this issue through additional seals and more temperature resilient grease being used for bearing lubrication.

- Uneven thermal expansion of rotor as well as in- and outlet stator necessitated using larger axial clearances on both rotor sides. It is further expected that the actual leakage gap varies significantly when the machine is thermal equilibrium. However, determination of the leakage gap in a compact, pressurised and hot environment remains a significant engineering challenge.

Acknowledgement

The authors would like to thank the Defence Science and Technology Laboratory (DSTL) for funding the project under the Defence and Security Accelerator *"Beyond Battery Power"* competition. The authors would further like to acknowledge the technical staff at the Powertrain and Vehicle Research Centre (PVRC) for their support in setting up the experimental facility as well as researchers Ian Kennedy, Yang Zhang and Tomasz Duda for their support in preparing instrumentation and data acquisition.

References

[1] R. Nalim, H. Li and P.Akbari, Air-Standard Aerothermodynamic Analysis of Gas Turbine Engines with Wave Rotor Combustion, Proceedings of the ASME Turbo Expo (2009) 445–456.

[2] P.H. Snyder and M.R. Nalim, Pressure Gain Combustion Application to Marine and Industrial Gas Turbines, Proceedings of the ASME Turbo Expo 5 (2012) 409–422.

[3] T. Nagashima, K. Okamoto and Y. Ribaud, Cycles and Thermal System Integration Issues of Ultra-Micro Gas Turbines, Educational Notes RTO-EN-AVT-131, 2005.

[4] P. Akbari, R. Nalim, N. Müller, Performance Enhancement of Microturbine Engines Topped with Wave Rotors, Journal of Engineering for Gas Turbines and Power 128 (2006) 190–202.

[5] R.D. Pearson, A Gas Wave-Turbine Engine Which Developed 35 HP and Performed Over a 6:1 Speed Range, in: Proceedings ONR/NAVAIR Wave Rotor Research and Technology Workshop, Naval Postgraduate School, 1985.

[6] B.D. Smith, M.D. Polanka, D.E. Paxson and J.L. Hoke, Scaling Study of Wave Rotor Turbo Normalization of an Internal Combustion Engine, 48th AIAA/ASME/SAE/ASEE Joint Propulsion Conference and Exhibit 2012 (2012).

[7] Y. Lei, D.S. Zhou and H.G. Zhang, Investigation on Performance of a Compression-Ignition Engine with Pressure-Wave Supercharger, Energy 35 (2010) 85–93.

[8] J.Q. Zhao, D.P. Hu, P.Q Liu, F.X. Liu and J.J. Gao, Thermodynamic Analysis of a Novel Wave Rotor Refrigeration Cycle, Advanced Materials Research 805-806 (2013) 537–542.

[9] D.Hu, R. Li, P. Liu and J. Zhao, The Loss in Charge Process and Effects on Performance of Wave Rotor Refrigerator, International Journal of Heat and Mass Transfer 100 (2016) 497–507.

[10] H.E. Weber, Shock Wave Engine Design, John Wiley & Sons, New York, 1996.

[11] P. Akbari, R. Nalim and N. Mueller, A Review of Wave Rotor Technology and Its Applications, Journal of Engineering for Gas Turbines and Power 128 (2006).

[12] G. Lenoble and S. Ogaji, Performance Analysis and Optimization of a Gas Turbine Cycle Integrated with an Internal Combustion Wave Rotor, Proceedings of the Institution of Mechanical Engineers, Part A: Journal of Power and Energy 224 (2010) 889–900.

[13] L. Yani, Z. Dasen, Z. Hongguang, J. Changwei, L. Jiangguo and Z. Tong, Experiment and CFD Investigation of Pressure-wave Supercharger, in: 2008 SAE

International Powertrains, Fuels and Lubricants Congress, SAE International, 2008.

[14] M. Mataczynski, J. Hoke, D.E. Paxson and M.D. Polanka, Design, Simulation, and Testing of a Pressure Wave Supercharger for a Small Internal Combustion Engine, in: SAE 2014 Aerospace Systems and Technology Conference, SAE International, 2014.

[15] S. Chan and H. Liu, Mass-Based Design and Optimization of Wave Rotors for Gas Turbine Engine Enhancement, Shock Waves 27 (2017) 313–324.

[16] F. Klein and S. Staudacher, Plausibility Study of Hecto Pressure Ratio Concepts in Large Civil Aero-Engines, Journal of Engineering for Gas Turbines and Power 140 (2018).

[17] A. Fatsis, Performance Enhancement of One and Two-Shaft Industrial Turboshaft Engines Topped with Wave Rotors, International Journal of Turbo and Jet Engines 35 (2018) 137–147.

[18] Chan, S. and Liu, H. and Xing, F. and Song, H., Experimental Method on the Port Flow of the Wave Rotor, 53rd AIAA/SAE/ASEE Joint Propulsion Conference, 2017 (2017).

[19] K.P. Lapp, M.D. Polanka, M.J. McClearn, J. Hoke and D.E. Paxson, Design and Testing of a Micro-Scale Wave Rotor System, in: 53rd AIAA/SAE/ASEE Joint Propulsion Conference, AIAA, 2017.

[20] M.R. Mataczynski, M.J. McClearn, F.R. Schauer, D.E. Paxson and J.L. Hoke, Design and Testing of a Small Pressure Wave Supercharger for an Industrial Diesel Engine, AIAA SciTech Forum - 55th AIAA Aerospace Sciences Meeting (2017).

[21] Haidinger, C. and Kriegler, W. and Millward-Sadler, A. and Eder, P., Feasibility and Design Analysis of a Pressure Wave Supercharger Adaption on a 600 cm3 Spark Ignited Engine, SAE Technical Papers 2017-March (2017).

[22] J.T. Reinhart, B.A. Beasley, J.L. Hoke, M.J. McClearn and F.R. Schauer, Experimental Observations of a Small-Scale Pressure-Wave Supercharger Coupled to a Compression Ignition Engine, AIAA Aerospace Sciences Meeting, 2018 (2018).

[23] D.Hu, R. Li, P. Liu and J. Zhao, The Design and Influence of Port Arrangement on an Improved Wave Rotor Refrigerator Performance, Applied Thermal Engineering 107 (2016) 207–217.

[24] J. Zhao and D. Hu, An Improved Wave Rotor Refrigerator Using an Outside Gas Flow for Recycling the Expansion Work, Shock Waves 27 (2017) 325–332.

[25] D. Hu, Y. Yu and P. Liu, Enhancement of Refrigeration Performance by Energy Transfer of Shock Wave, Applied Thermal Engineering 130 (2018) 309–318.

[26] D. Hu, Y. Yu, P. Liu, X. Wu and Y. Zhao, Improving Refrigeration Performance by Using Pressure Exchange Characteristic of Wave Rotor, Journal of Energy Resources Technology, Transactions of the ASME 141 (2019).

[27] R.R. Jagannath, S.P.M. Bane and M.R. Nalim, Wave Rotor Combustor Turbine Model Development, 51st AIAA/SAE/ASEE Joint Propulsion Conference (2015).

[28] J. Li, E. Gong, L. Yuan, W. Li and K. Zhang, Experimental Investigation on Pressure Rise Characteristics in an Ethylene Fuelled Wave Rotor Combustor, Energy & Fuels 31 (2017) 10165–10177.

[29] M.R. Nalim, P.H. Snyder and M. Kowalkowski, Experimental Test, Model Validation and Viability Assessment of a Wave-Rotor Constant-Volume Combustor, Journal of Propulsion and Power 33 (2017) 163–175.

[30] A. Tarraf, R. Ebrahimi, M.E. Feyz and R. Nalim, Application of Response Surface Methodology to Investigate the Hot-Jet Ignition of Methane-Hydrogen Mixtures in a Constant-Volume Combustor, volume 2017-April.

[31] S.C. Gülen, Pressure Gain Combustion Advantage in Land-Based Electric Power Generation, Journal of the Global Power and Propulsion Society 1 (2017) 288–302.

[32] J. Li, E. Gong, L. Yuan, W. Li and K. Zhang, Experimental Investigation on Flame Formation and Propagation Characteristics in an Ethylene Fuelled Wave Rotor Combustor, Energy & Fuels 32 (2018) 2366–2375.

[33] H.D. Perkins and D.E. Paxson, Summary of Pressure Gain Combustion Research at NASA, NASA/TM-2018-219874 (2018).

[34] J.A.C. Kentfield, The Performance of Pressure-Exchanger Dividers and Equalizers, Journal of Basic Engineering (1969) 361–369.

[35] J.A.C. Kentfield, An Examination of the Performance of Pressure Exchanger Equalisers and Dividers, PhD Thesis, University of London, 1963.

[36] J. Wilson and D. Fronek, Initial results from the NASA-Lewis Wave Rotor Experiment, AIAA-93-2521 (1993).

[37] J. Wilson, Design of the NASA Lewis 4-Port Wave Rotor Experiment, Technical Report, NASA Contractor Report 202351, 1997.

[38] J. Wilson, G.E. Welch and D.E. Paxson, Experimental Results of Performance Tests on a Four-Port Wave Rotor, NASA/TM2007-214488 (2007).

[39] M. Mataczynski, D.E. Paxson, M.D. Polanka, and J. Hoke, Performance and Design Improvements for a Small Scale Pressure Wave Supercharger, in: 54th AIAA Aerospace Sciences Meeting, AIAA SciTech Forum, AIAA, 2016.

[40] M.J. McClearn, M.D. Polanka, M.R. Mataczynski, F. Schauer, and D.E. Paxson, The Design of a Small-Scale Wave Rotor for Use As a Modified Brayton-Cycle Engine, in: 52nd AIAA/SAE/ASEE Joint Propulsion Conference, AIAA, 2016.

[41] M.J. McClearn, M.D. Polanka, M.R. Mataczynski, F. Schauer, and D.E. Paxson, The Testing of a Small-Scale Wave Rotor for Use As a Modified Brayton-Cycle Engine, in: 52nd AIAA/SAE/ASEE Joint Propulsion Conference, AIAA, 2016.

[42] R.D. Pearson, Thermodynamics and Gas Dynamics of Internal Combustion Engines, Volume II, in: D.E. Winterbone and S.C. Low (Ed.), The Oxford Handbook of Innovation, Oxford University Press, Oxford, 1986.

[43] A. Mathur, Design and Experimental Verification of Wave Rotor Cycles, in: Proceedings ONR/NAVAIR Wave Rotor Research and Technology Workshop, Naval Postgraduate School, 1985.

[44] R. Taussig, P. Cassady, J. Zumdieck, W. Thayer and E. Klostermannt, Investigation of Wave Rotor Turbofans for Cruise Missile Engines, Technical Report, Final Report Submitted by MSNW to DARPA, 1983.

[45] J. Piechna and D. Dyntar, Two-Dimensional Numerical Analysis of the Wave Jet Micro-Engine Operation, Proc. PowerMEMS 2007 Freiburg, Germany (2007).

[46] J. Piechna, Feasibility Study of the Wave Disk Micro-Engine Operation, J. Micromech. Microeng. 16 (2006).

[47] J. Piechna and D. Dyntar, Numerical Investigation of the Wave Disk Micro-Engine Concept, International Journal of Gas Turbine, Propulsion and Power Systems 2 (2008).

[48] J. Piechna and D. Dyntar, Hybrid Wave Engine Concept and Numerical Simulation of Engine Operation, The Archive of Mechanical Engineering LVII (2010).

[49] P. Parrage-Ramirez, M. Varney, E. Tarkleson, N. Müller, P. Akbari and J. Piechna, Development of a Wave Disk Engine Experimental Facility, 48th AIAA/ASME/SAE/ASEE Joint Propulsion Conference Exhibit (2012).

[50] N. Müller, J. Piechna, G. Sun and P.F. Parraga, Wave disc engine apparatus, Patent no. 9,856,791 (2018).

[51] J. Wilson, G.E. Welch and D.E. Paxson, Experimental Results of Performance Tests on a Four-Port Wave Rotor, NASA-TM-2007-214488 (2007).

[52] Gyarmathy, George, How Does the Comprex Pressure-Wave Supercharger Work?, in: SAE International Congress and Exposition, SAE International, 1983.

[53] ISO Central Secretary, Measurement of Fluid Flow - Procedures for the Evaluation of Uncertainties, Standard BS ISO 5168:2005, International Organization for Standardization, London, UK, 2005.

Addendum to Paper II

A few words shall be addressed to the definition of compression and expansion efficiency. The definition provided in Equation 5 of Paper II contains an additional temperature difference to account for heat transfer between hot and cold temperatures. While this is necessary yield reasonable efficiency data, it is necessary to be cautious when comparing wave rotor efficiency against the isentropic efficiencies of turbomachinery. It is important to highlight that significant simplifications are required to account for heat transfer and EGR in the wave rotor efficiency defintion, which renders a direct translation to isentropic efficiency of turbomachinery difficult and potentially not suitable. For instance, an increase in inlet enthalpy from 500°C to 600°C for turbomachines at constant mass flow rates incurs the same isentropic efficiency. When looking at Figure 20 of Paper II, there seems to be a discrepancy in wave rotor efficiency when increasing peak inlet temperature. While this is lower at higher rotational speeds, the difference amounts to approximately two percentage points at lower rotational speeds. Rather than a pure effect in increased inlet enthalpy, the drop in efficiency may stem from the uncertainty in mass flow rates, loop flow ratio. In general, this could also stem from changes in EGR, which in turn have direct effects on the averaged outlet temperature in the HPA duct.

3.2.1 Summary and Implications of Paper II

The experimental testing presented in this section has several implications for this thesis. First of all, the article has successfully shown the wave rotor turbine can both function as a power generating turbine as well as a pressure exchanging device at the same time. However, the data further indicate indicate that the transferred energy does not suffice to match the outlet pressure in the HPA duct with the inlet pressure from the HPG duct. On the one hand, this is a result of running at relatively low inlet temperatures of up to 600°C. On the other hand, uneven thermal expansion between the rotor, stators and outer casing required the tests to be carried out at a greater axial clearances to avoid damage to the rotor, namely up to 0.3 mm on inlet and outlet side instead of the targeted 0.1 mm. Increased axial clearances promote channel-to-channel interaction and effectively result in an attenuation of shock waves, which reinforces the findings of Okamoto et al. [91] and Liu et al. [92]. Nonetheless, the test results clearly highlight that greater inlet temperatures and decreased axial clearances mitigate the deficiency in pressure difference across the high pressure in- and outlet.

Secondly, the application of an enthalpy-based adiabatic efficiency definition leads to useful calculations only if the temperature difference between the two inlet

streams is small. The tested wave rotor turbine, however, operates at relatively high peak inlet temperatures, which leads to exceedingly high and low compression and expansion efficiencies respectively. Therefore, heat transfer between hot and cold gas streams needs to be taken into account. Internal EGR also plays an important role raising the temperature in the high pressure outlet duct and thus reducing the apparent compression efficiency, if not taken into consideration otherwise. The proposed method builds on formulation put forward by Wilson et al. [112] and includes heat transfer effects, as well as internal EGR. FAE is more difficult to estimate and is usually considerably lower than EGR, therefore it is not included in the efficiency formulation. Using the proposed efficiency calculation, the paper has shown that the shock and expansion waves within the wave rotor channels can achieve efficiency compression and expansion efficiencies of up to 80%. Despite the fact that the method cannot distinguish between compression and expansion efficiency and that the actual EGR rate may differ from its estimated value, the values are in the similar range to the ones computed by the numerical model in Section 2.2 and thus prove the high efficiency of shock compression compared to standard turbomachinery of similar size.

Thirdly, the parabolic variation of pressure ratio while shaft power remains roughly constant indicates that torque is predominantly generated as a consequence of blade shape rather than through instant turning of the flow as the gas streams from the angled inlet ports into the channels. If the incidence angle between the flow and the cambered passages is large, total pressure losses are inevitable. This will be addressed in subsequent chapters, where the channel shape is subjected to an optimisation routine in order to increase the power output of the wave rotor turbine.

3.3 Paper III: Validation of a Numerical Quasi-One-Dimensional Model for Wave Rotor Turbines with Curved Channels

Article published in the *ASME Journal of Engineering for Gas Turbines and Power*, [124]:

S. Tüchler and C.D. Copeland, "Validation of a Numerical Quasi One-Dimensional Model for Wave Rotor Turbines with Curved Channels," Journal of Engineering for Gas Turbines and Power, GTP-19-1313, Vol. 142, No. 2, pp. 0210171-02101715 ,2020.

and presented at ASME Turbo Expo 2019, Phoenix, United States and published in

the associated conference proceedings, [125]:

S. Tüchler and C.D. Copeland, "Validation of a Numerical Quasi One-Dimensional Model for Wave Rotor Turbines with Curved Channels," Proceedings of ASME Turbo Expo 2019: Turbomachinery Technical Conference and Exposition, GT2019-90868, Jun, 2019, Phoenix, Arizona, United States.

Statement of authorship

S. Tüchler (candidate): development and implementation of numerical model, data analysis, preparation of tables and graphs, writing and compilation of manuscript. Presented the contents of the paper at the conference.

C.D. Copeland (supervisor): supervision of numerical modelling work, review and editing of manuscript.

Copyright

Validation of a Numerical Quasi-One-Dimensional Model for Wave Rotor Turbines With Curved Channels

Stefan Tüchler[1]
Powertrain and Vehicle Research Centre,
Department of Mechanical Engineering,
University of Bath,
Bath BA2 7AY, UK
e-mail: S.Tuechler@bath.ac.uk

Colin D. Copeland
Powertrain and Vehicle Research Centre,
Department of Mechanical Engineering,
University of Bath,
Bath BA2 7AY, UK

A wave rotor is a shock-driven pressure exchange device that, while relatively rarely studied or indeed, employed, offers significant potential efficiency gains in a variety of applications including refrigeration and gas turbine topping cycles. This paper introduces a quasi-one-dimensional (Q1D) wave action model implemented in MATLAB *for the computation of the unsteady flow field and performance characteristics of wave rotors of straight or cambered channel profiles. The purpose here is to introduce and validate a rapid but reliable method of modeling the performance of a power-generating wave rotor where little such insight exists in open literature. The model numerically solves the laminar one-dimensional (1D) Navier–Stokes equations using a two-step Richtmyer time variation diminishing (TVD) scheme with minmod flux limiter. Additional source terms account for viscous losses, wall heat transfer, flow leakage between rotor and stator endplates as well as torque generation through momentum change. Model validation was conducted in two steps. First of all, unsteady and steady predictive capabilities were tested on three-port pressure divider rotors from open literature. The results show that both steady port flow conditions as well as the wave action within the rotor can be predicted with good agreement. Further validation was done on an in-house developed and experimentally tested four-port, three-cycle, throughflow microwave rotor turbine featuring symmetrically cambered passage walls aimed at delivering approximately 500 W of shaft power. The numerical results depict trends for pressure ratio, shaft power, and outlet temperature reasonably well. However, the results also highlight the need to accurately measure leakage gaps when the machine is running in thermal equilibrium.*
[DOI: 10.1115/1.4044286]

Introduction

Over the past decades, numerous research studies have been dedicated toward the investigation of dynamic pressure exchange machinery, such as wave rotors. These devices use the energy carried in moving shock waves to transfer energy from one stream of fluid to another without the need to incorporate additional mechanical parts. This advantage, in combination with relatively large pressure ratio gains through shock wave compression and a high efficiency associated with this process, renders wave action devices an attractive technology for power generation.

Opposed to crypto-steady flow devices, such as turbomachinery, wave rotors are inherently unsteady flow devices, where shock and expansion waves travel along discrete channels arranged around the circumference of a cylindrical drum. To each side of the spinning rotor, there are stator endplates containing port openings, as shown in Fig. 1. Exposing the rotor channels periodically to the ports then triggers shock and expansion waves.

The application range for wave rotors outlined by the literature is diverse. The bulk of early studies focused on pressure exchangers with straight passage profiles for gas turbine topping cycles [1–8] and supercharging devices for internal combustion engines [9–16]. In recent years, the application to refrigeration cycles [17–19] and pressure-gain combustors [20–22] has come into the focus of consideration.

In comparison, little amount of attention has been given to wave turbines with cambered passage walls aimed at acting both as pressure exchangers while producing shaft power through momentum change of the flow [23–27]. Documentation of these endeavors is unfortunately fragmentary. The best documented and most successful example of a wave rotor engine was done by Pearson [23,24] at the University of Bath. Initial tests were conducted on a single cycle, through-flow wave rotor with helical passage shape leading to a power output of around 26 kW at a rotational speed of 18,000 rpm. Further research was suspended after the engine was destroyed due to overspeeding. Further experiments by General Electric and General Power Corporation yielded insufficient shaft power generation and were not further pursued [25,26].

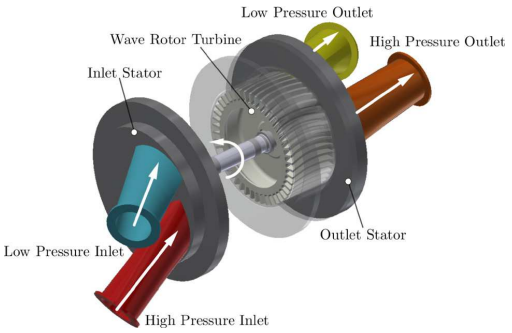

Fig. 1 Wave rotor structure showing wave rotor with discrete passages, in- and outlet stator as well as the arrangement of ports

[1]Corresponding author.
Manuscript received June 25, 2019; final manuscript received June 27, 2019; published online January 17, 2020. Editor: Jerzy T. Sawicki.

One limitation of early efforts on wave rotor design was partially due to a lack in computational power rendering performance estimation time consuming (in particular when done by hand calculations) and often inaccurate. To mitigate this and to accurately compute unsteady wave action in the rotor channels and steady conditions in the ports as well as wave rotor performance parameters, one-dimensional (1D) codes have established themselves as swift and reliable tools. This has been pursued by a number of institutions, ranging from the Naval Postgraduate School [28–32], University of Tokyo [6,33,34], ONERA [6,35,36], Michigan State University [37], NASA Glenn Research Center [38–42] as well as Xiamen University/Beihang University [43,44] most recently.

While most of the mentioned studies deal with straight channels, there is merely one study that incorporates passage curvature in a one-dimensional environment, albeit at reduced order through a passage-averaged description. This was conducted at NASA Glenn Research Center by Welch and Paxson [42] and compared port axial and tangential velocities as well as predicted power output to a two-dimensional computational fluid dynamics (CFD) simulation. However, no comparison with experimental data was done.

Against this background, this paper aims at addressing this gap by introducing a one-dimensional model that allows a reliable and cost effective insight into the performance of wave rotors with straight and arbitrarily shaped camber. To the authors' knowledge, this paper will present, for the first time, a quasi-one-dimensional (Q1D) model that allows direct computation of torque output for cambered wave rotor channels without the need for further model reduction. It is also the first time such a model has been compared to experiments. Conventional 1D models for turbines and compressors employ either a map-based approach that requires a priori experimental data in the form of mass flow rate, efficiency, and pressure ratio [45] or model the rotor wheel through an adiabatic pressure loss that is calibrated over the anticipated flow range against experimental data [46]. The proposed model, however, differs to that approach as directly models the unsteady wave action dynamics within the rotor while accounting for finite passage opening, friction, leakage, and inviscid forces.

The structure of the paper is thus as follows: first, the governing equations and model source terms for viscous and inviscid forces, flow leakage, and wall heat transfer are introduced; second, steady and unsteady validation of the code is done based on experimental data from the open literature on pressure dividers done by Kentfield [47] and NASA [48]. Further validation of the model is achieved through experimental data from a wave rotor turbine experiment performed in the gas stand at the University of Bath. The wave rotor turbine features a symmetrical, arc-shaped passage design that was designed to produce a power output of up to 500 W.

Simulation Model

The model was implemented in MATLAB R2017 and follows a single wave rotor passage of constant cross section as it passes ports along the circumference. It consists of numerical routines to solve the one-dimensional conservation equations accounting for channel curvature for shaft power extraction, heat transfer between fluid and rotor walls, flow leakage in the axial clearance between stator and rotor, as well as gradual passage opening effects. The code can be applied to both through-flow and reverse-flow wave rotor applications.

Finally, the user has the option of defining the gas composition for the operating medium. Throughout this study, this is assumed to be air, composed of 79% nitrogen and 21% oxygen.

For the derivation of the model, a number of assumptions are made; first of all, in order to justify a one-dimensional formulation, channel length is expected to be an order of magnitude larger than channel width and height. Furthermore, the flow path follows a single streamline through the passage. The quasi-one-dimensional formulation assumes that all quantities are uniform across the cross section. This does not hold for wave rotors, as high rotational speeds due to centrifugal effects, vortices due to finite passage opening effects, and shock-wave boundary layer interactions create secondary flows and skewed air/gas demarcation surfaces, which cannot be captured using one-dimensional wave action codes. While the effect of gradual passage opening on the primary shock strength can at least be qualitatively captured, interferences between neighboring channels and between the channel and leakage cavity, which become particularly pronounced for larger axial clearances between rotor and stator, cannot be depicted directly.

Governing Equations. The equations used to describe the unsteady, compressible, and viscous effects taking place within a wave rotor turbine are the one-dimensional Navier–Stokes equations, which can be written in conservative form as

$$\frac{\partial \mathbf{U}}{\partial t} + \frac{\partial \mathbf{F}(\mathbf{U})}{\partial m} = \mathbf{S} \tag{1}$$

The first term represents time-dependent variations, while the second term refers to advection. The source term $\mathbf{S}$ accounts for viscous as well as inviscid effects (i.e., friction and "blade" forces), as well as leakage losses and wall heat transfer. These will be explained in more detail in the section Source Terms. The state vector $\mathbf{U}$ and the flux vector $\mathbf{F}$ are defined as

$$\mathbf{U} = \begin{pmatrix} \rho \\ \rho u \\ \rho E \end{pmatrix}, \quad \mathbf{F} = \begin{pmatrix} \rho u \\ \rho u^2 + p - \tau_{mm} \\ \rho u\left(E + \dfrac{p}{\rho} - \tau_{mm} + q_m\right) \end{pmatrix} \tag{2}$$

Heat conduction within the fluid is addressed through Fourier's law of heat conduction. Furthermore, friction between particles is included through shear force. They can be more explicitly stated as

$$q_m = -k\frac{\partial T}{\partial m}, \quad \tau_{mm} = (2\mu + \lambda)\frac{\partial u}{\partial m} \tag{3}$$

The set of PDEs encompasses four primitive variables u, ρ, p, and e, which require the introduction of an additional equation to ensure closure of the equation system. This is done by the ideal gas equation relating pressure, temperature, and density

$$\frac{p}{\rho} = RT \tag{4}$$

The model further treats air as a calorically imperfect gas, where specific heat constant at constant pressure $c_p = f(T)$ varies with temperature. While this is less important for pressure exchangers, where temperatures can be close to ambient conditions, it becomes more important at elevated temperatures exhibited in gas turbines, where the peak cycle temperature delivered from the combustor exceeds 450–500 K [49]. Thermodynamic data for specific heat constant and internal energy used throughout this study stem from GRI-MECH [50] and the thermal database provided by Virginia Tech [51]. Finally, dynamic viscosity is modeled through the well-known Sutherland relation.

Source Terms

Viscous and Inviscid Forces. The previous one-dimensional models addressed merely viscous (friction) forces and did not directly address inviscid profile forces that account for shaft power generation. Fluid viscosity determines wall friction and promotes convective heat transfer. As a result, the corresponding source term affects both the momentum and the energy equation. Friction force is defined as

$$F_{f,\mathrm{res}} = -C_f \rho \frac{2f}{D_h} |u| u \tag{5}$$

It features a friction multiplier C_f that accounts for additional momentum losses that cannot be captured with the relatively simple approach taken. As stated by Winterbone and Pearson [52], the friction factor f is a function of the Reynolds number within the channel and is given by

$$f(\mathrm{Re}) = \begin{cases} \dfrac{0.25}{\left[\log_{10}\left(\dfrac{k}{3.7D_h} + \dfrac{5.74}{\mathrm{Re}^{0.9}}\right)\right]^2} & \text{for } 5000 \geq \mathrm{Re} \geq 10^8 \\ \dfrac{64}{\mathrm{Re}_D} & \text{for } \mathrm{Re} < 5000 \end{cases} \tag{6}$$

where k denotes the surfaces roughness value, which was set to 25 μm. Using the force diagram shown in Fig. 2(*c*), one can work out the tangential component of the friction factor and write the total source term as

$$\mathbf{S}_f = \begin{pmatrix} 0 \\ s_{f,2} \\ s_{f,3} \end{pmatrix} = \begin{pmatrix} 0 \\ -C_f \rho \dfrac{2f}{D_h} |u| u \\ \rho \dfrac{2f}{D_h} |u| c_p (T_w - T) - C_f \rho \dfrac{2f}{D_h} |u| u \dfrac{u_\theta}{u} \omega r \end{pmatrix} \tag{7}$$

Torque generation in wave rotors is pulsatile in nature and is primarily generated when the channels are exposed to a high pressure inlet port. Throughout this study, tangential forces and thus power generation are computed as a result of the momentum change as the fluid travels along the cambered channel walls.

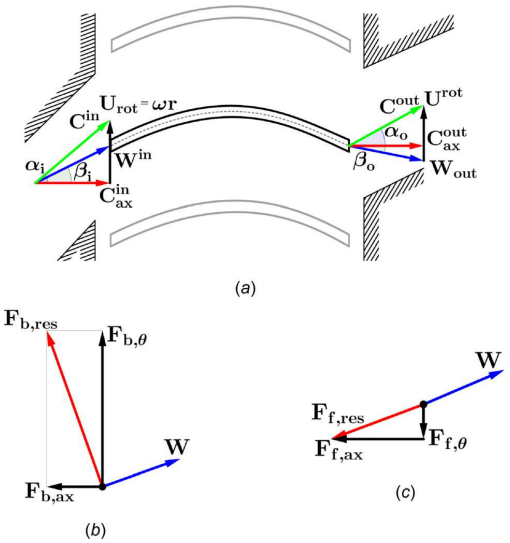

Fig. 2 (*a*) Velocity triangles at in- and outlet port over a curved rotor wall showing absolute velocity *C*, relative velocity *W*, tangential velocity *U*, and axial velocity C_{ax} with the respective absolute and relative flow angles α and β. (*b*) Inviscid blade forces and the relative flow vector. (*c*) Friction vector and the relative flow angle.

Overall, this is exemplified by the change in velocity triangles at leading and trailing edge of a passage wall, as shown in Fig. 2(*a*). The corresponding blade force source term affects momentum and energy equation and takes the form

$$\mathbf{S}_v = \begin{pmatrix} 0 \\ s_{b,2} \\ s_{b,3} \end{pmatrix} = \begin{pmatrix} 0 \\ F_{b,m} \\ F_{b,\theta} \omega r \end{pmatrix} \tag{8}$$

The tangential blade force per unit volume can be determined using the change in momentum, which is influenced by the difference in absolute tangential velocity C_θ across leading and trailing edge, the mass flow rate through the channel $\dot{m}$, and the channel volume V. In the discretized domain, this force is calculated for each element taking the difference in the tangential velocity vector from one cell to the next into account

$$F_{b,\theta} = \frac{\dot{m}}{V} (C_{\theta,o} - C_{\theta,i}) \tag{9}$$

Friction forces are accounted for by the previously suggested viscous source term. Thus, the blade force source term acts in an inviscid way so that one can assume the blade force vector to be orthogonal to the relative velocity vector, as given in Fig. 2(*b*). Hence, the scalar product of blade force vector and relative velocity vector equals zero and the equation can be rearranged to give the axial inviscid blade force per unit volume

$$\begin{aligned} &\mathbf{F}_b \cdot \mathbf{U} = 0 \\ &\text{so that } F_{b,\mathrm{ax}} = -F_{b,\theta} \frac{U_\theta}{C_{\mathrm{ax}}} \end{aligned} \tag{10}$$

In reality, the port angles will be aligned at a different angle than the passage walls angle. This can take place at off-design conditions or if an additional momentum change is desired at the stator rotor interface in order to create more torque. In addition, flow separation on the passage wall "suction side" can often be witnessed if the port angle is considerably larger than the passage wall angle. To account for such incidence losses, an additional entropy-based loss coefficient is introduced and applied in the form of a distributed loss factor. It can be calibrated through experimental data or three-dimensional CFD simulations

$$\begin{aligned} \Delta s &= -R \ln(1 - \zeta_{\mathrm{loss}}) \\ F_{\mathrm{loss},\theta} &= \frac{\rho T |C_{\mathrm{ax}}|}{|U|} \frac{\Delta s}{\Delta z} \end{aligned} \tag{11}$$

And the corresponding source term is thus

$$\mathbf{S}_{\mathrm{loss}} = \begin{pmatrix} 0 \\ s_{\mathrm{loss}_{b,2}} \\ s_{\mathrm{loss}_{b,3}} \end{pmatrix} = \begin{pmatrix} 0 \\ F_{\mathrm{loss},m} \\ F_{\mathrm{loss},\theta} \omega r \end{pmatrix} \tag{12}$$

The total tangential force and the corresponding shaft power generation are then computed as

$$\begin{aligned} F_{\theta,\mathrm{tot}} &= F_{b,\theta} - F_{f,\theta} - F_{\mathrm{loss},\theta} \\ P_{\mathrm{tot}} &= F_{\theta,\mathrm{tot}} r \omega \end{aligned} \tag{13}$$

Flow Leakage. The effect of leakage is a crucial factor in wave rotor performances and was modeled as a simple, nonlabyrinth leak in similar fashion as in the previous publications from Kentfield, NASA, and ONERA [35,39,53]. Leakage is modeled as a lumped capacitance model assuming steady flow equations. It concerns both continuity as well as energy equation, so that the leakage source term may be stated as

$$\mathbf{S}_v = \begin{pmatrix} s_{l,1} \\ 0 \\ s_{l,3} \end{pmatrix} = \begin{pmatrix} -C_D\sqrt{\frac{2\gamma}{\gamma-1}}\left(\frac{\delta_l}{h\Delta z}\right)\sqrt{p\rho}\Phi \\ 0 \\ -C_D\sqrt{\frac{2\gamma}{\gamma-1}}\left(\frac{\delta_l}{h\Delta z}\right)h\sqrt{p\rho}\Phi \end{pmatrix} \tag{14}$$

where C_D is the discharge coefficient, p and ρ the pressure and the density in channel or cavity, respectively, h denotes enthalpy, δ_l the axial clearance between rotor and stator, and Δz the cell size used for discretization. The leakage function Φ takes up the form, which allows to differentiate between flow entering and leaving the cavity depending on the pressure ratio in cell and leakage cavity

$$\begin{aligned} \Phi &= \sqrt{\left(\frac{p_{\text{cav}}}{p}\right)^{2/\gamma} - \left(\frac{p_{\text{cav}}}{p}\right)^{(\gamma+1)/\gamma}} \\ &\text{for } \frac{p_{\text{cav}}}{p} > \left(\frac{2}{\gamma+1}\right)^{\gamma/(\gamma-1)} \\ \Phi &= \sqrt{\left(\frac{2}{\gamma+1}\right)^{2/(\gamma-1)} - \left(\frac{2}{\gamma+1}\right)^{(\gamma+1)/(\gamma-1)}} \\ &\text{for } \frac{p_{\text{cav}}}{p} < \left(\frac{2}{\gamma+1}\right)^{\gamma/(\gamma-1)} \end{aligned} \tag{15}$$

The source terms are only active at the extremities of the rotor channel and are set to zero in the remainder of the domain. After each cycle, the mass and energy balance are computed, and the cavity pressure and temperature updated from a first-order system of differential equations as provided by Eq. (16). The equations designate continuity and the energy equation derived from the first law of thermodynamics and are integrated in time using an explicit Runge–Kutta scheme. Cavity pressure can be found by applying the equation of state for ideal gases

$$\begin{aligned} \frac{dm_{\text{cav}}}{dt} &= \sum_i \dot{m}_i \\ \frac{d}{dt}(m_{\text{cav}} e_{\text{cav}}) &= \dot{Q}_{\text{wht}} + \sum_i h_i \dot{m}_i \\ \text{where } e_{\text{cav}} &= c_v T_{\text{cav}} \end{aligned} \tag{16}$$

The heat transfer term stands for the heat transfer from the wave rotor wall temperature. For the respective heat transfer coefficient, a Nusselt number relation for annuli with inner cylinder rotation was used [54]

$$\text{Nu} = 0.015\left(1 + 2.3\frac{D_h}{L}\right)\left(\frac{D_o}{D_i}\right)^{0.45}\text{Re}_{\text{eff}}^{0.8}\,\text{Pr}^{1/3} = \frac{hD_h}{k} \tag{17}$$

Wall Heat Transfer. The viscous source term given in Eq. (7) features the wall temperature to compute convective heat transfer. During operation and constant inlet temperatures from the ports, the rotor temperature settles at a constant value. In order to include the effect of wall heat transfer, a lumped capacitance model that follows the first-order differential equation given in Eq. (18) was implemented

$$\begin{aligned} \frac{dT_w(t)}{dt} &= -\tau^{-1}(T_w(t) - T) \\ \text{with } \tau &= \frac{mc_p}{hA} \end{aligned} \tag{18}$$

where h is the convective heat transfer coefficient, A the surface area of heat transfer, and c_p the specific heat capacity of the solid material. The heat transfer coefficient h is determined from the Nusselt number relation for turbulent flow within a tube

$$\text{Nu} = 0.0243\ \text{Re}^{0.8}\,\text{Pr}^{0.4} = \frac{hD_h}{k} \tag{19}$$

Equation (18) is iteratively solved using a two-step Heun approach, as given in the following equation:.

$$\begin{aligned} \hat{T}_{w,i}^{n+1} &= T_{w,i}^n - \alpha\left(T_{w,i}^n - T_{g,i}^n\right)\Delta t \\ T_{w,i}^{n+1} &= T_{w,i}^n - \frac{\alpha}{2\Delta t}\left(T_{w,i}^n + \hat{T}_{w,i}^{n+1} - 2T_{g,i}^n\right) \end{aligned} \tag{20}$$

Domain Discretization. The explicit, second-order accurate scheme of Richtmyer in combination with a minmod flux limiter of Roe and Baines was selected for the discretization of the governing equations in space and time. This allows for an accurate resolution of flow discontinuities while obeying time variation diminishing criterion and preventing spurious oscillations from taking place in their vicinity. The proposed scheme suggests a two-step technique where additional half timesteps are introduced. The first step consists of a first-order accurate Lax-Friedrichs method, which can be obtained through the integration of Eq. (1) in space and time and assuming the intercell fluxes to be the average of two consecutive cells

$$\begin{aligned} \mathbf{U}_{i+1/2}^{n+1/2} &= \frac{1}{2}\left(\mathbf{U}_{i+1}^n + \mathbf{U}_i^n\right) - \frac{\Delta t}{2\Delta z}\left(\mathbf{F}_{i+1}^n - \mathbf{F}_i^n\right) - \frac{\Delta t}{4}\left(\mathbf{S}_{i+1}^n - \mathbf{S}_i^n\right), \\ \mathbf{U}_{i-1/2}^{n+1/2} &= \frac{1}{2}\left(\mathbf{U}_i^n + \mathbf{U}_{i-1}^n\right) - \frac{\Delta t}{2\Delta z}\left(\mathbf{F}_i^n - \mathbf{F}_{i-1}^n\right) - \frac{\Delta t}{4}\left(\mathbf{S}_i^n - \mathbf{S}_{i-1}^n\right) \end{aligned} \tag{21}$$

The second step uses a midpoint Leapfrog computation and consists of space and time centered differences of the mid-step solutions of $\mathbf{U}_{i\pm1/2}^{n+1/2}$ and gives

$$\mathbf{U}_i^{n+1/2} = \mathbf{U}_i^n - \frac{\Delta t}{\Delta z}\left(\mathbf{F}_{i+1/2}^{n+1/2} - \mathbf{F}_{i-1/2}^{n+1/2}\right) - \frac{\Delta t}{2}\left(\mathbf{S}_{i+1/2}^{n+1/2} - \mathbf{S}_{i-1/2}^{n+1/2}\right) \tag{22}$$

Boundary Conditions

For the implementation of boundary conditions, a cell-centered approach has been chosen. This involves the addition of an image cell lying just outside of the domain. In general, one can distinguish between inflow, outflow, and wall boundaries. For each of these types, one needs to determine the flow variables on the image cells. Walls are treated as reflective boundaries where pressure and density are equal to the neighboring interior cell node, while velocity is assigned the same value with the opposite sign.

Assuming subsonic inflow, it is necessary to specify two characteristics entering the domain, while one characteristic leaves the domain. Therefore, stagnation properties (temperature and pressure) are imposed, while velocity is extrapolated in the zeroth order. This approach further guarantees a simple way to compare results with experimental conditions. When computing the flow variables at the image cell, it is crucial to consider that the stagnation properties are defined in the absolute frame of reference, while the code operates in the relative frame of reference.

For outflows, one characteristic enters the domain, while two characteristics leave the domain. Thus, a single physical condition needs to be imposed (static outlet pressure) and the remaining two are extrapolated from the domain interior.

Unfortunately, this is only valid for fully exposed channels. There are, however, periods where only a certain portion of the channel is exposed to a port, as shown in Fig. 3(*a*). This gradual passage opening is of paramount importance in the formation of primary shock waves [55]. To account for this, a function is

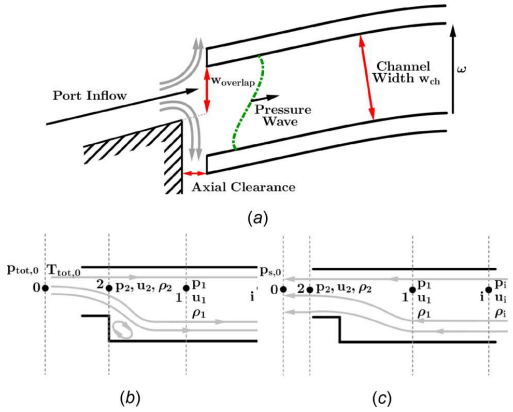

Fig. 3 (*a*) Gradual passage opening shown for port inflow. (*b*) Schematic for the boundary condition for partially open inflow. (*c*) Schematic for the boundary condition for partially open outflow.

defined that determines the amount of overlap based on port opening and closing positions, channel width, and the channel position at each time-step.

If this function is between zero and one, the port is only partially open and an alternative solution for the boundary conditions is calculated. In the case of inflow, the principle is given in Fig. 3(*b*). The gas enters the domain from a reservoir described by stagnation properties for pressure and temperature in the form of a jet through the cross section area at station 2. At station 1, the jet further expands to cover the entire width. The first cell in the domain is at station *i*. Assuming steady flow conditions, one can formulate the three conservative equations for mass, momentum, and energy between stations 1 and 2 as

$$\begin{aligned} \rho_1 u_1 A_1 &= \rho_2 u_2 A_2 \\ \left(p_1 + \rho_1 u_1^2\right) A_1 &= p_2 A_1 + \rho_2 u_2^2 A_2 \\ a_{tot} = a_1^2 + 0.5(\gamma - 1)u_1^2 &= a_2^2 + 0.5(\gamma - 1)u_2^2 \end{aligned} \tag{23}$$

giving three equations for six unknowns in total. The set of equations is closed using the energy equation and isentropic relation between stations 0 and 1 as well as wave and pathline compatibility relations [52]. In a similar fashion, one can formulate the problem for partially open outflows, as given in Fig. 3(*c*). Here, gas flowing through a cross-sectional area of A_1 exits the domain through area A_2. In the subsonic case, the pressure at station 2 equals the reservoir pressure at plane 2. Together with the conservation of mass and energy as well as the isentropic relation between stations 1 and 2 and the corresponding compatibility equations, all six unknowns can be determined.

Procedure

The solution procedure of the code shall be introduced using the example of a four-port throughflow wave rotor, as shown in the unfolded view of a single wave rotor cycle in the $z - t/\theta$ plane in Fig. 4. The ports are designated as high pressure gas inlet (HPG), high pressure air (HPA), low pressure air (LPA), and low pressure gas (LPG), referring to high pressure gas and air and low pressure air and gas, respectively.

It follows the steps outlined in Fig. 5(*b*). Initially, geometric dimensions of the rotor and target rotational speed of the wave rotor are specified. Furthermore, the number of cycles per rotation and the port solution needs to be provided. An initial guess and rough layout can be devised through the analytical tools given by

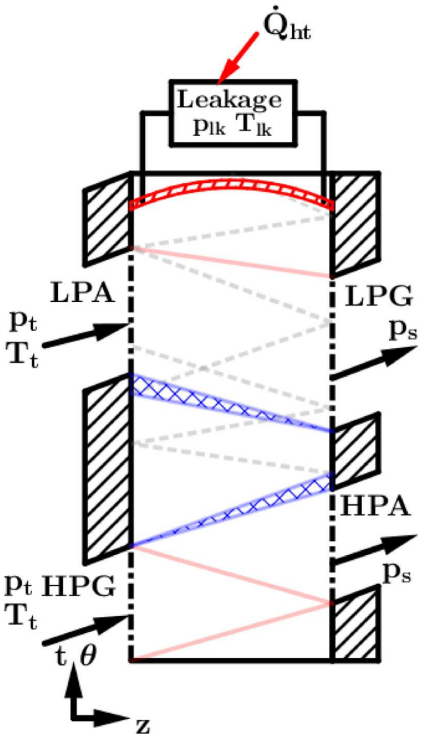

Fig. 4 Model schematic showing port arrangement and expected wave pattern for the Bath μ-wave rotor turbine. To comply with the experimental arrangement, the model was run in open loop without the inclusion of a combustor model.

Chan and Liu [43] and Müller and coworkers [56–58]. Subsequently, all matrices used throughout the computation are, along with the spatial domain, initialized. In terms of the time-step, an initial estimation is provided. While a uniform grid is used, the time-step size is allowed to vary depending on the maximum wave speed $\max_i\left(|u_i^n| + a_i^n\right)$ in the domain at the previous time-step and a fixed CFL number of 0.7 [52]. This allows us to save computational time as otherwise a constant time-step would need to suit the largest velocities in the domain and would thus have to be more on the conservative side.

In open loop configuration (without a closed combustor loop), stagnation properties in the HPG port are fixed, while static pressure in the HPA port is varied automatically using a simple proportional controller based on a simple Bernoulli relation until the mass flow rates are matched and within a 2% relative error. The low pressure inlet conditions generally involve ambient temperature of around 300 K, while the total inlet pressure again being varied in the same manner as for the HPA port and according to the desired loop flow ratio $\lambda = \dot{m}_{HPG}/\dot{m}_{LPA}$

$$p^{t+1} = p^t + \alpha \frac{\rho\left(\dot{m}_{actual}^2 - \dot{m}_{target}^2\right)}{2(\rho A)^2} \tag{24}$$

In the low pressure gas port, exhaust gases are expelled to the ambient and the static pressure is again automatically adjusted to give the desired inlet mass flow rate $\dot{m}_{HPG}$. At the end of each cycle, combustor and leakage cavity properties are updated and port flow conditions need to be determined. This is done through

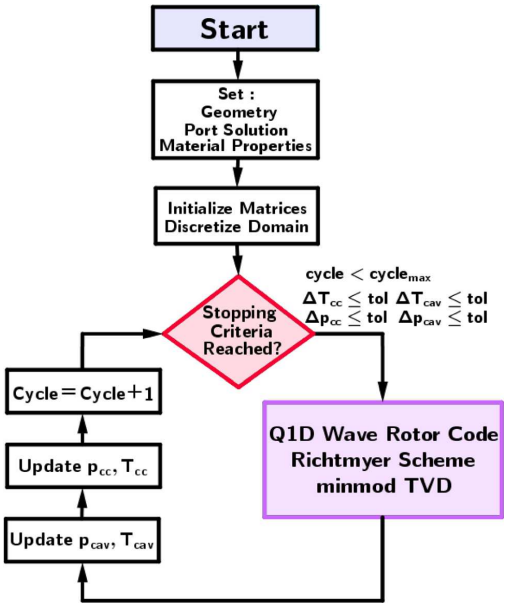

Fig. 5 Simulation model flowchart

mass flux averaging according to Eq. (25) and converting the values into the absolute frame of reference

$$\bar{\phi} = \frac{\sum_{i=N_o}^{N_c} (\phi_i \rho_i u_i)}{\sum_{i=N_o}^{N_c} (\rho_i u_i)} \tag{25}$$

Before the next cycle commences, conditions within the channel at the cycle end are set as initial conditions for the subsequent cycle, thus guaranteeing periodicity. Finally, the simulation is stopped either when the maximum number of cycles is reached or the relative changes of combustor and leakage temperature and pressures are below a predefined threshold.

Results and Discussion. The results presented in the section Results and Discussion seek to exhibit the code's ability to predict results from wave rotor experiments. This shall be done in two stages. First of all, performance data of two three-port pressure dividers are produced and compared with data from the open literature. These are Kentfield's pressure divider from the 1960s [47] and NASA pressure divider from the mid-1990 s [48]. After that, laboratory experiments conducted at the University of Bath on a μ-wave rotor turbine are used to test the code when dealing with four port, throughflow wave rotor turbines with symmetrically cambered profiles.

Table 1 Dimensions and operating conditions of Kentfield and NASA pressure divider used for the simulation

Parameter	Kentfield	NASA 3-Port
Rotor diameter (mm)	164.8	294.6
Number of channels	30	120
Channel shape	Straight	
Channel length (mm)	279.4	457.2
Channel width (mm)	15.2	6.4
Channel height (mm)	55.9	10.16
Nominal clearance (mm)	0.18	0.51
Number of cycles per revolution	3	1
Rotational speed (rpm)	6000	4150
T_{tM} (K)	308.3 K	353.9
p_{tM} (kPa)	110–150	207
p_{sL} (kPa)	100	51

Wave Rotor Pressure Dividers. The geometric dimensions and operating conditions of the two investigated designs are given in Table 1. The main characteristics of both designs shall be briefly introduced. Kentfield's device is characterized by relatively large channel width, while NASA's three-port design has four times the number of channels and has, as a consequence, a rather small channel width. Thus, it can be expected that finite opening timing effects are of minor importance. In terms of length, the NASA design is longer, so that viscous losses become more pronounced. Leakage plays a reduced role in Kentfield's experiments owing to tighter clearances between the rotor and stator endwalls.

Rotational speed of both designs and total inlet temperature in the medium pressure port are fixed in both simulations. Total inlet pressure in the medium pressure port is variable for the Kentfield experiments. In the model, the total outlet pressure of the high pressure port is varied in both cases to give a desired mass flow ratio $\dot{m}_M/\dot{m}_H$ ranging from 0.1 to 0.6. The NASA experiment was conducted at a constant mass flow ratio of 0.37. The unfolded midplane view for the two pressure exchangers with the anticipated wave pattern and relative positions of the three respective ports is given in Fig. 6. Solid red curves denote shock waves, hatched blue areas expansion fans, and dashed gray lines (weak) pressure waves.

Using the MATLAB code on Kentfield's three-port pressure divider yields the results depicted in Fig. 7. All data were produced with a grid resolution of $\Delta z/L = 0.0135$ and a discharge coefficient of 0.67 and a friction multiplier of 1.77. The plots show total pressure for the high pressure port on the ordinate and total pressure for the low pressure port on the abscissa for four different mass flow ratios. All values are nondimensionalized with respect to the inlet total pressure and inlet mass flow rate, respectively. Figure 7(*a*) shows a comparison of the 1D-Navier–Stokes equation (that includes particle friction and heat conduction in the fluid but without wall heat transfer, friction, and leakage model) compared with the experimental data. Clearly, the pressure level in the high pressure port is overpredicted with an increasing deviation toward lower pressure levels in the low pressure port. The

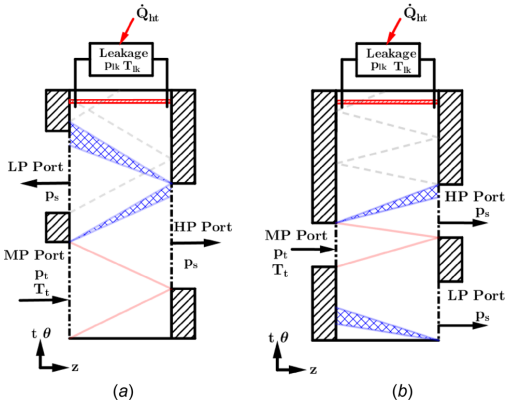

Fig. 6 Model schematic showing port arrangement and expected wave pattern for pressure dividers of (*a*) Kentfield and (*b*) NASA's Glenn Research Center

full model results are then shown in Fig. 7(*b*) outlining the effect losses impart. The main loss mechanisms responsible for the difference are leakage and friction, confirming the findings of the previous studies [35,39]. Since maximum temperatures in both cases are relatively low, wall heat transfer plays a minor role.

The same model parameters were then applied to perform unsteady validation using the NASA three-port wave rotor. This experiment featured static pressure traces at three locations, namely at $z/L = 0.025$, $z/L = 0.5$, and $z/L = 0.975$, within a wave rotor passage as it travels through the circumference. Evaluating the numerical results and normalized static pressure at the channel ends, namely at data against the numerical results, gives the distribution shown in Fig. 8. In comparison with Fig. 6(*b*), one can witness the initial expansion fan generated upon opening the low pressure port on the right-hand side. This is well captured in the model, although the expansion ratio at $z/L = 0.025$ remains slightly overpredicted. The subsequent shock discontinuity is sharper than in the experiments and features a sharp peak for both primary and secondary shock waves. The overall shock pressure ratio across all stations is, however, well depicted. The final expansion fan as well as the attenuation of the pressure wave takes place slightly sooner, as seen at around $\theta = 3.25$–3.5 rad in $z/L = 0.025$ and $z/L = 0.5$.

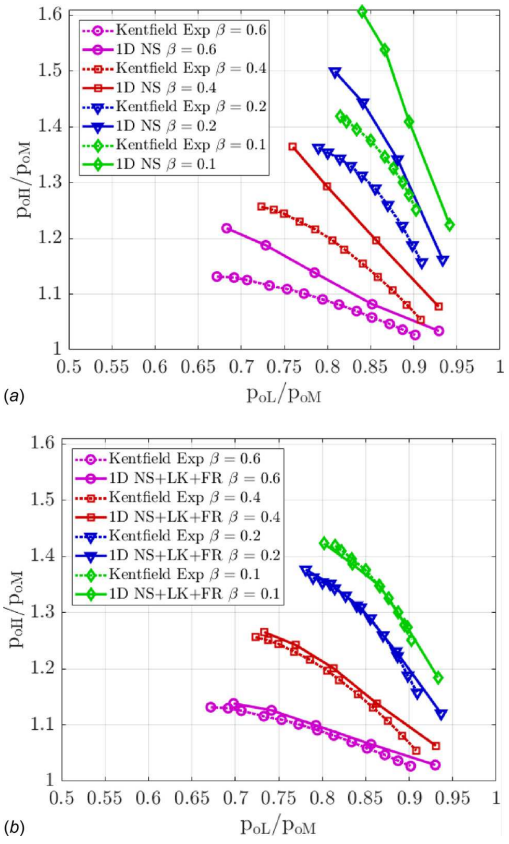

Fig. 7 Comparison of Kentfield's three-port wave rotor with the 1D simulation data. Plot shows normalized total pressure at the high pressure port versus the total pressure at the low pressure port for different mass flow ratios. (*a*) Illustrates simulation data for Euler equations without source terms, while (*b*) shows the effect of accounting for wall heat transfer, wall friction, and leakage.

Bath μ-Wave Rotor Turbine

Layout and Operating Conditions. The third validation case deals with a four-port, three-cycle throughflow wave rotor with symmetrically cambered wall profiles. The rotor was designed to yield approximately 500 W of shaft power output at a target peak cycle temperature of 750 °C and HPG total inlet pressure of 285 kPa. The port solution is shown in Fig. 4 and can be divided into a high pressure and low pressure section in the bottom and top, respectively. The former encompasses a HPG and a HPA outlet that would form the combustor loop in a gas turbine arrangement, while the latter houses the LPA inlet and a LPG outlet . A detailed view of the symmetrically cambered wall profiles and a photograph of the rotor and endplates with the corresponding port openings are given in Figs. 9(*a*) and 9(*b*).

Geometric dimensions and operating conditions that will be used for the simulations are given in Table 2. The rotor has a midwidth diameter of 60 mm, length of 30 mm, and features 46 symmetrically cambered channels with a maximum profile angle of 21.5 deg. In total, three cycles are covered in a single rotation and the design speed is set to 32,000 rpm, giving a tangential speed in the midwidth plane of 100 m/s.

The wave rotor test rig encompasses an open loop configuration, as shown in Fig. 10(*a*). A set of industrial compressors provides pressurized and dry air to the inlet side (HPG and LPA). The corresponding flow rates and thus the flow ratio λ are controlled through a set of pneumatically actuated gate valves and measured through differential mass flow meters. On the HPG leg, the incoming air is additionally directed through an air-to-air heat exchanger to use hot exhaust gases from the outlet side before being run through a set of 44 kW-electrical heaters that ensure the target inlet temperature is reached. Rotational speed and shaft power output is measured through an eddy-current dynamometer that modulates the load on the wave rotor. It is coupled to the wave rotor through a single-plane coupling. On the outlet side, further gate valves ensure the mass flow rates in the high pressure zone, i.e., between HPG and HPA, can be matched accurately before being expelled from the test chamber through extraction fans. Figure 10(*b*) exhibits a photograph from the test chamber displaying the electrical heaters as well as the wave rotor and dynamometer units and outlet gate valves.

The design of the wave rotor encompassed a variable nominal axial clearance between 0.1 and 0.4 mm. Unfortunately, it was found during the experiments that the nominal clearance differed significantly from its design value due to uneven thermal expansion. As the exact values of the actual clearances could not be determined, it was decided to use the nominal values for throughout the validation study.

Rotor Characteristics. Before moving on to the results, it is necessary to classify the wave rotor performance with respect to other existing machines. Table 3 lists a comparison of nondimensional performance parameters for finite passage opening T, viscosity F, and leakage flow G for various wave rotor types, as defined by Nagashima et al. [6] and Wilson and Fronek [48]. Although comparison is somewhat difficult for pure pressure exchangers and wave rotor turbines operating at high temperatures, one can see that the Bath μ-wave rotor performs similarly with respect to finite opening timing effects despite its short rotor length. As expected, due to the small size compared with larger designs, viscous losses become more pronounced and is similar to the microwave rotor study conducted at the University of Tokyo & ONERA [6]. The most critical loss mechanism for the investigated design is without a doubt leakage effects, which is at best similar to the ABB Comprex and the University of Tokyo. In reality, however, it is anticipated that uneven thermal expansion of stators and the shaft-rotor assembly account for a considerably

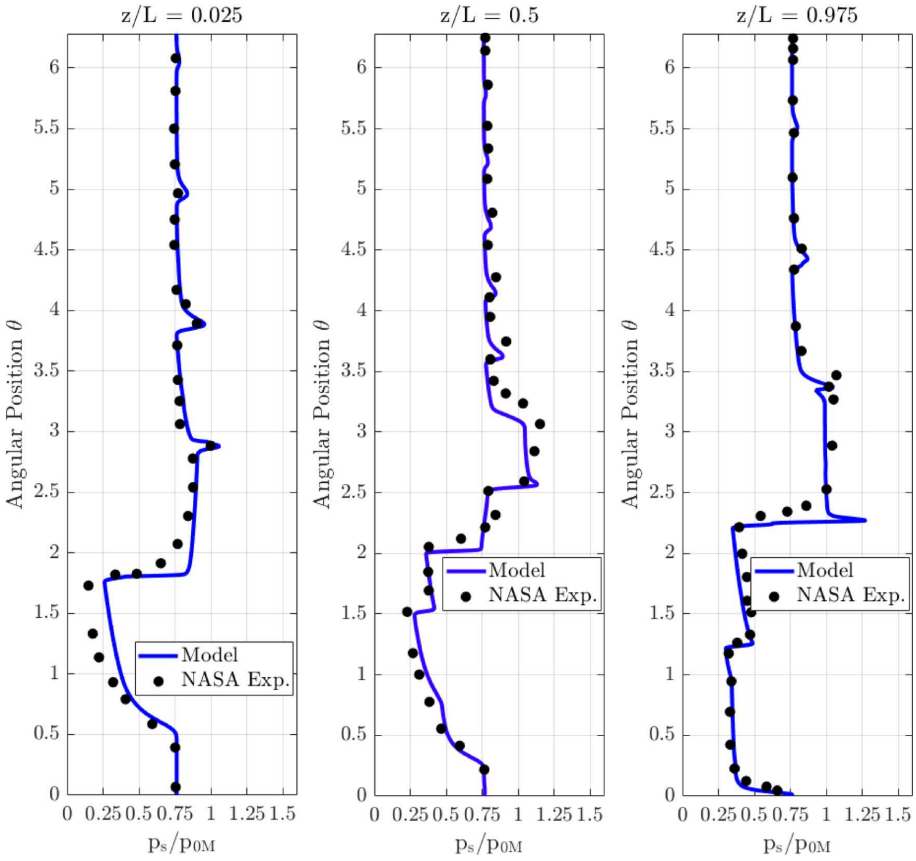

Fig. 8 Comparison of one-dimensional simulation data with experiments of a NASA three-port pressure divider at *z/L* = 0.025, *z/L* = 0.5, and *z/L* = 0.975

larger G-parameter approaching 0.2–0.23. This effect however, cannot be captured in a one-dimensional environment and needs to be taken into account through the leakage coefficient C_D. An additional effect of leakage that cannot be identified using one-dimensional code is that increasing leakage gaps promote the interaction between neighboring channels effectively attenuating in particular the reflected secondary shock extensively.

Model Validation. For the first part of the experimental validation, rotational speed was swept from 24,000 rpm to the design speed of 32,000 rpm in steps of around 2000 rpm. This is done for two different nominal leakage gaps, namely 0.20 mm on the inlet and 0.25 mm on the outlet side as well as 0.3 mm on both in- and outlet side, respectively. In addition, the peak cycle temperature $T_{t,\mathrm{HPG}}$ was varied from 500 °C to 600 °C. The loop flow ratio λ is maintained constant at 1.7. In the second part of the validation study, λ is varied in steps of 0.5 between 1.7 and 2.7. The total inlet pressure remains at approximately 270 kPa throughout.

Variations in rotational speed lead to different velocity triangles at both in- and outlet. To account for these variations and associated misalignment of the flow with the rotor profiles, a parameter fit was made for the loss coefficient ζ_{loss}. The linear relationship determined from this is given in Fig. 11(*a*) and used throughout the validation study. The same procedure was applied to the leakage coefficient C_D. Here, the situation becomes more complicated, as different leakage gaps account for slightly different characteristics, as illustrated in Fig. 11(*b*). The reason for this lies most likely in the fact that actual leakage gaps are not known and merely the nominal values were taken. Hence, the selected discharge coefficient partially accounts for this lack in information. The reason why one sees a variation of the leakage coefficient with speed can be explained by additional blockage or greater dynamic head created in the leakage gap through higher rotational speeds, similar as witnessed in turbomachinery [59]. Finally, the friction multiplier was set to 2.7 throughout the simulations. A similarly high value was witnessed in the studies by Paxson and Wilson [39].

At the design speed of 32,000 rpm Fig. 12 gives the numerically determined unfolded view of both wave pattern in the left-hand side contour plot and temperature distribution in the right-hand contour plot. The plot also shows the predicted velocity profiles in each port and the extent of gradual passage opening. Marked in stations S1 and S2 are primary (right running) and secondary shock (left running) waves generated upon opening of the high pressure gas (HPG) inlet and high pressure air (HPA) outlet. Further shown are expansion fans E1 and E2 produced as a result of HPG closing and LPG opening. The temperature distribution indicates inherent exhaust gas recirculation (EGR) characteristic to axial throughflow machines as well as a small amount of fresh air exhaustion (FAE) through the exhaust port LPG.

The effect of gradual passage opening is shown in Fig. 12(*b*), where mark T1 indicates the initiation of the primary shock wave

(*a*) (*b*)

Fig. 9 (*a*) Wave rotor turbine with and without outer sleeve showing channel curvature and (*b*) machined inlet stator exhibiting discrete port openings

before progressively increases toward the fully developed level at approximately T2. The predicted instantaneous and cycle-averaged power output for a single channel is given in Fig. 12(*c*). It becomes apparent that solely the flow entering through the HPG port results in torque generation, while opening of the LPG port and inflow through LPA does not significantly contribute to overall power generation. This is of course expected as the flow through the HPG port signifies the flow with the highest enthalpy. The total expected power output is then evaluated by multiplying the number of channels with the cycle-averaged value. The plot further indicates that the proposed symmetric, arc shape is not an optimum with respect to torque generation, which is outlined by positive regions in the instantaneous power trace near opening and closure of the HPG port.

Comparing power output, pressure ratio, and outlet temperature from the HPA duct for the experimentally determined dataset with the simulation model shows the group of plots displayed in Fig. 13. The first plot on the top left denotes total pressure ratio data obtained for a maximum inlet temperature of 500 °C and a nominal clearance of 0.20 mm on the inlet and 0.25 mm on the outlet side. The model accurately predicts the total pressure distribution well across the entire speed sweep. As expected, increased leakage gaps result in compromised energy transfer and thus lower achieved pressure ratio. This trend is reflected in the model results, although there is an overprediction in pressure ratio with a relative error between experiments and simulation of around 10–15%. Furthermore, the model predicts a pronounced drop-off in pressure ratio as one approaches lower rotational speeds, which has not been witnessed in the experiments. Opposed to the validation on pure pressure exchangers of Kentfield and NASA, there is a more pronounced discrepancy between simulation results and experimental data. This can at least partly be attributed to the fact that experimental work on pressure exchangers was done at nearly ambient temperature conditions. This renders thermal expansion effects; minimal and axial clearances between stator and rotors are likely to remain unchanged from their nominal values. For the wave rotor turbine under investigation here, peak temperatures differ significantly from ambient conditions and uneven thermal expansion between rotor and stators that cause the axial clearance gap to increase in size, which severely affects in particular the secondary shock wave strength and thus the achieved pressure ratio.

Raising maximum inlet temperature from 500 °C to 600 °C results in an increase in pressure ratio as a consequence of more enthalpy being directed to the wave rotor. While the overall trend is also reflected in the simulation results, the model indicates that the increase in temperature appears to outweigh the penalty in larger leakage flow, while in the experiments this is clearly not the case. This shortcoming exemplifies the sensitivity of the system that arises when choosing model factors, thus limiting its predictive capabilities.

Table 2 Dimensions and operating conditions of the Bath μ-wave rotor

Parameter	Bath μ-wave rotor
Rotor diameter (mm)	60
Number of channels	46
Channel shape	Sym. cambered max. $\lvert\beta_{ch}\rvert = 21.5$deg
Channel length (mm)	30
Channel width (mm)	2.9
Channel height (mm)	6
Nominal clearance (mm)	Variable 0.1–0.4
Number of cycles per revolution	3
Design rotational speed (rpm)	32,000
T_{HPG} (K)	773–883 K
p_{HPG} (kPa)	270–290
p_{LPG} (kPa)	99

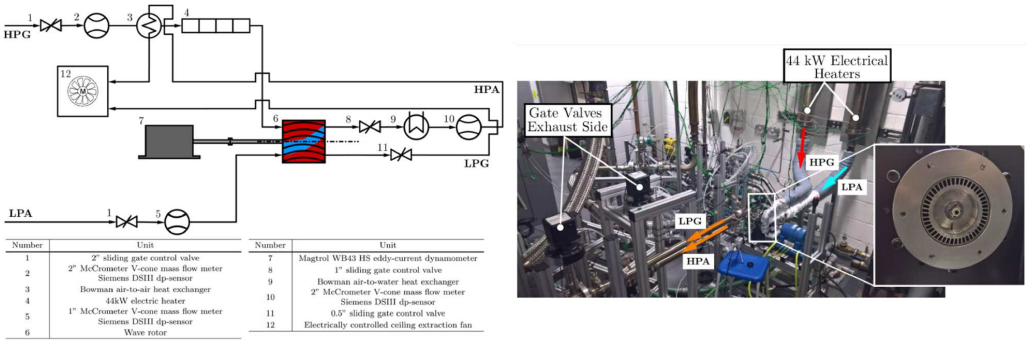

Number	Unit
1	2" sliding gate control valve
2	2" McCrometer V-cone mass flow meter Siemens DSIII dp-sensor
3	Bowman air-to-air heat exchanger
4	44kW electric heater
5	1" McCrometer V-cone mass flow meter Siemens DSIII dp-sensor
6	Wave rotor

Number	Unit
7	Magtrol WB43 HS eddy-current dynamometer
8	1" sliding gate control valve
9	Bowman air-to-water heat exchanger
10	2" McCrometer V-cone mass flow meter Siemens DSIII dp-sensor
11	0.5" sliding gate control valve
12	Electrically controlled ceiling extraction fan

(*a*) (*b*)

Fig. 10 (*a*) Schematic showing wave rotor open loop experimental setup and corresponding instrumentation. (*b*) Photograph taken from the test rig exhibiting the wave rotor, eddy-current dynamometer, electrical heaters, and outlet side gate valves.

The model yields good results with respect to predicted power output for all simulated conditions, shown in Fig. 13(*b*). Power is slightly overpredicted throughout with a relative error of around 5–10%. The power output increase shown in (b) stems from an increase in HPG mass flow rate of 34 g/s compared to 32 g/s in the low leakage case.

Finally, Fig. 13(*c*) gives a comparison of the averaged total temperature at the HPA outlet with the experimental data recorded through thermocouples close to the port outlet. Across all tested conditions, the relative error varies between 1% and 6%. While there seems to be moderate (left and right) to no (center) variation with respect to rotational speed changes, the model predicts steeper line gradients. This is a consequence of the model predictions regarding exhaust gas recirculation at the HPA port. The temperature distribution shown in Fig. 12 implies some FAE. Reducing FAE by allowing more fresh air being directed to the HPA port before the port closes. This reduces EGR rates at the HPA port and accounts for a slightly lower mixed-out temperature. This effect is well shown in Fig. 13(*a*). The simulation results in (center) and (right) almost show the same gradient with respect to speed as in the low leakage case in (left). The discrepancy between the two stems again from the effects of leakage, where increased leakage promotes interaction and flow between one channel, another channel, and the leakage cavities around it. Thus more hot air is ingested into the cold air stream leading to more or less the same average outlet temperature.

Figure 14 exhibits the effect of a variation in loop flow ratio from 1.7–2.2 and 2.7 with rotational speed. The model correctly predicts an increase in pressure ratio with increasing loop flow ratio. However, while there is a relatively small difference at a loop flow ratio of 1.7 of less than 3%, the model reacts more sensitively to an increase in loop flow ratio resulting in higher pressure ratios and increased error. Higher loop flow ratio signifies a reduced cold air mass being ingested into the wave rotor resulting in a higher average rotor temperature and thus altered thermal expansion. The Q1D-model cannot account for this change in leakage characteristic, which results in a greater error between the simulation results and the experimentally determined data.

Predicted shaft power output captures the trends of increasing power output with increasing loop flow ratio. The main mechanism for this is an increase in inlet mass flow rates to around 34 g/s at $\lambda = 2.2$ and 35.5 g/s at $\lambda = 2.7$. However, the increase indicated in the experiments is higher than shown for the simulation model, resulting at a maximum underprediction in shaft power at $\lambda = 2.7$ of approximately 8%.

Looking at the averaged temperature in the HPA port, the maximum relative error between experiments and simulations is at around 4%. The model is able to predict the effects of the decrease in fresh air flow well. Higher loop flow ratios increase EGR and thus mark a reduced effect of fresh air temperature on the mixed out average temperature. As a result, average temperatures increase as is both witnessed in the model and experiments. Furthermore, varying rotational speed has most influence on HPA outlet temperature at low loop flow ratios, where EGR rate is generally lower. At higher flow ratios, EGR rate is high and the HPA temperature less sensitive to a variation in rotational speed. This effect is recorded in the simulation results through a reduced gradient.

Conclusions and Outlook. This paper presented a numerical model that extends the previous one-dimensional codes to allow computation of torque generation in curved rotor passages through additional source terms that compute inviscid blade forces. The model was furthermore validated through both literature data and experimental data from a symmetrically cambered microwave rotor developed at the University of Bath. The main points of the paper can be summarized as follows:

- The objective of the study was to perform model validation through literature data for straight channeled pressure exchangers run at low temperature and through experimental data obtained from a symmetrically cambered microwave rotor developed at the University of Bath.
- The comparison with literature data for pressure exchangers at constant speed and inlet conditions yields good agreement for both steady and unsteady flow data. This gives confidence

Table 3 Comparison of previous wave rotors, both actually realized ones that were tested and conceptual ones (University of Tokyo/ONERA) with the Bath μ-wave rotor turbine (adapted from Ref. [6])

	Kentfield three-port PE	NASA three-port PE	NASA & R.R. Allison four-port TF	Univ. of Tokyo & ONERA micro wave rotor study	ABB Comprex four-port RF	Pearson six-port TF wave engine	Univ. of Bath four-port TF μ-wave turbine
T	0.39	0.082	0.19	0.31	0.467	0.3	0.37 at 32,000 rpm
F	0.0046	0.017	0.0037	0.012	0.0067	n.a.	0.013
G	0.0064	0.025–0.075	0.0090	0.067	0.030	n.a.	0.033–0.132

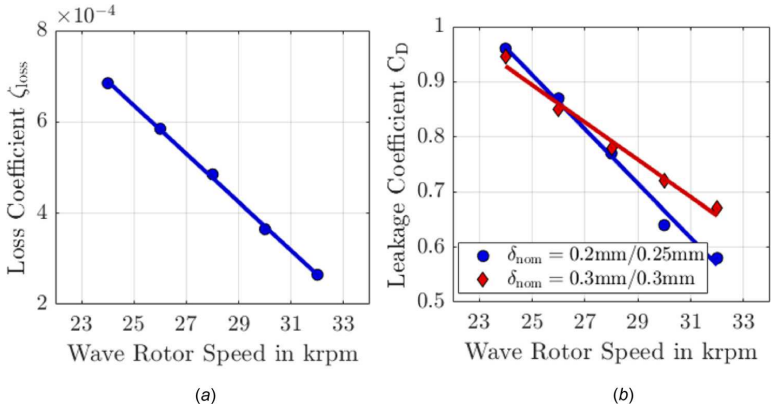

(*a*) (*b*)

Fig. 11 Parameter fit for (*a*) loss coefficient due to channel/flow misalignment and (*b*) flow leakage

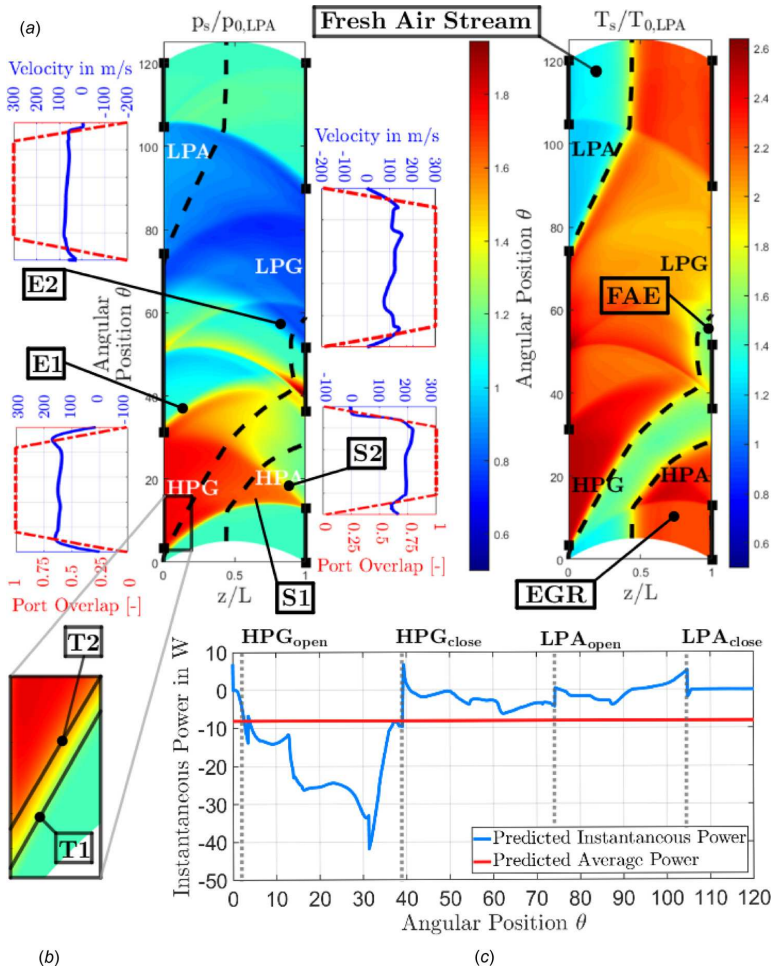

(*b*) (*c*)

Fig. 12 Q1D numerical results showing shock wave pattern, temperature field, port velocity distribution, and torque output at $\lambda = 1.7$, $N = 32{,}000$ rpm, $T_{t,\mathrm{HPG}} = 500\,^{\circ}\mathrm{C}$, and $\dot{m}_{\mathrm{HPG}} = 0.032$ kg/s

that the model is able to predict fundamental characteristics, such as wave patterns and port flow conditions. It further emphasizes the importance of loss mechanisms on the performance characteristics of wave rotors.

- A comparison of the model with sub-1 kW microwave rotor turbine data yielded promising results and showed that the model is able to identify the variation of pressure ratio and temperature with rotational speed. Predicted power output was also in very good agreement with the experimental data.

Nonetheless, a few restrictions in the model persist and can be listed as follows:

- The model appears to react more sensitively to changes in inlet temperature and leakage gap than witnessed in the experiments.
- Increases in nominal leakage lead to a larger relative error between the determined total pressure ratio for experiments and simulation. The issue is exacerbated if only the nominal, rather than the actual leakage gap for a thermally stable operating point is known rendering the determination of leakage coefficients difficult and results more deviating from experimentally determined ones.
- Power predictions are slightly overpredicted throughout, but show similar trends as in the experiments and vary only marginally with respect to changes in rotational speed. However, an additional loss factor is required to account for the (mis-)alignment of the flow at the port/rotor interface. For higher loop flow ratios, the increase in power output in the simulation results is lower

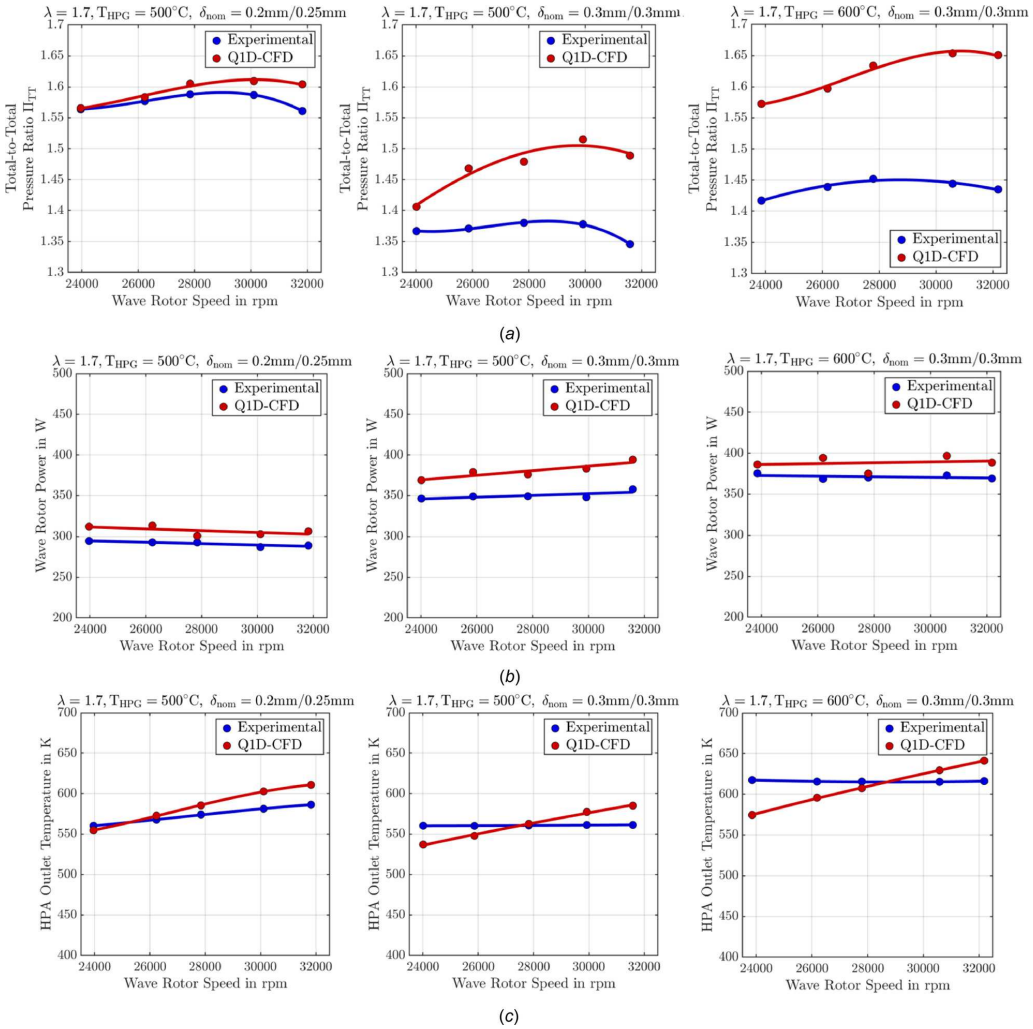

Fig. 13 Effect of leakage and peak cycle temperature variation on wave rotor performance. Comparison of experimental data and numerical model for (*a*) total-to-total pressure, (*b*) shaft power output, and (*c*) average outlet temperature in the HPA port. The graphs on the left denote data for a loop flow ratio $\lambda = 1.7$, a peak cycle temperature of 500 °C, and a nominal clearance gap of 0.2 mm on the in- and 0.25 mm on the outlet side, while graphs in the center show the effect of increased axial gap clearance to 0.3 mm and graphs on the right outline the effect of an increase in peak cycle temperature to 600 °C.

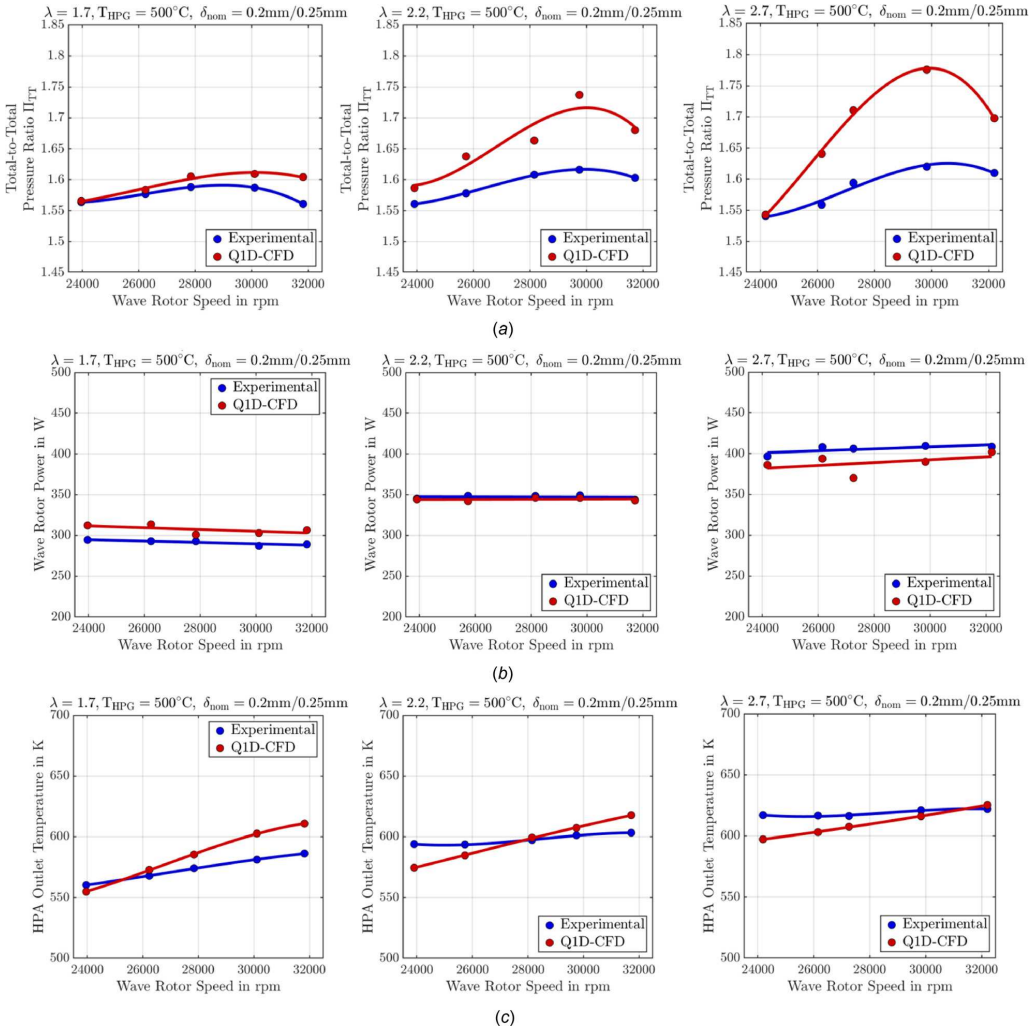

Fig. 14 Effect of loop flow ratio variation. Comparison of experimental data and numerical model for (*a*) total-to-total pressure, (*b*) shaft power output, and (*c*) average outlet temperature in the HPA port. The graphs on the left denote data for a loop flow ratio $\lambda = 1.7$, while the center plots show the results for $\lambda = 2.2$ and right-hand side graphs for $\lambda = 2.7$.

compared to the experiments, resulting in a slight underprediction for $\lambda = 2.2$.

The model is able to predict port outlet temperatures well, but fails to identify the effects larger leakage gaps incur. The effect of reduced EGR rates and thus more fresh air being directed through the HPA port appears to be more pronounced than witnessed in the experiments. Also, the ingestion of air from neighboring channels and the leakage cavity seem to become more pronounced at elevated leakage gaps, which cannot be identified by the model. However, trends showing the effect of increased loop flow ratio on the outlet temperature are captured well.

- The introduced model facilitates wave rotor turbine design process, as it provides the means to investigate both the pressure exchange capabilities of the wave rotor as well as its use as a power turbine. It can thus be used for initial sizing and as an inexpensive design tool to vary channel camber before more expensive CFD modeling tools are applied.

Acknowledgment

The authors would like to thank the Defence Science and Technology Laboratory (DSTL) for funding the project under the Defence and Security Accelerator *Beyond Battery Power* competition.

Nomenclature

a = speed of sound, m/s
A = cross-sectional area, m^2
C = absolute velocity, m/s

c_p = specific heat constant at constant pressure, J/kg K
c_v = specific heat constant at constant volume, J/kg K
C_D = leakage coefficient
C_f = friction multiplier
CFD = computational fluid dynamics
D = diameter, m
e = internal energy, J/kg
E = total energy per unit volume, J/m^3
EGR = exhaust gas recirculation
f = friction factor
F = flux vector, force per unit volume, N/m^3, nondimensional viscosity parameter
FAE = fresh air exhaustion
G = nondimensional leakage parameter in m
h = heat transfer coefficient, W/m^2 K, specific enthalpy, J/kg, channel height, m
HPA = high pressure gas
HPG = high pressure gas
k = surface roughness value, m, thermal conductivity, W/m K
LPA = low pressure air
LPG = low pressure gas
m = meridional coordinate
$\dot{m}$ = mass flow rate, kg/s
Nu = Nusselt number
p = pressure, Pa
Pr = Prandtl number
q = heat flux, W/m^2
Q = heat generation rate, W
r = radius, m
Re = Reynolds number
s = source term, specific entropy, J/kg K
t = time, s
T = temperature, K, nondimensional gradual passage opening parameter
u = velocity, m/s
U = state vector, tangential velocity, m/s
V = volume, m^3
W = relative velocity, m/s
x = spatial coordinate
α = absolute flow angle, rad, under-relaxation factor
β = relative flow angle, rad
γ = ratio of specific heats
δ = axial leakage gap, m
δz = cell size, m
ζ = loss coefficient
θ = azimuthal angle, rad
Θ = leakage function
λ = loop flow ratio
μ = dynamic viscosity, kg/m s
ρ = density, kg/m^3
τ = shear stress, N/m^2, time constant, s
ω = angular velocity, m/s

References

[1] Wilson, J., and Paxson, D. E., 1993, "Jet Engine Performance Enhancement Through Use of a Wave-Rotor Topping Cycle," NASA Memorandum No. 4486.
[2] E., Zauner, Y.-P., Chyou, F. W., and Althaus, R., 1993, "Gas Turbine Topping Stage Based on Energy Exchangers: Process and Performance," ASME Paper No. 93-GT-058.
[3] Snyder, P. H., and Fish, R. E., 1996, "Assessment of a Wave Rotor Topped Demonstrator Gas Turbine Engine Concepts," ASME Paper No. 96-GT-041.
[4] Welch, G. E., 1997, "Wave Engine Topping Cycle Assessment," AIAA Paper No. AIAA-97-0707.
[5] Welch, G. E., Jones, S. M., and Paxson, D. E., 1997, "Wave-Rotor-Enhanced Gas Turbine Engines," ASME J. Eng. Gas Turbines Power, **119**(2), pp. 469–477.
[6] Nagashima, T., Okamoto, K., and Ribaud, Y., 2005, "Cycles and Thermal System Integration Issues of Ultra-Micro Gas Turbines," RTO, Neuilly-sur-Seine, France, Educational Notes RTO-EN-AVT-131.
[7] Akbari, P., Nalim, R., and Müller, N., 2006, "Performance Enhancement of Microturbine Engines Topped With Wave Rotors," ASME J. Eng. Gas Turbines Power, **128**(1), pp. 190–202.
[8] Lenoble, G., and Ogaji, S., 2010, "Performance Analysis and Optimization of a Gas Turbine Cycle Integrated With an Internal Combustion Wave Rotor," Proc. Inst. Mech. Eng., Part A, **224**(7), pp. 889–900.
[9] Guzzella, L., Wenger, U., and Martin, R., 2000, "IC-Engine Downsizing and Pressure-Wave Supercharing for Fuel Economy," SAE Paper No. 2000-01-1019.
[10] Oguri, Y., Suzuki, T., Yoshida, M., and Cho, M., 2001, "Research on Adaption of Pressure Wave Supercharger (PWS) to Gasoline Engine," SAE Paper No. 2004-01-0368.
[11] Weber, F., Guzzella, L., and Onder, C., 2002, "Modelling of a Pressure Wave Supercharger Including External Exhaust Gas Recirculation," Proc. Inst. Mech. Eng., Part D, **216**(3), pp. 217–235.
[12] Suzuki, T., Oguri, Y., K, U., and Yoshida, M., 2004, "Experimental Investigation of Pressure Wave Supercharging for SI Engine," ASME Paper No. IMECE2004-62419.
[13] Spring, P., Onder, C. H., and Guzzella, L., 2007, "EGR Control of Pressure-Wave Supercharger IC Engines," Control Eng. Pract., **15**(12), pp. 1520–1532.
[14] Yan, L., Dasen, Z., Hongguang, Z., Changwei, J., Jiangguo, L., and Tong, Z., 2008, "Experiment and CFD Investigation of Pressure-Wave Supercharger," SAE Paper No. 2008-01-1631.
[15] Pohořelský, L., Macek, J., Polášek, M., and Vítek, O., 2004, "Simulation of a COMPREX Pressure Exchanger in a 1-D Code," SAE Paper No. 2004-01-1000.
[16] Lei, Y., Zhou, D. S., and Zhang, H. G., 2010, "Investigation on Performance of a Compression-Ignition Engine With Pressure-Wave Supercharger," Energy, **35**(1), pp. 85–93.
[17] Zhao, J., and Hu, D., 2017, "An Improved Wave Rotor Refrigerator Using an Outside Gas Flow for Recycling the Expansion Work," Shock Waves, **27**(2), pp. 325–332.
[18] Hu, D., Li, R., Liu, P., and Zhao, J., 2016, "The Loss in Charge Process and Effects on Performance of Wave Rotor Refrigerator," Int. J. Heat Mass Transfer, **100**, pp. 497–507.
[19] Hu, D., Li, R., Liu, P., and Zhao, J., 2016, "The Design and Influence of Port Arrangement on an Improved Wave Rotor Refrigerator Performance," Appl. Therm. Eng., **107**, pp. 207–217.
[20] Pekkan, K., and Nalim, M. R., 2003, "Two-Dimensional Flow and NO_x Emissions in Deflagrative Internal Combustion Wave Rotor Configurations," ASME J. Eng. Gas Turbines Power, **125**(3), pp. 720–730.
[21] Nalim, M. R., Izzy, Z. A., and Akbari, P., 2012, "Rotary Wave-Ejector Enhanced Pulse Detonation Engine," Shock Waves, **22**(1), pp. 23–38.
[22] M. Rajagopal, A. K., and Nalim, R., 2012, "Wave-Rotor Pressure-Gain Combustion Analysis for Power Generation and Gas Turbine Applications," ASME Paper No. GTINDIA2012-9741.
[23] Pearson, R. D., 1985, "A Gas Wave-Turbine Engine Which Developed 35 HP and Performed Over a 6:1 Speed Ranges," ONR/NAVAIR Wave Rotor Research and Technology Workshop.
[24] Pearson, R. D., 1986, "Thermodynamics and Gas Dynamics of Internal Combustion Engines, Volume II," *The Oxford Handbook of Innovation*, D. E. Winterbone, and S. C. Low, ed., Oxford University Press, Oxford, UK.
[25] Mathur, A., 1985, "Design and Experimental Verification of Wave Rotor Cycles," ONR/NAVAIR Wave Rotor Research and Technology Workshop.
[26] R., Taussig, P., Cassady, J. Z. W. T., and Klostermannt, E., 1983, "Investigation of Wave Rotor Turbofans for Cruise Missile Engines," Final Report Submitted by MSNW to DARPA (Contract N00140-82-C-9729).
[27] Weber, H. E., 1996, *Shock Wave Engine Design*, Wiley, New York.
[28] Mathur, A., and Shreeve, R. P., 1987, "Calculation of Unsteady Flow Processes in Wave Rotors," AIAA Paper No. 87–0011.
[29] Mathur, A., 1986, "Code Development for TurbofanEngine Cycle Performance With and Without a Wave Rotor Component," Naval Postgraduate School, Monterey, CA, Report No. NPS67-86-006CR.
[30] Roberts, J. W., 1990, "Further Calculations of the Performance of Turbofan Engines Incorporating a Wave Rotor," M.S. thesis, Naval Postgraduate School, Monterey, CA.
[31] Salacka, T. F., 1985, "Review, Implementation and Test of the QAZID Computational Method With a View to Wave Rotor Applications," M.S. thesis, Naval Postgraduate School, Monterey, CA.
[32] Johnston, D. T., 1987, "Further Development of a One-Dimensional Unsteady Euler Code for Wave Rotor Applications," M.S. thesis, Naval Postgraduate School, Monterey, CA.
[33] Okamoto, K., and Nagashima, T., 2003, "A Simple Numerical Approach of Micro Wave Rotor Gasdynamic Design," 16th International Symposium on Airbreathing Engines, Cleveland, OH, Aug. 31–Sept. 5, Paper No. ISABE-2003-1213.
[34] Okamoto, K., Nagashima, T., and Yamaguchi, K., 2003, "Introductory Investigation of Micro Wave Rotor," International Gas Turbine Congress 2003, Tokyo, Japan.
[35] Fatsis, A., Lafond, A., and Ribaud, Y., 1998, "Preliminary Analysis of the Flow Inside a Three-Port Wave Rotor by Means of a Numerical Models," Aerosp. Sci. Technol., **2**(5), pp. 289–300.
[36] Fatsis, A., Orfanoudakis, N. G., Pavlou, D. G., Panoutsopoulou, A., and Vlachakis, N., 2006, "Unsteady Flow Modelling of a Pressure Wave Supercharger," Proc. Inst. Mech. Eng. Part D, **220**(2), pp. 209–218.
[37] Iancu, F., Piechna, J., and Müller, N., 2005, "Numerical Solutions for Ultra-Micro Wave Rotors (UμWR)," AIAA Paper No. 2005-5034.
[38] Paxson, D. E., 1992, "A General Numerical Model for Wave Rotor Analysis," NASA Lewis Research Center, Cleveland, OH, Report No. NASA-TM-105740.
[39] Paxson, D., and Wilson, J., 1993, "An Improved Numerical Model for Wave Rotor Design and Analysis," AIAA Paper No. 93–0482.

[40] Paxson, D. E., and Wilson, J., 1995, "Recent Improvements to and Validation of the One Dimensional NASA Wave Rotor Model," NASA Lewis Research Center, Cleveland, OH, Report No. NASA-TM-106913.
[41] Paxson, D. E., 1995, "A Numerical Model for Dynamic Wave Rotor Analysis," AIAA Paper No. 95–2800.
[42] Welch, G. E., and Paxson, D. E., 1998, "Wave Turbine Analysis Tool Development," NASA Lewis Research Center, Cleveland, OH, Report No. NASA/TM–1998-208485.
[43] Chan, S., and Liu, H., 2017, "Mass-Based Design and Optimization of Wave Rotors for Gas Turbine Engine Enhancement," Shock Waves, **27**(2), pp. 313–324.
[44] Chan, S., Liu, H., Xing, F., and Song, H., 2018, "Wave Rotor Design Method With Three Steps Including Experimental Validation," ASME J. Eng. Gas Turbines Power, **140**(11), p. 111201.
[45] Mustafa, A., Martinez-Botas, R. F., Pesiridis, A., Chiong, M. S., and Rajoo, S., 2014, "Assessment of Turbocharger Turbine Unsteady Flow Modelling Methodology on Engine Performance," ASME Paper No. ESDA2014-20392.
[46] Costall, A., 2007, "A One-Dimensional Study of Unsteady Wave Propagation in Turbocharger Turbine," Ph.D. thesis, Imperial College London, London.
[47] Kentfield, J. A. C., 1969, "The Performance of Pressure-Exchanger Dividers and Equalizers," ASME J. Basic Eng., **91**(3), pp. 361–369.
[48] Wilson, J., and Fronek, D., 1993, "Initial Results From the NASA-Lewis Wave Rotor Experiment," AIAA Paper No. 93–2521.
[49] Witte, D. W., Tatum, K., and Williams, S. B., 1996, "Computation of Thermally Perfect Compressible Flow Properties," AIAA Paper No. 96-0681.
[50] Smith, G. P., Golden, D. M., Frenklach, M., Moriarty, N. W., Eiteneer, B., Goldenberg, M., Bowman, C. T., Hanson, R. K., Song, S., Gardiner, W. C., Jr., Lissianski, V. V., and Qin, Z., 2019, "GRI-Mech 3.0," The Gas Research Institute, accessed July 30, 2019, http://www.me.berkeley.edu/grimech/
[51] Martin, C. R., 2010, "HOT: Thermodynamic Tools for Matlab," Virginia Active Combustion Control Group, accessed July 29, 2019, http://hot-tdb.sourceforge.net/
[52] Winterbone, D. E., and Pearson, R. J., 2000, *Theory of Engine Manifold Design: Wave Action Methods for IC Engines*, Professional Engineering Publishing Limited, London.
[53] Kentfield, J. A. C., 1993, *Nonsteady, One-Dimensional, Internal, Compressible Flows*, Oxford Engineering Sciences, Oxford, UK.
[54] Kuzay, T. M., and Scott, C. J., 1977, "Turbulent Heat Transfer Studies in Annulus With Inner Cylinder Rotation," ASME J. Heat Transfer, **99**(1), pp. 12–19.
[55] Larosiliere, L. M., 1993, "Three-Dimensional Numerical Simulation of Gradual Opening in a Wave Rotor Passage," AIAA Paper No. 93–2526.
[56] Akbari, P., and Müller, N., 2003, "Preliminary Design Procedure for Gas Turbine Topping Reverse-Flow Wave Rotors," International Gas Turbine Congress, Tokyo, Japan.
[57] Akbari, P., and Müller, N., 2003, "Gas Dynamic Design Analyses of Charging Zone for Reverse-Flow Pressure Wave Superchargers," ASME Paper No. ICES2003-0690.
[58] Iancu, F., Piechna, J., and Müller, N., 2008, "Basic Design Scheme for Wave Rotors," Shock Waves, **18**(5), pp. 365–378.
[59] Denton, J. D., 1993, "Loss Mechanisms in Turbomachines," ASME J. Turbomach., **115**(4), pp. 621–656.

Errata Paper III

The references Figure 13(a) on page 021017-10 should refer to Figure 13(c).

Addendum to Paper III

It shall be noted that the azimuth angle in Figure 8 (page 106) is given in radians, while Figure 12 (page 109) is given in degrees. In addition, the data in Figure 8 stems from a single-cycle pressure divider, which accounts for an azimuth range from 0 to 360°. The wave rotor turbine, however, features three cycles per revolution, which reduces the range of a single cycle down to 0 to 120°.

3.3.1 Summary and Implications of Paper III

The article in Section 3.3 builds on the quasi-one-dimensional model presented in Chapter 1.5 and aims to provide a comprehensive validation study, which takes place in three steps. To begin with, the study correlates literature data reported by Kentfield [16, 17] originating from three-port pressure divider experiments. These experiments were focused on the steady-state conditions of pressure and temperature in the ports. In addition, the pressure divider was operated at ambient temperatures, so that one can expect nominal leakage gaps to remain unchanged. In combination with straight channels and thus negligible inviscid blade force terms, the data provide an excellent starting point for validation of the steady-state behaviour yielding excellent agreement. The experimental data produced by and Wilson et al. [108] at NASA on another low-temperature, three-port pressure divider expands on this by directly correlating the predicted shock pattern within the channels with experimental data. Again, the model reflects the physics within the channels well. As a result, the first two steps in the validation give sufficient fidelity in the model to accurately predict wave rotor physics.

In the final stage, two additional aspects are added, namely high temperature coupled with greater uncertainty in leakage and non-axial channel shapes. The increase in temperature alone does not appear to introduce a significant detriment in the predictive capabilities of the model. However, increases in leakage - be it through a consciously set large axial gap or due to uneven thermal expansion of stators and the rotor-shaft assembly - reveal the limitations of the modelling approach for one-dimensional wave rotor codes. On the one hand, the increase in leakage promotes interaction of the channels with the leakage cavity and neighbouring channels, resulting in significantly attenuated secondary shock waves and reduced pressure ratios. As wave rotor shaft power appears to be predominantly generated by the momentum change

as the flow follows the channel contour, the numerically predicted shaft power shows good agreement with the experimentally determined ones.

The numerical model uses a number of multipliers and parameters for friction, leakage and entropy losses, which pose a certain limitation with respect to its predictive capabilities. While friction and leakage can be expected to remain constant for geometries of similar channel shape and axial leakage gap respectively, this pertains in particular to the way power generation is modelled. This assumes that the flow follows the camberline contour exactly and is modelled to be orthogonal to the relative flow direction. Deviations from this produce no useful work and account for entropy generation, which is included through an entropy-based loss term. Traditionally, such loss terms require additional information through 3D CFD simulations or empirical correlations, both of which are not available for an extensive optimisation study. As further elaborated in the following chapter, a compromise is to perform such an aerodynamic shape optimisation using a reduced order quasi-two-dimensional model.

Chapter 4

Numerical Optimisation and Experimental Validation of Non-Axial Wave Rotor Turbines

4.1 Content Overview and Thesis Context

This chapter comprises of one manuscript under review and a published journal article. The first paper given in Section 4.2 introduces a numerical optimisation of the baseline wave rotor using a reduced order CFD model. A quasi-two-dimensional CFD model of the baseline wave rotor and stator ports was developed in Ansys Fluent and the rotor camberline geometry were parameterised using a Bézier curve with four control points. In addition, the number of channels and channel wall thickness are included in the scope of variables, resulting in a total number of six parameters.

The CFD model was coupled with a hybrid genetic algorithm (HGA) optimisation routine that combines a standard elitist GA with a Kriging-surrogate model. The objective function targets maximum power output with an additional constraint for pressure ratio. Prior to execution, the HGA was validated against a number of multimodal, non-convex mathematical test functions to estimate its performance and capabilities in detecting a global optimum among numerous local minima against standard elitist genetic algorithms (GA) and particle swarm optimisations (PSO). In addition, the model has been compared against a surrogate based optimisation library, termed MATSuMoTo. Both the HGA and MATSuMoTo are applied to the wave rotor optimisation problem. Subsequently, a detailed three-dimensional CFD analysis is conducted to a) investigate the fidelity of the quasi-two-dimensional approach and b)

shed light on the effects of the change in camberline shape to the internal gas dynamics and loss characteristics.

The second journal article in section 4.3 continues the analysis by performing an experimental and numerical back-to-back comparison of the baseline and optimised wave rotor geometry. The experimental setup follows the same open-loop layout as outlined in section 3.2. The study seeks to confirm the findings of the numerical optimisation. On the other hand, the investigation attempts to examine the behaviour of internal recirculation of exhaust gases as inlet mass flow rates are varied. Firstly, this is done qualitatively via experimental means through a number of temperature probes near the HPA outlet. Secondly, the quasi-one-dimensional model is used to obtain estimated data for EGR and FAE rates. The requirement for accurate EGR and FAE rates for a correct determination of rotor efficiency is discussed as well.

4.2 Paper IV: Numerical Optimisation of a Micro-Wave Rotor Turbine using a Quasi-Two-Dimensional CFD Model and a Hybrid Algorithm

Paper submitted to *Shock Waves* and under review at the time of writing.

Statement of Authorship

S. Tüchler (candidate): development and implementation of numerical optimisation and optimisation algorithm, data analysis, preparation of tables and figures, writing and compilation of manuscript.

C.D. Copeland (supervisor): supervision of numerical modelling work, review and editing of manuscript.

Shock Waves manuscript No.
(will be inserted by the editor)

Numerical optimisation of a micro-wave rotor turbine using a quasi-two-dimensional CFD model and a hybrid algorithm

Stefan Tüchler · Colin D. Copeland

Received: date / Accepted: date

Abstract Wave rotors are unsteady flow machines that exchange energy through pressure waves. This has the potential to enhance efficiency over a wide spectrum of applications, ranging from gas turbine topping cycles to pressure-gain combustors.

This paper introduces an aerodynamic shape optimisation of a power generating non-axial micro-wave rotor turbine and seeks to enhance the shaft power output while preserving the wave rotor's capacity to function as a pressure-exchanging device. The optimisation considers six parameters including rotor shape profile, wall thickness and number of channels and is done using a hybrid genetic algorithm that couples an evolutionary algorithm with a surrogate model. The underlying numerical model is based on a transient, reduced order, quasi-two dimensional computational fluid dynamics (CFD) model at a fixed operating condition.

The numerical results from the quasi-two-dimensional optimisation indicate that the best candidate design increases shaft power by a factor of 1.78 and imply a trade-off relationship between torque generation and pressure exchange capabilities. Further evaluation of the optimised design using three-dimensional CFD confirm the increase in power output at the cost of increased entropy production. It is further disclosed that increased incidence losses during the initial opening of the channel to the high pressure inlet duct compromise the shock strength of the primary shock wave and account for the decrease in pressure ratio. Finally, the numerical trends are validated using experimental data.

Keywords Shock Waves · Pressure Exchange · Wave Rotor · Optimisation · Hybrid Algorithm · CFD

List of Symbols

Stefan Tüchler
Institute for Advanced Automotive Propulsion Systems
Department of Mechanical Engineering
University of Bath
Bath, United Kingdom
E-mail: S.Tuechler@bath.ac.uk

Colin D. Copeland
Faculty of Applied Sciences
School of Sustainable Energy Engineering
Simon Fraser University
Vancouver, Canada
E-mail: ccopelan@sfu.ca

Variables

β	Blade angle [°], regression coefficient, search pattern
δ	Axial leakage gap [m]
η	Efficiency [-]
γ	Ratio of specific heats [-]
λ	Loop flow ratio [-]
$\dot{m}$	Mass flow rate [kg/s]
$\dot{Q}$	Heat release rate [W]
$\dot{S}$	Entropy generation rate per unit volume [W/(K·m^3)]
$\hat{f}$	Auxiliary function
μ	Dynamic viscosity [kg/m-s], Deterministic term
ν	Kinematic viscosity [m^2/s]
Ω	Design space, azimuthal position [m]
ω	Angular speed [rad/s], specific turbulence dissipation rate [1/s]
Π	Pressure ratio [-]
Ψ	EGR rate [-]
θ	Angular coordinate [rad]
ε	Turbulent dissipation rate [m^2/s^3]
c_p	Specific heat capacity at constant pressure [J/(kg·K)]
w	Channel width [m]
a	Speed of sound [m/s]
D	Diameter [m]
F	Friction parameter
f	Objective function
G	Leakage parameter
g,ĝ	Constraint function
h	Channel height [m]
L	Length [m]
N	Rotational speed [rpm], Number of channels
n	Number of cycles per revolution
P	Power [W]
Pr	Prandtl number
T	Temperature [K], finite passage opening parameter
t	time [s], thickness [m]
U	Tangential velocity [m/s]
u,v,w	Velocity
V	Volume [m^3]
x	Design parameters
x,y,z	Cartesian coordinates
y	Basis function
Z	Stochastic term

Sub- and Superscripts

θ	Azimuth
0	Start of simulation time
BL	Baseline
c	Cold
ch	Channel
cyc	Cycles per revolution
end	End of simulation time
h	Hot
p	Penetration

s Static
t Total, target
TT Total-to-total

Abbreviations

CAD Computer-aided design
CFD Computational fluid dynamics
DE Differential evolution
EGR Exhaust gas recirculation
FAE Fresh air exhaustion
GA Genetic algorithm
HPA High pressure air
HPG High pressure gas
lb Lower bound
LPA Low pressure air
LPG Low pressure gas
MRF Moving reference frame
MUSCL Monotone upwind scheme for conservation laws
OF Objective function
PSO Particle swarm optimisation
RANS Reynolds averaged Navier-Stokes
RBF Radial basis function
SST Shear stress transport
TF Throughflow
ub Upper bound
UDF User defined function

1 Introduction

1.1 Operating Principles and Characteristics

A wave rotor dynamically exchanges energy between gas streams of high enthalpy with gas flows of low enthalpy through means of shock and expansion waves. Opposed to turbomachinery, where the energy is transferred aerodynamically, wave rotors pressurise through wave action. Shock wave compression features high efficiencies and can take place over small volume making pressure exchange machinery particularly attractive for small scale power applications. The geometry of a wave rotor does not feature any complex surfaces and comprises simple channel shapes. Due to the presence of both the hot expanded gas stream and the cold air stream within the same machinery, the rotor is inherently self-cooled and the material temperature remains below the peak cycle temperature.

Several layouts of wave rotors have been introduced ranging from radial [1,2], non-axial [3–6], axial [7] and from throughflow [8], where the fluid predominantly flows in one direction only, to reverse flow models [9]. In addition, depending on the type of application the number of ports per cycle can vary between two-port [10], three-port [11], four-port [12], five-port [13] and nine-port[14]. The present paper is dedicated to a throughflow, four-port configuration with non-axial channel shape. In such a design, the wave rotor consists of a cylindrical drum with cambered channels arranged around the circumference. The rotor is located in between two stator end plates, which house discrete manifold openings. An example of such a wave rotor with curved channels is given in Figure 1. The basic principle of wave rotors revolves around energy exchange through shock and rarefaction waves. In the example design of Figure 1 it is the aim of using wave action to transfer energy from the high pressure inlet (HPG) to pressurise the low pressure charge induced via the low pressure air (LPA) duct. When rotating about its axis, the rotor channels are periodically and

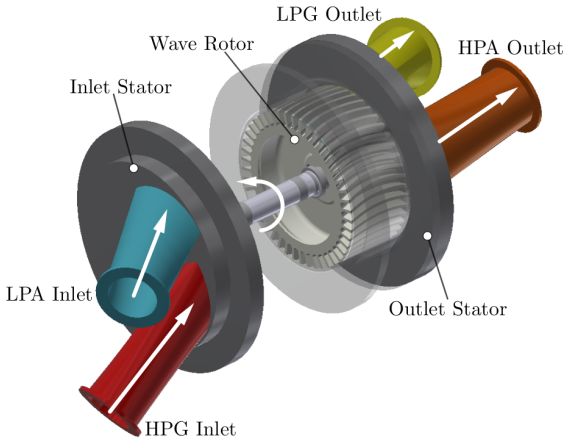

Fig. 1: Principal wave rotor components of a four-port device consisting of wave rotor with arranged circumstantially and flanked to each side by in- and outlet stator endplates.

almost instantaneously subjected to the pressure and temperature in the manifolds. This sparks the generation of shock and expansion waves. In addition, cambered wall profiles in combination with angled port manifolds introduce momentum change and enable the wave rotor to be applied as both a pressure exchange device and a power turbine.

The main arrangement of manifolds for a four-port throughflow device is shown in the schematic of Figure 2(a). Heat addition may take place using a steady-flow combustor as done in gas turbines or an internal combustion engine. The ducts comprise of a high pressure in- and out as well as a low pressure in- and outlet. To examine the behaviour within the channels during operating, it is helpful to follow a single channel as it rotates around the circumference and unfold its path on to a two-dimensional θ-z-plane, as done in Figure 2(b). This essentially allows to determine the distribution and location of shock and expansion fans as well as the distribution of hot and cold gas streams. The arrangement of ports needs to be carefully timed with the arrival of shock and expansion waves in order to maximise the strength of shock waves, limit attenuation and reduce backflow of gas from the channels into the inlet ducts.

Initially, air enters the wave rotor at low pressure and temperature through the low pressure air (LPA) at station 1. Compression of this low pressure charge air is achieved via three shock waves (S1, S2, S3). The two strongest compression waves (S1, S2) are generated at the bottom of Fig. 2(b) when the the channels are exposed to the outlet from the combustor, namely the high pressure gas (HPG, station 3). Prior to this, the gas within the channels are at pressures close to ambient. However, as soon as the channel is exposed to the high pressure conditions prevalent within the HPG port (station 3), a primary, right travelling shock wave (S1) is triggered. As soon as S1 reaches the right hand side end of the channel, the high pressure air (HPA) outlet is opened and the shock wave is reflected resulting in a secondary, left running shock wave (S2). Primary and secondary shock wave essentially exchange energy from the high pressure gas coming from the combustor to the low pressure charge air before it exits the wave rotor at an elevated pressure level through the HPA duct (station 2).

Closing the HPG port as soon as the secondary shock wave impinges on the inlet side, effectively stops the flow and inhibits spillage of gas back from the channel into the duct. In addition, port closure initiates an expansion or rarefaction wave (R1). This, in combination with an additional expansion fan (R2) that is generated upon exposing the channels to the LPG duct, gradually expands the hot exhaust gases towards the LPG port. Compared with a traditional gas turbine

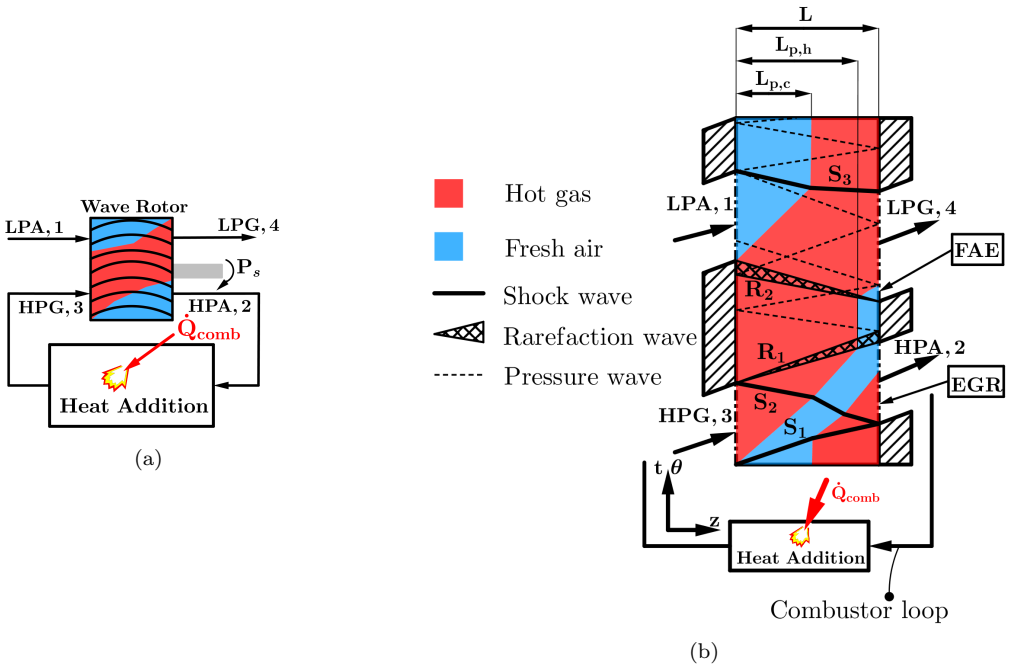

Fig. 2: (a) Schematic of wave rotor turbine arrangement within a gas turbine as one possible application for wave rotor turbines. The concept features a four-port throughflow wave rotor with cambered channels for shaft power extraction and is connected to a combustor through the high pressure zone (HPG-HPA) (b) Unwrapped view of the wave rotor in the θ-z plane outlining distribution and location of shock and expansion waves.

arrangement, rarefaction waves R1 and R2 effectively represent the function of a turbine. Finally, a weaker shock wave (S3) is the result of closure of the low pressure gas (LPG, station 4) port.

The ratio of inlet mass flow rates between HPG and LPA, termed loop flow ratio ($\lambda = \dot{m}_{\mathrm{HPG}}/\dot{m}_{\mathrm{LPA}}$), mainly governs scavenging of the ports of hot exhaust gases and thus the cold flow penetration length $L_{p,c}$. In general, λ will be greater than unity and $L_{p,c}<L$, which results in a certain amount of exhaust gas recirculation (EGR) being looped back to the combustor inlet. Furthermore, if the hot gas penetration length $L_{p,h}$ does not suffice to push the fresh charge air towards the HPA outlet, fresh air exhaustion (FAE) takes place and some of the compressed air gets expelled unused.

1.2 Literature Survey

Wave action devices have been subject to interest from a variety of research institutions. Earlier investigations started by the Brown Boveri Company in the 1940s sought to apply wave rotors as a topping device in gas turbines aiming at increasing system efficiency [15]. The concept has been further developed by Rolls Royce [16–18], ONERA [19,20] and NASA [21–23]. In addition to gas turbines, wave rotors have successfully been applied as pressure wave superchargers to both light and heavy duty internal combustion engines [24,25,16,26]. Recent research studies have taken up the concept and applied wave rotor technology to refrigeration cycles [27–29] and pressure-gain combustion [30–32,10,33]. Wave rotors characterised by a non-axial channel shape to extract shaft power while operating as a pressure-exchange device have first been used in a gas turbine arrange-

ment by Pearson [34]. The device achieved a power output of approximately 26 kW with a thermal efficiency of 10 %. The wave rotor unit comprised helically shaped passages and angled port ducts to maximise momentum transfer. Recently, Michigan State University and Warsaw University of Technology have developed a wave-disk engine concept housing a radial wave rotor unit with curved channels yielding thermal efficiencies of up to 10% [35].

Early wave rotor studies resorted to graphical methods, such as the method of characteristics, to design and analyse the compressible wave action within wave rotors. With the advent of computational fluid dynamics (CFD) and rising computational power elaborate one- and two-dimensional codes have been developed in order to examine wave rotor designs with greater accuracy, such as done by Paxson at NASA Glenn Resarch Center for axial wave rotors [36–40]. The model includes source terms to account for leakage, wall friction and accounts for finite passage opening effects through modification of the boundary conditions. The code was further used to examine the dynamic behaviour [41], area variation effects [42] and was further extended to account for channel curvature through a passage averaged approach [40]. Further one-dimensional codes were developed at the Mathematical Science Northwest Inc. [43], ONERA [19,20] and the Warsaw University of Technology in both one and two dimensions [44,45].

Compared to the number of one and two-dimensional studies, there are relatively few three-dimensional simulation studies available in the open literature. This is based on the fact that they are by far more resource intensive. Piechna et al. [46] compared the results of two-dimensional with three-dimensional results and found - besides a highly skewed contact surface - that centripetal and Coriolis accelerations cause a distortion of moving shock waves.

There has been no attempt in the open literature to optimise the wave rotor shape in order to maximise performance. The requirement to examine a sufficiently large number of design candidates is exacerbated by the need for transient CFD simulations for the evolution of moving shock and expansion waves. A quasi-steady approach using a moving frame of reference (MRF) is not feasible. This paper, for the first time to the author's knowledge, thus seeks to introduce a reduced order CFD model used to optimise the channel shape of an axial, throughflow wave rotor turbine. To reduce the computational cost, a hybridised genetic algorithm (GA) with a systematic design space exploration and exploitation strategy was used. The study will demonstrate that the reduced order model in combination with the hybrid optimisation method can efficiently and swiftly deliver an optimised wave rotor shape and reproduce the trends witnessed in experiments and higher order three-dimensional CFD. The structure of the paper is thus as follows: Section 2.1 introduces the baseline wave rotor model and compares its design with other existing wave rotor models. Section 2.2 presents the scope of the optimisation study and the main principles of the hybrid algorithm, followed by the numerical setup and domain discretisation for the quasi two-dimensional model along with results from the mesh and numerics sensitivity study. In Section 2.2 the numerical setup of the three-dimensional CFD model is given, while Section 2.4 gives a brief overview of the experimental layout. The results of the optimisation study are discussed in Section 3.1, which are further discussed by a loss and gas dynamic analysis using 3D-CFD. Finally, the trends witnessed in the numerical models are compared to experimental data.

2 Methodology

2.1 Baseline Wave Rotor

The wave rotor turbine forming the basis for this study and used as a baseline model for the optimisation has been extensively experimentally tested [47] and used for Q1D validation [6]. The prototype features symmetrically cambered wall profiles, following the shape of a parabola. A computer-aided design (CAD) image of the the baseline model is shown in Figure 3 illustrating the curved wall profile with further details on the geometric dimensions of the rotor given in Table 1.

Fig. 3: Baseline geometry with symmetrically cambered channels.

Table 1: Geometric dimensions of baseline wave rotor turbine.

Parameter	Unit	Value
Rotor diameter	mm	60
Number of channels		46
Channel shape		sym. cambered max. $\lvert\beta_{ch}\rvert = 21.5°$
Channel length	mm	30
Channel width	mm	2.9
Channel height	mm	6
Nominal clearance	mm	0.3
Number of cycles per revolution		3
Design rotational speed	rpm	32,000

In order to compare different wave rotor designs one can employ the relations developed by Wilson and Fronek [48] and Nagashima et al. [49], who defined non-dimensional parameters for finite passage opening T, viscosity F and leakage flow G. These are given as

$$\begin{aligned} T &= \frac{wa}{UL} \\ F &= \frac{\sqrt{\nu L/a}}{D_h} \\ G &= \frac{2\delta}{h} \end{aligned} \tag{1}$$

and tabulated in Table 2 along with geometric dimensions and rotational speed. Although most of the listed proponents are designed to be used purely for pressure exchange and were tested at relatively low temperatures, it becomes apparent the baseline model in this study features similar characteristics in terms of friction and finite opening timing effects. Leakage in the present model is variable and comparable to ABB's Comprex and the University of Tokyo's design. It is noteworthy that the figure holds only for cold conditions. In reality, however, thermal expansion will alter the figure. Compared with previous designs, the presented baseline model is considerably smaller in diameter, length and channel height. Nonetheless, in terms of mean tip speed the rotor is within comparable range.

2.2 Optimisation Campaign

2.2.1 Wave Rotor Optimisation

The optimisation seeks to achieve increased torque generation through modifications to the wall camber profile. This approach maintains the inlet- and outlet stator port solution, as well as channel/port height and the overall length of the rotor. In addition, the number of design parameters is reduced as well with benefits regarding computational effort, albeit at the cost of limiting its capacity for exploitation. With respect to experimental validation, it further ensures that same stator end plates can be employed and merely the rotor itself needs to be replaced rather then the entire wave rotor assembly for back-to-back comparisons.

To facilitate automatised geometry updates the wall camber profiles are approximated via Bézier curves with five control points giving full control over the contour shape, as given in Figure 4. Additional parameters are the number of channels, which, in combination with channel width, dictate the wall thickness t_w. Therefore, the optimisation deals with six design parameters in total. Lower

Table 2: Comparison of previous wave rotors, both actually realised ones that were tested and conceptual ones (University of Tokyo/ONERA) with wave rotor model used in this study (adapted from [49]).

	Kentfield 3-port PE	NASA 3-port PE	NASA & R.R.Allison 4-port TF	University of Tokyo & ONERA	ABB Comprex 4-port RF	University of Bath Baseline
T	0.39	0.082	0.19	0.31	0.467	0.37
F	0.0046	0.017	0.0037	0.012	0.0067	0.013
G	0.0064	0.025-0.075	0.0090	0.067	0.030	0.033 - 0.132
Diameter [mm]	148	300	163	46.5	93	60
Length [mm]	280	460	152	69	90	30
Cell height [mm]	55.9	10.2	8.8	3	10	6
Rotational speed [rpm]	6000	4000	16,800	32,000	14,000	32,000
U_θ [m/s]	46.5	62.8	143.4	77.9	68.2	100.5

and upper bounds to each of the parameters then establishes the design space and constrains the optimisation. The first control point is located at the leading edge and remains fixed. The subsequent control points are fixed with respect to the horizontal location, but are allowed to move in azimuthal direction.

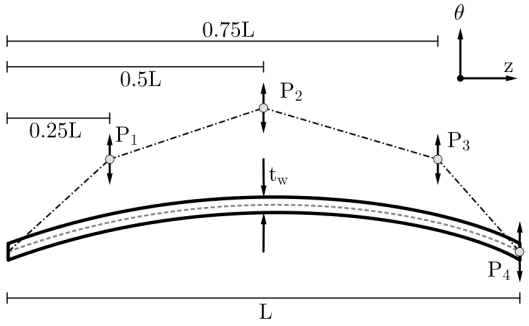

Fig. 4: Bézier curve parameterisation of the wave rotor wall camber.

Table 3: Lower and upper bounds for design variables for the optimisation.

Parameter	Unit	Lower bound	Upper bound
Nr. of channels	-	40	50
Channel wall thickness	mm	0.90	1.40
$\Delta\ \theta_{P1}$	mm	-1.75	1.75
$\Delta\ \theta_{P2}$	mm	-2.25	2.25
$\Delta\ \theta_{P3}$	mm	-1.75	1.75
$\Delta\ \theta_{P4}$	mm	-1.5	1.5

The objective function is formulated as given in Equation 2. The aim is to maximise the power output while maintaining the pressure exchange capabilities of the wave rotor. In this study, the energy transfer capacity is estimated through the achieved pressure ratio. The main objective function is defined as a relative error from the estimated power output to a target power output P_t (set to 1kW). Additional constraints for energy transfer capacity and manufacturability are defined.

$$OF(x_i) = \begin{cases} 10\left|\dfrac{P_\mathrm{t} - \overline{P}}{P_\mathrm{t}}\right|, & \text{if } \overline{\Pi}_\mathrm{TT} \geq 0.97\overline{\Pi}_\mathrm{TT,BL} \\ 10 - \overline{\Pi}_\mathrm{TT} & \text{if } \overline{\Pi}_\mathrm{TT} < 0.97\overline{\Pi}_\mathrm{TT,BL} \\ 20 - 1000|w_\mathrm{ch} - 0.0023| & \text{if } w_\mathrm{ch} < 0.0023 \text{ and } N_\mathrm{ch}\%n_{\mathrm{n_{cyc}}} \neq 0 \\ 20 & \text{if } N_\mathrm{ch}\%\mathrm{n_{cyc}}{=}0 \end{cases} \tag{2}$$

The optimiser then attempts to minimise the error between the actual power output and the target power output. Energy transfer through the shock waves may be compromised by mixing losses and incidence losses as the flow enters the channel from the ports. Therefore, one can expect a trade-off relationship between the ability to generate more power, while functioning as a pressure exchange device at the same time. Thus, in order to allow the optimiser to seek those designs with maximum power output and enable as many designs as possible to be considered without being discarded, a threshold is defined that permits a three percent drop in compression pressure ratio compared to the baseline model. The fitness value of each design candidate surpassing this limit is judged based solely on the predicted power output. The higher the power output, the better the objective function value of the design candidate. If, however, a particular design fails to achieve a compression ratio higher then the defined threshold, a high penalty is assigned.

In the same fashion as the baseline model, design candidates are required to be manufacturable through machining from solid. This translates into a minimum channel width of 2.3 mm. Finally, as power generation in wave rotors is generally pulsatile [47], the final optimisation constraint aims at generating power in a smooth as possible manner. This is done by imposing an offset between subsequent cycles and thus avoiding large torque amplitudes. In detail, this is achieved by assigning a large penalty to cases where the total number of channels is dividable by the number of cycles without any remainder. In such a scenario, the channel arrangement in each cycle would exhibit the same exact relative position with respect to the ports and would thus exacerbate torque amplitudes.

The steps taken during the optimisation are summarised in the flowchart displayed in Figure 5. The optimisation starts with the user parameterising the geometry and selecting the corresponding bounds. These are then normalised in the Matlab routine to a hypercube. In addition, the objective function is set along with the maximum number of expensive CFD computations. It is noteworthy that the optimisations can be continued from a given data set should it transpire that the initial computational budget was too optimistic. As soon as this is done, the actual optimisation is started following the framework outlined in Figure 6. At each iteration, the updated geometry is fed into the CFD solver, updated and a new mesh created. Then the CFD simulation is run based on the baseline flow field in order to minimise the number of iterations to reach a limit cycle, which is based on convergence of mass as well as pressures and temperatures in the ports. Finally, an averaging period is appended to obtain time averaged data for predicted power and pressure ratio, as defined in Equations 3 and 4.

$$\overline{P} = \frac{1}{t_\mathrm{end}\text{-}t_0}\int_{t_0}^{t_\mathrm{end}} \frac{\tau(t)2\pi N}{60} dt \tag{3}$$

$$\overline{\Pi}_\mathrm{TT} = \frac{1}{t_\mathrm{end}\text{-}t_0}\int_{t_0}^{t_\mathrm{end}} \Pi_\mathrm{TT}(t) dt \tag{4}$$

2.2.2 Surrogate Modelling

In general, optimisation problems can be mathematically expressed as

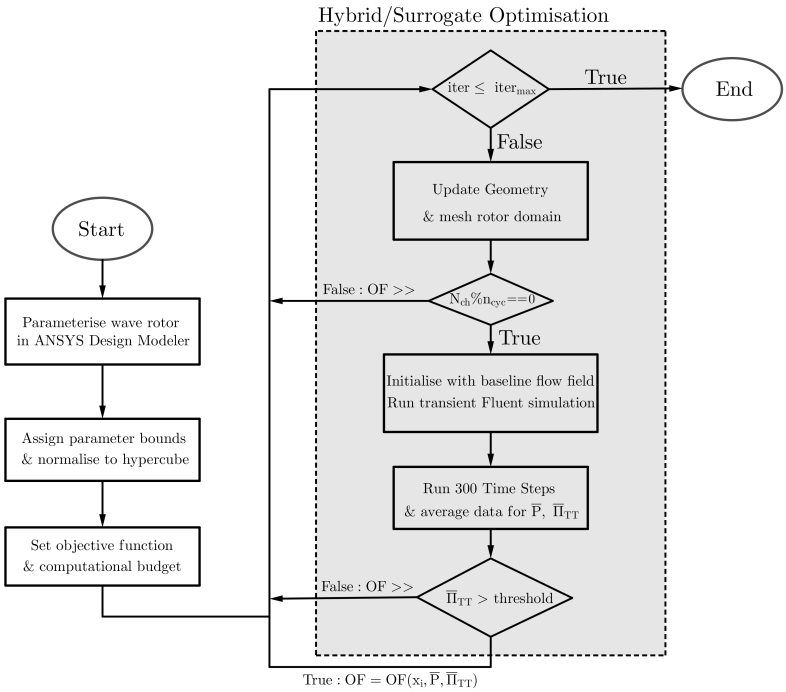

Fig. 5: Flowchart for transient wave rotor optimisation coupling an optimisation routine with CFD.

$$\begin{aligned} &\text{Minimise} && f(x_i) \quad \text{with i=1, 2, .., n;} \\ &\text{Subject to :} && x_i^{lb} \leq x_i \leq x_i^{ub}, \\ & && g(x_i) \leq 0 \end{aligned} \tag{5}$$

where $f(x_i)$ represents the original - usually unknown - objective function and x_i the corresponding design parameters that are subject to lower and upper bounds. The problem dimension is dictated by n. Furthermore, the objective function can be subject to additional constraints $g(x_i)$. In case of the wave rotor optimisation, evaluating $f(x_i)$ requires elaborate unsteady RANS simulations. This signifies considerable computational effort, in particular when considering several hundreds of these expensive simulations are necessary to cover the design space.

As a result it would be advantageous to carry out the optimisation on a function that is considerably cheaper (i.e. quicker) to execute. This can be done through replacing the original, costly objective function $f(x_i)$, with an auxiliary problem, as given in Equation 6.

$$\begin{aligned} &\text{Minimise} && \hat{f}(x_i) \quad \text{with i=1, 2, .., n;} \\ &\text{Subject to :} && x_i^{lb} \leq x_i \leq x_i^{ub}, \\ & && \hat{g}(x_i) \leq 0 \end{aligned} \tag{6}$$

where the surrogate models $\hat{f}(x_i)$ and $\hat{g}(x_i)$ replace the expensive original objective and constraint functions $f(x_i)$ and $g(x_i)$. The surrogate models are an approximation of the actual objective function, but are significantly cheaper to solve. Ideally, one would seek to be able to extract all the

necessary information from the surrogate model without the necessity to run the expensive black-box function $f(x_i)$. However, before this can be done it is necessary to train the surrogate model. In this paper, the surrogate model is constructed using a Kriging or Gaussian process regression method implemented in the DACE [50] library. The predicted output by the Kriging model $\hat{f}(x_i)$ comprises of a deterministic term $\mu(x)$, realised with polynomial function and a stochastic term $Z(x)$, represented by a Gaussian random function, as described in Equation 7.

$$\hat{f}(x_i) = \mu(x) + Z(x) = \sum_{i=1}^{k} y_i(x)\beta_i + Z(x) \tag{7}$$

where $y_i(x)$ and β_i denote the basis function and the corresponding regression coefficients respectively. $\hat{f}(x_i)$ is essentially a regression model, which can follow zeroth, first or second order polynomial forms. In the course of this study, the regression term is modelled through a second order polynomial which follow the form [51]

$$\mu(x) = \beta_0 + \sum_{i=1}^{k} x_i\beta_i + \sum_{i=1}^{k}\sum_{j=1}^{k} \beta_{ij}x_i x_j \tag{8}$$

where the regression coefficients β can be determined using least square methods minimising the error between the regression model and the actual function.

Finally, the stochastic term $Z(x)$ represents the error between the true model and the surrogate model and is approximated through a Gaussian correlation function with zero mean and constant variance. While DACE offers a number of different choices for regression and correlation, the two selected ones appeared to perform best when applied to the test cases introduced in Appendix 1 and 2.

2.2.3 Hybrid Genetic Algorithm

The first step in the optimisation routine is to generate a set of training data. In most cases for surrogate optimisation this is done via design of experiments, such as latin-hypercube sampling [52, 53]. For the purpose of this study we propose to run the expensive objective function using evolutionary algorithms, such as a GA or PSO, to produce the initial training set. After this is accomplished, the routine proceeds to build the Kriging surrogate model on which the optimisation routine is continued. This represents an approximation of the costly, original problem. The estimated optimum predicted by the surrogate model optimisation is subsequently compared against its objective function value by running the expensive black-box function. The information from that evaluation is then used to update the surrogate model. This measure is necessary as for most multidimensional engineering problems, the initial surrogate model will not be detailed enough to infer an optimal combination of design parameters.

Following the suggestion of Regis and Shoemaker [54], an iterative procedure is applied that alternates between local exploitation and exploration. The proposed method seeks to determine the minimum of the auxiliary problem while balancing both exploratory and local search. The former signifies that the algorithm seeks to search regions that have not yet been explored well, while the latter aims at further exploring and exploiting reasonably well explored regions in an effort to isolate a local optimum.

In detail, this signifies that one needs to determine the point within the design space Ω with the maximum possible distance to any previously evaluated points, which is termed as the *maximin* point and defined in mathematical terms, as done in Equation 9.

$$\tilde{x} = \max_{x \in \Omega} \min_{1 \leq i \leq n} |x - x_i| \tag{9}$$

Hence, by defining a search pattern β vector one can set the subsequent evaluation point to be at least $\beta\tilde{x}$ from all previously evaluated design points. If the subsequent evaluation point is in close proximity to previously evaluated points, the search is more geared towards local exploitation. Conversely, a point that is far from all previously evaluated points facilitates global exploration of the design space. This is implemented in an alternating manner and included as an additional constraint for solving the auxiliary optimisation problem. Figure 6 summarises the main steps of the hybrid optimisation routine, starting from the initial training set provided by a GA, which is run for a pre-specified number of generations, which is dependant on the dimensionality of the optimisation problem (usually in the range of 2-5 generations). Based on the initial dataset, a Kriging surrogate model is created before iterations commence solving the auxiliary optimisation problem periodically switching between exploration and exploitation. At the end of each iteration, the expensive problem is run and the surrogate model subsequently updated. As it is not possible to ascertain whether a minimum is local or global, the optimisation is run until the computational budget is exhausted and the maximum number of expensive evaluations reached.

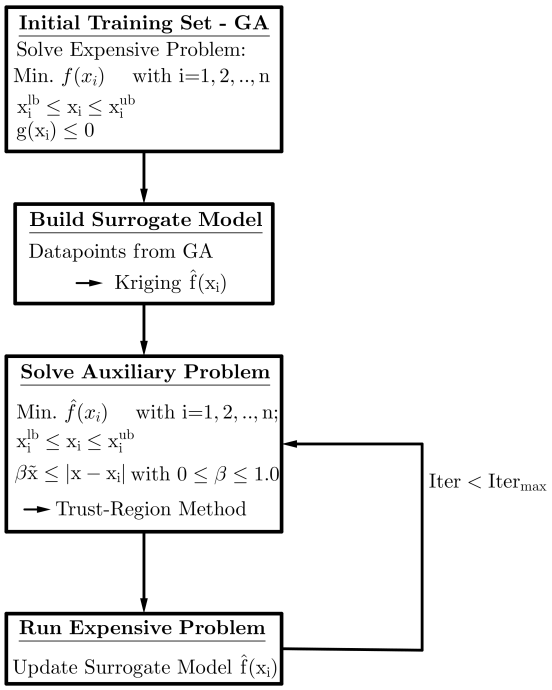

Fig. 6: Hybrid algorithm flow chart.

The principle of the optimisation algorithm is exemplified in Figure 7 when applied to the Ackley multimodal test function with two-parameters. The approximation of original function by the surrogate model at three different instances during the optimisation run is given. The first one after 51 iterations displays the surrogate mode just after completion of the initial GA. It further shows that the next data point to be evaluated is located at the extremities of the search space

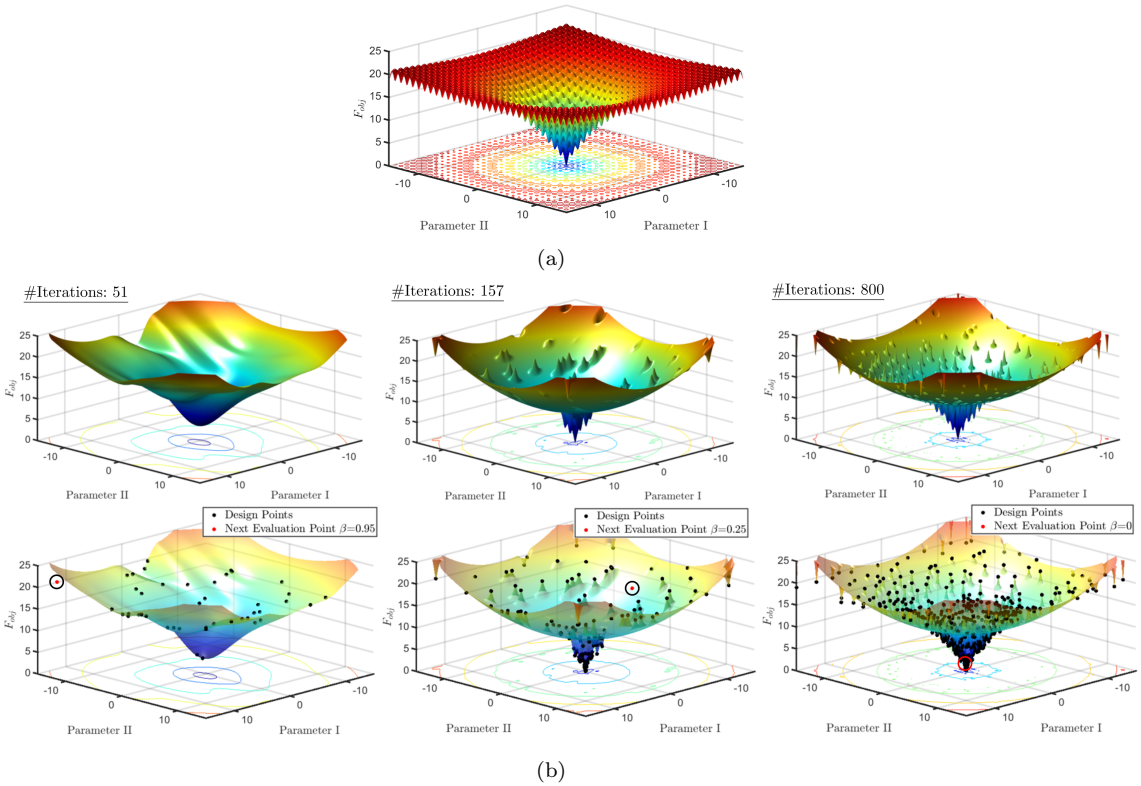

Fig. 7: (a) Example of the Ackley multimodal two-dimensional test function. (b) Convergence and evolution of the surrogate model employing the hybrid GA on the Ackley test function at three different instances throughout the optimisation.

as a consequence of a large β value of 0.95. After approximately 157 iterations and despite the large number of local minima, the routine is swiftly able to determine the location of the global minimum near $(0, 0)$. Further continuation of the search algorithm, results in further exploitation of the region in close vicinity of the global minimum as well as exploration of behaviour further away from it.

In order to further facilitate the search of the design space, the implementation of the hybrid method further includes a normalisation of the parameter ranges to a hypercube using Equation 10.

$$x_{\text{norm}} = \frac{x_i - \min(x)}{\max(x) - \min(x)} \tag{10}$$

In addition, objective functions characterised by a large spread between minimum and maximum function values are normalised using the paired log transformation introduced by Regis and Shoemaker [55]. Applying the transformation in Equation 11 to the dataset alleviates the discrepancy between extreme values, while retaining the location of maxima and minima. This is illustrated on the one-dimensional Rastrigin function in Figure 8. In order to avoid an already flat to flatten out further the paired log transformation is only applied if the maximum detected value after the initial GA dataset if three times higher than the median of all previously evaluated values.

$$\text{plog}(x) = \begin{cases} \log(1+x) & \text{if } x \geq 0 \\ -\log(1-x) & \text{if x} < 0 \end{cases} \tag{11}$$

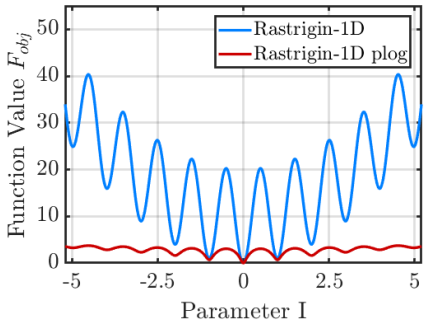

Fig. 8: Effect of paired log transformation on the one-dimensional Rastrigin function.

2.3 Numerical Campaign

2.3.1 Quasi Two-Dimensional CFD Model

In order to evaluate the performance of different wave rotor designs transient simulations were conducted using the commercial CFD solver ANSYS Fluent R19.1. The governing equations for continuity, momentum and energy were solved using the unsteady RANS equations with turbulence closure provided through Menter's k-ω SST model with enhanced wall treatment. Thus the flow is assumed to be fully turbulent, which is justified based on the wave rotor channel and port dimensions of approximately 2-5 mm and 15 mm respectively as well as the mass flow rate under investigation ($\dot{m}_{\text{HPG}}$=32 g/s). This results in Reynolds numbers in excess of 1.5e6.

Wave rotor simulations are inherently transient despite steady-state conditions prevailing in the ports. Throughout the optimisation study the boundary conditions set in the in- and outflow ports are kept constant. The high pressure inlet port (HPG) is designated as a mass flow inlet with a prescribed inlet mass flow rate of 32 g/s and 773 K inlet temperature. The static pressure in the corresponding high pressure outlet port is controlled via a user-defined function (UDF) in Fluent such that the mass flow error to the high pressure port inlet mass flow rate (i.e. 32 g/s) is minimised. As far as the low pressure region is concerned, the inlet mass flow rate in the LPA duct is again controlled via a UDF resulting in a loop flow ratio $\dot{m}_{\text{HPG}}/\dot{m}_{\text{LPA}}$ of 1.7 entering at 300 K. The low pressure outlet port (LPG) features a static backpressure according to ambient conditions.

The computational domain encompasses the rotor passages as well as the in- and outlet stator regions, which are connected via a sliding mesh interface, as shown in Figure 9. Since the approach aims at reducing the computational cost, the mid-plane was extracted at 60 mm between hub and shroud rendering the domain two-dimensional in the z-θ plane. The stator regions contain the constant axial leakage gap of 0.3 mm on in- and outlet side respectively and feature three cycles consisting of a high pressure in/out- and a low pressure in/outlet. Thus, the model does, however, not contain the leakage cavities and also cannot account for windage losses of the rotor within its casing.

Domain discretisation was done using hexahedral elements in Ansys Mesher. As the general flow direction follows the positive z-axis this approach ensures reduced deviation of face normals and

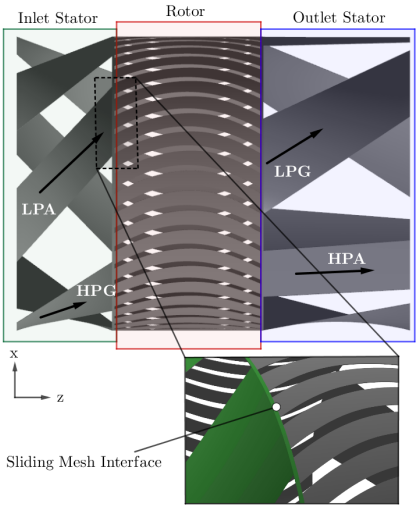

Fig. 9: Computational domain for the quasi two-dimensional optimisations containing stationary in- and outlet stator domains and a rotating region containing the rotor passages.

Table 4: Summary of boundary conditions used for the mesh sensitivity study

Analysis type	URANS
Rotational speed	32,000 rpm
Turbulence closure	k-ω SST with enhanced wall treatment
Walls	Adiabatic, no-slip
Inlet	HPG: mass flow inlet LPA: mass flow inlet
Outlet	HPA: mass flow outlet LPG: pressure outlet
Inviscid fluxes	Second-order Upwind
Turbulence	Second-order Upwind
Transient formulation	First-order
Time step size	1e-6 s
Convergence target	0.01 (relative)
Max. iterations/time step	15

the flow vector and thus limits the amount of numerical diffusion. Furthermore, the discretisation employs a single cell in radial direction with each side being modelled as a symmetry surface. An example of the discretised domain and mesh elements are shown in Figure 10. This renders the approach quasi-two dimensional. Prior to the optimisation study, a mesh convergence study was conducted. In total, four different mesh resolutions were evaluated ranging from approximately 58,000 to 350,000 cells, as presented in Table 5.

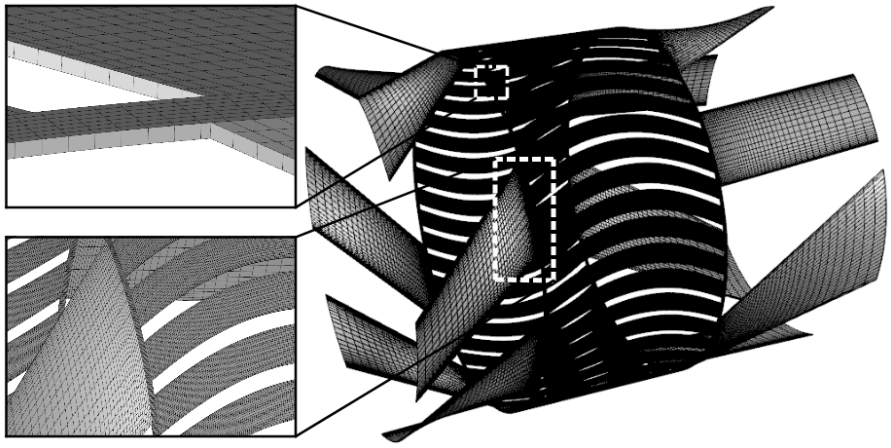

Fig. 10: Domain discretisation using hexahedral elements with a single cell in radial direction.

Table 5: Mesh sensitivity study and corresponding resolution for each sub-domain. The first number denotes the resolution in z-direction, whereas the second number refers to the prescribed number of nodes in lateral direction. For stators, two resolutions are given; the first for the duct itself and the second one for the discretisation of the axial leakage gap.

	Inlet Stator	Rotor	Outlet Stator	Total Cell Count	Norm. Elapsed Run Time
Very Coarse	85x10	30x25,5x1000	30x25,5x1000	58,105	0.34
Coarse	100x12	35x25,5x1000	30x25,5x1000	104,300	0.39
Medium	170x17	40x30,10x1250	30x25,10x1200	171,350	0.65
Fine	250x25	50x35,15x1400	50x35,15x1400	350,530	1.0

Hybrid initialisation was used for all simulations and the simulations run for 2500 time steps with a time step of $1e-6$s with a maximum number of 15 iterations and a CFL number of 25. The choice of time step corresponds to a rotation of 0.2° in between time steps. This was followed by an averaging period for pressure ratio and predicted output power for period of 300 iterations. In addition, all simulations were run employing the implicit, coupled density-based solver in double precision mode. The operating medium was assumed to be air behaving as an ideal gas with dynamic viscosity temperature dependency approximated by Sutherland's law. With respect to the numerical setup, second-order schemes were used for inviscid fluxes and turbulent kinetic energy and dissipation rate, while an implicit first-order formulation was used for temporal discretisation.

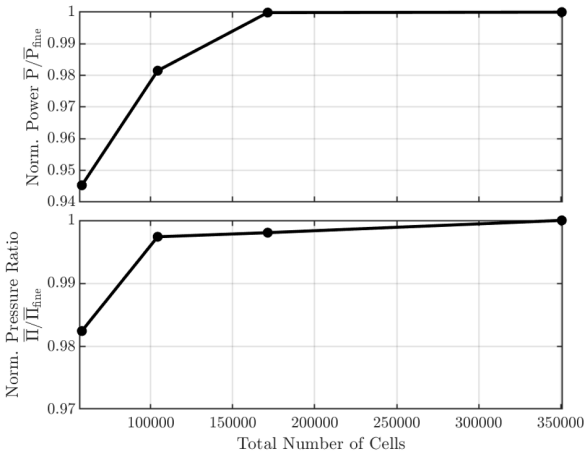

Fig. 11: Normalised results for averaged predicted power and pressure ratio as a function of cell count. Data from the finest grid solution were used for normalisation.

The results of the grid sensitivity study are given in Figure 11. The graphs depict the averaged predicted power and pressure ratio against the number of cells within the domain. The data were normalised by the solution of the finest grid and reveals that the error between the coarsest and the finest solution for power and pressure ratio is 5.5% and 2% respectively. For power, there is virtually no change between medium and fine mesh solutions, while for pressure ratio coarse, medium and fine mesh solution are well within 1 percent. Looking at the elapsed run time in Table 5 shows that there is a significant cost benefit associated with running on a medium or coarse mesh resolution.

In light of the large number of CFD evaluations necessary in the optimisation, it was decided to proceed the optimisation study with the coarse mesh and accept a slightly larger numerical uncertainty with regard to pressure ratio and power at the benefit of rendering the simulations substantially cheaper.

Table 6: Results of studies on the effect of numerical schemes for inviscid fluxes, turbulence and transient formulation. in addition, sensitivity to time step changes and the number of inner iterations is investigated as well. The relative changes in average predicted power and pressure ratio with respect to the original settings from coarse mesh solution are stated.

		rel. change $\overline{P}$	rel. change $\overline{\Pi}_{\mathrm{TT}}$	reduction CPU elapsed time
Numerical Schemes	first-order turbulence	-4.1%	1.5%	0.99
	first order flow first-order turbulence	-16.5%	-2.5%	0.73
	transient 2nd-order	-3.7%	2.0%	1.02
	MUSCL scheme flow transient 2nd-order	-2.8%	2.1%	1.10
Time Step	6e-7 (0.12°/Δ t)	<1%	<1%	1.6
	8e-7 (0.15°/Δ t)	<1%	<1%	1.2
	1e-6 (0.2°/Δ t)	<1%	<1%	1.0
	2.5e-6 (0.48°/Δ t)	5.2%	-5.9%	0.5
	5e-6 (1.0°/Δ t)	27.6%	-15.7%	0.3
Inner Iterations	20	<1%	<1%	1.19
	15	<1%	<1%	1.0
	10	<1%	<1%	0.83
	7	<1%	<1%	0.62

The next step is to look into the sensitivity of the result with respect to the numerical schemes, the time step size and the number of inner iterations. The results of this study are summarised in Table 6. At first, the turbulence scheme was set to first-order Upwind, which resulted in a 4.1 percent lower predicted power and a 1.5 percent higher pressure ratio. Computational effort remains more or less constant. Switching to first-order Upwind scheme leads to a larger deviation in terms of predicted power, while pressure ratio remains within 2.5 percent. The advantage with regards to CPU cost are as expected due to expedited convergence. Reverting back to second-order flow and turbulence schemes and switching transient formulation to second-order results in a 3.7 percent predicted power reduction and 2 percent increase in pressure ratio, while slightly increasing CPU costs. Finally, a simulation has been carried out with all numerical schemes set to second-order Upwind with the exception of spatial discretisation being approximated through third-order MUSCL scheme. This results in moderate changes to the predicted averaged power and pressure ratio, but a 10 percent increase in computational effort.

The subsequent study deals with the effect of time step size on the numerical accuracy. All studies were run with 15 as a maximum number of iterations per time step. Continuously increasing time step size from approximately 0.12° per time step up to 0.2° per time step does not seem to impair the solution accuracy and enhances computational efficiency. Approaching 0.48° or higher appears to have a more distinct effect on the recorded solution and exhibits a penalty on convergence rate.

Finally, the effect of the number of maximum iterations per time step was examined. This was varied between 20 and 7. Throughout this study, it showed that increasing this parameter to the maximum did not result in a significant change in the convergence rate and residual level at the end of each inner iteration. The residuals continued to drop approximately two orders of magnitude within 7 iterations, thus achieving the set relative convergence target of 0.01.
Based on the findings of the quasi two-dimensional study, it was decided to proceed with the coarse mesh solution, second-order spatial discretisation scheme for convection and turbulence terms, while using first-order temporal discretisation. All simulations are carried out with a time step of $1e$-6 and a maximum number of 7 inner iterations. Using this setup, each design point in the optimisation requires approximately 1.8 hours to perform geometry and mesh update and run the simulation on an Intel Xeon E5 3.40 GhZ processor of 12 physical cores and 24 threads.

2.3.2 Three-Dimensional CFD Model

The quasi-two-dimensional model represents an abstraction and simplification from the actual computational domain aiming at facilitating the computational effort while retaining major characteristics and flow features. In order to gain fidelity in the optimisation results and enhance the comparison between the best candidate design from the pool of design points with the baseline design, further in-depth 3D-CFD simulations are carried out. The objective of this is to include further details in the geometry that were omitted in the quasi two-dimensional study to reduce computational expense. This includes elements such as inlet guide vanes shown in Figure 12. The domain itself, however, is similarly structured with two stationary domains housing in- and outlets as well as a rotating domain representing the rotor. Channel-to-channel interaction is modelled through an axial leakage gap, while leakage cavities and paths around the rotor are omitted due to the complexity and expenditure of such an in-depth transient simulation. Similar to the quasi two-dimensional approach, the domain is meshed using Ansys ICEM CFD employing hexahedral elements for stationary and rotating domains. The mesh statistics and quality metrics are given in Table 7. The total number of cells used in the simulation was approximately 7.2 million cells. The rotor domain was discretised with 100 cells in longitudinal direction and 16x30 cells for the channel cross section. Overall the minimum mesh quality throughout the domain is 0.34, minimum face angle approximately 20° and maximum skewness 0.8.

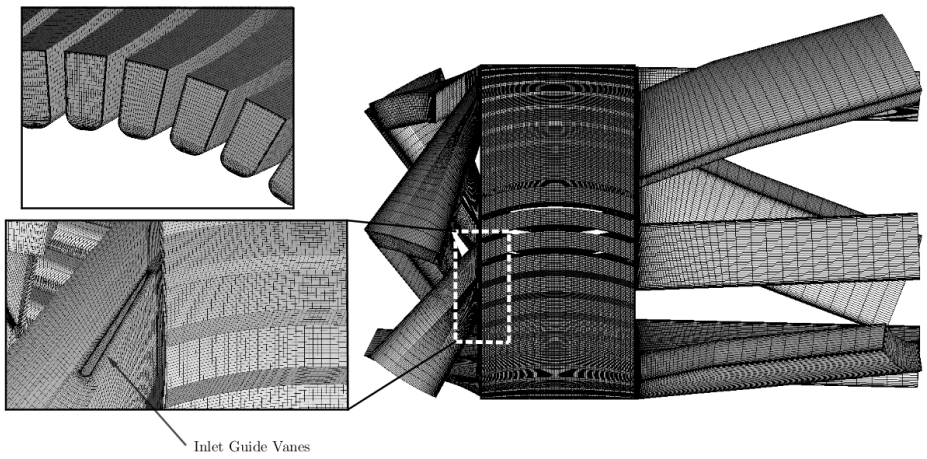

Fig. 12: Domain discretisation in three dimensions using hexahedral elements for inlet stator, outlet stator and rotor channels.

Table 7: Mesh statistics of the 3D-CFD simulations.

Mesh Cell Count	Quality	Min. Face Angle	Max. Skewness	Max. y^+	$\overline{y}^+$
847,000 (Inlet Stator)	0.40	23.9°	0.73	46.4	11.3
5,860,000 (Rotor)	0.34	19.6°	0.79	5.7	2.0
445,000 (Outlet Stator)	0.77	58.4°	0.35	57	13.1
7,150,000 (Total)					

The density-based solver of Ansys Fluent R19.1 was used in double-precision mode to solve the unsteady RANS equations with an additional species equation being solved allowing to track the gas entering through the high pressure inlet and the low pressure inlet separately and be able to infer the amount of FAE and EGR. Convective fluxes were modelled using Roe's flux-difference splitting approach with a third-order MUSCL discretisation for the flow equations, while second-order Upwind schemes were used for turbulence equations. Temporal discretisation was done using a second-order implicit formulation with a time step size of $1e$-6s and a maximum of ten iterations per time step.

All boundary conditions applied are in line with the quasi two-dimensional study. The working medium was defined as air behaving like a calorically imperfect gas using a seventh-order polynomial, as done in Equation 12, and a dynamic viscosity following Sutherland's law.

$$\begin{aligned} c_p(T) = 999.36 - 0.064T + 2.93e{-}4T^2 + 1.58e{-}7T^3 \\ - 4.54e{-}10T^4 + 2.84e{-}10T^5 - 7.51e{-}10T^6 + 7.40e{-}21T^7 \end{aligned} \tag{12}$$

Along with average pressure ratio and predicted power output, the effects of the optimisation on compression and expansion efficiency shall be examined. These are determined through considering hot and cold gas streams separately and taking EGR and FAE into account, as presented by Chan et al. [56]. In addition internal heat transfer is also taken into account as done by Wilson et al. [57]. Therefore, compression and expansion efficiency are defined as the ratio of actual work to the isentropic work. The additional temperature terms ΔT_c and ΔT_x account for the heat transfer between hot and cold gas streams within the wave rotor. These are generally not known and therefore assumed to be equal. In order to be able to solve Equations 13 both compression and expansion efficiency are assumed to be equal $\eta_{cx} = \eta_c{=}\eta_x$.

$$\begin{aligned} \eta_c &= \frac{\dot{m}_{\mathrm{LPA}} c_{p,c}\left(T^{is}_{\mathrm{HPA}} - T_{\mathrm{LPA}}\right) + \dot{m}_{\mathrm{EGR}} c_{p,h}\left(T^{is}_{\mathrm{HPA,h}} - T_{\mathrm{LPG}}\right)}{\dot{m}_{\mathrm{LPA}} c_{p,c}\left(T_{\mathrm{HPA,c}} - T_{\mathrm{LPA}} - \Delta T_c\right) + \dot{m}_{\mathrm{EGR}} c_{p,h}\left(T_{\mathrm{HPA,h}} - T_{\mathrm{LPG}} - \Delta T_c\right)} \\ \eta_x &= \frac{\dot{m}_{\mathrm{LPG}} c_{p,h}\left(T_{\mathrm{HPG}} - T_{\mathrm{LPG}} - \Delta T_x\right) + c_{p,c}\dot{m}_{\mathrm{FAE}}\left(T_{\mathrm{HPA}} - T_{\mathrm{LPG,c}} - \Delta T_x\right)}{\dot{m}_{\mathrm{LPG}} c_{p,h}\left(T_{\mathrm{HPG}} - T^{is}_{\mathrm{LPG}}\right) + c_{p,c}\dot{m}_{\mathrm{FAE}}\left(T_{\mathrm{HPA}} - T^{is}_{\mathrm{LPG,c}}\right)} \end{aligned} \tag{13}$$

Local evaluation of irreversibilites and thus potential penalties in efficiency are analysed on the basis of local entropy generation rate. According to Iandol and Sciubbia [58] and Herwig et al. [59] the total local entropy generation rate per unit volume $\dot{S}_{p,v}$ comprises of entropy production terms representing direct viscous dissipation from the averaged flow field ($\dot{S}_{p,\bar{D}}$), turbulent dissipation ($\dot{S}_{p,D'}$), heat transfer through the average temperature field ($\dot{S}_{p,\bar{C}}$) and heat transfer due to fluctuating temperature gradients ($\dot{S}_{p,C'}$).

$$\dot{S}_{p,v} = \dot{S}_{p,\bar{D}} + \dot{S}_{p,D'} + \dot{S}_{p,\bar{C}} + \dot{S}_{p,C'} \tag{14}$$

The detailed terms can be stated in cartesian coordinates as done in Equation 15, where μ denotes dynamic viscosity, T the static temperature, u,v,w the velocity components in the respective directions, ε the turbulent dissipation rate, c_p the specific heat at constant pressure and Pr_t the turbulent Prandtl number assumed to be 0.9. Equations 14 and 15 are implemented in Ansys Fluent via a custom field function.

$$\begin{aligned}
\dot{S}_{p,\bar{D}} &= \frac{\mu}{\overline{T}}\left[2\left[\left(\frac{\partial \overline{u}}{\partial x}\right)^2+\left(\frac{\partial \overline{v}}{\partial y}\right)^2+\left(\frac{\partial \overline{w}}{\partial z}\right)^2\right]+\left(\frac{\partial \overline{u}}{\partial y}+\frac{\partial \overline{v}}{\partial x}\right)^2\right. \\
&\quad \left.+\left(\frac{\partial \overline{u}}{\partial z}+\frac{\partial \overline{w}}{\partial x}\right)^2+\left(\frac{\partial \overline{v}}{\partial z}+\frac{\partial \overline{w}}{\partial y}\right)^2\right] \\
\dot{S}_{p,D'} &= \rho\frac{\varepsilon}{\overline{T}} \\
\dot{S}_{p,\bar{C}} &= \frac{\lambda}{\overline{T}^2}\left[\left(\frac{\partial \overline{T}}{\partial x}\right)^2+\left(\frac{\partial \overline{T}}{\partial y}\right)^2+\left(\frac{\partial \overline{T}}{\partial z}\right)^2\right] \\
\dot{S}_{p,C'} &= \frac{\mu_t c_p}{Pr_t\overline{T}^2}\left[\left(\frac{\partial \overline{T}}{\partial x}\right)^2+\left(\frac{\partial \overline{T}}{\partial y}\right)^2+\left(\frac{\partial \overline{T}}{\partial z}\right)^2\right]
\end{aligned} \tag{15}$$

Integrating $\dot{S}_{p,v}$ across a volume yields the total entropy generation rate, which can be further integrated over a time interval to give the the total entropy generation, as given in Equation 16.

$$\begin{aligned}
\dot{S}_p &= \int_V \dot{S}_{p,v} dV \\
S_p &= \int_{t_0}^{t_1} \dot{S}_p dt
\end{aligned} \tag{16}$$

2.4 Experimental Setup

After machining the optimised rotor, both the baseline and optimised rotor were tested experimentally on the University of Bath gas stand. Both rotor designs can be seen in Figure 13(a) and (b). The experimental setup used for validation follows an open-loop configuration, as shown in Figure 13c. A detailed explanation of the setup is beyond the scope of this paper, but follows the same layout as described in [47].

In general the setup features capabilities to vary dynamometer excitation load, loop flow ratio λ, mass flow rates and inlet pressures for both the high- and low pressure inflow ducts. In particular, pressurised air is directed to the wave rotor and can be heated up to target inlet temperature through the use of two 44kW electrical heaters. Loop flow ratio between HPG and LPA is controlled via two pneumatically actuated variable orifice control valves, while backpressure in the HPA duct is also modulated through an additional gate valve on the outlet side. Throughout testing pressures and temperatures at the wave rotor in- and outlet are recorded through pressure transducers and k-type thermocouples. Finally, wave rotor speed is controlled via a water cooled eddy-current dynamometer.

3 Results and Discussion

3.1 Wave Rotor Optimisation and Validation

The optimisation routine for the hybrid-GA considered 342 different designs, while MATSuMoTo dealt with 450 different design candidates. Plotting predicted power output versus compression

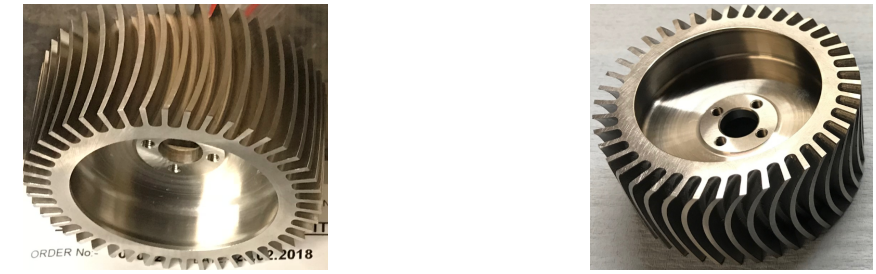

(a) (b)

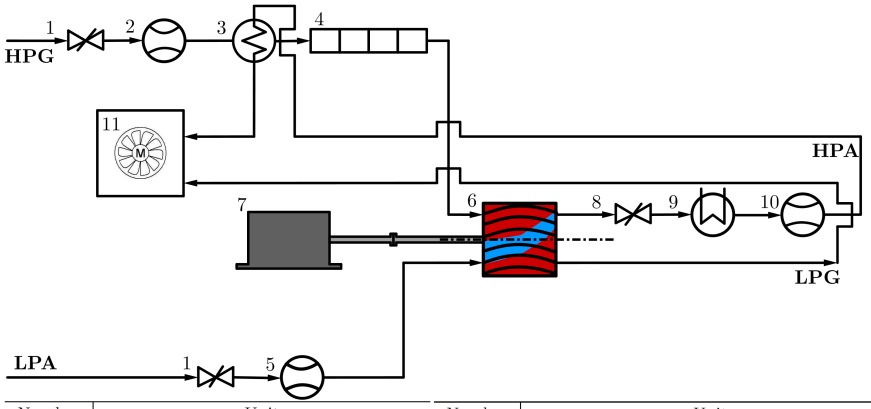

Number	Unit
1	2” sliding gate control valve
2	2” McCrometer V-cone mass flow meter Siemens DSIII dp-sensor
3	Air-to-air heat exchanger
4	44kW electric heater
5	1” McCrometer V-cone mass flow meter Siemens DSIII dp-sensor
6	Wave rotor

Number	Unit
7	Magtrol WB43 HS eddy-current dynamometer
8	1” sliding gate control valve
9	Air-to-water heat exchanger
10	2” McCrometer V-cone mass flow meter Siemens DSIII dp-sensor
11	Extraction fan

(c)

Fig. 13: (a) depicts the baseline wave rotor with symmetrically shaped channels, while (b) shows the optimised version. (c) Schematic showing the experimental layout and sensors used throughout experimental testing.

pressure ratio for both optimisation routines indicates a trade-off relationship between power and pressure ratio with a Pareto front, as illustrated in Figure 14. The results imply that there is a balance between the amount of energy that can be extracted through the change in momentum and the amount of energy being exchanged through the shock and rarefaction waves. The results shown in the graph were normalised by the baseline power output and pressure ratio with the baseline design marked by a red square. The 97 percent pressure ratio threshold introduced in Equation 2 is illustrated by the dashed line. The best candidate design across both optimisation campaigns, outlined as the filled, green circle, is located at this threshold and indicates an increase in power output of 1.78 at the cost of a 3 percent decrease in pressure ratio. Comparing the two optimisation techniques implies that MATSuMoTo features more of an emphasis on local search, while the results of the hybrid method are more scattered throughout the design space as the algorithm constantly iterates through the predefined search pattern.

However, as can be seen in the convergence plot of Figure 15a both methods swiftly decrease the objective function and find candidate designs with a significant increase in the predicted power

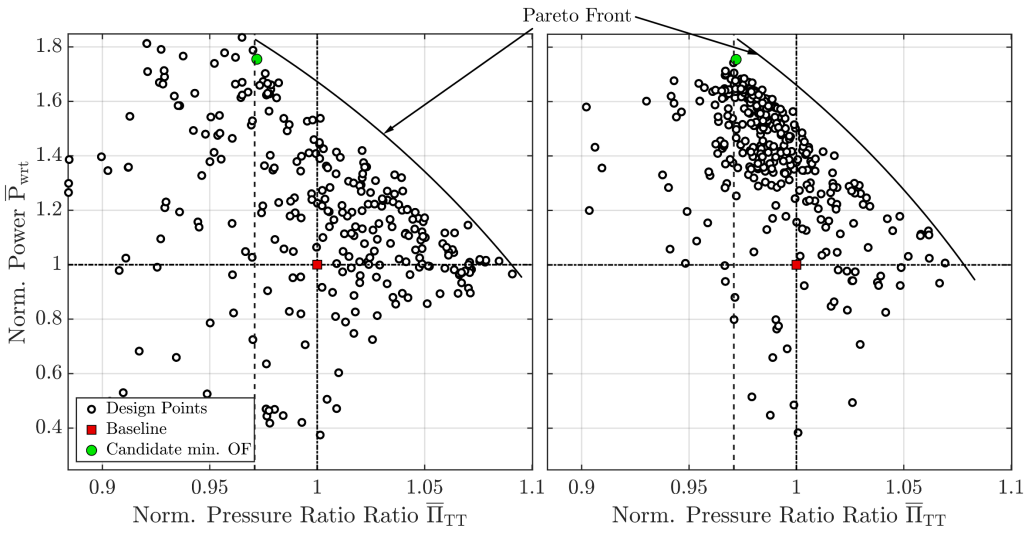

Fig. 14: Results from the optimisation results for the (a) hybrid-GA method and (b) the MATSuMoTo surrogate model.

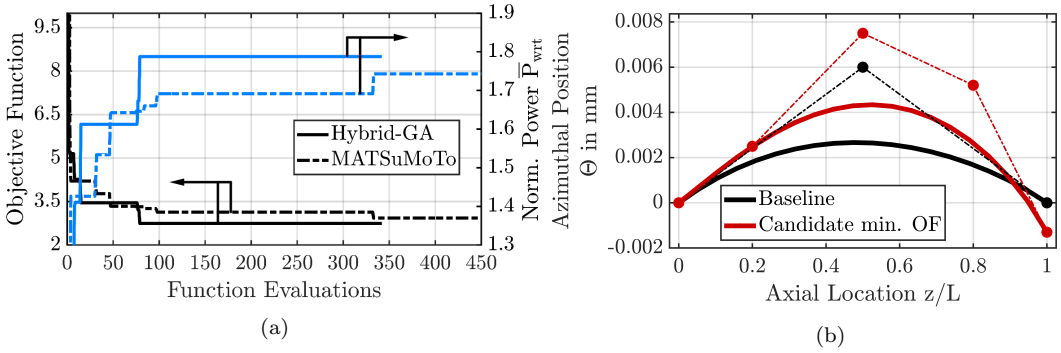

Fig. 15: (a) Convergence rate of objective function and normalised power output of hybrid method and MATSuMoTo. (b) Direct comparison of camberline distributions and Bézier control points for the baseline and optimised geometry.

output. In this instance, the hybrid method appears to converge sooner after fewer than 100 function evaluations, while MATSuMoTo requires approximately 350 iterations to determine a design with a similar objective function. However, it shall be noted that the final difference in the objective function and thus the estimated power benefit is relatively small. In addition, the optimisation settings (i.e. GA and LHS parameters as well as search patterns) may have the potential to be further optimised for the given optimisation problem. A comparison of the wall contour camberlines is given in Figure 15b. As opposed to the baseline design, the optimised design no longer features a symmetric shape. In addition camber increased with a higher deflection in the centre and more negative channel angles towards z/L=1. On top of the geometric modifications, the number of channels has been reduced to 43 resulting in greater channel width.

3.2 Further Examination of 3D-CFD Results

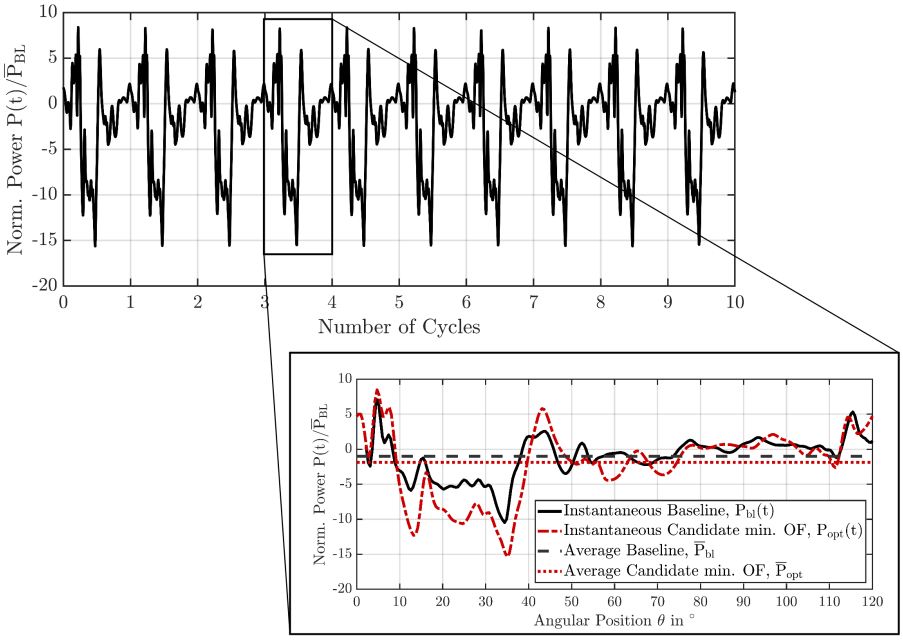

Fig. 16: Numerically determined instantaneous power generation of a single channel as it rotates around the circumference using 3D-URANS. The top graph shows the power distribution over multiple cycles showing the pulsatile nature of power generation. The detailed view below compares power distribution of baseline geometry (solid, black line) with the optimised model (dash-dotted, red line) along with cycle-averaged values.

In order to gain further insights and fidelity in the results of the quasi-two-dimensional model, 3D-URANS simulations on both baseline and the optimised rotor have been performed. Tracking a single channel as it rotates around the circumference and logging instantaneous power results in the distribution given in Figure 16. In the top graph, instantaneous power across multiple cycles (i.e. approximately three rotations) The detailed view below extract power distribution for a single cycle and compares results for baseline geometry (solid, black line) with the optimised model (dash-dotted, red line) along with cycle-averaged values.

All data shown were normalised by the average power output of the baseline design. Negative values denote shaft power extraction, while positive values represent power supplied to the rotor. First of all, it becomes apparent that the baseline camberline distribution is far from optimal with respect to extracting work. As expected, the power generation distribution emphasises the pulsatile manner, in which torque is generated in the wave rotor. The main contribution of torque generation stems from the opening of the HPG port to the channels. During approximately two-thirds of the cycle, the channel is idle and does not contribute to power generation. In addition, there are extended periods with positive power, reducing the overall power output.

The optimised model on the other hand exhibits increased loading and thus an greater power output. Overall, the increase outlined by 3D-CFD is approximately 1.85 and thus confirms the findings from the quasi-2D model used in the optimisation study. Thus, the quasi-2D model is able to yield represantitive results at a fraction of the computational cost of a full 3D simulation. The

reason for the small discrepancy between quasi-2D and 3D simulation results most likely resides in the greater model accuracy, such as the inclusion of the nozzle guide vane in both the HPG and LPA ducts, which help maintaining the inlet velocity triangles and effectively preventing premature flow turning. These guide vanes have been neglected in the optimisation campaign in order to minimise computational effort.
Despite an increase in predicted shaft power, the optimised design still features large periods of positive power, such as between 0° and 10° azimuth angle. This implies further potential for optimisation. The presented optimisation study focused on the rotor shape using an existing port arrangement, port angles and opening heights. It can therefore be deduced, that the current optimisation is too constrained in terms of parameters to provide the best possible overall design.

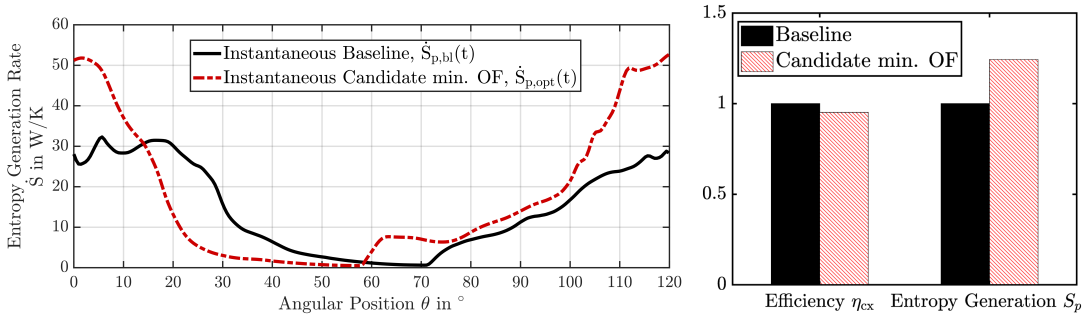

(a) (b)

Fig. 17: (a) Instantaneous entropy generation rate distribution as a function of azimuth angle. (b) Direct comparison of compression and expansion efficiency η_{cx} and integrated entropy generation within a single channel between baseline and power optimised geometry. The data were normalised by the corresponding baseline values.

The candidate design chosen from the pool of design iterations features a 3 percent lower pressure ratio in favour of greater power extraction. A decrease in pressure ratio hints towards an impeded ability to exchange energy between high and low pressure gas streams. To further investigate this, entropy generation rate has been integrated across the volume of a single channel using Equation 16 and recorded as the channel rotates. The results of this are given in Figure 17(a). The distribution shows that the largest amount of entropy is generated when the channels are exposed to the HPG duct. Subsequently, the entropy production reduces until the point, where the channels are exposed to the LPA duct, where low pressure, low temperature gas is flowing into the channels. An additional contribution is given by channel-to-channel interaction. This accounts for a gradual increase in entropy production from 70° azimuth angle onwards. Applying Equation 13 and computing compression and expansion efficiency for both baseline and optimised model, shows that the surplus in entropy is reflected in a reduced ability to compress and expand the gas streams efficiently through. This accounts for a five percentage points drop in the computed efficiencies, as shown in Figure 17b. The same trends are witnessed when integrating entropy production rate over an entire cycle, albeit in a stronger fashion.

The increase in entropy production that is particularly prominent during the opening of the HPG duct. This is the phase with the largest instantaneous power generation, as shown in the top graph of Figure 18. Evaluation of the corresponding incidence angle during this period, as exhibited in bottom graphs of Figure 18. The discrete manner in which the channels are exposed to the ducts results in a large variation of incidence angle. During the initial phase of channel exposure to the HPG duct at θ_1. The data suggest that, while the incidence angle distribution is similar between

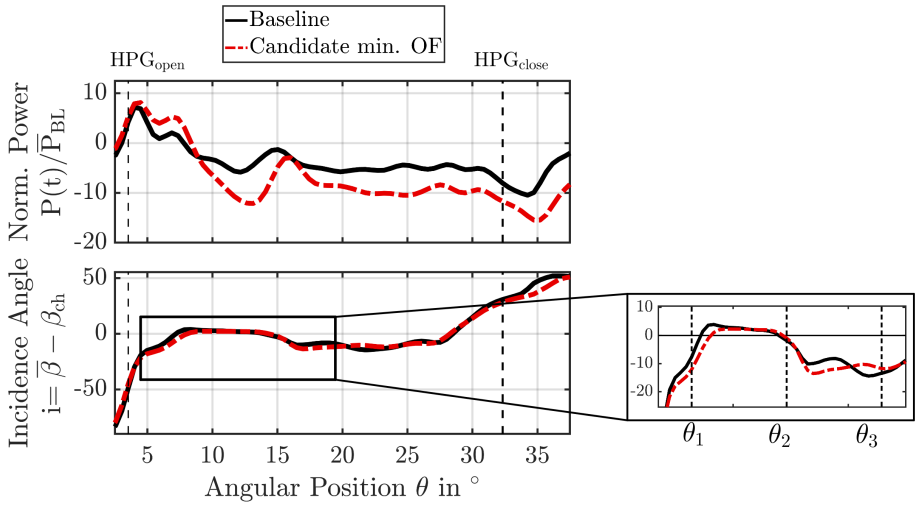

Fig. 18: Detailed view instantaneous power output (top) and the associated incidence angle comparing baseline and power optimised design.

baseline and optimised design, the incidence angle for the baseline design reaches positive values earlier than the optimised design. Subsequently, the incidence angle evolves in the phase between θ_1 to θ_2 to moderately positive incidence angles of up to 3.8°. During this stage, a single channel commences to generate shaft power. It continues to do so even though the incidence angle then changes again, at θ_3, to negative angles of -8° to -10°. Despite the negative incidence angle the channel continues to generate power, which is attributed to the non-axial camberline shape. Finally, a local peak in shaft power generation occurs as the HPG duct is in the process of closing and as incidence angle increases continuosly.

The contour plots presented in Figure 19 represent a single snapshot in time located in between channel hub and shroud. The given view focuses on the high pressure region in between the HPG and HPA duct comparing the baseline model (left hand side) with the optimised geometry (right hand side). Figure 19a displays static pressure for baseline and optimised geometry. Locations of the right running primary shock waves are indicated (marker $a1$). In case of the optimised design shown on the right hand side, it appears that the shock strength of the primary shock wave is slightly reduced compared to the baseline (left hand side plot). The secondary shock wave strength on the other hand remains unchanged (marker $a2$).

For the given loop flow ratio λ=1.7 the cold flow penetration length is below 50 percent of the channel width. This is marked ($b1$) in mass fraction contour plot in Figure 19b. A mass fraction of 1 signifies flow entering the wave rotor through the HPG port, while a mass fraction of zero denotes flow entering through the LPA port. This facilitates the analysis of mixing and interaction of cold and hot streams within the channels. As λ was kept constant there is no change in the scavenging characteristics for the optimised geometry. In both geometries the interface between hot and cold gases is highly skewed and three-dimensional (marker $b2$). In addition, the axial leakage path fosters mass transfer into the channels prior to the channels being exposed to the ports (marker $b3$).

Generation of irreversibilities shown in Figure 19c is achieved by applying Equation 14 and normalising the data for better visual representation for both baseline and optimised version by the same arbitrary number. Through comparison of the local entropy generation rate with the pressure and mass fraction field, it transpires that the bulk of the losses are generated at the demarcation surfaces between the hot and cold gas streams (marker $c2$). These losses appear to prevail over losses generated across the shock waves. Further losses are incurred as a consequence

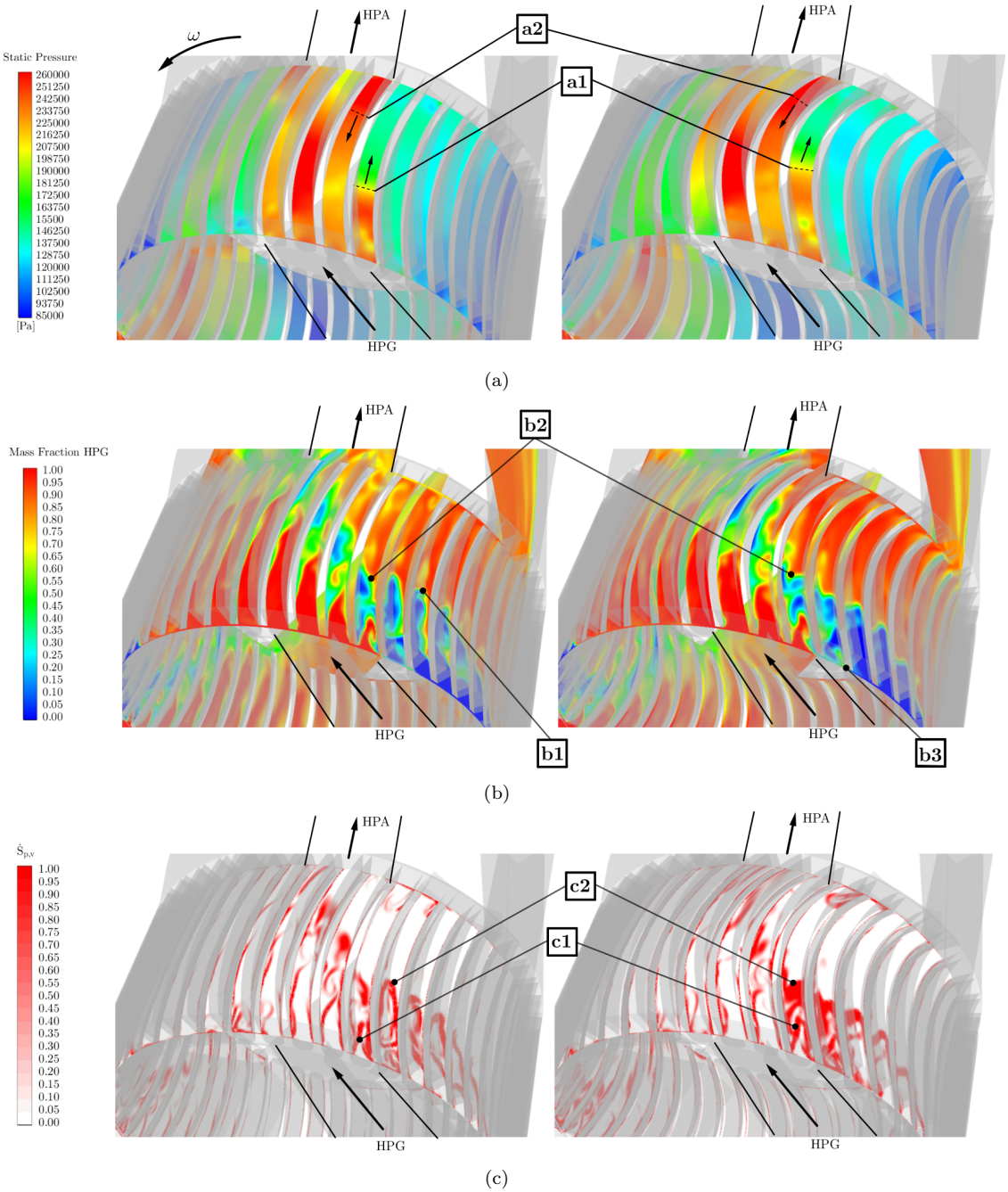

Fig. 19: Contour plots comparing (a) static pressure distribution with the locations for primary and secondary shock waves, (b) mass fraction of gas entering through the HPG port and (c) normalised local entropy generation rate for the high pressure zone of baseline (left hand side) and optimised geometry (right hand side).

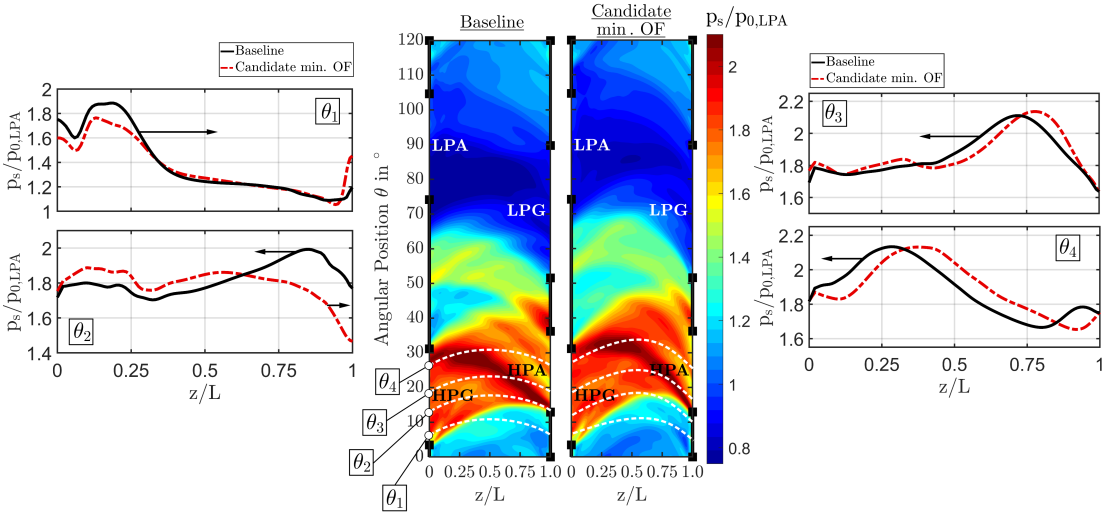

Fig. 20: Comparison of shock patterns for baseline (left) and optimised (right) designs. Static pressure distribution along the channel length in the high pressure zone at four different time instance (θ_1-θ_4) expose implications of the changes in geometry on the generation of primary and secondary shock waves.

of turbulence and flow separation as the flow enters from the port into the channels (marker *c*1). Hence, the increased torque extraction of the optimised model appears to take place in conjunction with an increase in entropy production. Overall, the local results support the observations made in Figure 17a and 17b attributing greater entropy production to the optimised rotor.

Figure 20 gives further insight into the change in gas dynamics between baseline and optimised geometry and the effect of the change in geometry and channel lengths on the shock patterns and pressure distributions. The left hand side contour plot represents the pressure distribution in the baseline geometry, while the right hand side contour plot denotes the optimised geometry. Qualitatively, the contour plots indicate differences, in particular visible in the high pressure zone in vicinity of the HPG and HPA ports.

Furthermore, extracting the static pressure distribution within the channel in the high pressure zone (i.e. during opening of HPG and HPA) at four different instances θ_1-θ_4 reveals ramifications on the generation of primary and secondary shock waves. Data extracted from the baseline model (solid, black line) are plotted against data from the optimised geometry (broken, red line).

Initially, upon opening the channel to the HPG port (at θ_1), increased incidence losses for the optimised geometry reduce the overall strength of the right travelling primary shock wave manifesting itself in a six percent decrease in shock strength. Due to the five percent smaller channel length for the baseline channel shape, the primary shock wave reaches the outlet side sooner compared to the optimised design. The distribution in Figure 20 at θ_2 shows that for the baseline geometry the wave is reflected back as a secondary shock wave. In case of the optimised geometry and at the same instance in time, the wave is still travelling to the right just about to impinge on the outlet side. Finally, time instances θ_3 and θ_4 illustrate the generation of the reflected, secondary shock wave. Again, as the secondary shock wave is generated earlier in case of the baseline model there is a time shift between baseline and optimised model. Nonetheless, the overall shock strength in both examples is comparable and appears to be unimpeded by the difference in geometry.

The pressure distribution in the ports through a single cycle at both in- and outlet side is

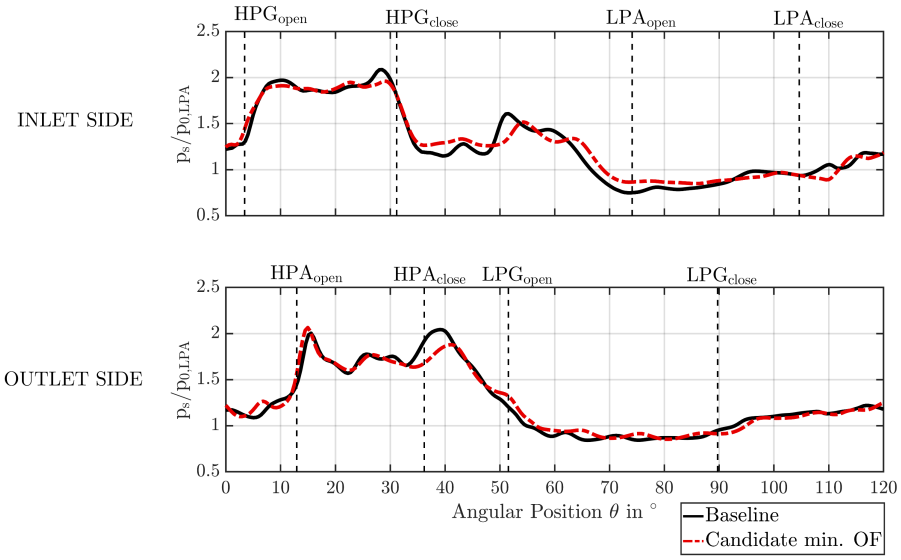

(a)

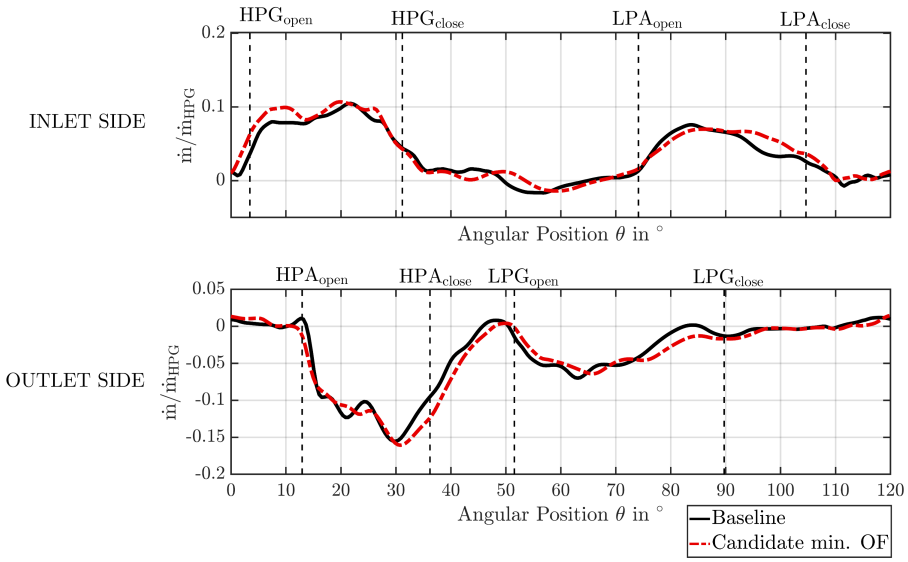

(b)

Fig. 21: (a) Comparison of pressure distribution and (b) mass flow rates at the inlet port side (upper) and outlet port side (lower) for baseline (solid, black curve) and optimised geometry (broken, red curve).

given in Figure 21. Despite the alterations in rotor geometry, there appears to be little qualitative difference between baseline and optimised geometry in terms of the pressure distributions in the inlet and outlet ports. Similarly, looking at instantaneous mass flow rates at inlet and outlet side exhibits no significant changes in flow rates. The mass flow rates through the ports depict that the predominant flow direection is indeed in axial direction, with no significant instances of flow

reversal. This situation persists for the optimised geometry.

Therefore, despite increased incidence and mixing losses determined from the loss audit, the modifications made to the channel shape appear not to have changed the overall gas dynamics significantly. The most prominent penalty can be witnessed with respect to the generation of the primary shock wave and altered impingement timing of the shock waves at the end plates. This is a consequence of larger incidence losses and is responsible for the decrease witnessed in pressure ratio. Nonetheless, secondary shock wave strength remains unaltered along with the pressure and mass flow distribution along the stator in- and outlet side.

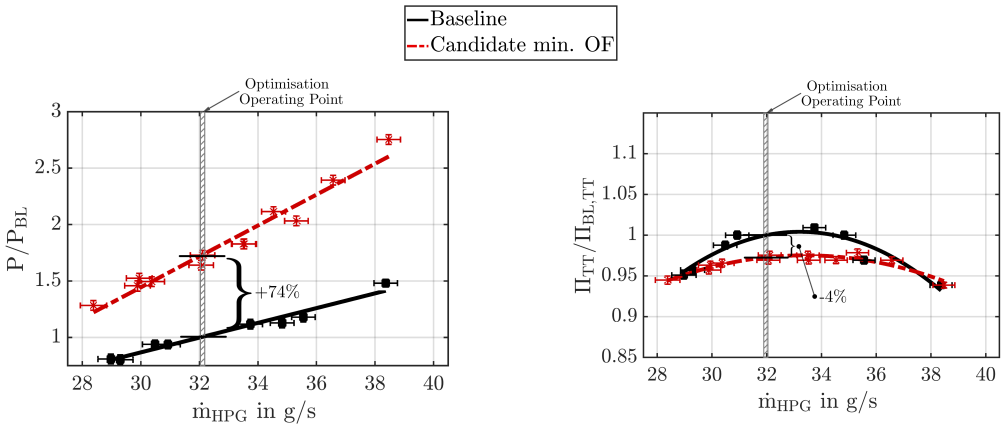

(a) (b)

Fig. 22: Experimental results for (a) power and (b) pressure ratio comparing baseline and optimised rotor. The data are plotted against inlet mass flow rate through the HPG duct and were normalised by the baseline data at the target optimisation point.

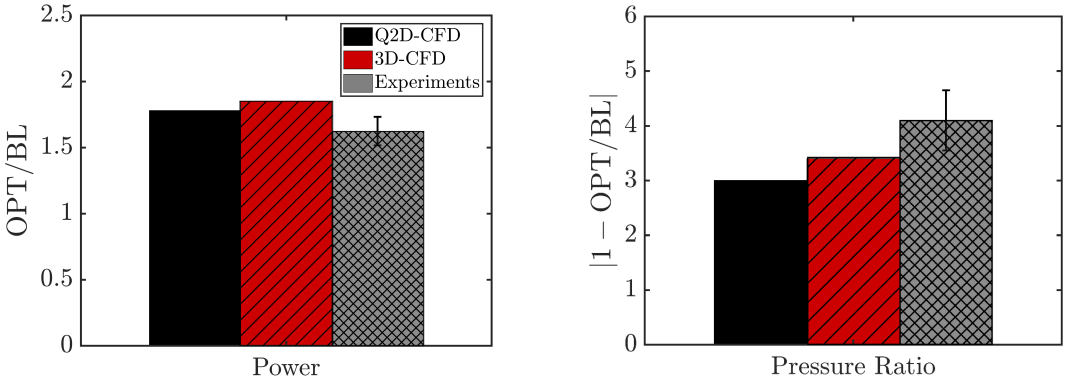

(a) (b)

Fig. 23: Comparison of performance difference between the baseline model and optimised design for Q2D-CFD, 3D-CFD and as witnessed in the experiments. (a) depicts the power increase and (b) the absolute pressure ratio difference expressed in percentage.

3.3 Experimental Validation

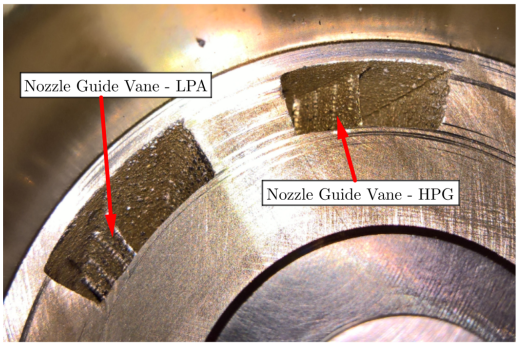

Fig. 24: Inlet guide vanes located in the high- and low pressure ports on the inlet side to maintain inlet velocity triangles.

Both rotor designs were tested experimentally on the University of Bath gas stand at the same operating conditions as imposed as boundary conditions in the CFD computations. Figure 22 shows a back-to-back comparison of the two wave rotor designs for power output and pressure ratio. At the target optimisation point of 32 g/s the data indicate a substantial increase in shaft power output of 74% and a slight decrease pressure ratio of approximately 4%. Figure 23 yields a comparison of the relative difference in performance between the baseline model and the optimised model for power (Fig. 23(a)) and pressure ratio (Fig. 23(b)) for the two numerical models used (Q2D-CFD and 3D-CFD) and data obtained from the laboratory tests. The data yield that the trends witnessed in the numerical models translates into experimental testing. The laboratory test data exhibit an increase in power by a factor of approximately 1.62 and hence lower than the figures predicted by CFD. This can most likely be attributed to manufacturing uncertainties with respect to the inlet guide vanes, as shown in Figure 24. This exhibits deviations from the ideal and smooth shape used in the numerical campaign. In terms of pressure ratio similar trends are visible. There clearly is a pressure ratio penalty for the optimised design, which increases from approximately three percent in the numerical model to 5.6 percent witnessed in the experiments. The reason for the increase is most likely founded in the fact that the CFD model does not consider any interaction of the flow within the channel with the leakage cavity. Nonetheless, the experimental data give fidelity in both the Q2D and 3D model to be able to reproduce trends with reasonable accuracy without the need to resort to higher fidelity models and greater domain detail.

4 Conclusions and Outlook

In this paper, a numerical optimisation of an axial, throughflow wave rotor turbine is presented for the first time. The approach employed a combined quasi-two-dimensional, transient CFD and hybrid evolutionary algorithm. The primary objective of the optimisation campaign was to improve the power output while ensuring pressure exchange capabilites are not significantly penalised.

A hybrid-GA has been proposed that first runs a predefined number of generations using a standard, elitist GA. The generated data is then used to train a surrogate model, which is then used to perform auxiliary optimisation. The surrogate model is then constantly updated as the optimisation routine minimises it using additional constraints. These constraints select the subsequent design candidate to undergo costly CFD simulations based on its distance from previously

evaluated points. The optimisation then runs through a defined search pattern, varying exploitation (local search) and exploration (global search).

For the wave rotor optimisation a single operating point was selected and the rotor channel camberline shape and wall thickness parameterised using five different parameters. The stator port solution and port angles were kept constant. In addition, the number of channels in the rotor was allowed to vary as well. The objective function aims at increasing power output with additional constraints on minimum pressure ratio, channel width and the number of channels.

Two optimisation runs were started, where one employed the hybrid-GA algorithm and the other MATSuMoTo. Both methods converge quickly to a minimum with the hybrid-GA requiring fewer than 100 design evaluations and MATSuMoTo approximately 350. The best candidate design of both optimisations indicated an increase in predicted power output by a factor of 1.78.

In order to evaluate the designs further a direct comparison of the optimised design with the baseline design in three dimensional CFD confirmed a higher channel loading and thus an increase in power output. The three dimensional CFD results confirm the findings of the quasi-two-dimensional model emphasising the validity of using such a reduced order model for optimsiation.

The results imply that the increase in momentum transfer results in an increase in entropy production, in particular at the HPG port inlet and at the highly skewed mixing interface between hot and cold gas streams. In addition, the evolution of inlet incidence angle exhibits that the incidence angle for the optimised design is initially more negative during the opening phase of the channel to the HPG duct. This accounts for a higher flow separation and thus entropy production. Overall, incidence angles appear to vary substantially as a consequence of finite passage opening and are predominantly negative throughout the phases with maximum shaft power generation implying that camberline curvature is the dominant driver to shaft power generation as opposed to incidence momentum change. However, the results indicate that further optimisation potential may be exploitable if the stator arrangement is included in the optimisation.

A gas dynamic analysis within the channels revealed that the geometry modification affects the generation of the primary shock wave as well as the timing at which waves impinge at in- and outlet side. The effect on primary shock wave generation is the main driver for the witnessed decrease in pressure ratio, while secondary shock waves and port pressure and mass flow distributions remain unchanged by the optimisation results.

Comparing baseline and optimised design on a gas stand indicates an increase in power output of approximately 1.65 and decrease in pressure ratio of 4 percent confirming the trends witnessed in the numerical models. It can thus be concluded that the quasi-two-dimensional represents a viable tool to efficiently optimise wave rotor designs.

Acknowledgements This research presented in this paper made use of the Balena High Performance Computing (HPC) Service at the University of Bath. The authors would also like to thank Juliane Müller for her guidance and help with the MATSuMoTo toolbox.

References

1. J. Piechna, P. Akbari, F. Iancu and N. Müller: Radial-Flow Wave Rotor Concepts, Unconventional Designs and Applications (2004). DOI 10.1.1.642.630. URL `https://doi.org/10.1.1.642.630`
2. K. Kurec, J. Piechna and N. Müller: Numerical Investigation of The Radial Disk Internal Combustion Engine. Archivum Combustionis **34**(1), 1–26 (2014)
3. R.D. Pearson: A Gas Wave-Turbine Engine Which Deveoped 35 HP and Performed Over a 6:1 Speed Ranges. In: Proceedings ONR/NAVAIR Wave Rotor Research and Technology Workshop. Naval Postgraduate School (1985)
4. R. Jagannath, S.P. Bane and M.R. Nalim: Wave Rotor Combustor Turbine Model Development. AIAA 2015-4188 (2015). DOI {10.2514/6.2015-4188}. URL `https://doi.org/10.2514/6.2015-4188`
5. R. Jagannath, S.P. Bane and M.R. Nalim: Numerical Modeling of a Wave Turbine and Estimation of Shaft Work. Journal of Fluids Engineering **140**, 101106–1–101106–13 (2018). DOI 10.1115/1.4040015. URL `https://doi.org/10.1115/1.4040015`

6. S. Tüchler and C.D. Copeland: Validation of a Numerical Quasi One-Dimensional Model for Wave Rotor Turbines with Curved Channels. Journal of Engineering for Gas Turbines and Power **142**(2) (2020). DOI 10.1115/1.4044286. URL https://doi.org/10.1115/1.4044286
7. S. Chan, H. Liu, F. Xing and H. Song: Wave Rotor Design Method With Three Steps Including Experimental Validation. J. Eng. Gas Turbines Power **140**(11), 111201–1–111201–13 (2018). DOI 10.1115/1.4038815. URL https://doi.org/10.1115/1.4038815
8. K. Okamoto, T. Nagashima and K. Yamaguchi: Introductory Investigation of Micro Wave Rotor. In: International Gas Turbine Congress 2003 Tokyo (2003)
9. M. Mataczynski, J. Hoke, D.E. Paxson and M.D. Polanka: Design, Simulation, and Testing of a Pressure Wave Supercharger for a Small Internal Combustion Engine. In: SAE 2014 Aerospace Systems and Technology Conference. SAE International (2014). DOI 10.4271/2014-01-2136. URL https://doi.org/10.4271/2014-01-2136
10. H.D. Perkins and D.E. Paxson: Summary of Pressure Gain Combustion Research at NASA. NASA/TM-2018-219874 (2018)
11. J. Wilson: An Experimental Determination of Losses in a Three-Port Wave Rotor. J. Eng. Gas Turbines Power **120**(4), 833–842 (1998). DOI 10.1115/1.2818476. URL https://doi.org/10.1115/1.2818476
12. J. Wilson: Design of the NASA Lewis 4-Port Wave Rotor Experiment. Tech. rep., NASA Contractor Report 202351 (1997). DOI 10.2514/6.1997-3139. URL https://doi.org/10.2514/6.1997-3139
13. M.R. Nalim, J.C. Moscari and E.L. Resler: Wave Cycle Design for NOX Limited Wave Rotor Core Engines for High Speed Propulsion. ASME Paper 93-GT-426 (1993). DOI 10.1115/93-GT-426. URL https://doi.org/10.1115/93-GT-426
14. W.J. Thayer, R.T. Taussig, J.F. Zumdieck, T.S. Vaidyanathan and W.C. Christiansen: Energy Exchanger Performance and Power Cycle Evaluation: Experiments and Analysis. Tech. rep., Final Report submitted by MSNW to DOE under Contract AC06-78ER01084 (1981)
15. A. Meyer: Recent Developments in Gas Turbines. Journal of Mechanical Engineering **69**(4), 273–277 (1947)
16. Taussig, R., Hertzberg, A.: Wave rotors for turbomachinery. In: J.F. Sladky (ed.) Winter Annual Meeting of the ASME, Machinery for Direct Fluid-Fluid Energy Exchange, pp. 1–7. AD-07 (1984)
17. R. Moritz: Rolls-Royce Study of Wave Rotors (1965–1970). In: Proceedings ONR/NAVAIR Wave Rotor Research and Technology Workshop, pp. 116–124. Naval Postgraduate School (1985)
18. P.H. Snyder: Wave Rotor Demonstrator Engine Assessment. ASME Paper 96-GT-041 (1996). DOI {10.1115/96-GT-041}. URL {https://doi.org/10.1115/96-GT-041}
19. A. Fatsis and Y. Ribaud: Numerical Analysis of the Unsteady Flow Inside Wave Rotors Applied to Air Breathing Engines. In: 13th International Symposium on Airbreathing Engines (1997)
20. A. Fatsis and Y. Ribaud: Thermodynamic Analysis of Gas Turbines Topped with Wave Rotors. Aerosp. Sci. Technol. **3**(5), 293–299 (1999). DOI {10.1016/S1270-9638(00)86965-5}. URL {https://doi.org/10.1016/S1270-9638(00)86965-5}
21. J. Wilson and D.E. Paxson: Jet Engine Performance Enhancement Through Use of a Wave-Rotor Topping Cycle. NASA TM-4486 (1993)
22. G.E. Welch, S.M. Jones and D.E. Paxson: Wave Rotor-Enhanced Gas Turbine Engines. J. Eng. Gas Turbines Power **119**(2), 469–477 (1997). DOI 10.1115/1.2815598. URL {https://doi.org/10.1115/1.2815598}
23. G.E. Welch: Overview of Wave-Rotor Technology for Gas Turbine Engine Topping Cycles. Novel Aero Propulsion Systems International Symposium pp. 2–17 (2000). London
24. M. Berchtold and F.J. Gardiner: The Comprex: A New Concept of Diesel Supercharging. ASME Paper 58-GTP-16 (1958). DOI {10.1115/58-GTP-16}. URL {https://doi.org/10.1115/58-GTP-16}
25. G. Zehnder: Calculating Gas Flow in Pressure-Wave Machines. Journal of Mechanical Engineering **71**(4-5), 172–176 (1971)
26. J. Piechna: Autonomous Pressure Wave Compressor Device. ASME Paper IGTC03-FR-305 (2003)
27. J. Zhao and D. Hu: An Improved Wave Rotor Refrigerator Using an Outside Gas Flow for Recycling the Expansion Work. Shock Waves **27**(2), 325–332 (2017). DOI {10.1007/s00193-016-0648-x}. URL {https://doi.org/10.1007/s00193-016-0648-x}
28. D. Hu, Y. Yu and P. Liu: Enhancement of Refrigeration Performance by Energy Transfer of Shock Wave. Applied Thermal Engineering **130**, 309–318 (2018). DOI 10.1016/j.applthermaleng.2017.11.040. URL {https://doi.org/10.1016/j.applthermaleng.2017.11.040}
29. D. Hu, Y. Yu, P. Liu, X. Wu and Y. Zhao: Improving Refrigeration Performance by Using Pressure Exchange Characteristic of Wave Rotor. Journal of Energy Resources Technology, Transactions of the ASME **141**(2) (2019). DOI 10.1115/1.4041722. URL {https://doi.org/10.1115/1.4041722}
30. J. Li, E. Gong, L. Yuan, W. Li and K. Zhang: Experimental Investigation on Pressure Rise Characteristics in an Ethylene Fuelled Wave Rotor Combustor. Energy & Fuels **31**(9), 10165–10177 (2017). DOI 10.1021/acs.energyfuels.7b01769. URL {https://doi.org/10.1021/acs.energyfuels.7b01769}
31. M.R. Nalim, P.H. Snyder and M. Kowalkowski: Experimental Test, Model Validation and Viability Assessment of a Wave-Rotor Constant-Volume Combustor. Journal of Propulsion and Power **33**(1), 163–175 (2017). DOI 10.2514/1.B36174. URL {https://doi.org/10.2514/1.B36174}
32. J. Li, E. Gong, L. Yuan, W. Li and K. Zhang: Experimental Investigation on Flame Formation and Propagation Characteristics in an Ethylene Fuelled Wave Rotor Combustor. Energy & Fuels **32**(2), 2366–2375 (2018). DOI {10.1021/acs.energyfuels.7b03055}. URL {https://doi.org/10.1021/acs.energyfuels.7b03055}

33. A. Tarraf, R. Ebrahimi, M.E. Feyz and R. Nalim: Application of Response Surface Methodology to Investigate the Hot-Jet Ignition of Methane-Hydrogen Mixtures in a Constant-Volume Combustor. 10th U.S. National Combustion Meeting (2017)
34. R.D. Pearson: Thermodynamics and Gas Dynamics of Internal Combustion Engines, Volume II. In: D.E. Winterbone and S.C. Low (ed.) The Oxford Handbook of Innovation. Oxford University Press, Oxford (1986)
35. J. Piechna and D. Dyntar: Hybrid Wave Engine Concept and Numerical Simulation of Engine Operation. The Archive of Mechanical Engineering **LVII**(1) (2010). DOI {10.4271/2017-01-2046}. URL {https://doi.org/10.4271/2017-01-2046}
36. D.E. Paxson: A General Numerical Model for Wave Rotor Analysis. NASA-TM-105740 (1992)
37. D.E. Paxson and J. Wilson: An Improved Numerical Model for Wave Rotor Design and Analysis. AIAA (1993). DOI {10.2514/6.1993-482}. URL {https://doi.org/10.2514/6.1993-482}
38. D.E. Paxson and J. Wilson: Recent Improvements to and Validation of the One Dimensional NASA Wave Rotor Model. NASA-TM-106913 (1995)
39. D.E. Paxson: A Numerical Model for Dynamic Wave Rotor Analysis. AIAA-95-2800 (1995). DOI {10.2514/6.1995-2800}. URL {https://doi.org/10.2514/6.1995-2800}
40. G.E. Welch and D.E. Paxson: Wave Turbine Analysis Tool Development. NASA/TM-1998-208485 (1998). DOI {10.2514/6.1998-3402}. URL {https://doi.org/10.2514/6.1998-3402}
41. D.E. Paxson: A Numerical Investigation of the Startup Transient in a Wave Rotor. J. Eng. Gas Turbines Power **119**(3), 676–682 (1997). DOI {10.1115/1.2817039}. URL {https://doi.org/10.1115/1.2817039}
42. D.E. Paxson and J.W. Lindau: Numerical Assessment of Four-Port Through-Flow Wave Rotor Cycles with Passage Height Variation. NASA TM-107490 (1997). DOI {10.2514/6.1997-3142}. URL {https://doi.org/10.2514/6.1997-3142}
43. Taussig, R., Hertzberg, A.: Wave rotors turbofan engines for aircraft. In: J.F. Sladky (ed.) Winter Annual Meeting of the ASME, Machinery for Direct Fluid-Fluid Energy Exchange, pp. 9–45. AD-07 (1984)
44. J. Piechna: Comparison of different methods of solution of Euler equations in application to simulation of the unsteady processes in wave supercharger. Arch. Mech. Eng. **XLV**(2), 87–106 (1998). Warsaw, Poland
45. J. Piechna: Numerical simulation of the comprex type of supercharger: comparison of two models of boundary conditions. Arch. Mech. Eng. **XLV**(2), 233–250 (1998). Warsaw, Poland
46. J. Piechna, R. Cerpa, S. Marcin, P. Akbari and Nüller: Numerical Analysis of the Wave Topping Unit for Small Turbojet. In: Proceedings of ASME Turbo Expo 2010: Power for Land, Sea and Air. International Gas Turbine Institute (2010). DOI {10.1115/GT2010-23064}. URL {https://doi.org/10.1115/GT2010-23064}
47. S. Tüchler and C.D. Copeland: Experimental Results from the Bath μ-Wave Rotor Turbine Performance Tests. Journal of Energy Conversion and Management **189**, 33–48 (2019). DOI {10.1016/j.enconman.2019.03.079}. URL {https://doi.org/10.1016/j.enconman.2019.03.079}
48. J. Wilson and D. Fronek: Initial results from the NASA-Lewis Wave Rotor Experiment. AIAA-93-2521 (1993). DOI {10.2514/6.1993-2521}. URL {https://doi.org/10.2514/6.1993-2521}
49. T. Nagashima, K. Okamoto and Y. Ribaud: Cycles and Thermal System Integration Issues of Ultra-Micro Gas Turbines. Educational Notes RTO-EN-AVT-131, Neuilly-sur-seine, France (2005)
50. S.N. Lophaven, H.B. Nielsen and J. Søndergaard: DACE - A Matlab Kriging Toolbox, Version 2.0. Technical University of Denmark (2002)
51. J. Müller and R. Piché: Mixture Surrogate Models Based on Dempster-Shafer Theory for Global Optimization Problems. Journal of Global Optimization **51**, 79–104 (2011). DOI {10.1007/s10898-010-9620-y}. URL {https://doi.org/10.1007/s10898-010-9620-y}
52. S.-B. Ma and K.-Y. Kim: Optimization of discrete cavities in a centrifugal compressor to enhance operating stability. Aerospace Science and Technology **68**, 308 – 319 (2017). DOI {10.1016/j.ast.2017.05.029}. URL {https://doi.org/10.1016/j.ast.2017.05.029}
53. S.-B. Ma, A. Afzal and K.-Y. Kim: Optimization of ring cavity in a centrifugal compressor based on comparative analysis of optimization algorithms. Applied Thermal Engineering **138**, 633 – 647 (2018). DOI {10.1016/j.applthermaleng.2018.04.094}. URL {https://doi.org/10.1016/j.applthermaleng.2018.04.094}
54. R.G. Regis and C.A. Shoemaker: Constrained Global Optimization of Expensive Black Box Functions Using Radial Basis Functions. Journal of Global Optimization **31**, 153 – 171 (2005). DOI {10.1007/s10898-004-0570-0}. URL {https://doi.org/10.1007/s10898-004-0570-0}
55. R.G. Regis and C.A. Shoemaker: A quasi-multistart framework for global optimization of expensive functions using response surface models. Journal of Global Optimization **56**, 1719–1753 (2013). DOI {10.1007/s10898-012-9940-1}. URL {https://doi.org/10.1007/s10898-012-9940-1}
56. S. Chan, H. Liu and F. Xing: Defining the Thermodynamic Efficiency in a Wave Rotor. J. Eng. Gas Turbines Power **140**(11), 112601–1–112601–11 (2016). DOI {10.1115/1.4033508}. URL {https://doi.org/10.1115/1.4033508}
57. J.Wilson, GE. Welch and D.E. Paxson: Experimental Results of Performance Tests on a Four-Port Wave Rotor. NASA/TM–2007-214488 (2017). DOI {10.2514/6.2007-1250}. URL {https://doi.org/10.2514/6.2007-1250}
58. C. L. Iandoli and E. Sciubba: 3-D Numerical Calculation of the Local Entropy Generation Rates in a Radial Compressor Stage. Int. J. of Thermodynamics **8**(2), 83–94 (2005). DOI {10.5541/ijot.148}. URL {https://doi.org/10.5541/ijot.148}

59. H. Herwig and F. Kock: Local Entropy Production in Turbulent Shear Flows: A Tool for Evaluating Heat Transfer Performance. Journal of Thermal Science **15**(2), 159–167 (2006). DOI {10.1007/s11630-006-0159-7}. URL {https://doi.org/10.1007/s11630-006-0159-7}
60. L.C.W. Dixon and G. Szegö: The Global Optimization Problem. An Introduction. Toward Global Optimization **2**, 1–15 (1978)
61. J. Müller and R. Piché: Mixture Surrogate Models Based on Dempster-Shafer Theory for Global Optimization Problems. Journal of Global Optimization **51**, 79–104 (2011). DOI {10.1007/s10898-010-9620-y}. URL {https://doi.org/10.1007/s10898-010-9620-y}
62. J. Müller, C.A. Shoemaker and R. Piché: SO-MI: A Surrogate Model Algorithm for Computationally Expensive Nonlinear Mixed-Integer Black Box Global Optimization Problems. Computers and Operations Research **40**, 1383–1400 (2013). DOI {10.1016/j.cor.2012.08.022}. URL {https://doi.org/10.1016/j.cor.2012.08.022}
63. J. Müller, C.A. Shoemaker and R. Piché: SO-I: A Surrogate Model Algorithm for Computationally Expensive Nonlinear Integer Programming Problems Including Global Optimization Applications. Journal of Global Optimization **59**, 865–889 (2014). DOI {10.1007/s10898-013-0101-y}. URL {https://doi.org/10.1007/s10898-013-0101-y}
64. J. Müller and C.A. Shoemaker: Influence of Ensemble Surrogate Models and Sampling Strategy on the Solution Quality of Algorithms for Computationally Expensive Black-Box Global Optimization Problems. Journal of Global Optimization **60**, 123–144 (2014). DOI {10.1007/s10898-014-0184-0}. URL {https://doi.org/10.1007/s10898-014-0184-0}
65. A. Châtel, T. Verstraete, G. Coussement and L. Mueller: Single-Point Optimization of the LS89 Turbine Cascade Using a Hybrid Algorithm. In: ASME Turbo Expo 2018: Turbomachinery Technical Conference and Exposition, Volume 2D: Turbomachinery. International Gas Turbine Institute (2018). DOI {10.1115/GT2018-75683}. URL {https://doi.org/10.1115/GT2018-75683}
66. A. Châtel, T. Verstraete and G. Coussement: Multi-Point Optimization of an Axial Turbine Cascade using a Hybrid Algorithm. In: Proceedings of ASME Turbo Expo 2019: Turbomachinery Technical Conference and Exposition. International Gas Turbine Institute (2019). DOI {10.1115/1.4046231}. URL {https://doi.org/10.1115/1.4046231}

Appendix 1

Numerical Test Cases

In order to obtain an estimate of the performance and gain fidelity in the routine, the hybrid method is tested on a number of synthetic optimisation problems for global optimisation. This includes the Dixon and Szegö test functions [60] (Branin, Goldstein-Price, Hartman 3, Hartman 6, Shekel 5, Shekel, 7 and Shekel 10) as well as the non-convex, non-linear Rosenbrock, Ackley and Rastrigin functions. A summary of the test problems is given in Table 8. Furthermore, the performance of the hybrid algorithm compared with a standard elitist GA, PSO as well as MATSuMoTo, another surrogate based optimisation routine [61–64]. MATSuMoTo differs as it uses design of experiments (such as latin-hypercube sampling) to create the initial training set and uses radial basis functions (RBF) to construct the surrogate model. Instead of a user defined search pattern, MATSuMoTo uniformly selects data points from the design space and perturbing them with a randomly chosen standard deviation. For each of the candidate points a weighted score based on their objective function value predicted by the surrogate model is computed and the candidate with the best score is selected as the subsequent evaluation point. Furthermore, the algorithm cycles through a predefined weight pattern in order to alternate between local exploitation and exploration.

The idea behind using the test problems is that they represent complex surfaces that pose a reasonable challenge for any optimisation routine with non-convex shapes, multiple parameters and multiple local minima. They may not be able to recreate the challenges for wave rotor optimisation, but are cheap to solve and should at least give an idea whether an optimisation routine has the potential of swiftly finding optimal solutions. Therefore, each optimisation routine is run through the test problems 30 times with a fixed computational budget of 1000 expensive function evaluations. The global optimum as well as its location of each function are known, so that the optimisation can be regarded as successful when the best confirmed function value falls within a threshold of 1 percent of the global optimum. In case the function value at the global optimum is zero, the

threshold is set to 0.05. For the hybrid algorithm, three different search patterns are examined with the aim of finding a universally applicable pattern that can be further used for optimising the wave rotor turbine. The search patterns used feature two of length six and one of length five β_1=[0.9, 0.75, 0.25, 0.05, 0.03, 0], β_2=[0.95 0.25 0.05 0.03 0] and β_3=[0.95 0.5 0.25 0.1 0.05 0].

For each test problem GA parameters of population size, crossover fraction were varied in order to estimate the sensitivity of results to the choice of these parameters. The same approach was done for PSO regarding swarm size, self adjustment and social adjustment weights. In both instances, only the results of the best set of options is used for comparison of the different optimisation methods. The results for these cases are reported in Section 4.

Table 8: List of mathematical functions used as test problems to compare a standard GA, PSO, MATSuMoTo and the hybrid algorithm.

Test function	Dimensions	Search space	Number of local minima	Number of global minima	Value global minimum/minima
Branin	2	[-5, 10], [0, 15]	3	3	0.398
Goldstein-Price	2	$[-2, 2]^2$	4	1	3
Hartman 3	3	$[0, 1]^3$	4	1	-3.86
Hartman 6	6	$[0, 1]^6$	4	1	-3.32
Shekel 5	4	$[0, 10]^4$	5	1	-10.1532
Shekel 7	4	$[0, 10]^4$	7	1	-10.4029
Shekel 10	4	$[0, 10]^4$	10	1	-10.5364
Rastrigin 2	2	$[-5.2, 5.2]^2$	>10	1	0
Rastrigin 3	3	$[-5.2, 5.2]^3$	>10	1	0
Rastrigin 4	4	$[-5.2, 5.2]^4$	>10	1	0
Rosenbrock	2	$[-2, 2]^2$	1	1	0
Ackley	2	$[-15, 30]^2$	>10	1	0

Appendix 2

Results Numerical Test Cases

The average number of function evaluations to reach a relative error of 1 percent of the known, global minimum for GA, PSO, hybrid algorithm and MATSuMoTo is given in Table 9. In addition the standard deviation is presented in parentheses along with the number of instances, when the algorithm was unable to detect the global optimum within 1000 iterations. In case a certain number of runs does not finish within the iteration limit, the run is excluded from being evaluated in the averaging process. For all pure GA runs a population size of ten was used and a crossover fraction of 0.6 was used, with the exception of Shekel 5, which required a crossover fraction of 0.5. Pertaining to PSO, the general trend across all trials implied lower swarm sizes leading to accelerated convergence. Therefore, the swarm size chosen varied in between 5 to 10 depending on the problem in conjunction with self- and social adjustment weights of varying between 1.49 and 1.59 respectively.

Nonetheless, even with a tweaked set of model parameters, the elitist GA and PSO, as implemented in Matlab R2017b, struggle to consistently detect the optimum over 1000 function evaluations. The two evolutionary algorithms face particular challenges with multi-dimensional functions

Table 9: Average number of function evaluations necessary to be within 1 percent of the global optimum for different optimisation algorithms on the test problems. The number in parentheses gives the standard deviation. The number in square brackets denotes the number of runs that failed to find the global optimum within 1000 iterations.

Test function	GA	PSO	Hybrid-GA β_1	Hybrid-GA β_2	Hybrid-GA β_3	MATSuMoTo SLHS-RBFtps
Branin	217.0 (23.4) [0]	137.0 (11.3) [0]	43.7 (1.7) [0]	35.1 (1.5) [0]	40.2 (1.8) [0]	54.7 (2.3) [0]
Goldstein-Price	484.0 (23.4) [0]	204.0 (23.5) [0]	71.6 (4.6) [0]	60.1 (4.1) [0]	64.2 (3.8) [0]	107.5 (7.1) [0]
Hartman 3	242.0 (19.4) [0]	100.3 (11.25) [0]	49.0 (3.3) [0]	42.7 (1.9) [0]	48.5 (2.3) [0]	42.1 (4.6) [0]
Hartman 6	521.7 (45.1) [7]	461.8 (38.1) [2]	236.1 (30.0) [0]	208.5 (33.9) [0]	203.3 (29.6) [0]	154.1 (19.9) [0]
Shekel 5	610.0 (101.9) [24]	643.5 (37.3) [3]	176.8 (19.8) [0]	181.6 (23.6) [0]	148.5 (11.1) [0]	202.5 (32.6) [0]
Shekel 7	633.3 (59.2) [21]	633.3 (41.5) [1]	132.4 (12.2) [0]	131.3 (13.2) [0]	123.1 (9.5) [0]	118.5 (18.3) [0]
Shekel 10	655.6 (50.1) [21]	622.6 (40.78) [1]	103.7 (8.3) [0]	105.3 (8.0) [0]	109.7 (16.6) [0]	111.9 (13.3) [0]
Rastrigin 2	692.4 (52.9) [1]	381.2 (32.6) [0]	69.0 (8.0) [0]	83.7 (12.0) [0]	81.3 (10.5) [0]	40.4 (9.2) [0]
Rastrigin 3	655.3 (39.7) [11]	632.4 (40.2) [7]	129.4 (17.6) [0]	118.3 (11.5) [0]	126.7 (8.4) [0]	163.9 (32.6) [0]
Rastrigin 4	591.1 (36.7) [21]	633.4 (64.0) [14]	313.3 (47.9) [1]	309.9 (47.7) [4]	199.8 (19.2) [2]	459.5 (73.2) [11]
Rosenbrock	299.1 (27.7) [2]	276.2 (42.2) [0]	297.0 (58.5) [6]	255.2 (46.4) [7]	195.9 (45.7) [0]	107.2 (12.2) [0]
Ackley	364.0 (17.9) [0]	246.2 (16.3) [0]	127.2 (8.4) [0]	106.0 (4.2) [0]	145.4 (10.9) [0]	366.5 (50.3) [1]

containing a large number of local minima. For such problems, such as higher order Rastrigin functions, higher numbers of failed searches are recorded. Overall, PSO appears to perform better with fewer failed cases and faster detection.

All hybrid variants as well as MATSuMoTo outperform GA and PSO. Among the different search patterns used for the hybrid-GA β_2 and β_3 perform better on all test functions with the exception of the two parameter Rastrigin function. Search pattern β_2 performs best on the two-dimensional Branin, Goldstein-Price and Ackley function, but exhibits comparably poor results for the multi-dimensional Rastrigin function as well as the Rosenbrock test. In general, it appears that search pattern β_3 performs marginally better than either of the two other search strategies, in particular for higher order, multimodal functions such as the four dimensional Rastrigin function.

Compared with the surrogate based optimisation of Müller's MATSuMoTo using thin plate splines RBF the hybrid approach performs better on the Branin, Goldstein-Price, Shekel 5, three and four dimensional Rastrigin as well as the Ackley function. It is particularly surprising that MATSuMoTo, at least with the proposed setup, struggles with the higher order Rastrigin problems resulting in eleven failed cases. Both approaches, however, yield similar results for Hartman 3, Shekel 7, Shekel 10. Applied to the multidimensional Hartman 6, two-dimensional Rastrigin and the Rosenbrock function, MATSuMoTo performs better.

Figure 24 shows box plots for a selection of test problems. Only cases without any failed trails are shown. Examining the data for Branin, Goldstein-Price, Hartman 3 and the two-dimensional Rastrigin demonstrates a wide spread of between the 25^{th} and 75^{th} percentile for both GA and PSO with a number of outliers in particular seen for the GA applied to the Branin problem. Overall, the data shows that PSO may converge faster than the standard elitist GA. Comparing the hybrid method with MATSuMoTo on the other hand proves to achieve convergence with little variation. However, there is still the possibility of outliers requiring a higher number of iterations for both surrogate-based models.

Finally, to see how the hybrid-GA, MATSuMoTo fares against other, recently introduced hybrid methods, two single trials are run on the Rastrigin function with five parameters and the

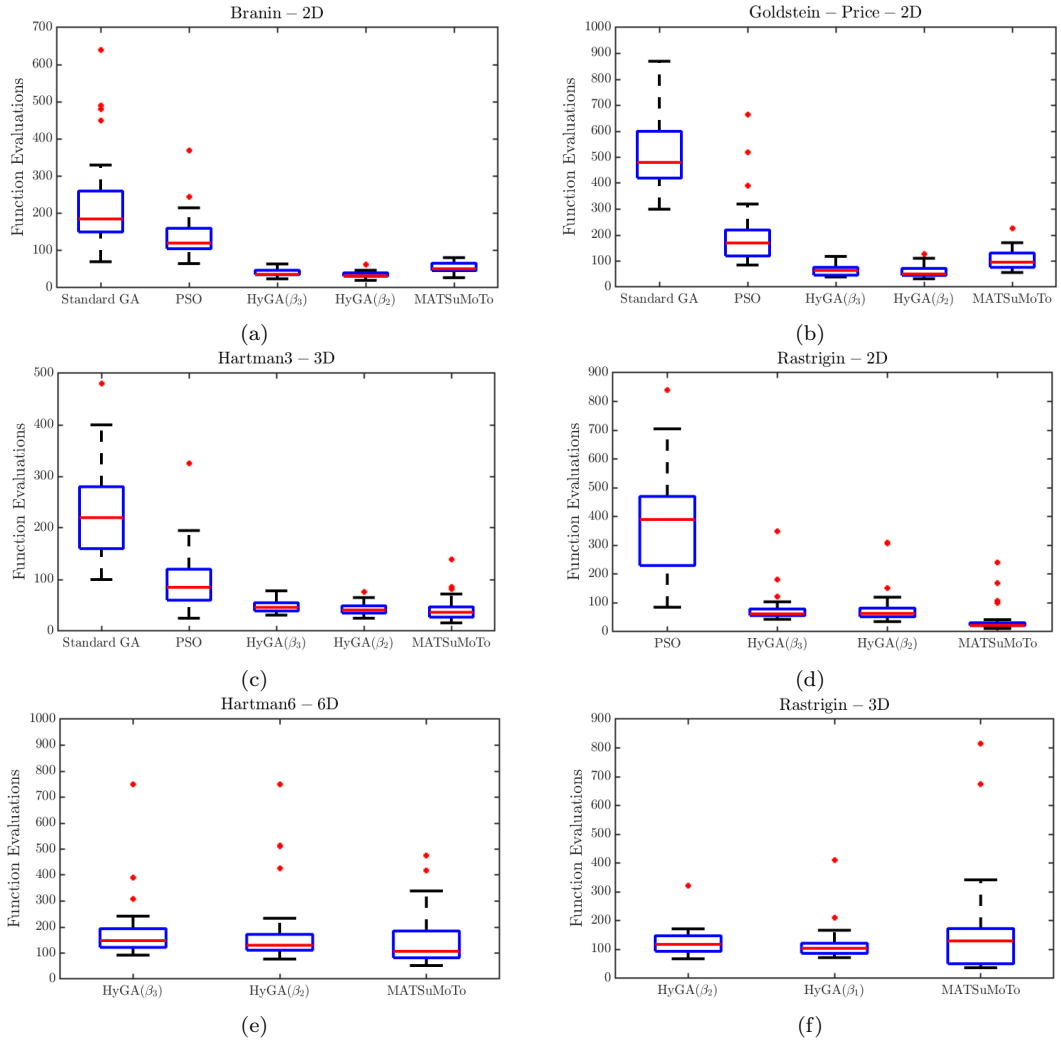

Fig. 24: Box plots showing the statistical data for the number of function evaluations to reach the global optimum with a relative error of 1 percent. For runs with failed cases no box plot is provided.

two-dimensional Rosenbrock function. The comparison is made with another evolutionary algorithm, namely a classical differential evolution (DE) algorithm, hybridised with a steepest descent method developed at the von Karman Institute [65,66]. The convergence rate for both test problems is presented in Figure 25 showing the best detected function value for Rastrigin in (a) and Rosenbrock in (b). Although, the hybrid-DE versions converge steadily and quicker compared to the original DE, both search patterns of the hybrid-GA exhibit steeper convergence and being able to detect the global optimum after approximately 1200 iterations. For the Rosenbrock function hybridised DE again shows a steady convergence rate, while the hybrid-GA with search pattern β_3 quickly determines the global optimum after less than 60 iterations. Both hybrid-GA with search pattern β_2 and MATSuMoTo exhibit extended constant periods, with the former finally reaching the global minimum after around 1000 iterations. The latter, however, does not manage to locate the optimum within the imposed 1500 iterations in the particular shown run.

In sum, the statistical evaluation implies that combining evolutionary algorithms with surrogate

models or substituting evolutionary algorithms completely can yield significant performance gains making these approaches particularly attractive for expensive CFD simulations, such as required for wave rotors.

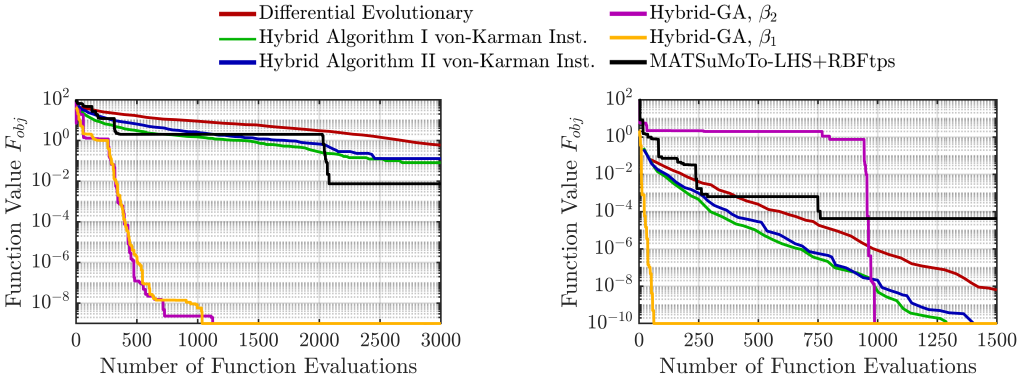

Fig. 25: Comparison of the convergence rate of the hybrid-GA and MATSuMoTo with other hybrid optimisation routines for the (a) five-dimensional Rastrigin function and the (b) two-dimensional Rosenbrock function [65,66].

4.2.1 Summary and Implications of Paper IV

In the first paper in Section 4.2, a numerical optimisation model is introduced that uses a quasi-two-dimensional and surrogate based optimisation routines to optimise the originally parabolically shaped channel camberline of the baseline wave rotor. To keep the overall optimisation run time low, two measures have been introduced consisting of reducing the computational expense of transient CFD computations and accelerating the convergence rate of the optimisation routine. Pertaining to the CFD model used throughout the optimisation study, a reduced model has been used with a single radial cell in the radial direction. This seeks to reduce the computational effort, which becomes particularly crucial for parametric optimisations with several hundreds or more design iterations. Instead of opting for a standard elitist GA or PSO to drive the actual optimisation a hybrid algorithm has been proposed. Initially, this method runs an elitist GA for a reduced number of generations to create a training data set that is fed into a Kriging surrogate model. Subsequently, optimisation is performed solely on the surrogate model, which includes an additional constraint. This ensures that the optimisation alternates the search space limits between global exploration far from all previously evaluated design points and local exploitation. The optimisation yields a design candidate with a 78% increase in power output, while the pressure ratio decreases by 3%. The subsequent detailed 3D-CFD simulation establishes fidelity in reduced order CFD model and attributes the decrease in pressure ratio to an increase in entropy generation due to incidence losses as the flow enters the channels from the HPG port.

The results from this study contain a number of implications for the PhD thesis. First of all, the rigorous validation of the HGA method on a number of test functions clearly indicates superior performance compared with a pure GA and PSO. The paper thus identifies the proposed technique as a well suited, effective and efficient tool for expensive parametric CFD optimisations. However, it is noteworthy that the main limitation of the method transpires for optimisation problems of significantly higher order. In such instances, the number of samples necessary to obtain sufficient accuracy from the surrogate model is severely restricted by the limitations in computational resources. For such applications adjoint optimisation methods are far better suited.

Secondly, the quasi-two-dimensional wave rotor model appears to be able to predict the trends and trade-offs with respect to shaft power extraction and pressure losses due to entropy generation, which compromise the ability to transfer energy. This is an important finding for future, more holistic and comprehensive optimisations in the field of pressure exchangers and wave rotors. As pointed out in the paper, including

port locations and angles in addition to the wave rotor channel shape may exploit the potential of a power generating wave rotor turbine even further, but will require an increased number in iterations as a direct result of the higher dimensionality of the problem. A relatively cheap to run quasi-two-dimensional model in combination with the HGA optimisation approach renders such an ambitious optimisation more feasible and less resource intense.

Thirdly, the results shed further light on the flow dynamics associated with power generation in wave rotors. As highlighted in Chapter 1.5, torque extraction is dominated by the high enthalpy flow entering the wave rotor through the HPG duct. This covers approximately a third of a single cycle meaning that for around 67 % of the cycle a single rotor channel remains idle and does not contribute to generation of shaft power. This appears to be exacerbated by the fact that the incidence angle does not seem to remain constant as the channel passes the port. Initially, as the channel is in the process of opening up to the port, gas enters the channel at very large negative incidence angles, creating pressure losses due to flow separation on the upper channel surface and a force that opposes the direction of rotation. Only during a period of full exposure to the port conditions, can a slightly positive incidence angle and channel curvature start generating shaft power. Overall, this variation in incidence angle, which is largely associated with finite passage opening effects, may thus be identified as a significant challenge in the pursuit for optimal power output of wave rotor turbines.

4.3 Paper V: Experimental and Numerical Assessment of an Optimised, Non-Axial Wave Rotor Turbine

Paper published in *Applied Energy*, [126]:

S. Tüchler and C.D. Copeland, "Experimental and Numerical Assessment of an Optimised, Non-Axial Wave Rotor Turbine," Applied Energy, Vol. 268, 115013, 2020.

Statement of authorship

S. Tüchler (candidate): development and implementation of numerical and experimental methodology, data analysis, preparation of tables and figures, writing and compilation of manuscript.

C.D. Copeland (supervisor): supervision of numerical and experimental work, review and editing of manuscript.

Copyright

Experimental and Numerical Assessment of an Optimised, Non-Axial Wave Rotor Turbine

Stefan Tüchler[a,*], Colin D. Copeland[b]

[a]*Institute for Advanced Automotive Propulsion Systems (IAAPS), Department of Mechanical Engineering, University of Bath, Claverton Down, Bath, Somerset, BA2 7AY, United Kingdom*
[b]*Faculty of Applied Sciences, School of Sustainable Energy Engineering, Simon Fraser University, 10285 University Drive, Surrey, BC V3T 4B7 Vancouver, Canada*

Abstract

Wave rotors exchange energy between different fluid streams via unsteady shock and expansion waves without the application of mechanical parts. This offers potential efficiency gains for a variety of thermodynamic cycles and applications ranging from refrigeration cycles to micro-gas turbines.

This study deals with the experimental and numerical examination of an optimised, four-port wave rotor turbine that functions both as a pressure exchange device and a power generating turbine. The wave rotor channels were optimised for increased power output at a single operating point and was based on a baseline wave rotor of 60 mm in diameter, 30 mm in length with symmetrical channel camber. Both units were experimentally tested on a gas stand in open-loop configuration using electrical heaters as a source of heat for the high pressure inlet and pressurised air for both inlet ducts. Throughout testing, the mass flow rates among high pressure in- and outlet were balanced. To gain further insights into the physics within the rotor, numerical simulations using a quasi-one-dimensional unsteady model were used alongside the experiments.

The experimental results indicate a power increase of 74% at the target operating conditions. The increase in shaft power results in a reduced capacity to exchange pressure yielding a 4% lower pressure ratio. The peak shaft power recorded reached approximately 730 W and the maximum pressure ratio of approximately 1.65. The numerical model indicates that the gas dynamics within the rotor channels prove to be largely insensitive to the changes in blade camber and effective channel length.

*Corresponding author
Email address: S.Tuechler@bath.ac.uk (Stefan Tüchler)

Preprint submitted to Applied Energy *April 14,2020*

Keywords: Wave rotor turbine, Wave action modelling, Wave action, Experimental testing, Pressure exchange

---

Nomenclature

$\dot{m}$ Mass flow rate [kg/s]

c_p Specific heat capacity at constant pressure [J/(kg·K)]

A Cross-section area [m^2]

D Diameter [m]

E Total energy per unit volume [J/m^3]

F Non-dim. friction [-]

G Non-dim. leakage [-]

L Length [m]

R Specific gas constant [J/(kg·K)]

T Temperature [K], non-dim. finite passage opening[-]

U Tangential velocity [m/s]

F Flux vector

S Source term

U State vector

a Speed of sound [m/s]

h Height [m]

k Thermal conductivity [$W/(m \cdot K)$]

p Pressure [Pa]

q Heat flux [W/m^2]

t Time [s]

u Relative velocity [m/s]

w Width [m]

z Axial coordinate [m]

Π Pressure ratio [-]

Ψ EGR rate [-]

α Relaxation factor

β Blade angle [°]

δ Leakage gap [m]

η Efficiency [-]

γ Ratio of specific heats [-]

λ Loop flow ratio [-]

μ Dynamic viscosity [kg/m-s]

ν Kinematic viscosity [m^2/s]

ω Angular speed [rad/s]

ρ Density [kg/m^3]

τ Shear stress [N/m^2]

θ Angular coordinate [rad]

CFD Computational fluid dynamics

EGR Exhaust gas recirculation

FAE Fresh air exhaustion

FS Full scale

HPA High pressure air

HPG High pressure gas

ICE Internal combustion engine

LPA Low pressure air

LPG Low pressure gas

OF Objective function

PCG Pressure gain combustion

PE Pressure exchanger

PWS Pressure wave supercharger
RF Reverse flow
TF Throughflow
b Blade
c Cold
ch Channel
h Hot
h Hydraulic, hot
is Isentropic
lk Leakage
m Mixed
s Static
t Total
v Viscous
x Expansion

1. Introduction

Wave rotors are nonsteady flow devices that transfer energy between different fluid streams through pressure waves without the use of mechanical parts, such as pistons. Typically, these so-called pressure-exchangers consist of a rotor with straight or cambered cellular channels arranged around a cylindrical drum. Stator endplates are mounted in close proximity to the rotor inlet and outlet side and house discrete gas ports. As the rotor spins each wave rotor channel is periodically exposed to the pressure within the ports. This sudden opening and closing of the ports sets off pressure waves compressing or expanding the fluid within the channel cells. Iancu et al. [1] outline that shock compression is an efficient process and results in pressure ratios higher than steady flow diffusers. Weber [2] argued that high shock compression efficiency in combination with simple channel shapes results in compact and lightweight machinery. Further advantages are lower rotational speeds compared with traditional turbomachinery and self-cooling capabilities due the presence of both hot and cold streams in the same device [3].

Wave rotors have been successfully applied to a wide spectrum of applications with the objective of optimising the use of energy resources and enhancing energy processes. Pressure exchange devices are therefore a highly attractive subject to many fields of research and a viable option in the pursuit of increasing thermodynamic efficiency of thermal machinery and thus reducing global energy consumption and greenhouse gas emissions. An overview of these applications is presented in Figure 1. Wave rotors have been applied to increase power output and efficiency of gas turbines through pressure gain combustion (PCG) [4] as well as through additional topping devices [5, 6], wave rotor turbines [7, 8], pressure wave superchargers (PWS) for internal combustion engines (ICE) [9, 10] and refrigeration cycles [11, 12].

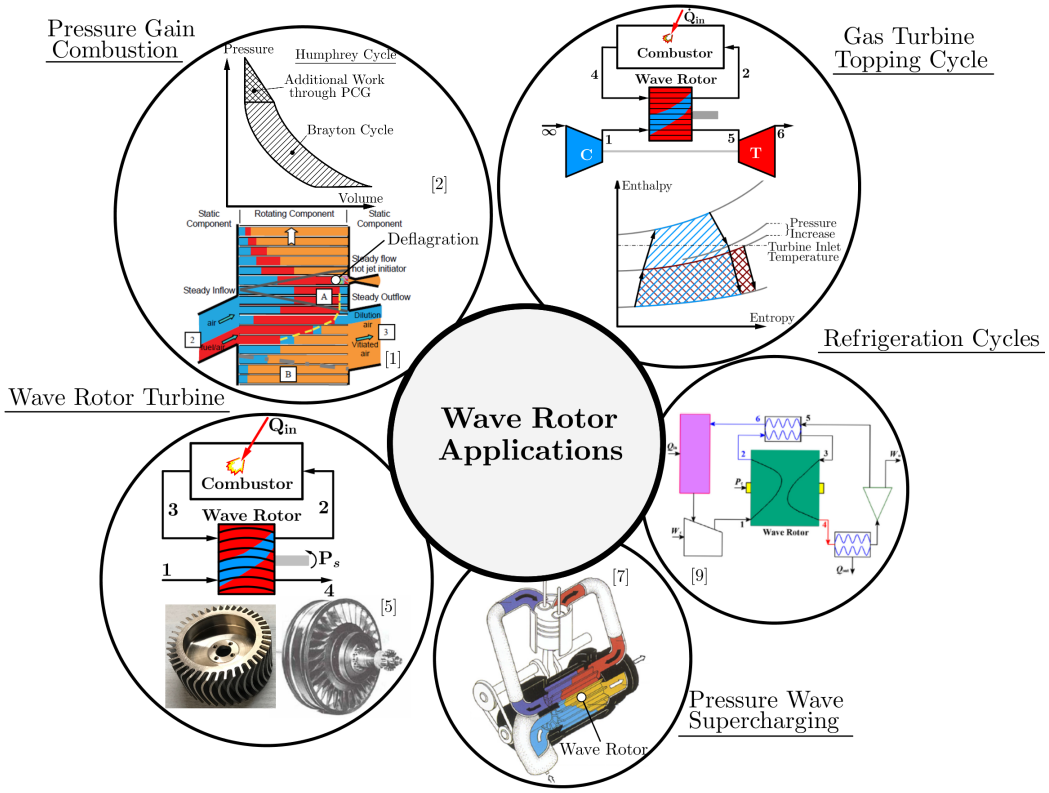

Figure 1: Overview of wave rotor applications ranging from gas turbine efficiency and power output enhancement through pressure gain combustion and the extension of the Brayton cycle with constant-volume combustion [4], topping cycles [5, 6] and wave rotor turbines [7, 8]. Furthermore, wave rotors can be applied to internal combustion engines as a supercharging device [9, 10] and to refrigeration cycles [11, 12] (adapted from [8]).

The commercially most successful and most mature technology using wave rotor technology is as a supercharging device for ICE [13–15]. In a similar fashion to classical turbomachinery, the pressure wave supercharger uses waste heat to pressurise the intake charge. The review done by Costiuc and Chiru [14] concludes that compared with turbocharging the pressure wave supercharging delivers rapid transient response and self-cooling capabilities but suffers severely from insufficient sealing and thermal expansion. Application of wave rotors to gas turbines as a topping device has received considerable attention as well. According to Fatsis [16, 17] and Jones and Welch [18] benefits with respect to power output and fuel consumption

are achievable although benefits of wave rotor topping are reduced in the presence of high cooling flow rates and high compression ratios. For large pressure ratios Klein and Staudacher [19] concluded that a wave rotor can increase both efficiency and net work when used as a constant-volume combustor combined with an intercooler. Most recent applications revolve around cycle enhancement of refrigeration cycles [20–23] and pressure-gain combustion [4, 24–26]. For the former application, Akbari et al. [20] introduced a wave rotor that can combine compression, desuperheating and condensation resulting in a compact refrigeration unit. Zhao and Hu [21] presented an improved refrigeration cycle, where expansion work is routed back to the wave rotor through an additional heat exchanger reducing energy losses by approximately 40%. Hu et al. [22] verified numerically that shock compression is close to isentropic efficiencies for small expansion ratios and relatively weak shock waves.

In the field of pressure-gain combustion, further enhancements in thermal efficiency of gas turbines can be accomplished by replacing the nearly constant pressure combustion of the Brayton cycle by internal, constant volume combustion. Gülen [27] identifies pressure gain combustion as the most potent technology to enhance gas turbine efficiency beyond 65%. Numerical simulations performed by Rajagopal et al. [28] indicated a 40% pressure gain and 20-30% benefit in fuel savings. Nalim [29] further concludes that on-rotor combustion can accommodate both premixed-deflagration as well as non-premixed combustion and premixed/non-premixed autoignition modes. It is furthermore noted that the internal gas dynamics strongly interact with the combustion characteristics leading to potentially higher sensitivity to variations in operating conditions and in particular the fuelling strategy. Additional investigation of the interaction of wave action with combustion dynamics by Nalim et al. [30, 31] found that both premixed and non-premixed combustion require high levels of turbulence to establish complete combustion.

Finally, wave rotors featuring non-axial channel shape enables to combine shaft power extraction with pressure-exchange characteristics. Such an application requires non-axial channel shapes and was successfully exploited by Pearson [7, 32], which achieved thermal efficiencies of 10 %. The wave rotor features passages in helical shape able to deliver a power output of around 26 kW at a design rotational speed of 18,000 rpm. Other campaigns by General Electric and General Power have failed due to insufficient power output [33, 34]. The wave-disk engine concept proposed by Michigan State University and Warsaw University of Technology deals with a radial, reverse flow wave-disk engine that uses shock-waves and curved channels to create shaft power and energy exchange [35, 36]. Numerical simulations indicated efficiencies of up to 10% [37].

At present, wave rotor designs are tweaked manually through the use of nu-

merical methods, including one-dimensional codes, such as introduced by Paxson [38], Okamoto and Nagashima [39] and Fatsis [40], and two-dimensional computational fluid dynamics (CFD) simulations, such as reported by Welch [41]. To the authors' knowledge there has not been any attempt reported in the open literature to improve wave rotor performance through numerical optimisation. Therefore, this study seeks to validate the results of a numerical optimisation of a baseline wave rotor with symmetrical, non-axial channel shape through experimental tests. The optimisation was targeted at enhancing the shaft power output of a baseline micro-wave rotor turbine without compromising its ability to transfer energy. The experimental data aim to establish the potential increase in shaft power output and possible effects on pressure-exchange capacity. In addition, numerical results from a quasi-one-dimensional model shall shed further insights on the impact of the channel curvature changes on the internal gas dynamics. Overall, the experimental results will establish the accuracy and effectiveness of the chosen wave rotor shape optimisation. Additionally it will be shown that micro-wave rotor turbines can achieve highly efficient shock compression while exploiting their potential as a power generating turbine at considerably lower rotational speeds than standard turbomachinery.

The structure of the paper is therefore as follows; firstly, in section 2 the main characteristics of throughflow wave rotor dynamics are briefly presented before outlining the scope and results of the optimisation study. Then the experimental setup is introduced as well as a brief description of the quasi-one-dimensional model that was used to enable further in-depth comparison of the baseline and optimised rotor. Finally, the results of both experiments and simulation are presented and discussed and conclusions drawn.

2. Methodology

2.1. Operating Principle

The most common way to look at the unsteady flow field within the wave rotor channels is through the unfolded z-θ/t-plane. The z-coordinate refers to the axial coordinate and follows the length of the channel, while θ denotes the azimuth position of the channel at a certain time t.

Figure 2 illustrates a schematic example of the pressure field and shows the location of shock and expansion waves with respect to the port opening and closing locations. The example shown here is a throughflow design with two inlet (HPG and LPA) and two outlet ports (HPA, LPG). The high pressure zone (regions II and III) comprise a high pressure exhaust gas (HPG) and high pressure air (HPA) port. These two ports are normally connected through a combustor and thus form

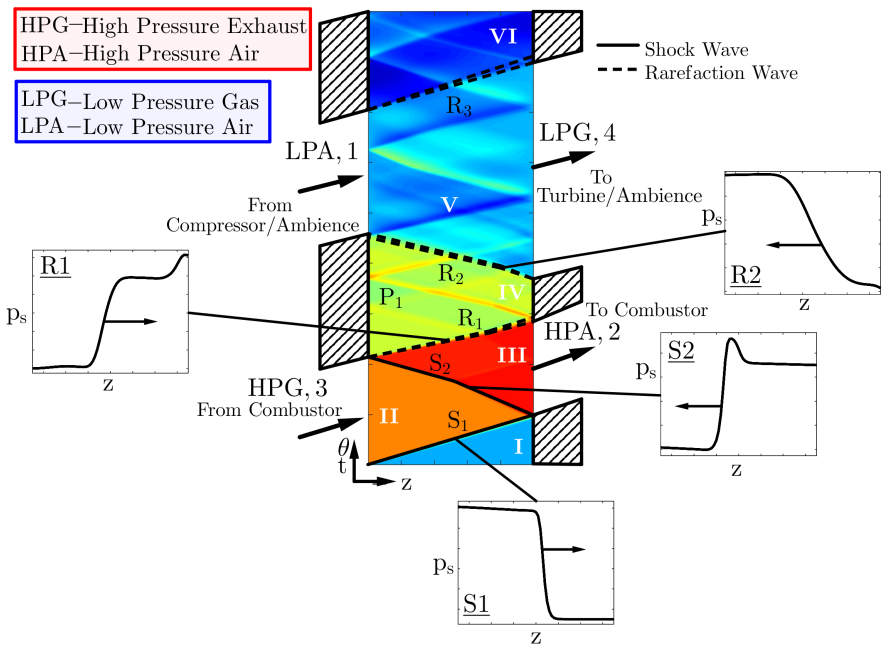

Figure 2: Z-θ/t-plane showing pressure contours and associated wave pattern. The plot indicates the location most prominent shock and expansion waves as a single wave rotor cell passes through the port arrangement of a four-port throughflow wave rotor.

the combustor loop. Further shown are two low pressure ports (region V) housing a low pressure air intake (LPA) port, from where the fresh air is drawn and the low pressure gas port (LPG), through which the hot exhaust gases are expelled to the ambient or alternatively further expanded by a turbine.

As given in region I, initial pressure and temperature within the channels are close to ambient conditions depending whether the LPA port draws fresh air directly from the ambient or from an upstream compressor. Proceeding further up opens exposes the channels to the HPG port. The high pressure conditions within the HPG port sets off a right travelling, primary shock wave (S1). Opening of the HPA port coincides with the impingement of S1 on the outlet side. The result of this is a reflected, secondary shock wave (S2) that travels back to the inlet side. As a result, shock waves S1 and S2 compress the low pressure charge air to the high pressure of the HPA port.

Closing the HPG port as soon as S2 impinges on the left hand side initiates a rarefaction wave (R1) expanding the hot exhaust gases from the combustor to an

intermediate pressure level in region IV. As soon as the head of R1 reaches the right hand side, the HPA port is closed resulting in the generation of a hammer shock wave. An additional expansion fan (R2) is created upon exposing the medium pressure in the channels to the near ambient pressure of the LPG port. Thus, R1 and R2 expand the high pressure gases emanating from the combustor down to near ambient level. Finally, closure of the LPA port generates weak pressure waves before the cycle is repeated.

2.2. Wave Rotor Redesign

Both baseline and optimised rotor feature a rotor length of 30 mm, a mean channel diameter of 60 mm and complete three cycles in a single revolution. The port solution or relative arrangement of the ports is identical for both designs and is presented in Figure 3. In addition, a summary of the most important geometric dimensions are given in Table 1.

The baseline design featured a simple and symmetric wall profile following a parabola [8]. To improve this, an optimisation was carried out that employs a transient quasi-two-dimensional CFD model of the wave rotor coupled with a hybrid algorithm. For the optimisation a total number of six parameters were considered including the number of channels, wall thickness and four control points for the Bézier curve that define channel shape.

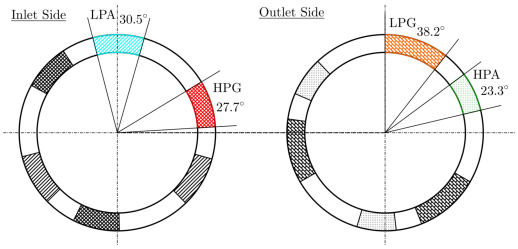

Figure 3: Schematic showing rotor dimensions as well as port solution.

Table 1: Summary of geometric parameters and design conditions for the Bath μ-wave rotor.

Parameter	Value
Rotor diameter [mm]	60
Number of channels baseline	46
Channel shape baseline LE	sym. camber max. $\lvert\beta_{ch}\rvert$=21.5°
Channel shape optimised LE	sym. camber max. $\lvert\beta_{ch}\rvert$=23.3°
Channel length [mm]	30
Channel baseline [mm]	2.9
Channel optimised [mm]	3.4
Channel height [mm]	6
Nominal clearance [mm]	0.15
Number of cycles per revolution	3
Design speed [rpm]	32,000

The results of the optimisation are given in Figure 4(a) showing the normalised, predicted output power by the CFD model on the ordinate and normalised pressure

ratio on the abscissa. In total, 450 different designs have been considered with the best candidate design being determined after fewer than 100 iterations. The graph indicates that the optimised candidate increases power output by approximately 80%, while higher pressure losses lead to a slight decrease in pressure ratio by 3%. A direct comparison of the increased blade camber for the optimised design is shown in Figure 4(b). While blade camber near the leading edge at z/L=0 remains comparable, the optimised camber shape features significantly higher deflection in the centre and more negative blade angles towards the TE. In addition to the changes to channel curvature, the number of channels has been reduced to 41 resulting in a greater channel width of 3.4 mm. The two manufactured rotor designs shown in Figure 5 without sleeve show further outline the differences in channel shape.

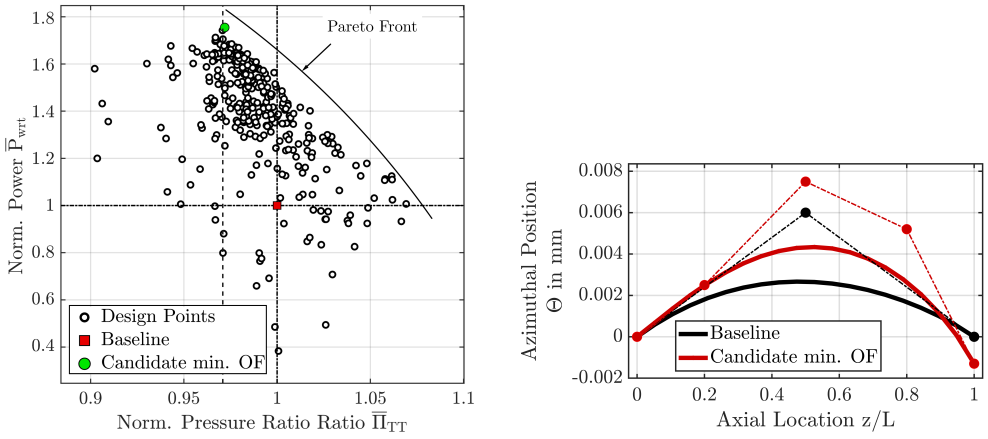

Figure 4: (a) measurement sections for thermocouple installation just downstream of the outlet stator. Each LPG measurement section features a single temperature probe located in the centre of each duct. For the HPA duct the temperature probes were arranged at different positions resulting in the distribution shown in (b).

Wilson and Fronek [42] and Nagashima et al. [5] have defined non-dimensional parameters for finite passage opening T, viscosity F and leakage flow G in order to facilitate the comparison between different wave rotor designs. They are given in Equation 1 and a comparison of different wave rotor examples is shown in Table 2.

$$T = \frac{wa}{UL}, \; F = \frac{\sqrt{\nu L/a}}{D_h}, \; G = \frac{2\delta}{h} \tag{1}$$

Due to the increase in channel width the optimised rotor experiences an increase in

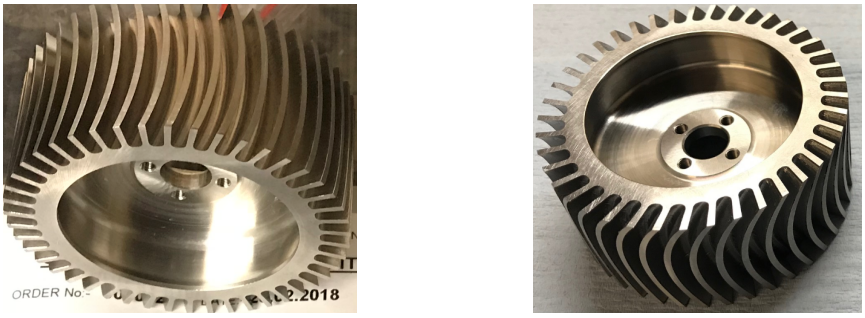

(a) (b)

Figure 5: (a) depicts the baseline wave rotor with symmetrically shaped channels, while (b) shows the optimised version.

finite passage opening effects and marginally lower viscous effects. As both designs are run at the same nominal (cold) clearance leakage effects do not change. Overall, the small size of the wave rotor renders it most comparable to the design of the University of Tokyo. Leakage and frictional effects are comparable, while the reduced channel width of the University of Tokyo rotor yields attenuated finite passage opening characteristics. Under hot operating conditions it can be expected that thermal expansion of stators and the shaft-rotor assembly account for a considerably larger G-parameter, as no particular measure to seal axial leakage was taken.

2.3. Experimental Setup and Campaign

The wave rotor tests follow the same setup as described in [8]. Both baseline and optimised rotor were tested on a gas stand following the setup shown in Figure 6.

The layout features an open-loop configuration that draws dry and pressurised air at 288 K from an external set of rotary type compressors and directs the incoming air to the HPG and LPA inlet legs. Mass flow and total pressure to high and low pressure inlets are controlled via pneumatically controlled orifice control valves (element 1 in Fig. 6). Modulation of these gate valves ensures the desired loop flow ratio can be set. This necessitates accurate measurement of mass flow rates, which is being achieved through two differential v-cone mass flow meters (elements 2 and 5 in Fig. 6) on both high and low pressure side. On the high pressure side, the pressurised air is first directed through an air-to-air heat exchanger (element 3 in Fig. 6) that transfers a portion of the the hot exhaust gases to the incoming, cold air. Downstream the preheated air is run through a 44 kW electric heaters (element 4 in Fig. 6).

The wave rotor itself is connected to an eddy current dynamometer (element 7 in Fig. 6). Excitation and load of the dynamometer is varied manually to reach

Table 2: Comparison of previous wave rotors, both actually realised ones that were tested and conceptual ones (University of Tokyo/ONERA) with wave rotor model used in this study (adapted from [5]).

	Kentfield 3-port PE	NASA 3-port PE	NASA & Allison 4-port TF	University of Tokyo	ABB Comprex 4-port RF	University of Bath Baseline	University of Bath Optimised
T	0.39	0.082	0.19	0.31	0.467	0.37	0.42
F	0.0046	0.017	0.0037	0.012	0.0067	0.013	0.012
G	0.0064	0.025-0.075	0.0090	0.067	0.030	0.05	
Diameter [mm]	148	300	163	46.5	93	60	
Length [mm]	280	460	152	69	90	30	
Cell height [mm]	55.9	10.2	8.8	3	10	6	
Rotational speed [rpm]	6000	4000	16,800	32,000	14,000	32,000	

the desired rotational speed. Both wave rotor bearing housing and eddy-current dynamometer have dedicated water cooling circuits to maintain stable operation. On the outlet side the low pressure outflow is directly vented. The high pressure side features an additional pneumatically actuated variable orifice control valve (element 8 in Fig. 6), which, in combination with a differential pressure v-cone mass flow meter located downstream, is used to ensure the same mass flow rates through HPG and HPA legs. Finally, an air-to-water heat exchanger is located upstream of the mass flow meter in order to reduce the hot exhaust gas temperature down to approximately 300 K.

Wave rotor performance data are gathered by means of the sensors listed in Table 3. The list gives an account of all the sensors used throughout the campaign including their measurement range and accuracy. Uncertainties are assumed to have rectangular distributions and thus equal probability for all values and are evaluated using the British Standard [43].

The list of sensors encompasses pressure transducers and thermocouples located just upstream of the intake manifolds and downstream of the outflow manifolds. Mass flow rates are determined through differential pressure sensors and Bernoulli's theorem for the conservation of energy along a streamline. PRT temperature sensors and pressure transducers located on the high pressure side of the v-cone allow calculation of flow density and together with the differential pressure yield flow velocity.

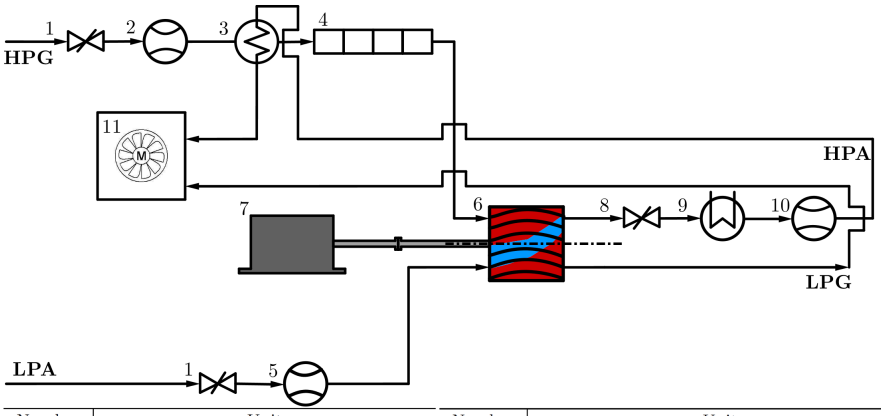

Number	Unit
1	2” sliding gate control valve
2	2” McCrometer V-cone mass flow meter Siemens DSIII dp-sensor
3	Air-to-air heat exchanger
4	44kW electric heater
5	1” McCrometer V-cone mass flow meter Siemens DSIII dp-sensor
6	Wave rotor

Number	Unit
7	Magtrol WB43 HS eddy-current dynamometer
8	1” sliding gate control valve
9	Air-to-water heat exchanger
10	2” McCrometer V-cone mass flow meter Siemens DSIII dp-sensor
11	Extraction fan

Figure 6: Schematic of the wave rotor gas stand test setup.

Table 3: List of sensors used throughout testing including their measurement range and their accuracy as stated by their manufacturers. It is noteworthy that response times and sampling frequency are not reported as the sensors measure steady state data.

Sensor	Range	Nominal Accuracy
Rotor Torque	0-1.5 Nm	±0.3% FS
Rotor Speed	0-65,000 rpm	±0.1% FS
1.5 mm K-type thermocouple	-200°C - 1260°C	±0.0075 T from 333°C to 1200°C ±2.5 °C from -40°C to 333°
PRT	-50°C - 200°C	$\pm 0.3 + 0.005T$
V-cone mass flow meter	0.015 kg/s - 0.015kg/s (HPG, HPA) 0.005 kg/s - 0.05kg/s (LPA)	±0.5%
Static pressure	0 barG - 7 barG (HPG, HPA) 0 barG - 2 barG (LPG) 0 barA - 3.5 barA (LPA)	0.08%
Differential pressure	0 bar-0.06 bar (HPG, HPA) 0 bar - 0.0049768 bar (LPA)	±0.5%

Using mass flow rates in conjunction with the static temperature and pressure probes one can determine total port properties through the first law of thermodynamics, as done in Equation 2.

$$p_t = p_s \left(1 + \frac{(\gamma - 1)}{2} \frac{\dot{m}^2 T_s R}{p_s^2 \gamma A^2} \right)^{\gamma/(\gamma-1)} \tag{2}$$

Total-to-total pressure ratio is thus defined as

$$\Pi_c = \frac{p_{t,HPA}}{p_{t,LPA}} \tag{3}$$

The ratio of the inlet mass flow rates is referred to as loop flow ratio λ, is defined as

$$\lambda = \frac{\dot{m}_{\mathrm{HPG}}}{\dot{m}_{\mathrm{LPA}}} \tag{4}$$

The main purpose of the gas stand experiments is to characterise the optimised rotor and compare it directly to the baseline version with respect to total-to-total pressure ratio (defined in Equation 3), power output as rotational speed, efficiency and outlet temperature distributions. This shall be done at a constant loop flow ratio of approximately 1.7 at a constant peak inlet temperature of 750 K. In addition, the effect of rotational speed on performance for both rotor designs is investigated by running at 32,000 rpm and 28,000 rpm. Finally, nominal axial leakage gaps are fixed at 0.15 mm at in- and outlet.

2.4. Exhaust Gas Recirculation and Wave Rotor Efficiency

Wave rotors experiencing large temperature discrepancies between the two inlets feature pronounced heat transfer effects between hot and cold gas streams. The two gas streams are in direct contact with each other, as shown in Figure 7, and experience heat conduction. Applying traditional adiabatic efficiency definition in such a scenario tends to overpredict expansion and underpredict compression efficiency [44]. To account for these two important effects, this study determines compression and expansion efficiency in a combined fashion following Wilson et al. [45]. In addition, internal exhaust gas recirculation (EGR) occurring in the HPA outlet duct (sketched in the detailed view of Figure 7) and is taken into account, as done in [8].

$$\begin{aligned}
\eta_c &= \frac{\dot{m}_{\mathrm{LPA}} c_{p,c} \left(T^{is}_{\mathrm{HPA}} - T_{\mathrm{LPA}} \right) + \dot{m}_{\mathrm{EGR}} c_{p,h} \left(T^{is}_{\mathrm{HPA,h}} - T_{\mathrm{LPG}} \right)}{\dot{m}_{\mathrm{LPA}} c_{p,c} \left(T_{\mathrm{HPA,c}} - T_{\mathrm{LPA}} - \Delta T_c \right) + \dot{m}_{\mathrm{EGR}} c_{p,h} \left(T_{\mathrm{HPA,h}} - T_{\mathrm{LPG}} - \Delta T_c \right)} \\
\eta_x &= \frac{\dot{m}_{\mathrm{LPG}} c_{p,h} \left(T_{\mathrm{HPG}} - T_{\mathrm{LPG}} - \Delta T_x \right)}{\dot{m}_{\mathrm{LPG}} c_{p,h} \left(T_{\mathrm{HPG}} - T^{is}_{\mathrm{LPG}} \right)}
\end{aligned} \tag{5}$$

where $c_{p,c}$=1005 J/(kg·K) and $c_{p,h}$=1160 J/(kg·K) refer to specific heats at constant pressure for cold and hot stream respectively, while $\dot{m}_{\mathrm{LPA}}$ and $\dot{m}_{\mathrm{LPG}}$ denote mass flow rates through the respective low pressure in- and outlet ports. The system of equation only becomes solvable assuming that $\Delta T_c = \Delta T_x$ and $\eta_c = \eta_x$. It is, recognised that the proposed efficiency calculation is a major simplification. Nonetheless, it should give at least some indication whether there are significant differences in the change in efficiency between baseline and optimised rotor.

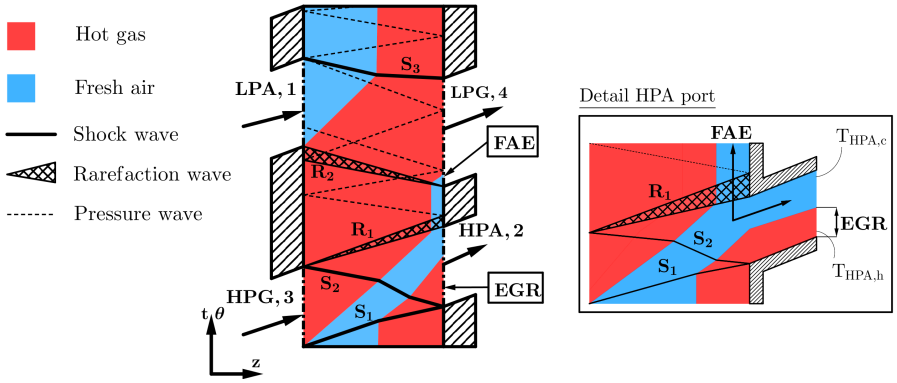

Figure 7: Wave rotor cycle schematic showing general distribution of fresh and hot exhaust gases within the rotor leading to fresh air exhaustion (FAE) through the LPG port and exhaust gas recirculation (EGR) through the HPA port. The amount of EGR and FAE are a function of the hot and cold mass flow rates. (b) shows a closeup of a scenario including solely EGR without FAE while (c) depicts a situation, where both EGR and FAE occur (adapted from [8]).

Internally recycled exhaust gases are a common characteristics of throughflow wave rotors. This is exemplified in Figure 7 exhibiting an unfolded wave rotor schematic with a characteristic distribution of both hot (coloured in red) and cold (coloured in blue) gas streams that are in direct contact with each other. In this scenario, both fresh air exhaustion (FAE) through the LPG port and exhaust gas recirculation (EGR) through the HPA port take place. The amount of EGR and FAE are in general a function of the hot and cold mass flow rates and the scavenging characteristics of the rotor channels.

In order to derive qualitative conclusions with respect to the behaviour of internal exhaust gas recirculation (EGR) common to throughflow wave rotors [46] an additional measurement section with a set of six thermocouples was installed approximately one rotor length downstream of the rotor-outlet stator interface, as shown in Figure 8. To accommodate for the small outlet pipe diameter of 15 mm and to minimise the disruption of the thermocouples to the outlet flow, each single mea-

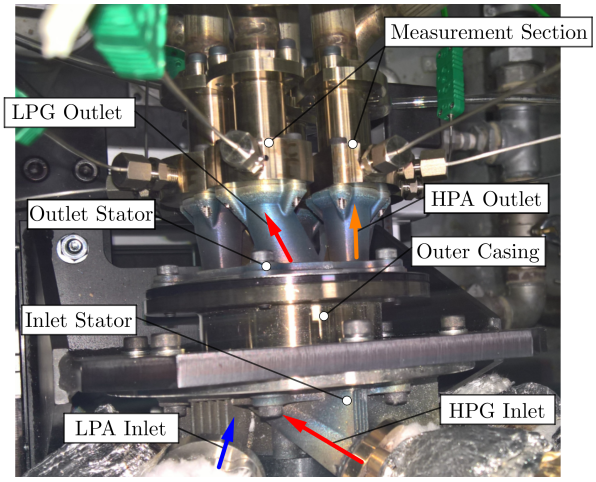

(a)

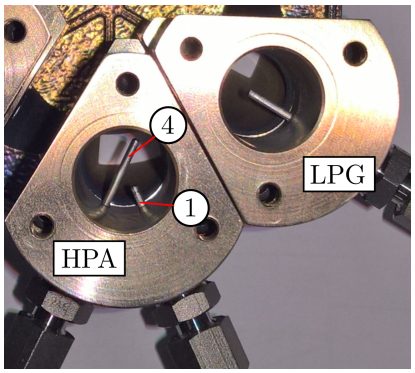

(b)

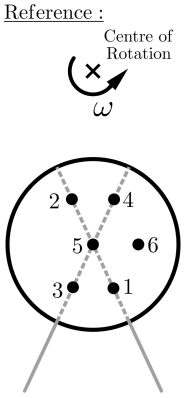

(c)

Figure 8: (a) detail photograph of wave rotor rig with inlet and outlet stator and an additional temperature measurement section downstream of the outlet stator. The general flow direction is from bottom to the top. (b) measurement sections for thermocouple installation just downstream of the outlet stator. Each LPG measurement section features a single temperature probe located in the centre of each duct. For the HPA duct the temperature probes were arranged at different positions resulting in the distribution shown in (c).

surement section contains two temperature probes. Initial tests with and without the thermocouples showed minimal effects ($< 1.0\%$) on additional pressure losses due to local recirculation downstream of the probes. The setup makes use of the fact that the wave rotor design features three cycles per full rotation. As shown by

previous numerical simulations performed by Piechna [47], steady state conditions (limit cycle) are reached within several hundreds revolutions, so that the conditions in each outlet cycle can be expected to be approximately identical.

The photograph in Figure 8(a) shows the distance of the measurement section with respect to in- and outlet stators, while (b) depicts a detailed view of the arrangement of temperature couples in the outlet ducts. Overall, this amounts to six probes across all three HPA ducts and the corresponding arrangement given in Figure 8(c). The main limitation of the approach is that the number of probes is insufficient to obtain a quantitative comparison of experimentally determined EGR rates with numerically determined values. This is partially exacerbated by the fact that the measurement section is not directly located at the rotor/stator interface, which gives rise to diffusive effects that partially smear out the temperature differences. Therefore, to obtain quantitative values for the EGR rates that are suitable for the computation of efficiencies, numerical data from the validated quasi-one-dimensional model introduced in the following section is used.

2.5. Numerical Campaign

The used numerical model is similar to the wave rotor models introduced by Paxson et al. [38, 48, 49], Fatsis et al. [40, 50], Nagashima and Okamoto [5, 39, 51] and has been extended to account for non-axial channel shape and torque extraction. The code has has been validated with experimental data in [52] and its foundations have been further documented in [53]. Therefore, only a brief introduction shall be given here.

The model seeks to determine the wave dynamics within a single wave rotor channel as it rotates around the rotational axis as it encounters varying boundary conditions from the respective ports to each side. In detail, it is based on a quasi-one-dimensional code that solves the unsteady laminar flow equations of mass, momentum and energy, as given in Equation 6, 7 and 8 using the second-order accurate scheme of Richtmyer [54] with a minmod flux limiter of Roe and Baines to reduce dispersive errors in the vicinity of shock waves.

$$\frac{\partial \mathbf{U}}{\partial t} + \frac{\partial \mathbf{F}(\mathbf{U})}{\partial z} = \mathbf{S} \tag{6}$$

where the state and flux vector take the form

$$\mathbf{U} = \begin{pmatrix} \rho \\ \rho u \\ \rho E \end{pmatrix}, \quad \mathbf{F} = \begin{pmatrix} \rho u \\ \rho u^2 + p - \tau_{zz} \\ \rho u \left(E + \frac{p}{\rho} - \tau_{zz} + q_z \right) \end{pmatrix} \tag{7}$$

Heat flux is given by Fourier's law and viscous stress simplified through Stokes' hypothesis to yield

$$q_z = -k\frac{\partial T}{\partial z}, \quad \tau_{zz} = \frac{4}{3}\mu\frac{\partial u}{\partial z} \tag{8}$$

The equations are discretised using finite-differences and solved discretely in a time-marching manner on an equidistant cartesian grid.

$$\begin{aligned}
\mathbf{U}_{i+1/2}^{n+1/2} &= \frac{1}{2}\left(\mathbf{U}_{i+1}^{n} + \mathbf{U}_{i}^{n}\right) - \frac{\Delta t}{2\Delta z}\left(\mathbf{F}_{i+1}^{n} - \mathbf{F}_{i}^{n}\right) - \frac{\Delta t}{4}\left(\mathbf{S}_{i+1}^{n} - \mathbf{S}_{i}^{n}\right), \\
\mathbf{U}_{i-1/2}^{n+1/2} &= \frac{1}{2}\left(\mathbf{U}_{i}^{n} + \mathbf{U}_{i-1}^{n}\right) - \frac{\Delta t}{2\Delta z}\left(\mathbf{F}_{i}^{n} - \mathbf{F}_{i-1}^{n}\right) - \frac{\Delta t}{4}\left(\mathbf{S}_{i}^{n} - \mathbf{S}_{i-1}^{n}\right)
\end{aligned} \tag{9}$$

The second step uses a mid-point Leapfrog computation and consists of space and time centred differences of the mid step solutions of $\mathbf{U}_{i\pm1/2}^{n+1/2}$ and gives

$$\mathbf{U}_{i}^{n+1/2} = \mathbf{U}_{i}^{n} - \frac{\Delta t}{\Delta z}\left(\mathbf{F}_{i+1/2}^{n+1/2} - \mathbf{F}_{i-1/2}^{n+1/2}\right) - \frac{\Delta t}{2}\left(\mathbf{S}_{i+1/2}^{n+1/2} - \mathbf{S}_{i-1/2}^{n+1/2}\right) \tag{10}$$

The working fluid is treated as a calorically imperfect gas, while dynamic viscosity is modelled as a function of temperature using Sutherland's law.

$$\mathbf{S}_{lk} = \begin{pmatrix} s_{lk,1} \\ 0 \\ s_{lk,3} \end{pmatrix}, \quad \mathbf{S}_{\mathrm{v}} = \begin{pmatrix} 0 \\ s_{v,2} \\ s_{v,3} \end{pmatrix}, \quad \mathbf{S}_{\mathrm{b}} = \begin{pmatrix} 0 \\ s_{b,2} \\ s_{b,3} \end{pmatrix} \tag{11}$$
$$\text{where} \quad \mathbf{S} = \mathbf{S}_{\mathrm{lk}} + \mathbf{S}_{\mathrm{v}} + \mathbf{S}_{\mathrm{b}}$$

Similar to the approach by Paxson et al. [38, 48, 49] additional source terms (Equation 11) account globally for wall friction and heat transfer and locally at the extremities of the channel for leakage at the rotor/stator interface. The leakage flows at in- and oulet side are connected via a leakage cavity assumed to be perfectly sealed. This source term $\mathbf{S}_{\mathrm{lk}}$ only pertains to the first and last cell and influence mass and energy equations. Viscous ($\mathbf{S}_{\mathrm{v}}$) and inviscid force ($\mathbf{S}_{\mathrm{b}}$) source terms, on the other hand, affect both momentum and energy equations. The inviscid force terms are incorporated to account for non-axially shaped wall profiles. Losses due to misalignment of the blade force vector with the radial direction causing a rise in entropy are accounted for through a distributed entropy loss term that is based on experimental data.

Boundary conditions are implemented on a characteristics basis and uses a cell-centred approach with ghost cells. The code distinguishes between in- outflow and wall boundary conditions. To allow easy comparison with experimental conditions,

inflow boundary conditions are specified as stagnation properties (pressure and temperature) in the absolute frame of reference and outflow as static pressure. Furthermore, the model takes finite passage opening effects into account that. This is exemplified in in Figure 9(a) and results in a gradual formation of shock waves as shown in Figure 9(b).

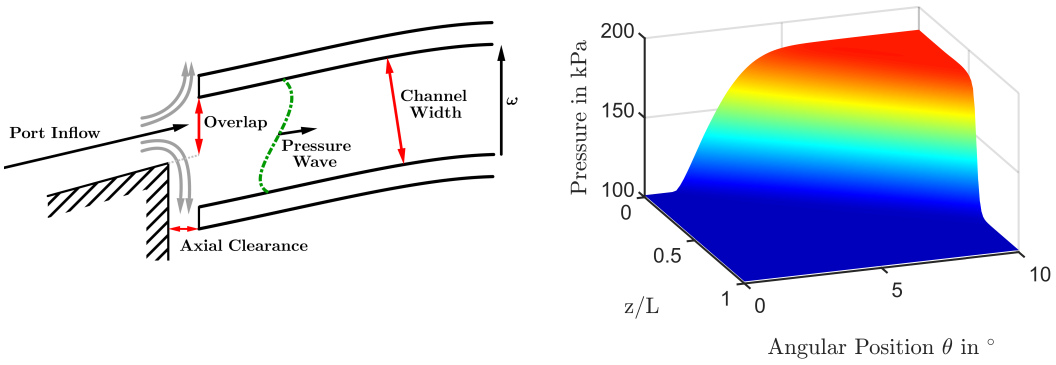

(a) (b)

Figure 9: (a) Schematic outlining situation where gradual passage opening effects are generated shown for port inflow [52]. (b) depicts a gradual formation of a shock wave as a consequence of finite passage opening effects [53].

The model can alternatively run as a closed-loop model, where the high pressure zone (HPG-HPA) is connected via a steady flow combustor model. For the purpose of this paper, the model is set up in the same fashion as in the experimental layout, namely as an open-loop model.

The procedure for the wave rotor simulations is summarised in the flowchart of Figure 10. Initially, the conditions within the channel is assumed to be close to ambient, while the initial conditions in the leakage cavity are assumed to be the average between the peak pressure and temperature and ambient conditions. Rotational speed is set and held constant. For the boundary conditions in the ports, high pressure inlet (HPG) conditions (inlet temperature and pressure) are specified in accordance with the experimental data. The model is then run over multiple cycles until a limit cycle, that is, steady state port conditions, has been reached. In the process, boundary conditions in the high pressure in- and outlet as well as low pressure inlet are varied dynamically using a simple proportional controller as specified in Equation 12 to meet the experimental operating conditions. Static pressure in the HPA duct is varied until the mass flow rates in both HPG and HPA ducts are within 1%.

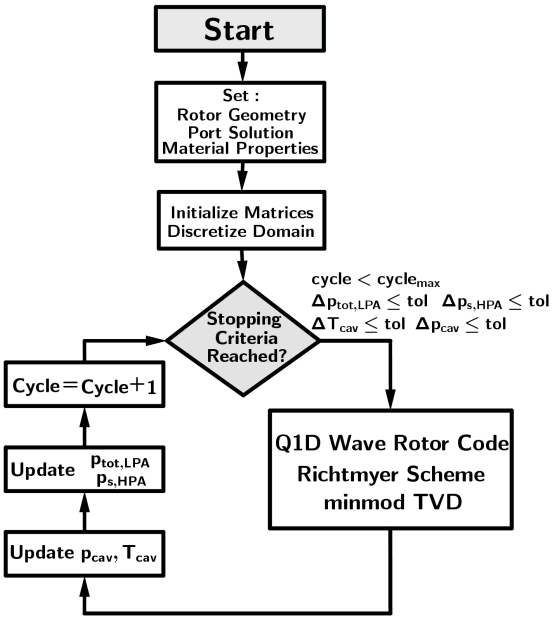

Figure 10: Flowchart for the simulation model starting with the definition of the wave rotor geometry and the associated port solution. The material properties set by the user will affect the lumped capacitance model for wall heat transfer. Subsequently, each cycle is calculated using the second-order Richtmyer scheme with a minmod flux limiter and values for cavity pressure and temperature, LPA inlet pressure and HPA outlet pressure updated after each cycle calculation is completed (adapted from [52]).

$$p^{t+1} = p^t + \alpha \frac{\rho\left(\dot{m}^2_{actual} - \dot{m}^2_{target}\right)}{2\left(\rho A\right)^2} \tag{12}$$

Furthermore, in order to ensure the simulated loop flow ratio corresponds to the experimental value, total inlet pressure in the LPA duct is varied after each cycle until the inlet mass flow ratio is, again, within 1% of its target. An additional requirement regarding the limit cycle is imposed through the cavity pressure and temperature and the simulation is only deemed converged when the relative change of the conditions within the cavity over the past five cycles is within 3 %. Finally, in a similar fashion to Wilson et al. [55], the static pressure in the LPG duct is varied until the inlet mass flow rate through the HPG duct is in line with the experimental value. Efficiency

calculation for the numerical model follows the form given in Equation 5, but also includes possible effects of fresh air exhaustion (FAE) and is thus defined as

$$\eta_c = \frac{\dot{m}_{\mathrm{LPA}} c_{p,c}\left(T^{is}_{\mathrm{HPA}} - T_{\mathrm{LPA}}\right) + \dot{m}_{\mathrm{EGR}} c_{p,h}\left(T^{is}_{\mathrm{HPA,h}} - T_{\mathrm{LPG}}\right)}{\dot{m}_{\mathrm{LPA}} c_{p,c}\left(T_{\mathrm{HPA,c}} - T_{\mathrm{LPA}} - \Delta T_c\right) + \dot{m}_{\mathrm{EGR}} c_{p,h}\left(T_{\mathrm{HPA,h}} - T_{\mathrm{LPG}} - \Delta T_c\right)}$$

$$\eta_x = \frac{\dot{m}_{\mathrm{LPG}} c_{p,h}\left(T_{\mathrm{HPG}} - T_{\mathrm{LPG}} - \Delta T_x\right) + c_{p,c}\dot{m}_{\mathrm{FAE}}\left(T_{\mathrm{HPA}} - T_{\mathrm{LPG,c}} - \Delta T_x\right)}{\dot{m}_{\mathrm{LPG}} c_{p,h}\left(T_{\mathrm{HPG}} - T^{is}_{\mathrm{LPG}}\right) + c_{p,c}\dot{m}_{\mathrm{FAE}}\left(T_{\mathrm{HPA}} - T^{is}_{\mathrm{LPG,c}}\right)} \tag{13}$$

3. Results and Discussion

3.1. Experimental Results

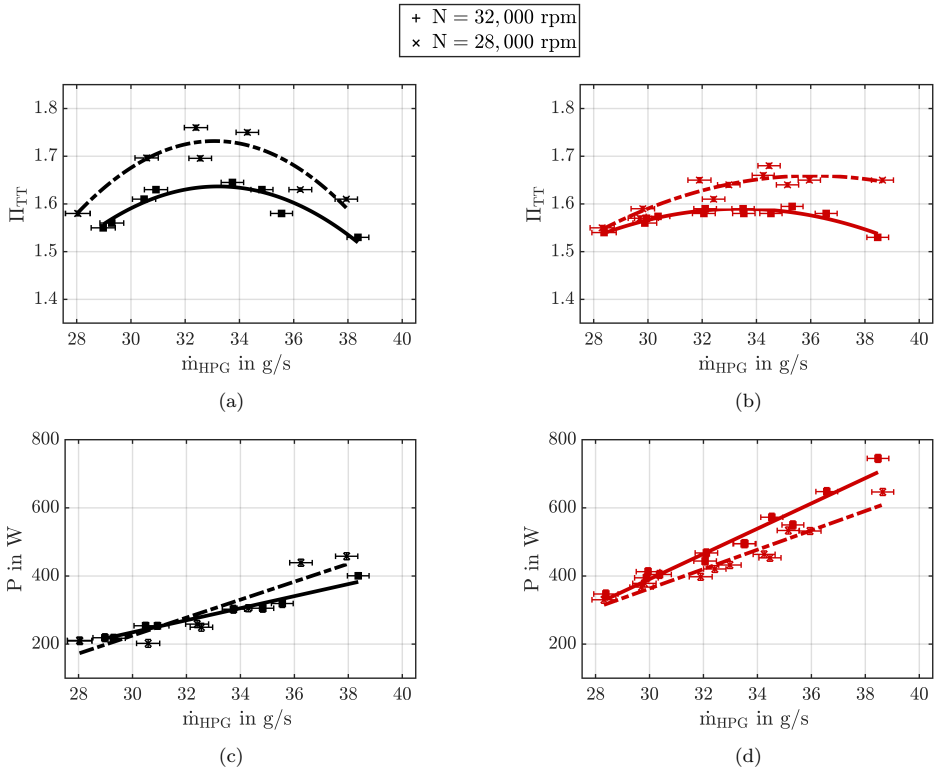

Figure 11: Comparison of wave rotor performance data for baseline (left hand side column) and optimised rotor (right hand side column). The graphs show variations in total-to-total pressure ratio (a-b), shaft power (c-d) plotted against inlet mass flow rate. Two different speedlines are presented at design speed of 32,000 rpm (solid fitted curve) and at 28,000 rpm (dashed fitted curve). All data were gathered at 750 K HPG inlet temperature and a nominal clearance of 0.15 mm on inlet and 0.15 mm on outlet side.

The data shown in Figure 11 shows a back-to-back comparison of wave rotor global performance parameters of total-to-total pressure ratio, shaft power and combined compression and expansion efficiency between baseline (left column) and optimised rotor (right hand side column) as a function of inlet mass flow rate $\dot{m}_{\mathrm{HPG}}$ and two rotational speeds of 32,000 rpm and 28,000 rpm. All data were gathered for a constant nominal leakage gap of 0.15 mm at in- and outlet and a peak inlet

temperature $T_{\mathrm{t,HPG}}$ of 750 K.

For both baseline and optimised rotor variation of pressure ratio with inlet mass flow ratio roughly follows a parabolic shape with a peak in the range between 32 g/s and 34 g/s. As already witnessed in the experimental campaign of the baseline rotor [8], higher pressure ratios are achieved at lower rotational speeds of approximately 28,000 rpm. This trend does not change between baseline and optimised rotor as a consequence of the unchanged stator port arrangement. Overall, the baseline model appears to achieve a slightly higher pressure ratio at in the range from 32 g/s - 34 g/s.

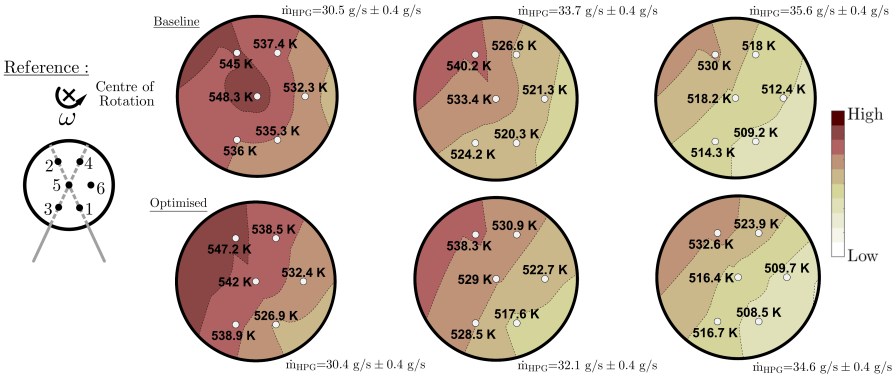

Figure 12: Contour plots illustrating the temperature distribution in the measurement section downstream of the HPA port for different inlet mass flow rates. The top row of plots represents data from the baseline rotor, while the lower row shows data from the optimised rotor. The contour plots are an indication of EGR distribution and exhibit comparable characteristics between both rotor models.

Generated shaft power, as shown in Figures 11(c) and (d) shows a linear variation with inlet mass flow rate for both models. It becomes immediately clear that the optimised rotor does achieve a considerably higher power output ranging between approximately 350 W to 770 W over the investigated inlet mass flow range. The baseline model on the other hand achieves a power output ranging between 200 W and 450 W.

The aforementioned change in EGR rate inlet mass flow rate is reduced is exemplified in the temperature contour plots in Figures 12. At lower mass flow rates there clearly is a higher temperature region on the inner side near measurement point 2,

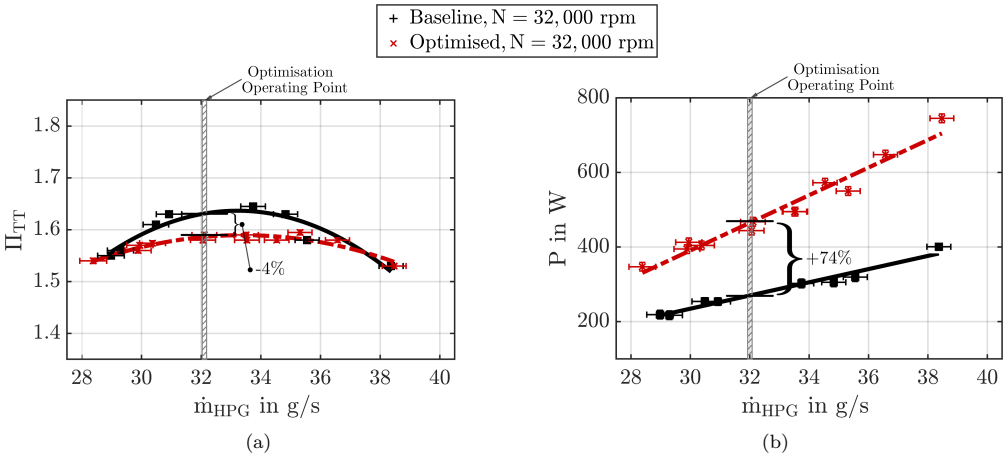

Figure 13: Back-to-back comparison of wave rotor performance data for baseline (black, solid line) and optimised rotor (red, dashed line). (a) outlines the variation of total-to-total pressure ratio, while (b) gives the variation of wave rotor power with inlet mass flow rate. At the target operating point, the optimised rotor delivers a 74% increase in shaft power at a 4% decrease in pressure ratio.

while the lower temperature flow is pushed towards the outside (measurement point 1) due to centrifugal forces. Increasing mass flow rates leads to an overall reduction in the average temperature and, as a consequence of this, a reduction in EGR rate. As expected, this trend does not change between baseline and optimised rotor.

A direct comparison of pressure ratio and power output between baseline and optimised rotor confirms the findings from the numerical optimisation study at 32,000 rpm. This is given in Figure 13. The optimised rotor delivers an increase in power output of approximately 74% at the cost of a 4% decrease in the achieved pressure ratio. This further emphasises the trade-off relationship between pressure exchange capabilities and power extraction. The increase in power output for the optimised rotor can thus be at least partially attributed to increased incidence losses. Overall, the data suggests that the baseline model's ability to exchange pressure is slightly more sensitive to changes in inlet mass flow rate and is comparable to the optimised rotor at flow rates around 29 g/s and 38 g/s respectively.

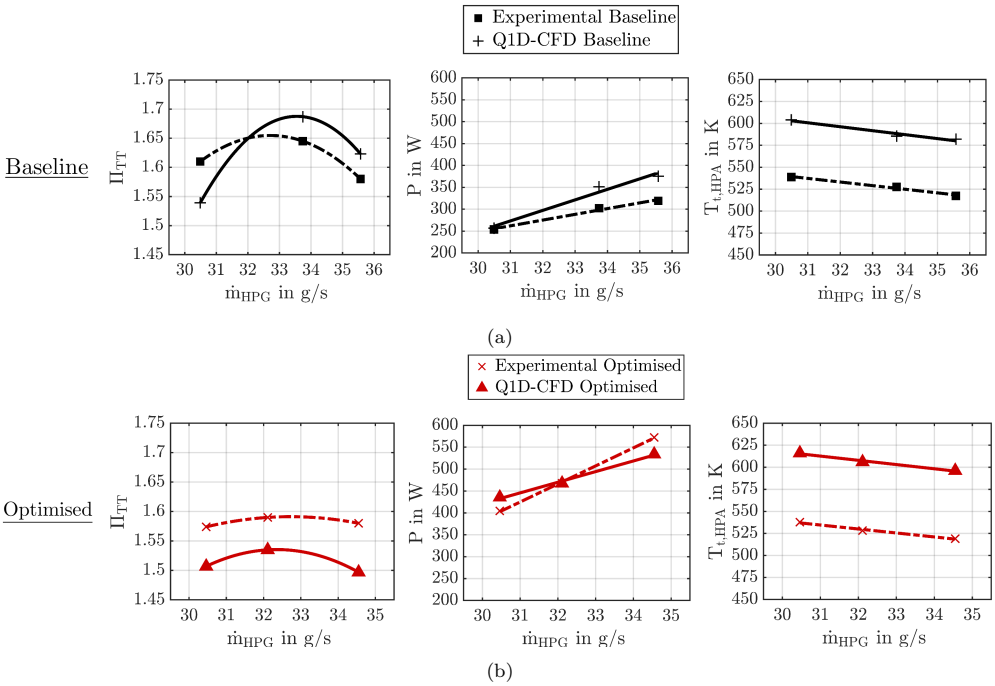

Figure 14: (a) outlines a comparison of experimental (black, solid line) and numerical data ((black, dashed line) for the baseline design of the variation of total-to-total pressure ratio (left), wave rotor power (centre) and HPA outlet temperature (right) with HPG inlet mass flow rate. (b) depicts a comparison of numerical (red, dashed line) with laboratory data (red, solid line) for the optimised design for the same global parameters.

Applying the quasi-one-dimensional model to both baseline and optimised rotor shall give further insights into the gas dynamics within the rotor channels that the experiments cannot provide. Before this is done, it is necessary to establish how well the model results in terms of global variables correlate with the experimental data. This is shown in Figure 14 for pressure ratio, power output and average outlet temperature in the HPA duct given for both baseline (a) and optimised geometry (b). Model parameters for friction multiplier, leakage coefficient were the same as used in [52]. This also holds for the additional entropy-based loss coefficient in case of the baseline geometry. Since the optimised rotor features different incidence angles, the value was adapted to match the power output at the target optimisation point of 32 g/s.

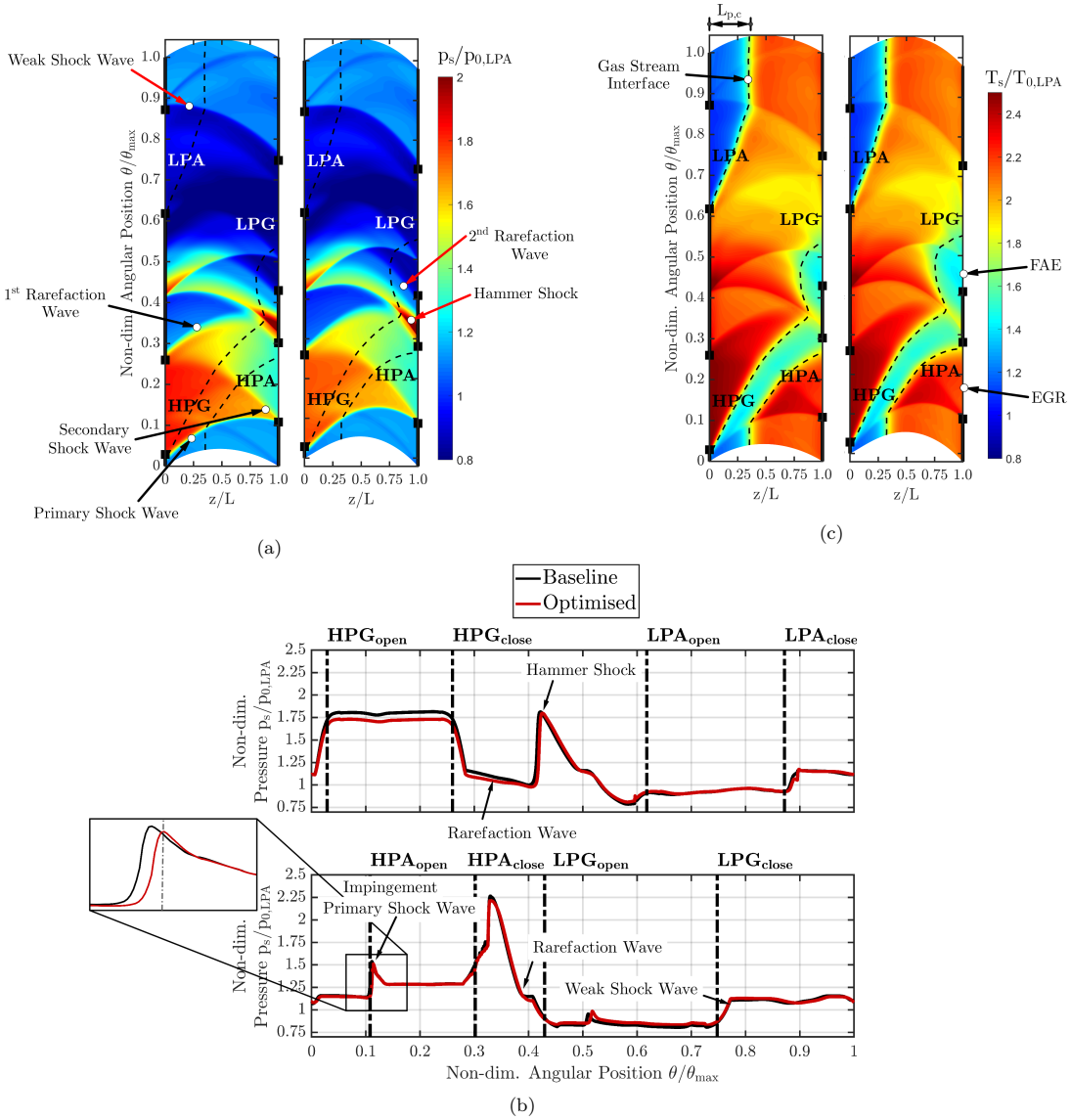

Figure 15: (a) Unfolded pressure contours of baseline (left) and (optimised) rotor channels. Overall, the changes in the wave pattern are minimal, despite a slight reduction of static pressure in primary zone. (b) depicts the non-dimensionalised pressure trace at inlet (top) and outlet (bottom) side confirming the decrease in static pressure in the primary zone during opening of the HPG port. (c) depicts contour plots of non-dimensional static temperature for baseline and optimised rotor. The plots show the interface between hot and cold gas streams within the rotor channels and exhibit minor differences in EGR and FAE.

Figure 14(a) illustrates the change of pressure ratio with inlet mass flow rate for experiments and numerical model. In general, there is good agreement with the experimental data and trends are reasonably well represented. The model accurately predicts a drop in pressure ratio for the optimised design, albeit the decrease remains overestimated. In addition, the drop off in pressure ratio towards the maximum and minimum mass flow rates appears overestimated for both designs. Compared to the initial validation presented in [52] the absolute error between numerical and experimental data is significantly reduced as a consequence of lower nominal clearances and reduced inlet temperature $T_{t,HPG}$.

Figure 14(b) compares predicted power against the experimentally determined data. Despite differences in the line gradients the numerical data are reasonably close to the empirical ones. As given in Figure 14(c), the model is also able to capture the trends for average outlet temperature distribution $\overline{T}_{HPA}$ in the HPA duct. There is, however, a nearly constant offset, which is largely due to the fact that the numerical temperature data is taken directly at channel exit, while in the experiments the temperature probes are located approximately two rotor lengths further downstream in the port resulting in higher heat dissipation.

The effects of the change in channel wall profile on the gas dynamics within the rotor is presented in the back-to-back comparison of the pressure contours shown in Figure 15(a). The contour plot outlines the location of primary and secondary shock waves as well as the hammer shock that is created after the channel passes the HPA port. Furthermore, both rarefaction waves are indicated as well along with the final weak shock wave that is created after the LPG port is closed. Overall, there are negligible changes in the wave pattern, which is mainly a result of the same relative arrangement of the ports. The most prominent change is in the high pressure zone during opening of the HPG port. This is also shown in the static pressure distribution near the inlet side of Figure 15(b). The reduction in pressure is a consequence of higher incidence losses and results in a drop of the primary shock wave leading to the overall reduction in pressure ratio. Also, as a result of the increased channel length the waves have to travel through it is shown that there is slight delay in the impingement of the primary shock wave of less than 1°.

The temperature contours in Figure 15(c) confirm the similarities between the two designs and show the relative position of hot and cold gas streams within the rotor channels. Overall, the operating point is characterised by relatively high EGR rates shown in the HPA port and FAE rates in the LPG port. In addition, the graphs indicate comparable scavenging and penetration lengths as well as well as EGR and FAE rates between the two designs. As already indicated by the temperature contours in Figure 12 an increase in inlet mass flow rate results in reduced EGR rates

expressing itself through lower average outlet temperatures.

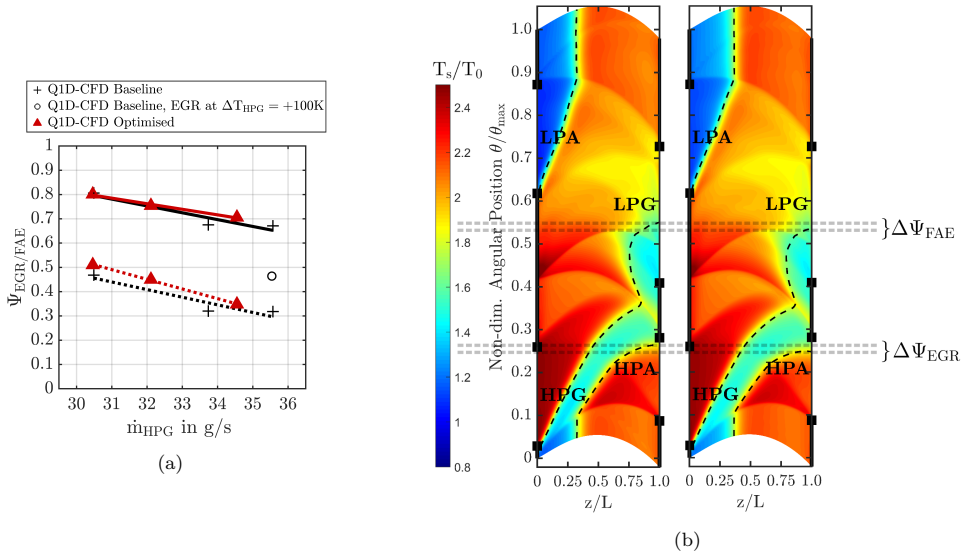

Figure 16: (a) gives the numerically determined trends for EGR and FAE as inlet mass flow rate is varied. The additional circular data point outlines the predicted EGR rate for an increased peak inlet temperature $T_{t,HPG}$ resulting in a significant reduction of EGR rate. (b) qualitatively illustrates the change in the location of the cold gas stream and reduction in EGR as mass flow rate is increased from 30 g/s to 35 g/s for the optimised rotor.

This trend is further exemplified in Figure 16(a) and (b), which clearly outlines a reduction in EGR rate as inlet mass flow rates are increased. In the temperature contours of Figure 16(b) the reduction in EGR rate between inlet mass flow rates of 30 g/s to 35 g/s is expressed through a shift of the dotted interface line downwards. The absolute values in this scenario, however, remain relatively high and are in the range of 60% for EGR and 30% for FAE. Significant reductions in EGR and FAE rate can be achieved by increasing inlet temperature given by the circular point in Fig. 16(a), which, at the same mass flow rate, results in a possible reduction by more than 10%.

3.3. Combined Approach for Compression and Expansion Efficiency

Combining Equation 5 with the numerically determined EGR rates gives the efficiency distribution illustrated in Figure 17 for (a) baseline (b) optimised. The data illustrate compression/expansion efficiency for two speedlines of 28,000 and 32,000 rpm plotted against inlet mass flow rate through the HPG inlet port. Overall, the

results yield similar trends for both designs. The data reinforce the findings reported in [8] with efficiency values being in the range of 60 % to 80 % and does not appear to be a substantial difference in efficiency between the two designs. The trendlines for both designs consistently imply higher efficiency at the lower rotational speed of 28,000 rpm, which is in line with a higher pressure ratio achieved at 28,000 rpm compared to 32,000 rpm given in Figure 11. This implies more favourable incidence angles at lower rotational speeds leading to reduced losses, higher achieved pressure ratio and as a consequence higher compression/expansion efficiency. The downward trend in efficiency with increasing HPG inlet mass flow rate is a direct result of a reduction in EGR rate accompanied by a reduction in FAE equivalent to an increase in overall outlet temperature through the LPG duct. Although FAE remains an undesired phenomenon with a portion of the flow being expelled without passing through the combustor loop, it leads to greater expansion efficiencies by lowering the LPG outlet temperature.

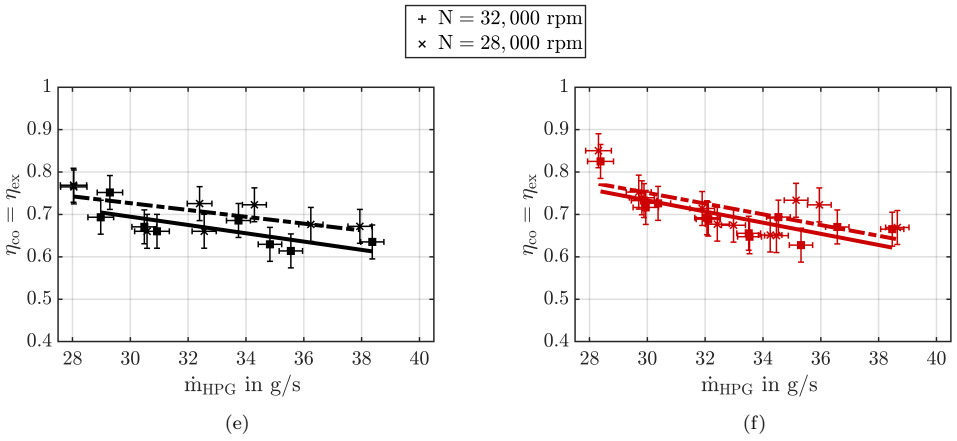

Figure 17: Combined compression/expansion efficiency plotted against inlet mass flow rate. The data for EGR rates were taken from the numerical data from the quasi-one-dimensional mode. Two different speedlines are presented at design speed of 32,000 rpm (solid fitted curve) and at 28,000 rpm (dashed fitted curve). All data were gathered at 750 K HPG inlet temperature and a nominal clearance of 0.15 mm on inlet and 0.15 mm on outlet side.

A back-to-back comparison of numerically predicted and experimentally determined efficiency values is presented in Figure 18. The numerical data reflect the trends with respect to changes in mass flow rate and wave rotor design well. There is, however, a significant discrepancy between numerical nad experimental efficiency data, which primarily stems from the fact that the numerical calculations include

FAE effects in the efficiency. Since FAE leads to a reduction in the outlet temperature through the LPG duct, this effectively raises expansion efficiency in the process. FAE has not been explicitly included in the efficiency calculation of the experimental calculations and thus yields the offset to lower efficiency values as witnessed in Figure 18.

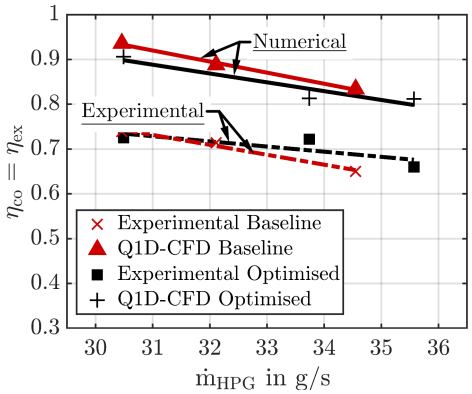

Figure 18: Comparison of numerically determined and experimentally gathered efficiency data plotted against inlet mass flow rate.

4. Conclusions and Outlook

In this paper an optimised rotor of a four-port, three-cycle small scale wave rotor turbine has been characterised by laboratory experiments and compared to its baseline design. In addition, numerical simulations were conducted to infer the impact of channel shape changes on the internal wave dynamics. To conclude, the main points of the study are summarised as follows:

- The optimisation was targeted at improving the shaft power output with minimal compromises with respect to pressure exchange capabilities. Only the rotor channel shape has been optimised with the port solution remaining the same between both baseline and optimised design. The numerical optimisation outlined an increase in power output by a factor of approximately 1.8 at a pressure ratio decrease of 3%.

- Both rotors were tested back-to-back in an open-loop configuration using an electrical heater and a set of external compressors as a source of heated and pressurised air. An eddy-current dynamometer was used as a load cell to

measure speed and torque output. All tests were carried out at a constant loop flow ratio and peak inlet temperature of 750 K.

- The experimental results indicate a parabolic variation of pressure ratio with inlet mass flow rate, while power increases in a linear fashion. The data furthermore confirm the results from the optimisation and indicate an approximate power output increase of 70%, while pressure ratio decreases by around 4%. This agrees very well with the predictions from the numerical optimisation study.

- Temperature distribution measurements in the high pressure outlet duct indicate that an increase in inlet mass flow rate results in reduced internal exhaust gas recirculation rates and thus lower overall outlet temperatures. This is confirmed by the numerical results. Further reductions in exhaust gas recirculation rates can be achieved by raising the inlet temperature while keeping mass flow rate constant.

- A combined numerical and experimental approach was used to compute compression and expansion efficiency by using the exhaust gas recirculation trends from the numerical model as an input for the experimentally determined efficiency. The results show consistency over both baseline and optimised results with efficiency values ranging in the 60 to 80 percent range. The study further highlights the inclusion of fresh air exhaustion through the low pressure exhaust ports.

- Higher pressure ratios and efficiency for both baseline and optimised rotor at rotational speeds of 28,000 rpm indicate more favourable incidence angles and thus reduced losses.

- The numerical data obtained from the quasi-one-dimensional model reveals that incidence losses lead to a reduction in primary shock wave. Overall, however, despite the change in camber and an increase in effective channel length, the gas dynamics within the channels prove relatively insensitive to the modifications channel shape and do not significantly affect the wave patterns.

- Finally, the findings from this study confirm that highly efficient shock compression and expansion as well as shaft power extraction can be achieved through non-axial wave rotor machines at a fraction of the rotational speed of turbomachinery of comparable power output. In addition, the experimental data

validate the presented optimisation routine, which lends itself to future, efficient numerical optimisation studies targeting different objective functions more suited to enhance the performance of wave rotor pressure gain combustion, wave rotor refrigeration applications or gas turbine topping cycles.

Acknowledgement

The authors would further like to acknowledge the technical staff at the Institute for Advanced Automotive Propulsion Systems (IAAPS) for their support in setting up the experimental facility as well as Adamos Adamou for assistance in preparing instrumentation and data acquisition.

References

[1] F. Iancu and N. Müller, Efficiency of shock wave compression in a microchannel, Microfluid Nanofluid 2 (2006) 50–63.

[2] H.E. Weber, Shock Wave Engine Design, John Wiley & Sons, New York, 1996.

[3] J.A.C. Kentfield, Nonsteady, One-Dimensional, Internal Compressible Flow, Oxford University Press, Oxford, 1993.

[4] R. Nalim, H. Li and P.Akbari, Air-Standard Aerothermodynamic Analysis of Gas Turbine Engines with Wave Rotor Combustion, Proceedings of the ASME Turbo Expo (2009) 445–456.

[5] T. Nagashima, K. Okamoto and Y. Ribaud, Cycles and Thermal System Integration Issues of Ultra-Micro Gas Turbines, Educational Notes RTO-EN-AVT-131, 2005.

[6] P. Akbari, R. Nalim, N. Müller, Performance Enhancement of Microturbine Engines Topped with Wave Rotors, Journal of Engineering for Gas Turbines and Power 128 (2006) 190–202.

[7] R.D. Pearson, A Gas Wave-Turbine Engine Which Developed 35 HP and Performed Over a 6:1 Speed Range, in: Proceedings ONR/NAVAIR Wave Rotor Research and Technology Workshop, Naval Postgraduate School, 1985.

[8] S. Tüchler and C.D. Copeland, Experimental Results from the Bath μ-Wave Rotor Turbine Performance Tests, Energy Conversion and Management 189 (2019) 33–48.

[9] B.D. Smith, M.D. Polanka, D.E. Paxson and J.L. Hoke, Scaling Study of Wave Rotor Turbo Normalization of an Internal Combustion Engine, 48th AIAA/ASME/SAE/ASEE Joint Propulsion Conference and Exhibit 2012 (2012).

[10] Y. Lei, D.S. Zhou and H.G. Zhang, Investigation on Performance of a Compression-Ignition Engine with Pressure-Wave Supercharger, Energy 35 (2010) 85–93.

[11] J.Q. Zhao, D.P. Hu, P.Q Liu, F.X. Liu and J.J. Gao, Thermodynamic Analysis of a Novel Wave Rotor Refrigeration Cycle, Advanced Materials Research 805-806 (2013) 537–542.

[12] D.Hu, R. Li, P. Liu and J. Zhao, The Loss in Charge Process and Effects on Performance of Wave Rotor Refrigerator, International Journal of Heat and Mass Transfer 100 (2016) 497–507.

[13] J.T. Reinhart, B.A. Beasley, J.L. Hoke, M.J. McClearn and F.R. Schauer, Experimental Observations of a Small-Scale Pressure-Wave Supercharger Coupled to a Compression Ignition Engine, AIAA Aerospace Sciences Meeting, 2018 (2018).

[14] I. Costiuc and A. Chiru, Evolution of the Pressure Wave Supercharger Concept, IOP Conf. Ser.: Mater. Sci. Eng. 252 (2017).

[15] M.R. Mataczynski, M.J. McClearn, F.R. Schauer, D.E. Paxson and J.L. Hoke, Design and Testing of a Small Pressure Wave Supercharger for an Industrial Diesel Engine, AIAA SciTech Forum - 55th AIAA Aerospace Sciences Meeting (2017).

[16] A. Fatsis, Design point analysis of two-shaft gas turbine engines topped by four-port wave rotors for power generation systems, Propulsion and Power Research 8 (2019) 183–193.

[17] A. Fatsis, Performance Enhancement of One and Two-Shaft Industrial Turboshaft Engines Topped with Wave Rotors, International Journal of Turbo and Jet Engines 35 (2018) 137–147.

[18] Performance Benefits for Wave Rotor-Topped Gas Turbine Engines, volume Volume 1: Turbomachinery of *Turbo Expo: Power for Land, Sea, and Air*, 1996.

[19] F. Klein and S. Staudacher, Plausibility Study of Hecto Pressure Ratio Concepts in Large Civil Aero-Engines, Journal of Engineering for Gas Turbines and Power 140 (2018) 051201.

[20] A.A. Kharazi, P. Akbari and N. Müller, Preliminary Study of a Novel R718 Compression Refrigeration Cycle Using a Three-Port Condensing Wave Rotor, Journal of Engineering for Gas Turbines and Power 127 (2005) 539–544.

[21] J. Zhao and D. Hu, An Improved Wave Rotor Refrigerator Using an Outside Gas Flow for Recycling the Expansion Work, Shock Waves 27 (2017) 325–332.

[22] D. Hu, Y. Yu and P. Liu, Enhancement of Refrigeration Performance by Energy Transfer of Shock Wave, Applied Thermal Engineering 130 (2018) 309–318.

[23] D. Hu, Y. Yu, P. Liu, X. Wu and Y. Zhao, Improving Refrigeration Performance by Using Pressure Exchange Characteristic of Wave Rotor, Journal of Energy Resources Technology, Transactions of the ASME 141 (2019).

[24] R.R. Jagannath, S.P.M. Bane and M.R. Nalim, Wave Rotor Combustor Turbine Model Development, 51st AIAA/SAE/ASEE Joint Propulsion Conference (2015).

[25] P.H. Snyder and M.R. Nalim, Pressure Gain Combustion Application to Marine and Industrial Gas Turbines, Proceedings of the ASME Turbo Expo 5 (2012) 409–422.

[26] H.D. Perkins and D.E. Paxson, Summary of Pressure Gain Combustion Research at NASA, NASA/TM-2018-219874 (2018).

[27] S.C. Gülen, Pressure Gain Combustion Advantage in Land-Based Electric Power Generation, Journal of the Global Power and Propulsion Society 1 (2017) 288–302.

[28] M. Rajagopal, A. Karimi and R. Nalim, Wave-Rotor Pressure-Gain Combustion Analysis for Power Generation and Gas Turbine Applications, Proceedings of the ASME 2012 Gas Turbine India Conference (2012).

[29] M.R. Nalim, Assessment of Combustion Modes for Internal Combustion Wave Rotors, Journal of Engineering for Gas Turbines and Power 121 (1999) 265–271.

[30] M.R. Nalim, P.H. Snyder and M. Kowalkowski, Experimental Test, Model Validation and Viability Assessment of a Wave-Rotor Constant-Volume Combustor, Journal of Propulsion and Power 33 (2017) 163–175.

[31] M. R. Nalim, Z. A. Izzy and P. Akbari, Rotary wave-ejector enhanced pulse detonation engine, Shock Waves 22 (2012) 23–38.

[32] R.D. Pearson, Thermodynamics and Gas Dynamics of Internal Combustion Engines, Volume II, in: D.E. Winterbone and S.C. Low (Ed.), The Oxford Handbook of Innovation, Oxford University Press, Oxford, 1986.

[33] A. Mathur, Design and Experimental Verification of Wave Rotor Cycles, in: Proceedings ONR/NAVAIR Wave Rotor Research and Technology Workshop, Naval Postgraduate School, 1985.

[34] R. Taussig, P. Cassady, J. Zumdieck, W. Thayer and E. Klostermannt, Investigation of Wave Rotor Turbofans for Cruise Missile Engines, Technical Report, Final Report Submitted by MSNW to DARPA, 1983.

[35] J. Piechna and D. Dyntar, Two-Dimensional Numerical Analysis of the Wave Jet Micro-Engine Operation, Proc. PowerMEMS 2007 Freiburg, Germany (2007).

[36] J. Piechna and D. Dyntar, Numerical Investigation of the Wave Disk Micro-Engine Concept, International Journal of Gas Turbine, Propulsion and Power Systems 2 (2008).

[37] J. Piechna and D. Dyntar, Hybrid Wave Engine Concept and Numerical Simulation of Engine Operation, The Archive of Mechanical Engineering LVII (2010).

[38] D. Paxson, J. Wilson, An Improved Numerical Model for Wave Rotor Design and Analysis, AIAA (1993).

[39] K. Okamoto, T. Nagashima and K. Yamaguchi, Introductory Investigation of Micro Wave Rotor, in: Proceedings of the International Gas Turbine Congress 2003 Tokyo, GTSJ, 2003.

[40] A. Fatsis, A. Lafond and Y.Ribaud, Preliminary analysis of the flow inside a three-port wave rotor by means of a numerical model, Aerospace Science and Technology 5 (1998) 289–300.

[41] G.E. Welch, Recent Improvements to and Validation of the One Dimensional NASA Wave Rotor Model, Army Research Laborator Technical Report, (1996). ARL-TR-924.

[42] J. Wilson and D. Fronek, Initial results from the NASA-Lewis Wave Rotor Experiment, AIAA-93-2521 (1993).

[43] ISO Central Secretary, Measurement of Fluid Flow - Procedures for the Evaluation of Uncertainties, Standard BS ISO 5168:2005, International Organization for Standardization, London, UK, 2005.

[44] S. Chan, H. Liu and F. Xing, Defining the Thermodynamic Efficiency in a Wave Rotor, J. Eng. Gas Turbines Power 140 (2016) 112601–1–112601–11.

[45] J. Wilson, G.E. Welch and D.E. Paxson, Experimental Results of Performance Tests on a Four-Port Wave Rotor, NASA-TM-2007-214488 (2007).

[46] S. Chan, H. Liu, F. Xing and H. Song, Wave Rotor Design Method With Three Steps Including Experimental Validation, J. Eng. Gas Turbines Power 140 (2018) 111201–1–111201–13.

[47] J. Piechna, Feasibility Study of the Wave Disk Micro-Engine Operation, J. Micromech. Microeng. 16 (2006).

[48] D.E. Paxson and J. Wilson, Recent Improvements to and Validation of the One Dimensional NASA Wave Rotor Model, NASA-TM-106913 (1995).

[49] D.E. Paxson, A Numerical Model for Dynamic Wave Rotor Analysis, AIAA-95-2800 (1995).

[50] A. Fatsis, N.G. Orfanoudakis, D.G. Pavlou, A. Panoutsopoulou and N. Vlachakis, Unsteady Flow Modelling of a Pressure Wave Supercharger, Proceedings of the Institution of Mechanical Engineers Part D Journal of Automobile Engineering 220 (2006) 209–218.

[51] K. Okamoto, T. Nagashima and S.Teramoto, Multi-Passage Gasynamic Interactions in Wave Rotor, in: 24th International Congress of the Aeronautical Sciences, The International Council of the Aeronautical Sciences (ICAS), 2004.

[52] S. Tüchler and C.D. Copeland, Validation of a Numerical Quasi One-Dimensional Model for Wave Rotor Turbines with Curved Channels, J. Eng. Gas Turbines Power. (2019). GTP-19-1313.

[53] S. Tüchler and C.D. Copeland, Parametric Numerical Study on the Performance Characteristics of a Micro-Wave Rotor Gas Turbine, in: Proceedings of the International Gas Turbine Congress 2019 Tokyo, GTSJ, 2019.

[54] D.E. Winterbone and R.J. Pearson, Theory of Engine Manifold Design: Wave Action Methods for IC Engines, Professional Engineering Publishing Limited, 2000.

[55] J. Wilson, G.E. Welch and D.E. Paxson, Experimental Results of Performance Tests on a Four-Port Wave Rotor, NASA/TM—2007-214488 (2007).

Addendum to Paper V

The experimental setup used in Paper V corresponds to the same open-loop layout presented in Paper II. Nonetheless, testing conditions were slightly different. In paper II the minimum axial clearance was 0.20/0.25 mm on in- and outlet side, while temperatures were varied from 500°C to 600°C. The experimental tests reported in Paper V reduced the axial clearance down to 0.15/015 mm on in- and outlet side. To compensate for this reduction in clearance and reduce risk of thermal expansion effects leading to contact of the rotor with the inlet stator face, peak inlet temperature was slightly reduced to approximately 475°C. This renders a direct comparison of results difficult. However, the overall trends are comparable and reasonable. At a loop flow ratio of 1.7, a rotational speed of 28,000 rpm and a mass flow rate through the HPG port of approximately 32 g/s the reduced clearance results in greater achieved pressure ratio of approximately 1.75 and a power output of 250 W (Figure 11(c) in Paper V). In the first experimental campaign, a similar operating point yields a pressure ratio of 1.58 and a power output of approximately 300 W (Figure 13 in Paper II). This is in line with the trends observed in both experiments and simulation, where a decrease in leakage enhances pressure ratio. In turn, the increase in backpressure from the HPA duct in combination with the reduced peak inlet temperature account for a decrease in power output.

4.3.1 Summary and Implications of Paper V

The paper discussed in Section 4.3 addresses the question of whether the trends observed from the numerical quasi-two- and three-dimensional simulations can be reproduced by experimental means. To this end, the study employs the same open-loop layout using electrical heaters as a supply of heat and an eddy current dynamometer to measure torque and control rotational speed, as already put forward in Chapter 2.2. Since only the rotor shape itself was optimised and stators were kept unchanged, both rotors could be tested easily to perform a back-to-back comparison. The experimental results show good agreement with the numerical data with a power output increase of 74 % while pressure ratio decreased by about 4 % at the target operating point. This is highlighted in Figure 23 in Paper IV. This shows a direct, back-to-back comparison of relative shaft power increase and pressure ratio drop predicted by the Q2D-CFD and 3D-CFD models and the experiments. From this, it can be concluded that the reported experimental work further augments the fidelity of the optimisation method and results.

In addition to validation, the paper also aims to further investigate the wave

rotor performance behaviour as inlet mass flow rates are changed. This involves the variation of pressure ratio and wave rotor power as well as internal EGR rate. While power increases linearly with the increase in mass flow rate and the higher momentum it is accompanied by, pressure ratio features a parabolic variation with mass flow rate indicating a clear optimum in terms of incidence angle. Deviating from this optimum yields a rise in flow separation and thus entropy production that compromises the wave rotor's ability to exchange energy.

Furthermore, the paper seeks to provide further information on the behaviour of EGR and its effects on wave rotor efficiency in combination with FAE. Overall, the data emphasise that higher inlet mass flow rates (for a given peak inlet temperature) result in improved scavenging outlined by the lower overall outlet temperature in the HPA outlet duct the higher the inlet mass flow rate. A reasonably accurate estimate of EGR rate is crucial to estimate wave rotor efficiency with good accuracy. Against this background, the experimentally measured temperature distribution proves too restricted to compute EGR rate and can thus merely serve as a qualitative indicator. To mitigate this issue, additional numerical simulations were conducted using the quasi-one-dimensional model of Chapter 1.5 and 2.2. Since the simulations provide an abundance of data in the entire computational domain, it is a relatively simple task to compute an estimate for EGR rates for different operating conditions and wave rotor channel shapes. Combining the data with the experimental temperatures and pressures allows compute wave rotor efficiency to be computed. Although, the uncertainty in efficiency somewhat renders a direct comparison between baseline and optimised rotor difficult, the trendlines through the discrete data points show a consistently higher efficiency for lower rotational speeds among both rotor designs. This is in line with the higher pressure ratio witnessed at lower rotational speeds and also in line with the findings from Chapter 1.5, where lower rotational speeds indicate higher efficiencies and pressure ratios.

Chapter 5

Conclusions and Future Work

Despite their versatility, maturity and high energy density, achieving acceptable component and system efficiencies with micro-scale turbomachinery in the sub-1 kW shaft power output range remains challenging. High rotational speeds in excess of several 100,000 rpm are necessary in order to maintain similar enthalpy and pressure changes. This impairs service life and reliability and poses rotordynamic issues while losses increase considerably due to larger relative tip leakage, surface roughness and trailing edge mixing losses. Combined, this accounts for a substantial drop in component and system efficiency.

A shock-driven, power generating wave rotor turbine may posses the potential to mitigate some of these challenges. Wave rotors have successfully been applied as topping devices to gas turbine cycles, internal combustion engines and refrigeration cycles with the objective of increasing power output and raising thermal efficiency. The literature review in Chapter 1 has revealed that the majority of devices in the open literature resort to purely axial pressure exchangers that are driven externally via an electric motor or are coupled to a crankshaft via a belt. Non-axial wave rotors that allow power extraction through momentum change while functioning as a pressure exchanging device, however, have enjoyed limited attention in the research community. In fact, most research efforts failed to yield the targeted power output. This thesis has, therefore, contributed to closing this gap and focused on the development, numerical modelling and experimental testing of non-axial micro-wave rotor turbine. The results achieved advance the understanding of the interaction between loop flow ratio, leakage, speed sensitivity and EGR rates. In addition, the presented work has advanced modelling capabilities by accounting for cambered rotor channels and providing an efficient computational framework to optimise pressure exchange machinery.

5.1 Conclusions

This thesis has aimed to address the following objectives, namely (i) understand the characteristics of a wave rotor-based gas turbine, (ii) explore the sensitivity of wave rotor performance to boundary and operating conditions (iii) validate one-dimensional modelling approach and outline its capabilities and limitations and (iv) explore the optimisation potential and investigate the relationship between pressure exchange and power generation.

The first objective has been addressed through the numerical study in Chapter 2. It explored the concept of replacing the turbomachinery arrangement in a gas turbine with a wave rotor turbine with symmetrically cambered channels via numerical means. Although constrained by a number of simplifying assumptions, the results reveal that foremost axial leakage and combustor pressure loss are the most dominant performance affecting parameters. The wave rotor gas turbine appears, however, less sensitive to backpressure from the low pressure exhaust port. Additionally, the data suggest that the internal heat recuperation render an additional external heat recuperator detrimental as a consequence of increased combustor pressure losses. The issue of leakage could potentially be addressed through the application of appropriate seals and accommodation for thermal expansion between rotating and stationary components, while the combustor pressure loss can be alleviated using pressure-gain combustion. However, power generation appears to be the main limitation of power generating wave rotor turbines. The pulsatile nature of power generation results in poor thermal efficiency despite reasonably high component efficiency for compression and expansion. While this can be partially be addressed through an increased number of cycles per revolution and thus a greater number of high pressure inlets, there are limitations with respect to ducting complexity.

Subsequently, Chapter 3 sought to assess whether the numerical data from Chapter 2 are transferable when examined experimentally and aimed at characterising a micro-wave rotor turbine, further elaborating on the performance potential and trade-offs of objectives. The results from this comprehensive set of experiments achieve the objectives set out in (ii) and reinforce the sensitivity of pressure ratio and outlet temperatures to axial leakage, which can be exacerbated by uneven thermal expansion between different components. This highlights the requirement for good leakage control when running at elevated temperatures. The detriment incurred by larger leakage can potentially be compensated by increasing peak inlet temperature, although this potentially intensifies uneven thermal expansion. However, the experiments give testimony to reasonably high compression/expansion efficiencies achieved via shock compression.

Interestingly, the results are relatively insensitive to changes in rotational speed and the associated change in gas dynamics and wave arrival times.

The numerical validation study in Chapter 3 illustrates the capabilities and limitations of the quasi-one-dimensional model introduced in Chapter 2. This addresses objective (iii). Overall, when compared with low temperature results from the open literature, the model achieves good agreement with experimental data in both steady-state and transient. This exemplifies that the wave dynamics in the model are well established. The model's capacity to estimate shock wave pattern as well as outlet temperatures, shaft power and pressure ratio distributions for wave rotor turbines at higher temperatures is reasonably good as well. However, the data reinforce that the model loses accuracy with excessive leakage due to a greater level of channel-to-channel interaction causing substantial shock wave attenuation. Such effects cannot be captured by the model. In addition, the uncertainty with respect to the actual clearance when running under hot conditions adds to greater discrepancy between the experimental and simulation results.

The final objective (iv) of this thesis has been achieved through the articles presented in Chapter 4. First of all, an effective and efficient optimisation framework to improve the power output of the initial baseline wave rotor model is proposed. The constrained optimisation successfully coupled a quasi-two-dimensional model with a hybrid algorithm and yielded a considerable increase in power output. This was confirmed by both extensive 3D-CFD simulations and subsequently via back-to-back experimental tests. However, both numerical and experimental data suggest that careful handling is required to control flow incidence as a channel passes through an inlet port. Finite passage opening effects account for a large variation in flow incidence with large negative incidence during opening and large positive values during closing periods. Nonetheless, the data show that although the flow incidence remains negative for large portions of the channel exposure to the port, the channel achieves torque generation as a consequence of momentum change along the channel camberline. The results thus shed light on the relationship between pressure exchange and power generation. End effects increase incidence losses and compromise efficiency as well as power generation.

To summarise, this thesis has extended the current state of wave rotor research to non-axial designs both through experimental and numerical means. The key achievements in this thesis include the introduction of a quasi-one dimensional model that can be used to estimate the performance of both axial and non-axial wave rotor designs. The capabilities and limitations of the model have been reported and as well. In addition, an efficient optimisation framework has been put forward that is not limited to wave rotors, but can be applied to any expensive numerical model. Fi-

nally, the shortcomings of wave rotor power generation and their implications on the pressure-exchange have been established as well.

5.2 Future Work

There is great scope to continue the work at hand on non-axial wave rotor turbines. In the following paragraphs, a number of aspects are highlighted that merit the consideration from the academic and industrial community. The first aspect concerns the numerical modelling approach. Firstly, the proposed optimisation study in Chapter 4 was focused on the wave rotor channel shape and was constrained to the port arrangement and sizing of the baseline geometry. A more holistic optimisation approach that parameterises port solution as well as wave rotor channel shape can potentially eliminate some of the issues witnessed. Such an approach can alleviate the effects of increased entropy production due to the large variation range of flow incidence angles from the port into the channels. However, such an optimisation will increase considerably in dimensionality as the numbers of dependant variables increase from six to approximately 22 considering four additional parameters per port, governing port angle as well as port length and azimuthal position.

Secondly, in its current version the quasi-one-dimensional model features a distributed entropy related loss term to account for misalignment of the flow and the camberline shape. This, however, requires some *a priori* knowledge from experiments or more elaborate and higher order CFD simulations to adjust the parameters. In order to enhance the predictive capabilities of the model, it is necessary to compute the velocity of the flow within the inlet ports to infer the incidence angle in combination with the port angle. For cases with incidence angles larger than zero a *vena contracta* will form as a consequence of the sharp channel edge. Using an empirical fit for the pressure loss coefficients as a function of incidence angle, the losses could be computed at an instantaneous instance as the flow enters the channel.

The final aspects that deserve attention from future research concern the experimental approach. Throughout this thesis, the wave rotor turbines have been tested as a standalone unit in an open-loop fashion. While this allows a high degree of flexibility and freedom with respect to performance characterisation, it effectively uncouples the high pressure in (HPG) and the high pressure outlet side (HPA). Therefore, to obtain more reliable predictions regarding system behaviour and performance, it is necessary to test the wave rotor turbine in combination with a combustor. In its simplest form, this can be a can-type, swirl-stabilised combustor. In order to minimise pressure losses, one may also resort to catalytic combustor types that do not

require measures for flame stabilisation and thus suffer from reduced pressure losses. To account for the larger combustor outlet temperature compared to testing, particular attention needs to be drawn to ensure cooling of critical components, such as bearings. Also, thermal expansion issues may be exacerbated at higher temperatures and larger nominal clearances beyond 0.3 mm may be necessary to ensure stable and safe operation.

Axial leakage has been identified as one of most crucial parameters to obtain optimal pressure-exchange performance in any type of wave rotor. One of the limitations of the experimental setup in this thesis is the uncertainty that surrounds the actual clearance between the rotor faces and the stator endplates when running in thermal equilibrium. From the author's perspective it requires a substantial effort to tackle this issue. The wave rotor unit is particularly compact, which poses a particular obstacle when it comes to measuring leakage gap while running. In addition to size requirements and accessibility constraints, any sensor used for such a purpose needs to be able to withstand a pressurised environment and may require a dedicated cooling circuit to be able to operate in an environment at elevated temperatures for extended periods of time.

It is noteworthy to stress that while the aforementioned suggestions would further enhance the knowledge of shock-driven wave rotors, the contributions provided by this thesis shall not be clouded. Establishing a numerical framework used to develop and optimise wave rotor turbines and carrying out comprehensive experimental wave rotor characterisation testing remains a significant achievement.

Bibliography (Complementary to Publications)

[1] Special Interest Group, Robotic & Autonomous Systems, "RAS 2020 Robotics and Autonomous Systems," The Knowledge Transfer Network, July 2014.

[2] Defence Science and Technology Laboratory (2016, Nov. 10) *Competition document: beyond battery power* [Online]. Available: https://www.gov.uk/government/publications/cde-themed-competition-beyond-battery-power/competition-document-beyond-battery-power

[3] T. Pearson, Z. Alsalihi and R.A. Van den Braembussche, "Numerical Study of the Heat Transfer in Micro Gas Turbines," *Journal of Turbomachinery*, Vol. 129, pp. 835-841.

[4] A. Marcellan, W.P.J. Visser and P. Colonna, "Potential of Micro Turbine Bassed Propulsion Systems for Civil UAS: A Case Study," *Proceedings of ASME Turbo Expo 2016: Turbomachinery Technical Conference and Exposition*, June 13-17, Seoul, South Korea, 2016.

[5] R.A. Van den Braembussche, "Micro Gas Turbines - A Short Survey of Design Problems," , *Micro Gas Turbines*, Educational Notes RTO-EN-AVT-131, Paper 1, Neuilly-sur-Seine, France, pp. 1-1-1-18.

[6] M.J. Vick, "High Efficiency Recuperated Ceramic Gas Turbine Engines for Unmanned Air Vehicle Propulsion," Ph.D. dissertation, Department of Mechanical Engineering, Imperial College London, UK, 2012.

[7] N. Müller and L.G. Fréchette, "Performance Analysis of Brayton and Rankine Cycle Microsystems for Portable Power Generation," *Proceedings of IMECE2002*

ASME International Mechanical Engineering Congress & Exposition, November 17-22, New Orleans, USA, 2002.

[8] A.J. Head and W.P.J. Visser, "Scaling 3-36kW Microturbines," *Proceedings of ASME Turbo Expo 2012 GT2012*, June 11-15, Copenhagen, Denmark, 2012.

[9] P. Akbari and N. Müller, "Preliminary Design Procedure for Gas Turbine Topping Reverse-Flow Wave Rotors," *Proceedings of the International Gas Turbine Congress*, 2-7 November 2003, Tokyo, Japan.

[10] P. Akbari and N. Müller, "Gas Dynamic Design Analyses of Charging Zone for Reverse-Flow Pressure Wave Superchargers," *Proceedings of ICES03 2003 Spring Technical Conference of the ASME Internal Combustion Engine Division*, 11-14 May 2003, Salzburg, Austria.

[11] F. Iancu, J. Piechna and N. Müller, "Basic Design Scheme for Wave Rotors," *Shock Waves*, Vol. 18, pp. 365-378, 2008.

[12] D.E. Paxson, "A General Numerical Model for Wave Rotor Analysis," *NASA TM 105740*, 1992.

[13] D.E. Paxson and J. Wilson, "An Improved Numerical Model for Wave Rotor Design and Analysis," *AIAA-93-0482*, 1993.

[14] D.E. Paxson and J. Wilson, "Recent Improvements to and Validation of the One Dimensional NASA Wave Rotor Model," *NASA Technical Memorandum 106913*, 1995.

[15] D.E. Paxson, "An Incidence Loss Model for Wave Rotors with Axially Aligned Passages," *NASA/TM-1998-207923*, 1998.

[16] J.A.C. Kentfield, "The Performance of Pressure-Exchanger Dividers and Equalizers," *Journal of Basic Engineering*, pp.361-369 ,1969.

[17] J.A.C. Kentfield, "An Examination of the Performance of Pressure Exchanger Equalisers and Dividers," *PhD Thesis*, University of London, 1963.

[18] D.E. Paxson, "A Numerical Model for Dynamic Wave Rotor Analysis," *AIAA-95-2800*, 1995.

[19] D.E. Paxson, "A Numerical Investigation of the Startup Transient in a Wave Rotor," *Journal of Engineering for Gas Turbines and Power*, Vol. 119, Issue 3, pp. 676-682, 1997.

[20] J. Wilson and D.E. Paxson, "Optimization of Wave Rotor for Use as Gas Turbine Engine Topping Cycles," *NASA Technical Memorandum 106951*, 1995.

[21] D.E. Paxson and M.R. Nalim, "A Modified Through-Flow Wave Rotor Cycle With Combustor Bypass Duct," *Journal of Propulsion and Power*, Vol. 5, Issue 3, pp. 462-467, 1999.

[22] D.E. Paxson and J.W. Lindau, "Numerical Assessment of Four-Port Through-Flow Wave Rotor Cycles with Passage Height Variation," *NASA Technical Memorandum*, 107490, 1997.

[23] G.E. Welch and L.M. Larosiliere, "Passage-Averaged Description of Wave Rotor Flow," *NASA Technical Memorandum*, NASA/TM-1997-107518, 1997.

[24] G.E. Welch and D.E. Paxson, "Wave Turbine Analysis Tool Development," *NASA Technical Memorandum*, NASA/TM-1998-208485, 1998.

[25] R.R. Jagannath, S.P.M. Bane and M.R. Nalim, "Numerical Modeling of a Wave Turbine and Estimation of Shaft Work," *Journal of Fluids Engineering*, Vol. 140, pp. 101106-1-101106-13, 2018.

[26] M.R. Nalim and D.E. Paxson, "A Numerical Investigation of Premixed Combustion in Wave Rotors," *Journal of Engineering for Gas Turbines and Power*, Vol. 119, pp. 668-675, 1997.

[27] R.R. Jagannath, S.P.M. Bane, M.E. Feyz and M.R. Nalim, "Assessment of Incidence Loss and Shaft Work Production for Wave Rotor Combustor with Non-Axial Channels," *55th AIAA Aerospace Sciences Meeting 2017*, 9-13 January 2017, Grapevine, Texas, United States.

[28] A. Fatsis, A. Lafond and Y. Ribaud, "Preliminary Analysis of the Flow inside a Three-Port Wave Rotor by means of a Numerical Model," *Aerospace Science and Technology*, Vol. 5, pp. 289-300, 1998.

[29] A. Fatsis, N.G. Orfanoudakis, D.G. Pavlou, A. Panoutsopoulou and N. Vlachakis, "Unsteady Flow Modelling of a Pressure Wave Supercharger," *Proceedings of the Institution of Mechanical Engineers Part D Journal of Automobile Engineering*, Vol. 220, Issue 2, pp. 209-218, 2006.

[30] T. Nagashima, K. Okamoto and Y. Ribaud, "Cycles and Thermal System Integration Issues of Ultra-Micro Gas Turbines," in *Micro Gas Turbines* (pp.4-1 -

4-66), Educational Notes RTO-EN-AVT-131, Paper 4, Neuilly-sur-Seine, France, 2005.

[31] P. Akbari, M.R. Nalim, E.S. Donovan and P.H. Snyder, "Leakage Assessment of Pressure-Exchange Wave Rotors," *Journal of Propulsion and Power*, Vol. 24, Issue 4, pp. 732-740, 2008.

[32] J. Piechna, "Wave Machines, Models and Numerical Simulation," *Prace Naukowe Politechniki Warszawskiej*, Issue 205, pp. 3-165, 2005.

[33] F. Iancu, J. Piechna and N. Müller, "Numerical Solutions for Ultra-Micro Wave Rotors (UμWR)," *35th AIAA Fluid Dynamics Conference and Exhibit*, 6-9 June 2005, Toronto, Canada.

[34] J. Piechna, R. Cerpa, S. Marcin, P. Akbari and N. Müller, "Numerical Analysis of the Wave Topping Unit for Small Turbojet," *Proceedings of ASME Turbo Expo 2010: Power for Land, Sea and Air*, June 14-18, Glasgow, United Kingdom.

[35] S. Chan, H. Liu, F. Xing and H. Song, "Wave Rotor Design Method With Three Steps Including Experimental Validation," *Journal of Engineering for Gas Turbines and Power*, Vol. 140, pp. 111201-1-111201-13, 2018.

[36] Y. Oguri, T. Suzuki, M. Yoshida and M. Cho, "Research on Adaption of Pressure Wave Supercharger (PWS) to Gasoline Engine," *SAE Technical Paper 2001-01-0368*, 2001.

[37] T. Suzuki, Y. Oguri, K. Uchida and M. Yoshida, "Experimental Investigation of Pressure Wave Supercharging for SI Engine," *2004 ASME International Mechanical Engineering Congress and Exposition*, 13-20 November, 2004, Anaheim, USA.

[38] Y. Lei, D.S. Thou and H.G. Zhang, "Investigation on performance of a compression-ignition engine wih pressure-wave supercharger," *Energy*, Vol. 35, pp. 85-93, 2010.

[39] L. Guzzella, U. Wenger and R. Martin, "IC-Engine Downsizing and Pressure-Wave Supercharging for Fuel Economy," *SAE Technical Paper*, 2000-01-1019, 2001.

[40] M. Mataczynski, J. Hoke, D. Paxson and M.D. Polanka , "Design, Simulation, and Testing of a Pressure Wave Supercharger for a Small Internal Combustion Engine," *SAE Technical Paper*, 2014-01-2136, 2014.

[41] A. Mayer, J. Oda, K. Kato, W. Haase and R. Fried, "Extruded Ceramic—A New Technology for the Comprex® Rotor," *SAE Technical Paper*, 890453, 1989.

[42] L. Guzzella and R. Martin, "The Save Engine Concept," *Motortechnische Zeitschrift*, Vol. 10, pp. 9-12, 1998.

[43] H. Hiereth, "Car Tests with a Free-Running Pressure-Wave Charger—A Study for an Advanced Supercharging System," *SAE Paper 890453*, 1989.

[44] R.T. Taussig and A. Hertzberg, "Wave Rotors for Turbomachinery," *Winter Annual Meeting of the ASME, Machinery for Direct Fluid-Fluid Energy Exchange*, edited by J.F. Sladky, AD-07, pp.1-7, 1984.

[45] A. Fatsis, "Design point analysis of two-shaft gas turbine engines topped by four-port wave rotors for power generation systems," *Propulsion and Power Research*, Vol. 8, Issue 3, pp.183-193, 2019.

[46] P. Akbari, R. Nalim and N. Müller, "Performance Enhancement of Microturbine Engines Topped With Wave Rotors," *Journal of Engineering for Gas Turbines and Power*, Vol. 128, pp.190-202, 2006.

[47] G.E. Welch, S.M. Jones and D.E. Paxson, "Wave-Rotor-Enhanced Gas Turbine Engines," *Journal of Engineering for Gas Turbines and Power*, Vol. 128, pp.469-477, 1997.

[48] G.E. D.E. Paxson, J. Wilson and P.H. Snyder, "Wave-Rotor-Enhanced Gas Turbine Engine Demonstrator," *NASA/TM-1999-209459*, 1999.

[49] P.H. Snyder, "Wave Rotor Demonstrator Engine Assessment," *NASA Contractor Report 198496*, 1996.

[50] A. Fatsis and Y. Ribaud "Thermodynamic analysis of gas turbines topped with wave rotors," *Aerospace Science and Technology*, Vol. 5, pp.293-299, 1999.

[51] F. Klein and S. Staudacher, "Plausibility Study of Hecto Pressure Ratio Concepts in Large Civil Aero-Engines," *Journal of Engineering for Gas Turbines and Power*, Vol. 140, pp.051201-1-051201-10, 2018.

[52] J. Wilson and D.E. Paxson, "Jet Engine Performance Enhancement Through Use of a Wave-Rotor Topping Cycle," *NASA Technical Memorandum 4486*, 1993.

[53] L. Pohořelský, P. Sané, T. Sozsas and N. Müller, "Wave Rotor Design Procedure for Gas Turbine Enhancement," *Proceedings of ASME Turbo Expo 2008: Power for Land, Sea and Air*, 9-13 June 2008, Berlin, Germany.

[54] E. Zauner, Y.-P. Chyou, F. Walraven and R. Althaus, "Gas Turbine Topping Stage Based on Energy Exchangers: Process and Performance," *ASME 1993 International Gas Turbine and Aeroengine Congress and Exposition*, 24-27 May 1993, Cincinnati, USA.

[55] G. E. Welch, "Wave Engine Topping Cycle Assessment," *35th Aerospace Sciences Meeting & Exhibit*, AIAA-97-0707, 6-10 January 1997, Reno, USA.

[56] G. Lenoble and S. Ogaji, "Performance analysis and optimization of a gas turbine cycle integrated with an internal combustion wave rotor," *Proc. IMechE Vol. 224 Part A: J. Power and Energy*, Vol. 224, Issue 7, 2010.

[57] M.R. Nalim, "Longitudinally Stratified Combustion in Wave Rotors," *Journal of Propulsion and Power*, Vol. 16, No. 6, 2000.

[58] M.R. Nalim, P.H. Snyder and M. Kowalkowski, "Experimental Test, Model Validation, and Viability Assessment of a Wave-Rotor Constant-Volume Combustor," *Journal of Propulsion and Power*, Vol. 33, No. 1, 2017.

[59] M.R. Nalim, H. Li and P. Akbari, "Air-Standard Aerothermodynamic Analysis of Gas Turbine Engines with Wave Rotor Combustion," *Proceedings of ASME Turbo Expo 2009: Power for Land, Sea and Air*, GT2009-60055, Jun, 2009, Orlando, Florida, United States.

[60] M. Rajagopal, A. Karimi and R. Nalim, "Wave-Rotor Pressure-Gain Combustion Analysis for Power Generation and Gas Turbine Applications," *Proceedings of the ASME 2012 Gas Turbine India Conference*, GTINDIA2012-9741, Dec, 2012, Mumbai, Maharashtra, India.

[61] M.R. Nalim, "Assessment of Combustion Modes for Internal Combustion Wave Rotors," *Journal of Engineering for Gas Turbines and Power*, Vol. 121, pp. 265-271, 1999.

[62] M.R. Nalim and D.E. Paxson, "A Numerical Investigation of Premixed Combustion in Wave Rotors," *Journal of Engineering for Gas Turbines and Power*, Vol. 119, pp. 668-675, 1997.

[63] M.R. Nalim and E.L. Resler Jr., "Wave Cycle Design for Wave Rotor Turbine Engines with Low NO_x Emissions," *Journal of Engineering for Gas Turbines and Power*, Vol. 118, pp. 474-480, 1996.

[64] M.R. Nalim,, Z.A. Izzy and P. Akbari, "Rotary wave-ejector enhanced pulse detonation engine," *Shock Waves*, Vol. 22, pp. 23-38, 2012.

[65] K. Pekkan and M.R. Nalim, "Two-Dimensional Flow and NO_x Emissions in Deflagrative Internal Combustion Wave Rotor Configurations," *J. Eng. Gas Turbines Power*, Vol. 125, Issue 3, pp. 720-733, 2003.

[66] J. Li, E. Gong, L. Yuan, W. Li and K. Zhang, "Experimental Investigation on Pressure Rise Characteristics in an Ethylene Fuelled Wave Rotor Combustor," *Energy Fuels*, Vol. 31, No. 9, pp. 10165-10177, 2017.

[67] J. Li, E. Gong, L. Yuan, W. Li and K. Zhang, "Experimental Investigation on Flame Formation and Propagation Characteristics in an Ethylene Fuelled Wave Rotor Combustor," *Energy Fuels*, Vol. 32, No. 2, pp. 2366-2375, 2018.

[68] J. Li, K. Zhang, W. Li and L. Yuan, "Investigation of Pressure Rise and Flame Acceleration Characteristics in a Single Channel of Wave Rotor Combustor with Spoilers," *International Journal of Aerospace Engineering*, 2019.

[69] A.A. Kharazi, P. Akbari and N. Müller, "Preliminary Study of a Novel R718 Compression Refrigeration Cycle Using a Three-Port Condensing Wave Rotor," *Journal of Engineering for Gas Turbines and Power*, Vol. 127, 2005, pp. 539-544.

[70] D. Hu, Y. Yu, P. Liu, X. Wu and Y. Zhao, "Improving Refrigeration Performance by Using Pressure Exchange Characteristic of Wave Rotor," *Journal of Energy Resources Technology*, Vol. 141, 2019, pp. 022004-1-022004-8.

[71] D. Hu, R. Li, P. Liu and J. Zhao, "The design and influence of port arrangement on an improved wave rotor refrigerator performance," *Applied Thermal Engineering*, Vol. 107, pp. 207-217, 2016.

[72] D. Hu, R. Li, P. Liu and J. Zhao, "The loss in charge process and effects on performance of wave rotor refrigerator," *International Journal of Heat and Mass Transfer*, Vol. 100, pp. 497-507, 2016.

[73] D. Hu, Y. Yu and P. Liu, "Enhancement of refrigeration performance by energy transfer of shock wave," *Applied Thermal Engineering*, Vol. 130, pp. 309-318, 2018.

[74] Y. Dai, D. Hu and M. Ding, "Study on wave rotor refrigerators," *Front. Chem. Eng. China*, Vol. 3, pp. 83-87, 2009.

[75] J. Zhao and D.Hu, "An improved wave rotor refrigerator using an outside gas flow for recycling the expansion work," *Shock Waves*, Vol. 27, Issue 2, pp. 325-332, 2017.

[76] R. D. Pearson, "A Gas Wave-Turbine Engine Which Deveoped 35 HP and Performed Over a 6:1 Speed Range," *Proceedings ONR/NAVAIR Wave Rotor Research and Technology Workshop*, Naval Postgraduate School, Monterey, CA, Report NPS-67-85-008, pp. 125.

[77] R. D. Pearson, Pressure Exchangers and Pressure Exchange Engines, *Thermodynamics and Gas Dynamics of Internal Combustion Engines, Volume II*, edited by D.E. Winterbone and S.C. Low, Oxford University Press, 1986.

[78] H.E. Weber, *Shock Wave Engine Design*, John Wiley & Sons, New York, 1995.

[79] R. Taussig, P. Cassady, J. Zumdieck, W. Thayer and E. Klostermann, "Investigation of Wave Rotor Turbofans for Cruise Missile Engines," *Final Report Submitted by MSNW to DARPA*, 1983.

[80] A. Mathur, "Design and Experimental Verification of Wave Rotor Cycles," *Proceedings ONR/NAVAIR Wave Rotor Research and Technology Workshop*, Naval Postgraduate School, Monterey, CA, Report NPS-67-85-008, pp. 215-219.

[81] P. Akbari, R. Nalim and N. Müller, "A Review of Wave Rotor Technology and its Applications," *Journal of Engineering for Gas Turbines and Power*, Vol. 128, Issue 4, pp.717-735, 2016.

[82] J. Piechna, P. Akbari, F. Iancu and N. Müller, "Radial-Flow Wave Rotor Concepts, Unconventional Designs and Applications," *Proceedings of IMECE04 2004 ASME International Mechanical Engineering Congress*, IMECE2004-59022, Nov, 2004, Anaheim, California, United States.

[83] J. Piechna and D. Dyntar, "Numerical investigation of the Wave Disk Micro-Engine concept," *International Journal of Gas Turbine, Propulsion and Power Systems*, Vol. 2, No. 1, pp.1-8, 2008.

[84] J. Piechna and D. Dyntar, "Hybrid Wave Engine Concept and Numerical Simulation of Engine Operation," *The Archive of Mechanical Engineering*, Vol. LVII, No. 1, pp.69-95, 2010.

[85] J. Piechna, "Feasibility study of the wave disk micro-engine operation," *Journal of Micromechanics and Microengineering*, Vol. 16, No. 9, pp.S270-S281, 2006.

[86] P. Parraga-Ramirez, M. Varnez, E. Tarkleson, N. Müller, P. Akbari and J. Piechna, "Development of a Wave Disk Engine Experimental Facility," *48th AIAA/ASME/SAE/ASEE Joint Propulsion Conference & Exhibit*, AIAA 2012-3703, Jul-Aug, 2012, Atlanta, Georgia, United States.

[87] P. Akbari and I. Agoos, "Two-Stage Wave Disk Engine Concept and Performance Prediction," SAE Technical Paper 2017-01-2046, 2017.

[88] J. Hongde, "Two Dimensional Unsteady Flow in Comprex Rotor," *Scientia Sinica*, Vol. 27, Number 8, pp. 847-858, 1984.

[89] H.S. Zhang and R.M.C. So, "Calculation of the material interface in a pressure-wave supercharger," *Proceedings of the Institution of Mechanical Engineers, Part A: Journal of Power and Energy*, Vol. 204, pp. 151-161, 1990.

[90] H.S. Zhang and R.M.C. So, "A Flux-Coordinate-Splitging Technique for Flows with Shocks and Contact Discontinuities," *Computers Fluids*, Vol. 20, No. 4, pp. 421-442, 1991.

[91] K. Okamoto, T. Nagashima and S. Teramoto, "Multi-Passage Gasdynamic Interactions in Wave Rotor," *24th International Congress of the Aeronautical Sciences*, , Aug-Sep, 2004, Yokohama, Japan.

[92] C. Liu and H. Liu, "Nonsteady Shock Wave Attenuation Due to Leakage," *Energies*, Vol. 11, No. 12, pp. 1-20, 2018.

[93] L.M Larosiliere, "Three-Dimensional Numerical Simulation of Gradual Opening in a Wave Rotor Passage," *AiAA-93-2526*, 1993.

[94] G.E. Welch, "Two-Dimensional Computational Model for Wave Rotor Flow Dynamics," *NASA Technical Memorandum 107192*, 1996.

[95] S. Deng, K. Okamoto and S. Teramoto, "Numerical Investigation of Heat Transfer Effects in Small Wave Rotor," *Journal of Mechanical Science and Techology*, Vol. 29, Issue 3, pp. 939-950, 2015.

[96] Y. İçingür, C. Haşimoğlu and M.S. Salman, "Effect of comprex supercharging on diesel emissions," *Energy Conversion and Management*, Vol. 44, pp. 1745-1753, 2003.

[97] G.M. Schruf and T.A. Kollbrunner, "Application and Matching of the Comprex Pressure-Wave Supercharger to Automotive Diesel Engines," *SAE Technical Paper 840133*, 1984.

[98] P. Spring, C.H. Onder and L. Guzzella, "EGR control of pressure-wave supercharged IC engines," *Control Engineering Practice*, Vol. 15, pp. 1520-1532, 2007.

[99] Y. Lei, D. Zhou, H. Zhang, C. Ji, J. Li and T. Zhao, "Experiment and CFD Investigation of Pressure-wave Supercharger," *SAE Technical Paper*, 2008-01-1631, 2008.

[100] B.A. Beasley, *Investigation of a Pressure Wave Supercharger for an Industrial Diesel Engine*, MSc thesis, Department of Aeronautics and Astronautics, Air Force Institute of Technology, AFIT-ENY-MS-18-S-055, Wright-Patterson Air Force Base, Ohio, United States, 2018.

[101] K.P. Lapp, *Design and Testing of a Micro-Scale Wave Rotor System*, MSc thesis, Department of Aeronautics and Astronautics, Air Force Institute of Technology, AFIT-ENY-MS-17-S-067, Wright-Patterson Air Force Base, Ohio, United States, 2016.

[102] K.P. Lapp, M.D. Polanka, M.J. McClearn, J.L. Hoke and D.E. Paxson, "Design and TEsting of a Micro-Scale Wave Rotor System," *AIAA Propulsion and Energy Forum*, Jul, 2017, Atlanta, Georgia, United States.

[103] M.J. McClearn, *Design, Manufacturing, and Testing of a Small Through-Flow Wave Rotor for Use Within the Brayton Cycle*, MSc thesis, Department of Aeronautics and Astronautics, Air Force Institute of Technology, AFIT-ENY-MS-16-J-054, Wright-Patterson Air Force Base, Ohio, United States, 2018.

[104] B.D. Smith, M.D. Polanka, D.E. Paxson and J.L.Hoke, "Scaling Study of Wave Rotor Turbo Normalization of an Internal Combustion Engine," *48th AIAA/ASME/SAE/ASEE Joint Propulsion Conference & Exhibit*, AIAA 2012-3837, Jul-Aug, 2012, Atlanta, Georgia, United States.

[105] M.R. Mataczynski, M.J. McClearn, F.R. Schauer, D.E. Paxson and J.L.Hoke, "Design and Testing of a Small Pressure Wave Supercharger for an Industrial Diesel Engine," *55th AIAA Aerospace Sciences Meeting*, AIAA 2017-1624, Jan, 2017, Grapevine, Texas, United States.

[106] M.R. Mataczynski, *Design and Simulation of a Pressure Wave Supercharger for a Small Two-Stroke Engine*, MSc thesis, Department of Aeronautics and Astronau-

tics, Air Force Institute of Technology, AFIT-ENY-14-M-34, Wright-Patterson Air Force Base, Ohio, United States, 2014.

[107] M.R. Mataczynski, D.E. Paxson, M.D. Polanka and J.L.Hoke, "Performance and Design Improvements for a Small Scale Pressure Wave Supercharger," *54th AIAA Aerospace Sciences Meeting*, AIAA 2016-0768, Jan, 2016, San Diego, California, United States.

[108] J. Wilson and D. Fronek, "Initial Results from the NASA-Lewis Wave Rotor Experiment," *29th Joint Propulsion Conference and Exhibit cosponsered by the AIAA, SAE, ASME, and ASEE*, AIAA-93-2521, Jun, 1993, Monterey, California, United States.

[109] J. Wilson, "An Experimental Determination of Losses in a 3-Port Wave Rotor," *Journal of Engineering for Gas Turbines and Power*, Vol. 120, pp. 833-842, 1998.

[110] R.C. Hendricks, J. Wilson, T. Wu and R. Flower, "Bidirectional Brush Seals," *NASA Technical Memorandum 107351*, 1997.

[111] J. Wilson, "Design of the NASA Lewis 4-Port Wave Rotor Experiment," *NASA Contractor Report 202351*, 1997.

[112] J. Wilson, G.E. Welch and D.E. Paxson, "Experimental Results of Performance Tests on a Four-Port Wave Rotor," *NASA/TM—2007-214488*, 2007.

[113] J.W. Slater and G.E. Welch, "Design of a Wave-Rotor Transition Duct," *35th AIAA Fluid Dynamics Conference and Exhibit*, AIAA 2005-5143, Jun, 2005, Toronto, Ontario, Canada.

[114] D.E. Paxson, J. Wilson and G.E. Welch, "Comparison Between Simulated and Experimentally Measured Performance of a Four Port Wave Rotor," *NASA/TM—2007-214985*, 2007.

[115] Y. Matsutomi, S.E. Meyer, S.D. Wijeyakulasuriya, Z. Izzy, M.R. Nalim, M. Shimo, M. Kowalkowski and P.H. Snyder, "Experimental Investigation on the Wave Rotro Constant Volume Combustor," *46th Joint Propulsion Conference*, AIAA Paper 210-7043-210, Jul, 2010, Nashville, Tennessee, United States.

[116] Y. Matsutomi, C. Hein, C. Lian, S. Meyer, C. Merkle and and S. Heister "Facility Development for Testing of Wave Rotor Combustion Rig," *43rd AIAA/ASME/SAE/ASEE Joint Propulsion Conference and Exhibit*, AIAA-2007-5052, Jul, 2007, Cincinnati, Ohio, United States.

[117] M. Araki, T. Ishima, T. Obokata, M. Arai and K. Okamoto, "LDA Measurement of an Intermittent High-Speed Flow inside a Micro Wave Rotor Cell," *SAE Technical Paper*, 2007-01-0010, 2007.

[118] K. Okamoto, K. Yamaguchi, M. Araki and T. Nagashima, "Shock Wave Observations in Narrow Tubes for Parametric Study on Micro Wave Rotor Design," *Proceedings of the 8th International Symposium on Experimental and Computational Aerothermodynamics of Internal Flows*, ISAIF8-0068, Jul, 2007, Lyon, France.

[119] J. Li, E. Gong, W. Li and K. Zhang, "Investigation on Combustion Properties in Simplified Wave Rotor Constant Volume Combustor," *21st AIAA International Space Planes and Hypersonics Technologies Conference*, Mar, 2017, Xiamen, China.

[120] P. Parraga-Ramirez, M. Varney, E. Tarkleson, N, Müller, P. Akbari and J. Piechna, "Development of a Wave Disk Engine Experimental Facility," *48th AIAA/ASME/SAE/ASEE Joint Propulsion Conference & Exhibit*, AIAA 2012-3703, Jul, 2012, Atlanta, Georgia, United States.

[121] P. Akbari, C.J. Tait, M.D. Polanka and B.C. Sell, "Development and Initial Testing of a Radial Wave Engine," *Proceedings of ASME Turbo Expo 2019: Turbomachinery Technical Conference and Exposition*, GT2019-90608, Jun, 2019, Phoenix, Arizona, United States.

[122] S. Tüchler and C.D. Copeland, "Parametric Numerical Study on the Performance Characteristics of a Micro-Wave Rotor Gas Turbine," *Proceedings of the International Gas Turbine Congress 2019 Tokyo*, IGTC-2019-200, Nov, 2019, Tokyo, Japan.

[123] S. Tüchler and C.D. Copeland, "Experimental Results from the Bath μ-Wave Rotor Turbine Performance Tests," *Journal of Energy Conversion and Management*, Vol. 189, pp.33-48, 2019.

[124] S. Tüchler and C.D. Copeland, "Validation of a Numerical Quasi One-Dimensional-Model for Wave Rotor Turbines with Curved Channels," *Journal of Engineering for Gas Turbines and Power*, GTP-19-1313, Vol. 142, No. 2, pp. 0210171-02101715, 2020.

[125] S. Tüchler and C.D. Copeland, "Validation of a Numerical Quasi One-Dimensional-Model for Wave Rotor Turbines with Curved Channels," *Proceedings*

of ASME TurboExpo 2019: Turbomachinery Technical Conference and Exposition, GT2019-90868, Jun, 2019, Phoenix, Arizona, United States.

[126] S. Tüchler and C.D. Copeland, "Experimental and Numerical Assessment of an Optimised, Non-Axial Wave Rotor Turbine," *Applied Energy*, Vol. 268, 115013, 2020.

[127] E.F. Toro, *Riemann Solvers and Numerical Methods for Fluid Dynamics*, 3rd ed., Springer Verlag, Berlin, 2009.

[128] D.E. Winterbone and R.J. Pearson, *Theory of Engine Manifold Design - Wave Action Methods for IC Engines*, Professional Engineering Publishing Limited, London, UK, 2000.

[129] D.E. Winterbone and R.J. Pearson, *Design Techniques for Engine Manifolds - Wave Action Methods for IC Engines*, Professional Engineering Publishing Limited, London, UK, 1999.

[130] T. Ikeda and T. Nakagawa, "On the SHASTA FCT Algorithm for the Equation $\partial\rho/\partial\mathrm{t}) + [\partial(\nu(\rho)\rho)/\partial\mathrm{x}] = 0$," *Math. Comp.*, Vol. 33, pp. 1157-1169, 1979.

[131] S.F. Davis, "TVD Finite Difference Schemes and Artificial Viscosity," *NASA Contractor Report - 172373*, 1984.

[132] S.F. Davis, "A Simplified TVD Finite Difference Scheme via Artificial Viscosity," *SIAM J. Sci. Comput.*, Volume 8, pp. 1-18, 1987.

[133] P.L. Roe, "Characteristic-based Schemes for the Euler Equations," *Annu. Rev. Fluid Mech.*, Volume 18, pp. 337-365, 1986.

Appendix A

Finite Difference Schemes and Shock Resolution

A.1 First- and Second-Order Numerical Schemes

The flow within a wave rotor features flow discontinuities, such as shock and expansion waves, which is particularly challenging for flow solvers. In general it is desirable that the flow features be accurately reproduced. Nevertheless, this depends largely on the order of accuracy of the employed scheme as well as the level of grid resolution. First-order schemes are robust, relatively resource efficient and simple to implement, yet they tend to smear discontinuities. Second-order schemes on the other hand are able to capture shock patterns well, but suffer from dispersive errors, expressed by spurious oscillations in the vicinity of large gradients. In this section, the first-order accurate scheme of Lax-Friedrichs and the second-order scheme of Richtmyer were compared for their aptitude in capturing the features of shock waves, contact discontinuities and rarefaction waves. The schemes are explicit and based on the finite-difference method. They do not require the formulation of the Jacobian matrix and hence facilitate implementation into a computational code.

A.1.1 Lax-Friedrichs

The mathematical fundamentals of one-dimensional, unsteady, inviscid flow equations within a wave rotor channel are described by the Euler equations. Throughout this thesis, the governing equations are based on conserved variables for the mathematical formulation, as opposed to a formulation based on non-conservative (primitive)

variables. According to Toro [127], this ensures jump conditions, such as shock speed, location and strength, are computed correctly. This set of equations includes partial differential equations (PDE) for the conservation of mass, momentum and energy and can be formulated - in the absence of source terms - as

$$\frac{\partial \mathbf{U}}{\partial t} + \frac{\partial \mathbf{F}(\mathbf{U})}{\partial x} = \mathbf{0} \tag{A.1.1}$$

The first term represents time dependant variations, while the second term refers to advection. The state vector $\mathbf{U}$ and the flux vector $\mathbf{F}$ are defined as

$$\mathbf{U} = \begin{pmatrix} u_1 \\ u_2 \\ u_3 \end{pmatrix} = \begin{pmatrix} \rho \\ \rho u \\ \rho E \end{pmatrix}, \quad \mathbf{F} = \begin{pmatrix} f_1 \\ f_2 \\ f_3 \end{pmatrix} = \begin{pmatrix} \rho u \\ \rho u^2 + p \\ \rho u \Big(E + \frac{p}{\rho}) \end{pmatrix} \tag{A.1.2}$$

The set of PDEs encompasses four primitive variables u, ρ, p and e, which requires the introduction of an additional equation to ensure closure of the equation system. This is done by the ideal gas equation, which relates pressure, temperature and density, from which the specific internal energy e can be deduced.

$$\frac{p}{\rho} = RT \tag{A.1.3}$$

$$e = f(p, \rho) = \frac{p}{(1-\gamma)\rho} \tag{A.1.4}$$

where R denotes the specific gas constant for dry air, for which holds $R = 287\text{J/kgK}$. For most industrial applications it is hardly possible to obtain an analytical solution to the Euler equations. Thus, numerical techniques have been developed that transform the system of PDEs into algebraic equations that can be solved discretely. To do so, the computational domain (i.e. the wave rotor channel) needs to be discretised into a finite number of elements. Integrating the governing Equation A.1.1 with respect to time and space and rearranging yields

$$\mathbf{U}_i^{n+1} = \mathbf{U}_i^n - \frac{\Delta t}{\Delta x} \Big(\mathbf{F}_{i+1/2}^n - \mathbf{F}_{i-1/2}^n \Big) \tag{A.1.5}$$

According to Toro [127], the resulting scheme is unconditionally unstable. The Lax-Friedrichs scheme rectifies this by defining the intercell flux $\mathbf{F}^{\mathrm{n}}_{\mathrm{i+1/2}}$ by

$$\mathbf{F}^n_{i+1/2} = \frac{1}{2}\left(\mathbf{F}(\mathbf{U}_{i+1}) + \mathbf{F}(\mathbf{U}_i)\right) \tag{A.1.6}$$

and substituting $\mathbf{U}^n_i$ by the average of the two neighbouring values, so that one obtains a scheme of first order accuracy.

$$\mathbf{U}^{n+1}_i = \frac{1}{2}\left(\mathbf{U}^n_{i+1} + \mathbf{U}^n_{i-1}\right) - \frac{\Delta t}{2\Delta x}\left(\mathbf{F}^n_{i+1} - \mathbf{F}^n_{i-1}\right) \tag{A.1.7}$$

A.1.2 Two-Step Richtmyer

Increasing the order of accuracy and thus remedying the shortcomings of first-order methods requires central differences for both space and time derivatives. The proposed scheme by Richtmyer suggests a two-step technique where additional half timesteps are introduced. The first step consists of the Lax-Friedrichs method thus giving

$$\begin{aligned}
\mathbf{U}^{n+1/2}_{i+1/2} &= \frac{1}{2}\left(\mathbf{U}^n_{i+1} + \mathbf{U}^n_i\right) - \frac{\Delta t}{2\Delta x}\left(\mathbf{F}^n_{i+1} - \mathbf{F}^n_i\right) \\
\mathbf{U}^{n+1/2}_{i-1/2} &= \frac{1}{2}\left(\mathbf{U}^n_i + \mathbf{U}^n_{i-1}\right) - \frac{\Delta t}{2\Delta x}\left(\mathbf{F}^n_i - \mathbf{F}^n_{i-1}\right)
\end{aligned} \tag{A.1.8}$$

The second step uses central differences to obtain

$$\mathbf{U}^{n+1/2}_i = \mathbf{U}^n_i - \frac{\Delta t}{\Delta x}\left(\mathbf{F}^{n+1/2}_{i+1/2} - \mathbf{F}^{n+1/2}_{i-1/2}\right) \tag{A.1.9}$$

A.1.3 Shock Tube Test I

In order to investigate the shock capturing abilities of the two mentioned schemes, they are applied to a shock tube test. The well established and documented test consists of a straight channel, which, at t=0s, is divided into two sections through a diaphragm of different condition (for the primitive variables p, ρ and u). Upon opening the diaphragm, a shock, expansion wave and a rarefaction wave are created travelling along the shock tube. The test serves as an excellent opportunity to show how accurately a numerical scheme can reproduce the flow discontinuities in comparison with

the exact solution of the shock tube problem.

Table A.1: Shock tube test initial conditions. Note that density if given in kg/m^3, velocity in m/s and pressure kPa.

ρ_L	1
u_L	75
p_L	100
ρ_R	0.125
u_R	0
p_R	1

A comparison of shock tube results for the Lax-Friedrichs and the Richtmyer scheme is given in Figure A-1. The distribution at t=7e-4 s of four different variables, pressure, density, velocity and specific internal energy are presented. As expected, the first order scheme of Lax-Friedrichs excessively smears gradients, while Richtmyer's scheme produces dispersive errors near discontinuities.

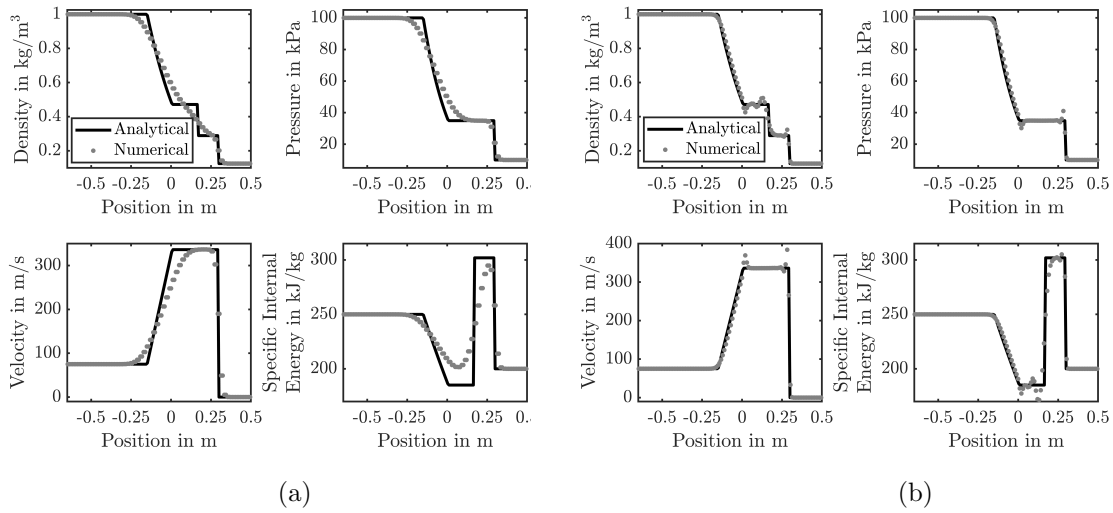

Figure A-1: Shock tube test to analyse shock capturing abilities of (a) Lax-Friedrichs and (b) Richtmyer numerical schemes. The plots show the distribution of density, pressure, velocity and specific internal energy at t=7e-4 s after breaking of the diaphragm. From left to right, the flow first experiences a left running expansion wave, followed by right running contact discontinuity and shock wave. While the Lax-Friedrichs scheme smears large gradients, the Richtmyer scheme reproduces the flow phenomena well albeit creating spurious oscillations.

A.2 High Resolution Schemes

The virtue of second-order accuracy and its supremacy over first-order schemes is exhibited by Figure A-1. Nonetheless, neither of the two schemes can deliver what is desirable when it comes to dissipation and dispersion. To mitigate the effect of dispersion while maintaining second-order accuracy, a number of measures are available. First of all, one can introduce second or fourth order terms into the system of equations to foster diffusive behaviour. However, the amount of dissipation is then controlled via a single parameter, which needs to be adjusted given the respective problem at hand. One should bear in mind that a value holding for one problem, may not be suitable for a different one. Therefore, the more elaborate techniques of flux corrected transport (FCT) and time variation diminishing (TVD) are investigated further.

A.2.1 Flux Corrected Transport

The FCT method is a post-processing scheme as it uses the original second-order solution and updates it using a diffusive flux aimed at eradicating any dispersive errors. It then applies an anti-diffusive flux to counteract the effect of the added diffusion in areas, where no large gradients are needed.

Diffusion Stage

After the states at the new time step are calculated, a diffusive flux θ is defined as

$$\theta(\mathbf{U}^n) = \frac{\omega}{4}\left(\mathbf{U}^n_{i+1} - \mathbf{U}^n_i\right) \tag{A.2.1}$$

where ω is a weighting factor that according to Winterbone and Pearson [129] affects the stability limit and may require fine-tuning to ensure dispersion does not occur. The diffusion stage is completed by updating the states through the diffusion operator $\mathbf{D}$.

$$\begin{aligned} \widetilde{\mathbf{U}}^{n+1} &= \mathbf{U}^{n+1} + \mathbf{D}(\mathbf{U}^n) \\ \text{with } \mathbf{D}(\mathbf{U}^n) &= \theta(\mathbf{U}_{i+1/2}) - \theta(\mathbf{U}_{i-1/2}) \end{aligned} \tag{A.2.2}$$

Anti-Diffusion Stage

The approach for the anti-diffusion stage is not entirely different from the diffusion stage. It essentially comprises the application of an anti-diffusion operator $\mathbf{A}$,

which yields

$$\mathbf{A}\big(\mathbf{U}^{n+1}\big) = \Psi\big(\mathbf{U}^{n+1}_{i-1/2}\big) - \Psi\big(\mathbf{U}^{n+1}_{i+1/2}\big) \tag{A.2.3}$$

The anti-diffusion operator is based on the anti-diffusion flux Ψ. In order not to create new dispersive errors, Ψ requires a limiter. The limited flux presented by Ikeda and Nakagawa [130] proved to exhibit good results and reads

$$\begin{aligned} \Psi(\mathbf{U}_{i+1/2}) &= s\max\big[0,\ \min(5/8s\Delta\mathbf{U}_{i-1/2}, 1/8|\Delta\mathbf{U}_{i+1/2}|,\ 5/8s\Delta\mathbf{U}_{i+3/2})\big] \\ &\text{with } s = \operatorname{sgn}\big(\Delta\mathbf{U}_{i+1/2}\big) \end{aligned} \tag{A.2.4}$$

Finally, the new states can be computed from

$$\widehat{\mathbf{U}}^{n+1} = \widetilde{\mathbf{U}}^{n+1} + \mathbf{A}\big(\widetilde{\mathbf{U}}^{n+1}\big) \tag{A.2.5}$$

A.2.2 Time Variation Diminishing

The TVD scheme is based on the notion that the total variation of a particular solution does not increase as one proceeds from one time step to another. Winterbone and Pearson [128, 129] define the total variation of the state vector for a given time as

$$\mathrm{TV}(\mathbf{U}^n) = \sum_i \big|\mathbf{U}^n_{i+1} - \mathbf{U}^n_i\big| \tag{A.2.6}$$

and state that the criterion of TVD is fulfilled when Equation A.2.2 holds.

$$\mathrm{TV}(\mathbf{U}^{n+1}) \leq \mathrm{TV}(\mathbf{U}^n) \tag{A.2.7}$$

In this project, the TVD scheme of Davis [131, 132] is used. Similar to FCT, TVD is applied as a post-processing method. Davis' scheme employs an additional dissipative term that ascertains the level of dissipation necessary to comply with TVD requirements. Moreover, the approach does not contain any free parameters that require user tweaking. After the states of the next time step are computed by the

second-order method, the following terms are added to the states

$$\widehat{\mathbf{U}}^{n+1} = \mathbf{U}^{n+1} + \left[\bar{\mathbf{G}}^{+}(r_i^{+}) + \bar{\mathbf{G}}^{-}(r_{i+1}^{-})\right]\mathbf{U}_{i+1/2}^{n} - \left[\bar{\mathbf{G}}^{+}(r_{i-1}^{+}) + \bar{\mathbf{G}}^{-}(r_i^{-})\right]\mathbf{U}_{i-1/2}^{n} \tag{A.2.8}$$

where the vector $\bar{\mathbf{G}}$ is defined as

$$\begin{aligned} \bar{\mathbf{G}}^{\pm}(r_i^{\pm}) &= \frac{1}{2}C(v)[1-\phi(r_i^{\pm})] \\ \text{with} \quad C(v) &= \begin{cases} v(1-v) & \text{for } v \leq 0.5 \\ 0.25 & \text{for } v > 0.5 \end{cases} \end{aligned} \tag{A.2.9}$$

The gradients of the data are computed as defined by Winterbone and Pearson [129]

$$\begin{aligned} r_{i-1}^{+} &= \frac{\langle \Delta\mathbf{U}_{i-3/2}, \Delta\mathbf{U}_{i-1/2}\rangle}{\langle \Delta\mathbf{U}_{i-1/2}, \Delta\mathbf{U}_{i-1/2}\rangle}, \quad r_i^{-} = \frac{\langle \Delta\mathbf{U}_{i-1/2}, \Delta\mathbf{U}_{i+1/2}\rangle}{\langle \Delta\mathbf{U}_{i-1/2}, \Delta\mathbf{U}_{i-1/2}\rangle} \\ r_i^{+} &= \frac{\langle \Delta\mathbf{U}_{i-1/2}, \Delta\mathbf{U}_{i+1/2}\rangle}{\langle \Delta\mathbf{U}_{i+1/2}, \Delta\mathbf{U}_{i+1/2}\rangle}, \quad r_{i+1}^{-} = \frac{\langle \Delta\mathbf{U}_{i+1/2}, \Delta\mathbf{U}_{i+3/2}\rangle}{\langle \Delta\mathbf{U}_{i+1/2}, \Delta\mathbf{U}_{i+1/2}\rangle} \end{aligned} \tag{A.2.10}$$

There exists a myriad of flux limiters with different levels of dissipative behaviour. For all wave rotor simulations, the minmod limiter by Roe [133], was used. It is formulated as

$$\phi(r) = \max[0, \min(1, r)] \tag{A.2.11}$$

A.2.3 Shock Tube Test II

Comparison of FCT and TVD schemes is completed via a modified shock tube test with the initial conditions given by Table A.2. Velocities and densities are the same in both sections. The pressure in the left part, however, is by a factor 10^5 higher. This shall test the solver robustness when dealing with strong shock waves.

Table A.2: Shock tube test initial conditions for FCT and TVD Richtmyer scheme. Note that density if given in kg/m^3, velocity in m/s and pressure kPa.

ρ_L	1
u_L	75
p_L	10000
ρ_R	1
u_R	0
p_R	1

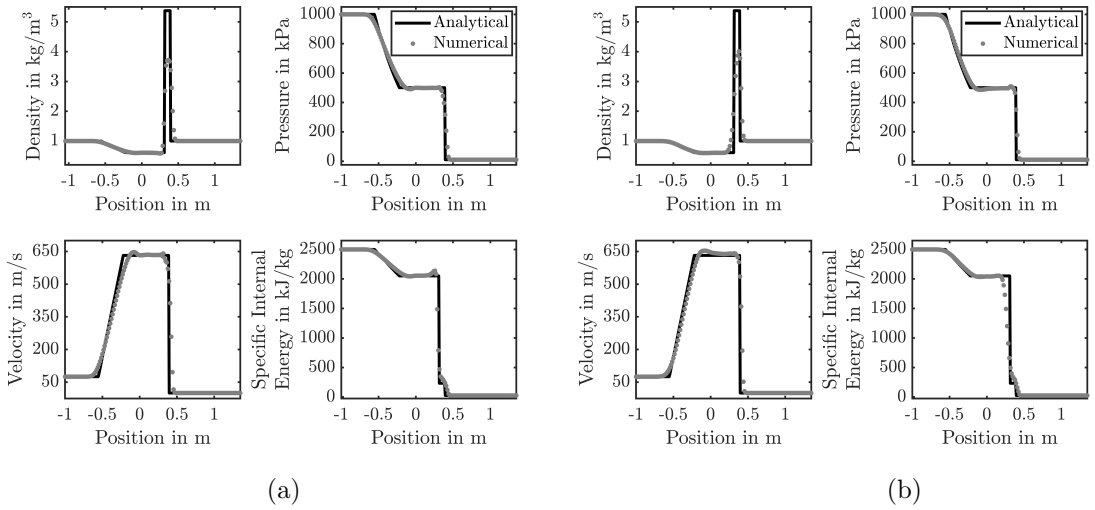

Figure A-2: Shock tube test comparing shock capturing abilities of (a) Richtmyer-FCT and (b) Richtmyer-TVD numerical schemes. The plots show the distribution of density, pressure, velocity and specific internal energy at t=7e-4 s after breaking of the diaphragm. From left to right, the flow first experiences a left running expansion wave, followed by right running contact discontinuity and shock wave. Both schemes feature good agreement with the analytical data. The FCT scheme produces an overshoot in velocity at the left running expansion wave and specific internal energy near the shock wave. The TVD scheme with the minmod flux limiter exhibits a minor overshoot of pressure in the vicinity of the shock wave and a slightly smaller overshoot for velocity.

The results of the shock tube test for Richtmyer-FCT and Richtmyer-TVD in comparison with analytical data is shown in Figure A-2. In general, both schemes yield similar results. In terms of velocity and specific internal energy, the FCT scheme produces both an overshoot near the left running expansion wave for the former and also near the shock wave for the latter. The TVD scheme with the minmod flux limiter exhibits a minor overshoot of pressure in the vicinity of the shock wave and a slightly smaller overshoot for velocity.

Although both schemes give comparable and satisfying results, the Richtmyer-

TVD scheme will be used throughout further computations. The reason for this lies in the fact, that the FCT scheme comprises a free parameter, which may not be determined that easily. Furthermore, Winterbone and Pearson [128] suggest using the TVD scheme, as it is derived from a more stringent mathematical foundation.